Award Number: W81XWH-20-1-0576

TITLE: Low-Cost, High-Throughput 3D Pulmonary Imaging Using Hyperpolarized Propane Gas

PRINCIPAL INVESTIGATOR: Eduard Y. Chekmenev, Ph.D.

CONTRACTING ORGANIZATION: Wayne State University, Detroit, MI

REPORT DATE: August 2021

TYPE OF REPORT: Annual

PREPARED FOR: U.S. Army Medical Research and Materiel Command
                            Fort Detrick, Maryland, 21702-5012

REPORT DOCUMENTATION PAGE

1. REPORT DATE	2. REPORT TYPE	3. DATES COVERED
August 2021	Annual	15Jul2020-14Jul2021

4. TITLE AND SUBTITLE	5a. CONTRACT NUMBER
Low-Cost, High-Throughput 3D Pulmonary Imaging Using Hyperpolarized Propane Gas	W81XWH-20-1-0576
	5b. GRANT NUMBER
	5c. PROGRAM ELEMENT NUMBER

6. AUTHOR(S)	5d. PROJECT NUMBER
Eduard Y. Chekmenev, Ph.D.	
	5e. TASK NUMBER
E-Mail: chekmenev@wayne.edu	**5f. WORK UNIT NUMBER**

7. PERFORMING ORGANIZATION NAME(S) AND ADDRESS(ES)	8. PERFORMING ORGANIZATION REPORT NUMBER
Wayne State University 5101 Cass Ave DETROIT, MI, 48202	

9. SPONSORING / MONITORING AGENCY NAME(S) AND ADDRESS(ES)	10. SPONSOR/MONITOR'S ACRONYM(S)
U.S. Army Medical Research and Materiel Command Fort Detrick, Maryland 21702-5012	
	11. SPONSOR/MONITOR'S REPORT NUMBER(S)

12. DISTRIBUTION / AVAILABILITY STATEMENT

Approved for Public Release; Distribution Unlimited

13. SUPPLEMENTARY NOTES

14. ABSTRACT

This report covers the first year of this three-year project. During the indicated period of performance, we have focused our activities on two specific aims. With regards to Aim #1 (to develop a clinical low-cost and high-throughput device for production and administration of HP propane contrast agent for ultimate research use in volunteers), we have designed the proposed device and have been testing this device. With respect to Aim #2 (To develop a safe method for HP propane gas administration and utilization, and test the purity and safety of the HP contrast agent produced by our device) we have been primarily focusing on developing approaches and testing the quality of the produced gas in the context of reaction completeness. While the progress of working on all aims of this project has been substantially impacted by the COVID-19 pandemic, we could not make any progress towards Aim #3 (To assess the feasibility of MRI using HP propane gas for *in vivo* functional imaging of normal lungs and in a bleomycin-induced COPD model in sheep) primarily because the required instrumentation (0.35 T MRI) installation process could not be completed due to the pandemic restrictions. We expect to make substantially more progress towards all three aims of the project in the next year after the pandemic-related restrictions have been largely lifted and both performance sites have been re-opened.

15. SUBJECT TERMS
low-field MRI; pulmonary imaging, high-throughput; low cost

16. SECURITY CLASSIFICATION OF:			17. LIMITATION OF ABSTRACT	18. NUMBER OF PAGES	19a. NAME OF RESPONSIBLE PERSON USAMRMC
a. REPORT	**b. ABSTRACT**	**c. THIS PAGE**	Unclassified	99	**19b. TELEPHONE NUMBER** *(include area code)*
Unclassified	Unclassified	Unclassified			

Table of Contents

1. Introduction

We are developing a low-cost and high-throughput propane hyperpolarization and 3D sub-second imaging technology that can be used for functional MRI imaging of lungs, and that can be deployed to remote areas without specialized infrastructure (e.g. cryogens). The other essential component, the FDA-approved 0.35 T MRI scanner, is already commercially available. Thus, the integrated imaging platform (0.35 T MRI scanner and propane hyperpolarizer) will enable high-throughput population screening and monitoring response to treatment for a wide range of lung diseases. The end result of the project will be the development of a clinical propane hyperpolarizer, *in vivo* validation of the hyperpolarizer and contrast agent administration system, and commercialization. The next step will be an FDA-approved clinical trial. We focus our research effort on the high-risk critical challenges that must be solved to enable clinical implementation of hyperpolarized gases for pulmonary imaging.

Here, we propose taking the next significant step to develop and test a hyperpolarized propane production technology device under the Specific Aims described below:

Specifically, the research efforts during Year 1 have focused on two specific aims as described in the Statement of Work (Appendix 1). The work under Aim #3 was postponed due to covid-19 pandemic effects.

<u>Aim 1</u>. Develop a clinical low-cost and high-throughput biomedical device for production of hyperpolarized propane contrast agent: the future propane hyperpolarizer will be developed to enable its Good Manufacturing Practices (GMP), mass-production, and robust use;

The plastic propane polarizer device (using commercially available components) originally proposed did not meet the requirements for temperature handling. As a result, our efforts quickly switched to a copper-based housing of the reactor with sufficiently wide diameter to accommodate the flow rate required for the clinical-scale production in 1-2 seconds. The Accomplishments section below details our efforts related to the overall design, optimization and multi-parametric testing of the disposable polarizer (in line with the SOW).

<u>Aim 2.</u> Develop a safe method for HP propane gas administration and utilization, and test the purity and safety of the HP contrast agent produced by our device;

The activities during Year 1 of the project primarily focused on developing new approach for safe gas administration and some efforts were spent to develop approached for quantitative testing of propylene impurities.

<u>Aim 3</u>. Assess the feasibility of MRI using HP propane gas for *in vivo* functional imaging of normal lungs and in a bleomycin-induced COPD model in sheep. We will compare the effectiveness of hyperpolarized propane MRI to that using a more established contrast agent (hyperpolarized ^{129}Xe gas—created using a polarizer we developed in our previous DOD-funded work), and also to the standards of care: computed tomography and spirometry. Furthermore, we will also investigate the effectiveness of hyperpolarized propane gas MRI to monitor the progression of bleomycin-induced lung injury in the sheep animal model.

No progress was made towards this Aim due to effect of the pandemic, because 0.35 T MRI scanner (proposed for this work) could not be installed during Year 1. The scanner installation is scheduled for September 2021. To partially mitigate this challenge, we performed some imaging studies using 3.0 T clinical MRI scanner at Michigan State University in Dr. Qian lab – our new collaborator. The rationale for these studies was to test the feasibility of packaging and utilization of disposable hyperpolarizer to demonstrate feasibility of imaging studies. The details are provided under Aim #1 Accomplishments below.

2. Keywords

Low-field MRI, lung imaging, molecular imaging, functional imaging; propane; xenon-129; NMR; MRI; hyperpolarization.

3. ACCOMPLISHMENTS

Please refer to Appendix 1 for the statement of work (SOW) of the entire project. The following sections describe the specific areas/tasks of the project conducted during Year 1 of this project.

Aim 1. To develop a clinical low-cost and high-throughput device for production and administration of HP propane contrast agent for ultimate research use in volunteers

Subtask #1-1: Design of the clinical propane hyperpolarizer

A new clinical hyperpolarizer design has been developed that employs a mixture of propylene and parahydrogen. When these two gases are flowed over a heterogeneous PHIP catalyst, pairwise parahydrogen addition renders a propane product molecule in a proton-hyperpolarized state (shown farther below in Figure 2). In our originally proposed design, we planned on employing on-site dispensing of propylene and parahydrogen in a clinical gas bag. During the hyperpolarization procedure, the bag would be compressed to enable reagent flow through the reactor. In our initial testing of this design, two challenges were uncovered. First, the mixing procedure is not trivial and would be challenging in the clinical setting from the perspective of robustness, cost of the infrastructure, and fire safety. Second, the reactor jacket made of plastic could not sustain elevated temperature.

Design. As a result of the above limitations, a new container for parahydrogen storage was tested. We tested aluminum cans (~120 cm^3 and ~250 cm^3) equipped with a high-flow valve (>0.5 standard liters per second (SLS)). This type of aluminum can is a standard container employed for storage and dispensing of a wide range of sprays (*e.g.*, deodorants, oils, drugs, etc.). The prototype valve available to us contained a steel spring, and the valve was mounted on a tin cup (also made of steel). The cup is needed to seal the can and to maintain high pressure (Figure 1).

Tests. We developed an approach to test the quality of parahydrogen gas (parahydrogen fraction) using benchtop NMR spectroscopy (Nantogma, et al. *Anal. Chem*. **2021** and Chapman, et al. *Anal. Chem*. **2021**, see Products below). Our initial test revealed that the decay rate of parahydrogen in these cans is mono-exponential with T_1 decay constant of 5.4±1.6 days. We have also tested the decay rate of parahydrogen in mixtures with propylene and concluded that the decay rate is similar, indicating the presence of propylene gas does not impact parahydrogen decay. Based on our previous studies with aluminum storage containers for parahydrogen, this finding indicates that paramagnetic components of the current prototype (magnetic spring and magnetic cup) are most likely the dominant contributing factors that limit the lifetime of parahydrogen potency in these containers. We are now working (with commercial vendors) on replacing these magnetic components with non-standard non-magnetic parts to potentially substantially lengthen the lifetime of parahydrogen in these containers. Based on our prior study (Feng, et al. *J. Magn. Reson*. **2012**, *214*, 258-262) we believe it will be possible to extend the lifetime of parahydrogen in this storage container to 64±8 days, thereby allowing for long-term storage of parahydrogen-propylene mixtures for many weeks without substantial potency loss of produced hyperpolarized propane. This means it would become possible to produce the desired parahydrogen-propylene mixture in small, single-dose pressurized containers in a centralized facility, which could then be distributed to clinical facilities in the future envisioned clinical use. We note that the cost of this disposable container is negligible (less than $1). Moreover, we have recently demonstrated high-throughput parahydrogen production (Nantogma, et al. *Anal. Chem*. **2021**) with production rate of up to 4 standard liters per minute (SLM). Because the loading ("charge") for each can requires less than 2 standard liters of parahydrogen, one such parahydrogen generator can enable production of up to 120 filled cans per hour or up to ~0.3 million cans per year. This high throughout is important for two reasons. First, it reduces the per-dose cost of the produced mixture (to $1-$2) and one device can enable many simultaneous future clinical studies.

Feasibility studies. We have performed two kinds of feasibility studies with our storage containers. In the first kind, we have filled the cans on-site and employed them for longitudinal studies of parahydrogen decays as described above. For the second group of studies, the cans were filled and transported to a different site (~1.5 h driving distance) to validate that these mixtures can produce hyperpolarized propane suitable for imaging studies using a 3 T clinical MRI scanner. In our first non-optimized feasibility studies, we have demonstrated that EPI imaging of hyperpolarized propane gas yields signal-to-noise similar to that of thermally polarized water at 3 T. These feasibility studies clearly demonstrate that we can fill the can with a parahydrogen-propylene mixture in a centralized location (our lab) and deploy such cans to a different site after transportation without any deleterious effects beyond those that we measured in our on-site longitudinal studies.

Reactor. The reactor was connected to the can via adapters shown in Figure 1. In our feasibility studies, we have employed several in-line adapters to maintain the convenience and versatility of our device. In the clinical future studies, we envision replacing all adapters by a single actuator that allows releasing the gas from the can

and direct it to a reactor that is mated to a commercially available mouth piece. The reactor is made of food-grade copper tubing filled with catalyst and food-grade copper beads. The catalyst is made of Rh nanoparticles deposited on titania (TiO_2), which is commonly used in foods and pharmaceutical applications. The current design employs approximately 200 mg of titania and 2 mg of Rh. The total cost of materials for the can, adapters, and the reactor is less than \$20—with the bulk of the cost realized in the brass fittings, noting that only very small amounts of Rh are used (Figure 1). The future refinement of this design on commercial-production scale can potentially reduce the cost of the components to less than \$10 per device.
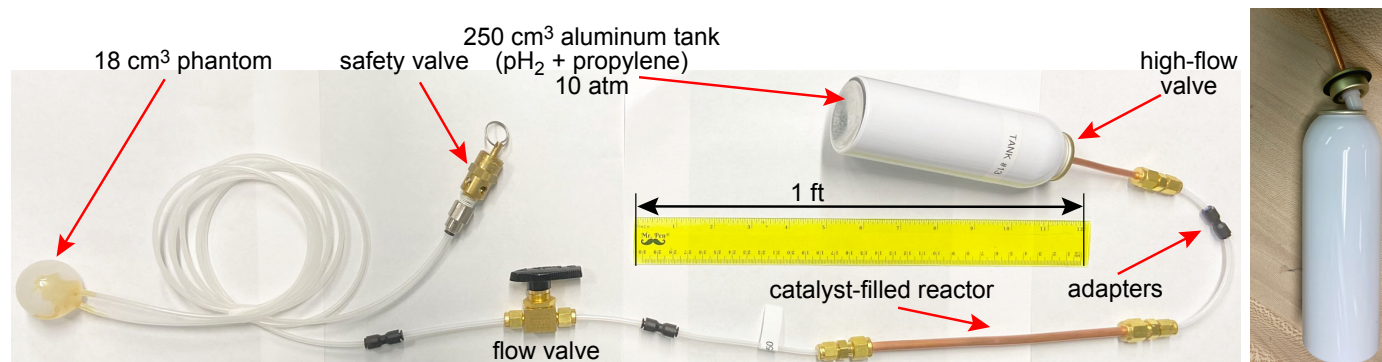

Figure 1. (left) Photograph of the clinical polarizer prototype. The components after the catalyst-filled reactor are optional, because they are required only for phantom studies conducted at elevated pressure of ~2-4 atm pressure. **(right)** Close-up photo of aluminum can and high-flow valve (white plastic) mounted on magnetic cup. The cup is mounted on the can using compression crimp tool. The cup is needed to seal the (otherwise open) can and to maintain high pressure.

The work during Year 2 (in line with SOW) will focus on the optimization of the polarizer design in the following key areas: improving the gas flow (from current maximum of 0.1 SLS to 0.5 SLS), improving the simplicity of the can-to-reactor connections (via custom fitting already in production), improving the overall potency of produced hyperpolarized propane, and extending the lifetime of parahydrogen in the storage can.

Subtask #1-3: Optimize propane hyperpolarizer performance

Although these activities were originally planned for Year 2 (see SOW below), the dramatic changes induced by the COVID-19 pandemic allowed us to make advances only in selected areas. As a result of these limitations, our team has focused on developing assays to quantitatively measure the performance of the polarizer with the following metrics: (i) level of polarization in produced hyperpolarized propane; (ii) maximum reactor flow rate; and (iii) fraction of completeness of chemical conversion of propylene + parahydrogen mixture to hyperpolarized propane. Note that the last parameter (iii) also affects the calculation of the level of polarization (i). When the lifetime of the hyperpolarized state is short (*i.e.*, on the order of seconds), there are practical challenges with hyperpolarized signal measurement (due to fast decay and delay needed to acquire the signal) before it decays back to equilibrium. The challenge is exacerbated by the fact that we aim to produce over 0.1-0.5 SL, whereas the detection volume of a conventional high-resolution NMR spectrometer is at least three orders of magnitude lower. Two additional complications arise (as the aftermath of the above challenges): (1) the travel time from the reactor to our detector must be substantially shorter than the decay rate of hyperpolarized state. While this issue is well mitigated by the high flow rate of hyperpolarized gas exiting the reactor, fast-flowing gas results in significantly diminished NMR signal, which (2) makes polarization quantification non-trivial.

Sub-second gas-phase 1.4 T bench-top NMR spectroscopy was developed to probe the level of propane polarization. In our approach, we rapidly acquire 64 NMR spectra every 0.5 seconds, thereby capturing the dynamics of gas flow and relaxation. During gas flow, the NMR lines of HP propane are broadened, resulting in low apparent propane polarization. Once the hyperpolarized gas is stopped, full NMR signal is observed, Figure 2. Subsequent NMR acquisitions with low (~12 degree) excitation RF pulses allow detection and measurement of polarization decay. After this experiment is completed, we performed similar experiments on thermally polarized propane, which serve two purposes: thermal reference for measurement of signal enhancements and detecting conversion of propylene to propane. We have tailored previously developed MATLAB code (for hyperpolarized [129]Xe studies) for the automated data processing and fitting of hyperpolarized propane gas.
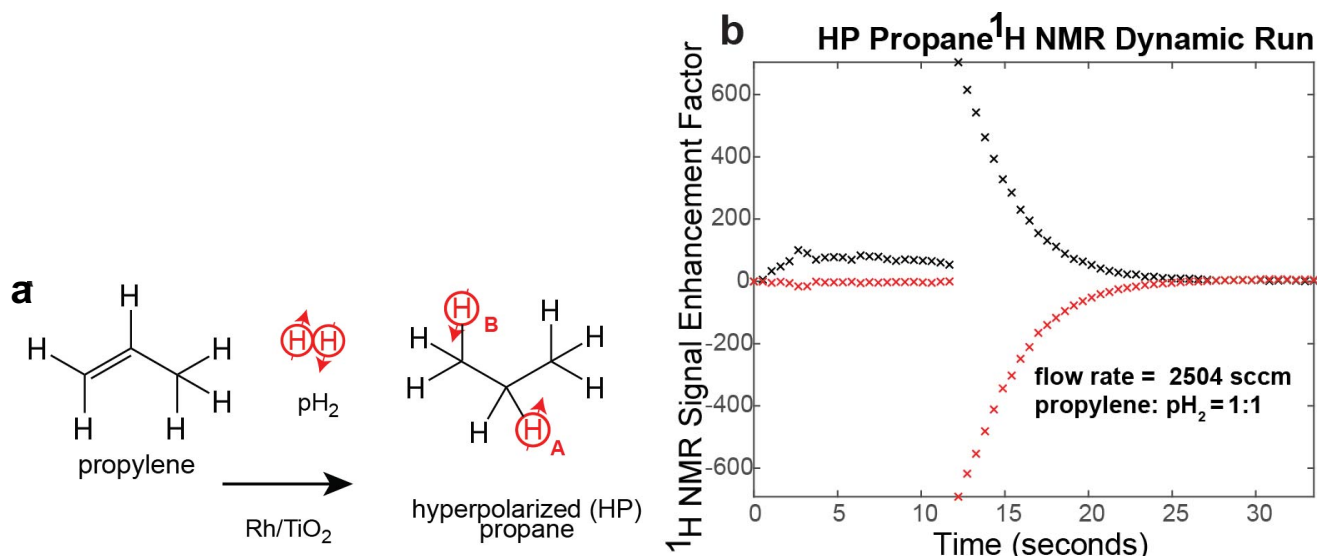
Figure 2. **(a)** Pairwise parahydrogen addition to propylene leads to production of hyperpolarized propane gas with H_A and H_B protons polarized. **(b)** Fast pseudo 2D signal acquisition method: Signal acquisition is started along with the gas flow and the flow is terminated after a few seconds while continuing the spectral acquisition: flowing gas-broad lines, stopped gas T_1 decay. Continuous signal acquisition over gas flow to monitor hyperpolarized signal build up and hyperpolarized signal decay. Each data point (for H_A and H_B) corresponds to individual NMR spectrum acquisition. In display b, the black trace corresponds to hyperpolarized proton H_A, and the red trace corresponds to H_B.

The diagam of the developed experimental setup is shown in Figure 3.
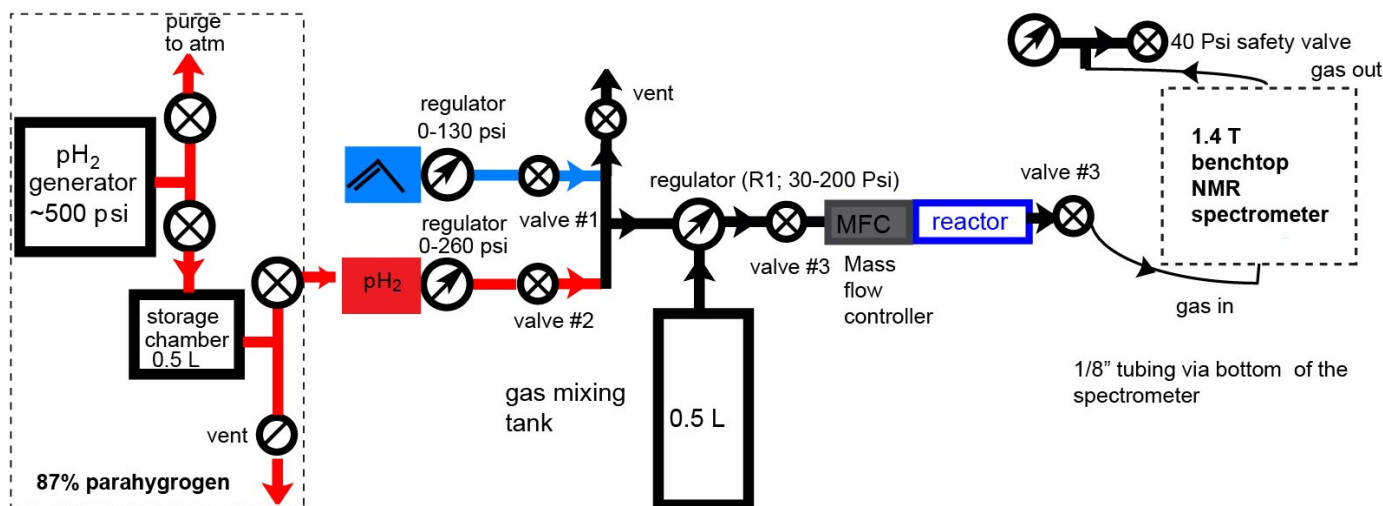
Figure 3. Schematic of the experimental setup employed for sub-second pseudo-2D NMR acquisition studies. Two gas handling approaches are established. In one approach, we employ a portable 87% parahydrogen generator to fill 0.5 L mixing tank to prepare custom propylene-parahydrogen mixtures. In the other approach, the schematic shown in Figure 1 is employed with a 1.4 T NMR spectrometer.

Toward clinical-scale production at 1 atm reactor pressure. Our previous limited studies indicated that the degree of parahydrogen pairwise addition (and by extension the degree of propane polarization) may benefit substantially from elevated reaction mixture pressure and parahydrogen pressure in particular. The new setup shown in Figure 3 allowed us to perform more systematic studies, Figure 4. While the increase of parahydrogen pressure (by a factor of 4) does indeed increase the level of propane polarization (by approximately a factor of 1.5), this increase is too small to balance the resulting dilution of the produced hyperpolarized propane (by residual unreacted parahydrogen) by a factor of 3. On the other hand, the pressure dependence of signal enhancement on the total reaction pressure clearly shows a nearly flat line. This is important, because high levels of propane polarization can be obtained even at low pressure – most importantly at physiological pressure of 1 atm.

Figure 4. Dependence of produced hyperpolarized propane polarization on the reactor total pressure using 1:1 propylene:parahydrogen mixture (left) and 1:4 propylene:parahydrogen mixture (right).

Clinical hyperpolarized propane gas administration. As a result of this finding, we will proceed with direct administration of hyperpolarized propane (exiting from the reactor shown in Figure 1) via a mouth piece using a concept already established comme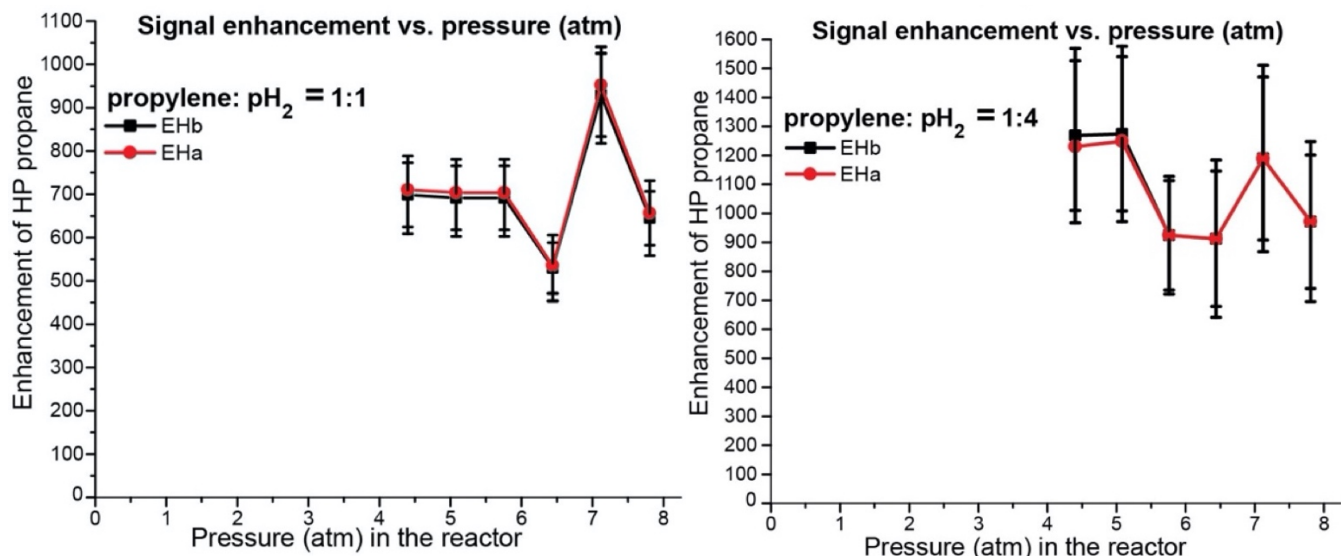rcially. Figure 5 shows the Boost oxygen product (~2 standard liter capacity, 110 mL volume), which features a mouth piece that allows direct gas administration from a pressurized (~18 atm) can into a human mouth. The excess pressure is released via a second safety opening. This safety opening will be connected to a carbon filter (in our design) to capture potentially flammable propane. We have already begun initial testing of this approach in some of our feasibility studies. Our work during Year 2 will focus on thorough studies of the efficacy of this approach in terms of feasibility, speed, and efficacy of propane capture by a carbon filter.

Figure 5. (left) Boost-oxygen aluminum can containing 2 standard liters (SL) of 95% O_2. The mouth piece is placed directly in the mouth of a person (right) to eject pressurized (~18 atm) gas. Excess pressure is balanced by a safety exit opening in the mouth piece. We plan on using the same approach for hyperpolarized propane administration after gas exits from the reactor.

Polarizer optimization. When propylene-parahydrogen mixture flows over the catalyst bed in the reactor, a substantial amount of heat is released internally, leading to reactor self-activation. As a result, it is possible to employ our reactor without an additional heating source. The exiting gas has low thermal capacity, resulting in rapid temperature drop (as warm gas exits)—suitable for administration. The activation happens quickly (likely after ~0.02 SL of reaction mixture passes through the reactor). Figure 6 shows the time course dependence showing robust polarizer performance during a ~15-second-long production period with the flow rate of 3 SLM

(over 0.5 SL of HP propane is produced in that period of time). This is important, because operation of the polarizer at ambient temperature substantially simplifies the polarizer operation in a clinical setting. Note that signal enhancement of 1,500-fold (Figure 6) corresponds to ~1% propane polarization.
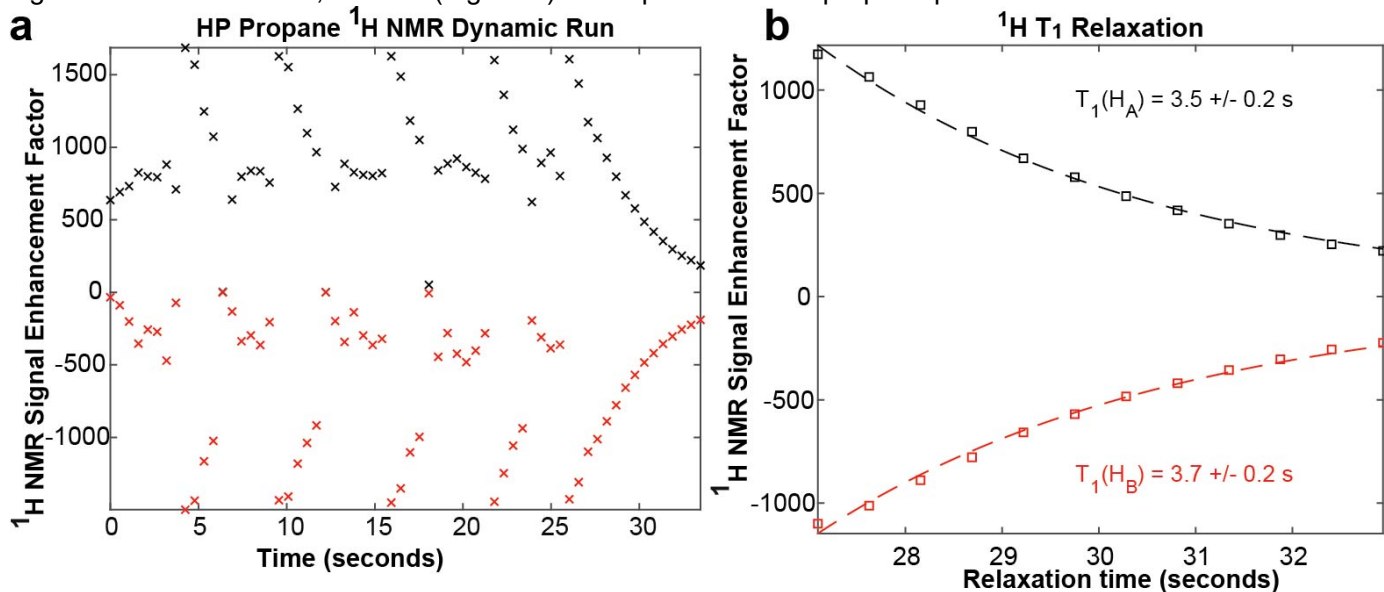
Figure 6. **(left)** Propane hyperpolarization signal enhancement dependence detected during the hyperpolarization process. The gas is flowing during ~4 s-long periods, followed by flow cessation to detect signal enhancement; the process is repeated 5 times. **(right)** Decay of flow-stopped HP propane gas after the final gas flow cessation. Decay constant is determined using automated MATLAB processing code. The reactor employed is built using ¼-inch Cu tube filled with ~7 g of Cu particles and ~200 mg of 1% Rh / TiO$_2$. Reproducible HP propane signal enhancements with gas flow duration with complete chemical conversion. Flow rate: ~3 SLM. Note signal enhancement of 1,500-fold corresponds to ~1% propane polarization.

We have also investigated the dependence of the resulting signal enhancement of hyperpolarized propane gas on the flow rate of produced hyperpolarized propane gas. As expected, when the condition of fast gas transfer is met (i.e., the polarization losses due to relaxation are negligible), the propane polarization level is approximately constant at various gas flow rates (Figure 7).
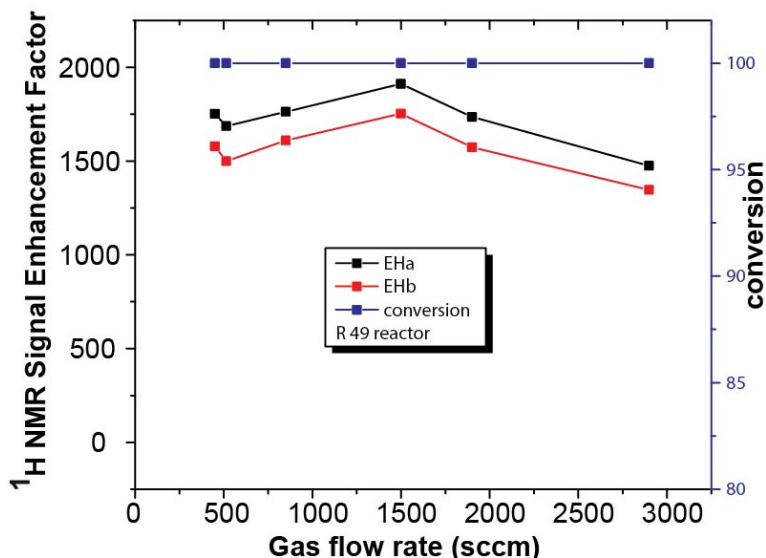
Figure 7. Hyperpolarized propane signal enhancement dependence on the gas flow rate using conditions of complete chemical conversion. The reactor employed is built using ¼-inch Cu tube filled with ~7 g of Cu particles and ~200 mg of 1% Rh / TiO$_2$.

Note the experiments presented in Figure 7 employed a maximum flow rate of ~3 SLM. These experiments were performed using our setup designed for systematic studies of trends. The ongoing experiments in Year 2 will focus on studying the reactor performance at substantially higher flow rates of 20-30 SLM, *i.e.* under conditions when a clinically relevant dose (ca. 0.5-1 L) is produced substantially faster than the polarization decay rate (*i.e.* in 2-3 seconds).

9

Disposable versus recyclable polarizer. Our polarizer can certainly be disposed as it inexpensive and (more importantly) does not contain any harmful materials: It will contain food-grade aluminum, food-grade copper, <2 mg of Rh and <500 mg of food-grade titania, and medical-grade particle filters. Because of low cost (cost of materials is ~$10) and harmless composition, it can be readily disposed after a single patient use. However, our pilot studies clearly indicate that the polarizer can also be re-used numerous times (current limited data indicate that many tens if not hundreds of cycles are feasible). As a result, the polarizer can in principle be recycled after sterilization instead of disposal. At this point of our research project, we leave the option to dispose or recycle our future product to future pilot clinical studies.

Specific Aim 2 - To develop a safe method for HP propane gas administration and utilization, and test the purity and safety of the HP contrast agent produced by our device

Subtask #2-2: Assess purity of produced HP propane gas by detecting the excipients

During Year 1 we have established a spectroscopic protocol to record gas-phase NMR spectra of the produced thermally polarized gas mixture. As a result, it became possible to measure the % of unreacted propylene gas – one potential unwanted excipient. For example, Figure 8 illustrates an example of incomplete chemical conversion (and thus high levels of unreacted propylene in the produced hyperpolarized mixture). We will continue using this spectroscopy assay in our final reactor optimization studies that take into account the length and diameter of the reactor, quality of catalyst, and its distribution along the reactor length.
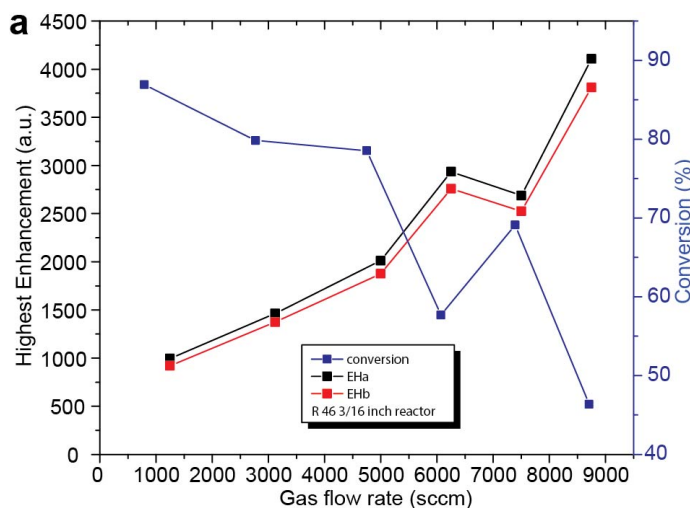
Figure 8. NMR spectroscopy detects incomplete chemical conversion of propylene:parahydrogen mixture using 3/16 inch reactor diameter, 10 cm long Cu tube reactor filled with ~4 g of Cu particles and ~100 mg of Rh / TiO$_2$. Data shows an increase of HP propane signal enhancement with gas flow rate at the expense of chemical conversion.

Moreover, we will perform elemental analysis for excipients (Rh, Ti, Si, Al, Cu) after completing the design after hyperpolarized propane production at high flow rates of 20-30 SLM,

Specific Aim 3 - To assess the feasibility of MRI using HP propane gas for *in vivo* functional imaging of normal lungs and in a bleomycin-induced COPD model in sheep

Because we could not make progress towards Aim 3 due to covid-19 pandemic restrictions as described above, our activities for Aim #3 were focused on maintaining the capability to produce hyperpolarized [129]Xe gas for future in vivo studies. We have also developed automated MATLAB processing tools to enable fast mapping of [129]Xe gas hyperpolarization process – see J. R. Birchall, R. K. Irwin, M. R. H. Chowdhury, P. Nikolaou, B. M. Goodson, M. J. Barlow, A. Shcherbakov, E. Y. Chekmenev, *Anal. Chem.* **2021**, *93*, 3883-3888 in the Products section.

What opportunities for training and professional development has the project provided?

Several trainees from Wayne State University (WSU) and from the partnering site Southern Illinois University Carbondale (SIUC) attended the 62nd (virtual) Experimental Nuclear Magnetic Resonance Conference (ENC) and 2nd (virtual) Parahydrogen Enhanced Magnetic Resonance Meeting (PERM).

How were the results disseminated to communities of interest?

Via oral and poster presentations (see below).

4. IMPACT

What was the impact on the development of the principal discipline(s) of the project?

Nothing to Report.

What was the impact on other disciplines?

Nothing to Report.

What was the impact on technology transfer?

Nothing to Report.

What was the impact on society beyond science and technology?

Nothing to Report.

5. CHANGES / PROBLEMS

As with much of the world, we have been impacted by Covid-19 in a number of ways. First, the pandemic has limited (or in some cases outright eliminated) opportunities for outreach, career development for trainees, and personnel exchange; it has also caused us to postpone certain technologies: most importantly the 0.35 T MRI scanner (key instrument required for Aim #3) installation has been delayed until Sept. 2021. To mitigate some of these issues, we have continued our regular teleconferences. Our labs are still recovering from several months of complete closure (the PI's lab and collaborative PI's lab partially re-opened from their complete closures in June 2020 and September 2020, respectively), and then several more months of partial (25%-75%) operation, with full operation more-or-less returning in May and June 2021, respectively. Social-distancing requirements, at least until relatively recently, have also made some types of experiments more difficult. While considerable time was lost, we have been working hard to gain back our full activity and productivity. We continue to remain ever hopeful that the pandemic will resolve soon so that we may fully return to normal operation (and indeed steps have moved in the right direction). Finally, our overall efforts are still recovering from the untimely passing of one of our key long-time collaborators (and friend): Dr. Kirill Kovtunov of ITC Novosibirsk, Russia. His role and expertise has been replaced by Dr. Larisa Kovtunova. Nevertheless, we look forward to hosting other scientists and trainees at our labs when it becomes easier to travel--which we hope will occur sometime in the months to come. Importantly, we have sought – and obtained – permission to re-budget some aspects of the funding at both sites—including to allow purchase of new low-field (0.065 T) Hyperfine MRI scanners; delivery of the first scanner, at the partnering site, is tentatively scheduled for mid-September 2021.

6. PRODUCTS

Oral Presentations

1) Goodson BM. "Hyperpolarizing nuclear spins of atoms and molecules with light and parahydrogen." Invited virtual seminar for the Department of Physics and Astronomy, Western Kentucky University, 9/14/2020.
2) Goodson BM. "Enhancing Magnetic Resonance Imaging with SABRE and LASERS", invited virtual seminar for ISTC R&D Index +Researchers to Know, 9/16/2020.
3) Goodson BM. "Hyperpolarizing nuclear spins of atoms and molecules with light and parahydrogen". Invited Chemistry Department Seminar(virtual), Wayne State University, 9/23/2020.
4) Goodson BM. "Hyperpolarizing nuclear spins of atoms and molecules with light and parahydrogen". Invited Chemistry Department Seminar(virtual), North Carolina State University, 9/29/2020.
5) Goodson BM. "Enhancing Magnetic Resonance Imaging with SABRE and LASERS", invited virtual seminar for "Advancing Research in Imaging", Research Enabled, 10/28/2020.
6) Goodson BM. "Hyperpolarizing nuclear spins of atoms and molecules with light and parahydrogen". Invited Chemistry Department Seminar(virtual), Southern Illinois University Carbondale, 3/26/2021.
7) Goodson BM. "Updates on Efforts to Hyperpolarize 131Xe and 117Sn." NOPTREX Meeting on Polarized Targets (virtual). 4/30/2021.
8) Goodson BM. "Updates on Efforts to Hyperpolarize 117Sn via SABRE" NOPTREX Meeting (virtual). 6/25/2021.
9) Chekmenev EY. Current & Future Clinical Oncology Applications. 22nd International Society for Magnetic Resonance in Medicine (ISMRM)& SMRT Virtual Conference & Exhibition 08-14 August 2020. Session Title: **Spectroscopy & Molecular Imaging of Cancer**, 11 August 2020, 14:30-15:15 UTC.
10) Chekmenev EY. "Hyperpolarized MRI contrast agents". Presented at Molecular Imaging Program 2021 Annual Retreat at Karmanos Cancer Institute (KCI), Wayne State University; 2021, May 05; Wayne State University, Virtual presentation, Detroit, MI, USA.
11) Chekmenev EY. "Hyperpolarized MRI contrast agents". Presented at Molecular Imaging Program External Expert Review Panel Meeting, Karmanos Cancer Institute (KCI) Wayne State University; 2021, June 29; Virtual presentation, Detroit, MI, USA.
12) Chekmenev EY. Virtual Undergraduate Seminar Series at San Francisco State University "Parahydrogen Induced Polarization for New MRI Contrast Agents and Jovian Planets" March 17, 2021.

Conference Abstracts

13) Ariyasingha, N. M.; Salnikov, O. G.; Joalland, B.; Younes, H. R.; Chukanov, N. V.; Kovtunov, K. V.; Kovtunova, L. M.; Bukhtiyarov, V. I.; Koptyug, I. V.; Gelovani, J. G.; Chekmenev, E. Y. In *Parahydrogen hyperpolarized diethyl ether for MRI*, EUROMAR, December 7-8; Virtual Conference, 2021.
14) Ariyasingha, N. M.; Samoilenko, A.; Kovtunova, L.; Koptyug, I. V.; Chekmenev, E. Y. In *Toward clinical-scale heterogeneous hyperpolarization of propane gas at 1 atm*, PERM: Parahydrogen Enhanced Resonance Meeting, June 21-23; Virtual Conference, 2021.
15) Birchall, J. R.; Irwin, Robert K.; Chowdhury, M. R. H.; Nikolaou, P.; Goodson, B. M.; Barlow, M. J.; Shcherbakov, A.; Chekmenev, E. Y. In *Automated Low-Cost in situ IR and NMR Spectroscopy for Clinical-Scale 129Xe Spin-Exchange Optical Pumping*, PERM: Parahydrogen Enhanced Resonance Meeting, Virtual Conference, June 21-23; Virtual Conference, 2021.
16) Chapman, B.; Joalland, B.; Meersman, C.; Ettedgui, J.; Swenson, R. E.; Krishna, M. C.; Nikolaou, P.; Kovtunov, K. V.; Salnikov, O. G.; Koptyug, I. V.; Gemeinhardt, M. E.; Goodson, B. M.; Shchepin, R. V.; Chekmenev, E. Y. In *SABRE Hyperpolarization of Sodium [1-13C]Pyruvate Using Our Low-cost High-Pressure Clinical-Scale Liquid Nitrogen-Based Parahydrogen Generator*, PERM: Parahydrogen Enhanced Resonance Meeting, Virtual Conference, June 21-23; Virtual Conference, 2021.
17) Chapman, B.; Joalland, B.; Meersman, C.; Ettedgui, J.; Swenson, R. E.; Krishna, M. C.; Nikolaou, P.; Kovtunov, K. V.; Salnikov, O. G.; Koptyug, I. V.; Gemeinhardt, M. E.; Goodson, B. M.; Shchepin, R. V.; Chekmenev, E. Y. In *Low-cost High-Pressure Clinical-Scale Parahydrogen Generator Using Liquid Nitrogen at 77 K*, Experimental NMR Conference, Virtual Conference, March 29-31; Virtual Conference, 2021.
18) Chowdhury, M. R. H.; Birchall, J. R.; Nikolaou, P.; Barlow, M. J.; Shcherbakov, A.; Goodson, B. M.; Chekmenev, E. Y. In *Pilot Quality Assurance Study of Batch-Mode Clinical-Scale Automated*

Generation-3 Xenon-129 Hyperpolarizer, PERM: Parahydrogen Enhanced Resonance Meeting, Virtual Conference, June 21-23; Virtual Conference, 2021.

19) Chowdhury, M. R. H.; Birchall, J. R.; Nikolaou, P.; Barlow, M. J.; Shcherbakov, A.; Goodson, B. M.; Chekmenev, E. Y. In *Pilot Quality Assurance Study of Batch-Mode Clinical-Scale Automated Generation-3 Xenon-129 Hyperpolarizer*, Experimental NMR Conference, March 29-31; Virtual Conference, 2021.

20) Nantogma, S.; Joalland, B.; Wilkens, K.; Chekmenev, E. Y. In *Next-Generation Equipment for Parahydrogen-Based Hyperpolarization Experiments*, PERM: Parahydrogen Enhanced Resonance Meeting, June 21-23; Virtual Conference, 2021.

21) Nantogma, S.; Joalland, B.; Wilkens, K.; Chekmenev, E. Y. In *Next-Generation Equipment for Parahydrogen-Based Hyperpolarization Experiments*, Experimental NMR Conference, March 29-31; Virtual Conference, 2021.

Peer-Reviewed Manuscripts, Dissertation & Book Chapters

1. Birchall, J. R.; Irwin, R. K.; Chowdhury, M. R. H.; Nikolaou, P.; Goodson, B. M.; Barlow, M. J.; Shcherbakov, A.; Chekmenev, E. Y., Automated Low-Cost In Situ IR and NMR Spectroscopy Characterization of Clinical-Scale 129Xe Spin-Exchange Optical Pumping. *Analytical Chemistry* **2021,** *93* (8), 3883-3888.
2. Chapman, B.; Joalland, B.; Meersman, C.; Ettedgui, J.; Swenson, R. E.; Krishna, M. C.; Nikolaou, P.; Kovtunov, K. V.; Salnikov, O. G.; Koptyug, I. V.; Gemeinhardt, M. E.; Goodson, B. M.; Shchepin, R. V.; Chekmenev, E. Y., Low-Cost High-Pressure Clinical-Scale 50% Parahydrogen Generator Using Liquid Nitrogen at 77 K. *Analytical Chemistry* **2021,** *93* (24), 8476–8483.
3. Joalland, B.; Ariyasingha, N. M.; Younes, H. R.; Nantogma, S.; Salnikov, O. G.; Chukanov, N. V.; Kovtunov, K. V.; Koptyug, I. V.; Gelovani, J. G.; Chekmenev, E. Y., Low-Flammable Parahydrogen-Polarized MRI Contrast Agents. *Chemistry – A European Journal* **2021,** *27* (8), 2774-2781.
4. Joalland, B.; Nantogma, S.; Chowdhury, M. R. H.; Nikolaou, P.; Chekmenev, E. Y., Magnetic Shielding of Parahydrogen Hyperpolarization Experiments for the Masses. *Magnetic Resonance in Chemistry* **2021**, doi: 10.1002/mrc.5167.
5. Khan, A. S.; Harvey, R. L.; Birchall, J. R.; Irwin, R. K.; Nikolaou, P.; Schrank, G.; Emami, K.; Dummer, A.; Barlow, M. J.; Goodson, B. M.; Chekmenev, E. Y., Enabling Clinical Technologies for Hyperpolarized Xenon-129 MRI and Spectroscopy. *Angew. Chem. Int. Ed.* **2021**, DOI: 10.1002/anie.202015200.
6. Nantogma, S.; Joalland, B.; Wilkens, K.; Chekmenev, E. Y., Clinical-Scale Production of Nearly Pure (>98.5%) Parahydrogen and Quantification by Benchtop NMR Spectroscopy. *Analytical Chemistry* **2021,** *93* (7), 3594–3601.
7. Salnikov, O. G.; Svyatova, A.; Kovtunova, L. M.; Chukanov, N. V.; Bukhtiyarov, V. I.; Kovtunov, K. V.; Chekmenev, E. Y.; Koptyug Igor, V., Heterogeneous Parahydrogen-Induced Polarization of Diethyl Ether for Magnetic Resonance Imaging Applications. *Chemistry - A European Journal* **2021,** *27*, 1316–1322.

Inventions, patent applications and licenses:

Nothing to Report.

Funding applied for based on work supported by this award

1. Title "*Next-generation ultrafast functional 3D pulmonary imaging*"
   1F32HL160108-01 (PI=Ariyasingha, mentor=Chekmenev)
   Performance period: 09/01/2021-08/31/2024
   Supporting agency: NIH/NHLBI
   Level of funding: total direct costs to support salary and training of Dr. Ariyasingha.
   Time Commitment: Principal Investigator: 12 calendar months; Mentor: 0 calendar months
   We propose developing next-generation ultrafast MRI to assess lung function using hyperpolarized propane gas as an inhalable contrast agent. The proposed low-cost and high-throughput technology for clinical-scale production of hyperpolarized propane can be employed for sub-second gas MRI, which we envision as a novel contrast agent for functional regional mapping of lung functions in a wide range of lung diseases. Here, we will study three contrast mechanisms in excised sheep lung model to demonstrate the robustness of this new quantitative 3D imaging method.
   Aim 1: 3D MRI of lungs with deuterated HP propane. We will employ previously developed deuterated HP propane to acquire 3D MRI of excised sheep lungs. Deuterated HP propane has long-lived HP state

and can be imaged directly on clinical MRI scanners. This aim will enable to investigate the feasibility of this approach and to investigate the effect of background signal interference from the protons of tissue.

Aim 2: 3D MRI of lungs using HP propane. The advantage of HP propane versus deuterated HP propane is the possibility to employ specialized pulse sequences to filter the background signal of tissue protons. We will study the effectiveness of this filtering approach to obtain background-free images.

Aim 3: Creation of ultra-long-lived spin states (ULLS) in partially deuterated HP propane. We will investigate on the use of highly symmetric molecules to enable ultra-long lived spin states that can potentially lengthen to in vivo utility window to 1-2 minutes.

Overlap: Although this project is focused around propane, there is no overlap with the specific aims of the project. Moreover, this is a training award designed to shape the next-generation researchers in the area of pulmonary imaging. The project additionally differs from this award in two ways. First, it emphasizes the contrast mechanism (rather than applications). Second, it focuses on mechanistic studies in excised lungs versus animal model used under this award.

7. PARTICIPANTS & OTHER COLLABORATING ORGANIZATIONS

Individuals who worked on the project

The following personnel worked on the project

Name:	Eduard Chekmenev
Project Role:	Initiating PI (Wayne State University)
Researcher Identifier (ORCID ID):	orcid.org/0000-0002-8745-8801
Nearest person month worked:	3
Contribution to Project:	Dr. Chekmenev was responsible for the overall progress of the project, performing some experiments with hyperpolarized propane and hyperpolarized xenon-129, developing RF coils, analyzing some of the data for the above-mentioned experiments, preparing the manuscripts.
Funding Support:	DOD W81XWH-15-1-0271; W81XWH-20-10576; NIH 1R21CA220137; NSF CHE-1904780, NIBIB 1R01EB029829, NHLBI 1R21HL154032

Name:	Nuwandi M. Ariyasingha
Project Role:	PhD / PD Fellow
Researcher Identifier (ORCID ID):	
Nearest person month worked:	5
Contribution to Project:	Nuwandi M. Ariyasingha worked on many of the experiments concerning hyperpolarized clinical-scale propane hyperpolarization. She also analyzed the data, prepared figures, and manuscripts.
Funding Support:	DOD W81XWH-15-1-0271; W81XWH-20-10576 and NHLBI 1R21HL154032, NCI 1R21CA220137.

Name:	Jonathan R. Birchall https://orcid.org/0000-0003-3920-4038
Project Role:	PhD / PD Fellow
Researcher Identifier (ORCID ID):	
Nearest person month worked:	6
Contribution to Project:	Dr. Jonathan R. Birchall worked on many of the experiments concerning hyperpolarized clinical-scale Xenon hyperpolarization. He also analyzed the data, prepared figures, and manuscripts.
Funding Support:	W81XWH-20-10576 and DOD W81XWH-15-1-0271

Name:	Baptiste Joalland
Project Role:	PhD
Researcher Identifier (ORCID ID):	http://orcid.org/0000-0003-4116-6122
Nearest person month worked:	2
Contribution to Project:	Dr. Baptiste Joalland worked on PHIP hyperpolarization aspect of this project. He performed experiments, and also analyzed the data, prepared figures, and manuscripts.

Funding Support:	DOD W81XWH-20-10576 and DOD W81XWH-15-1-0271, NSF CHE-1904780.

Name:	Md Raduan Chowdhury
Project Role:	PhD student
Researcher Identifier (ORCID ID):	
Nearest person month worked:	3
Contribution to Project:	Raduan worked on Xenon-129 hyperpolarizer to ensure that HP 129Xe would be available for the in vivo part of this proposal. He also worked on the parahydrogen component of this award by providing upgrade to our parahydrogen production facility. He also developed and constructed custom mixing manifold to prepare mixtures of propylene and parahydrogen.
Funding Support:	Wayne State University teaching fellowship and NSF CHE-1904780.

Name:	Anna Samoilenko
Project Role:	Pharm D
Researcher Identifier (ORCID ID):	
Nearest person month worked:	3
Contribution to Project:	Anna contributed to this project by working on the development of clinical-scale propane hyperpolarizer and its testing. She prepared reactors, collected and processed data, and prepared reports.
Funding Support:	NSF CHE-1904780, W81XWH-20-10576, NCI 1R21CA220137.

Name:	Igor V. Koptyug
Project Role:	consultant
Researcher Identifier (ORCID ID):	https://orcid.org/0000-0003-3480-7649
Nearest person month worked:	1
Contribution to Project:	Wrote contents for presentations and manuscripts. Consulted in aspects of parahydrogen addition mechanism.
Funding Support:	DOD W81XWH2010576

Name:	Larisa Kovtunova
Project Role:	consultant
Researcher Identifier (ORCID ID):	https://orcid.org/0000-0003-0922-6594
Nearest person month worked:	1
Contribution to Project:	Wrote contents for manuscripts. Consulted in aspects of heterogeneous catalyst preparation for propane hyperpolarization.
Funding Support:	DOD W81XWH2010576

Name:	Juri G. Gelovani
Project Role:	consultant
Researcher Identifier (ORCID ID):	https://orcid.org/0000-0002-8413-6161
Nearest person month worked:	1

Contribution to Project:	Wrote contents for manuscripts. Consulted in aspects of clinical translation of hyperpolarized inhalable gases.
Funding Support:	DOD W81XWH2010576

Name:	Anton Scherbakov
Project Role:	consultant
Researcher Identifier (ORCID ID):	
Nearest person month worked:	2
Contribution to Project:	Provided support for Xenon-129 hyperpolarizer.
Funding Support:	DOD W81XWH2010576

Name:	Boyd M. Goodson
Project Role:	Partnering PI (SIUC)
Researcher Identifier (ORCID ID):	orcid.org/0000-0001-6079-5077
Nearest person month worked:	1
Contribution to Project:	Prof. Goodson was responsible for the overall progress of the project at the partnering site, performing some experiments with hyperpolarized xenon-129, xenon-131, and ODESR polarization measurements, analyzing some of the data for the above-mentioned experiments, contributed to efforts with hyperpolarizer development at the SIUC site, and preparing manuscripts and presentations.
Funding Support:	SIUC DOD W81XWH2010578 NSF-CHE-1905341 NSF DMR-1757954

Name:	Abdulbasit Tobi ("Tobi") Gafar
Project Role:	PhD chemistry graduate student
Researcher Identifier (ORCID ID):	
Nearest person month worked:	2
Contribution to Project:	Participated in xenon-129 and xenon-131 spin-exchange optical pumping experiments, as well as ODESR experiments; contributed to efforts with hyperpolarizer development at the SIUC site. Processed and analyzed data, wrote up contents for presentations and manuscripts.
Funding Support:	SIUC / NMR Facility

Name:	Panayiotis "Peter" Nikolaou
Project Role:	consultant
Researcher Identifier (ORCID ID):	Contributed significantly to various aspects of hyperpolarizer design and assembly. Wrote contents for presentations and manuscripts.
Nearest person month worked:	1
Contribution to Project:	
Funding Support:	DOD W81XWH2010578

Name:	Rashik Shadman
Project Role:	MS graduate student researcher
Researcher Identifier (ORCID ID):	
Nearest person month worked:	3
Contribution to Project:	Led student efforts with hyperpolarizer design and assembly at the SIUC site. Worked with vendors, facilitated discussions with the consultant.
Funding Support:	DOD W81XWH2010578

Name:	Kierstyn Albin
Project Role:	Undergraduate student researcher
Researcher Identifier (ORCID ID):	
Nearest person month worked:	1
Contribution to Project:	Assisted with some xenon-129 spin-exchange optical pumping experiments and laser characterization experiments, analyzed data.
Funding Support:	DOD W81XWH2010578 Research Corporation Cottrell SEED Award

Name:	Md Shahabuddin ("Alam") Alam
Project Role:	PhD chemistry graduate student
Researcher Identifier (ORCID ID):	
Nearest person month worked:	2
Contribution to Project:	Participated in xenon-129 and xenon-131 spin-exchange optical pumping experiments, as well as ODESR experiments; contributed to efforts with hyperpolarizer development at the SIUC site. Processed and analyzed data. Contributed to manuscripts and conference presentations.
Funding Support:	SIUC / NMR Facility

Name:	Anthony Petrilla
Project Role:	undergraduate student researcher
Researcher Identifier (ORCID ID):	
Nearest person month worked:	1
Contribution to Project:	Assisted with hyperpolarizer design and assembly at the SIUC site.
Funding Support:	DOD W81XWH2010578

Has there been a change in the active other support of the PD/PI(s) or senior/key personnel since the last reporting period?

Yes, non-competitive *Two-Year Extension for Special Creativity* was awarded by NSF to the PI (Chekmenev) and partnering PI (Goodson) of this award. Provided below, please see the detailed information.

Title "Collaborative Research: Exploiting Spin Networks and Efficient Catalyst/Substrate Separations for NMR 'SABRE' Enhancement of Complex Systems"

(Eduard Y Chekmenev, Wayne State University)

Time Commitment: PI (1.0 summer months)

(Boyd M Goodson, Southern Illinois University Carbondale)

Time Commitment: PI (1.0 summer months)
Collaborating PI award: NSF CHE-2140037 (Wayne State University)
Level of funding: (total award including IDC)
Lead PI award: NSF CHE-2140135 (Southern Illinois University Carbondale)
Level of funding: (total award including IDC)
Supporting agency: NSF CHEMISTRY
Program Contact Name: Dr. Kelsey Cook
Program Contact Phone:
Program Contact Email: kcook@nsf.gov
Performance period: 09/01/2022 to 08/31/2024

Under this supplement granted by the NSF, we plan to work in the same overall area as our current NSF project: In particular, we will be focused on systems where nuclear spin networks can be exploited to enhance parahydrogen (p-H_2)-sourced hyper-polarization, both to provide new fundamental understanding of underlying processes, and to enable new applications of highly spin-polarized systems (noting that the proposed instrumentation will be helpful in both efforts). Below, please find examples of key areas of interest that have emerged from our ongoing work that we plan to pursue in our future efforts:

Aim 1. SABRE-Hyperpolarized ^{117}Sn for Potential Use in Neutron Optics Searches for Time-Reversal Invariance Violation.

Aim 2. Enhancing SABRE Using Liquid-Crystalline (LC) Matrices.

Aim 3. Investigating Anomalous Creation of Hyperpolarized Orthohydrogen from MOF-Based Heterogeneous SABRE Catalysts.

Aim 4. Exploring New Regimes of Direct SABRE Hyper-polarization of Carboxylic Acid Derivatives.

Aim 5. PHIP RASER hyperpolarization of biomolecules.

Overlap: none

Personnel exchanges with collaborators:
No in-person exchanges were possible due to Covid-19 pandemic.

Instead, we have been interacting with collaborating scientists remotely.
Organization Name: University of Nottingham
Location of Organization: Nottingham, UK
Partner's contribution to the project:
In-kind support: Our collaborators provided their insights in the imaging aspects of hyperpolarized gases.
Collaboration: We have enjoyed regular (weekly to bi-weekly) teleconferences with the Nottingham team (lead PI: Dr. Michael J. Barlow). Moreover, we hosted a (virtual) twelve-week long exchange visit with two MsC students Rebecca Harvey and Alixander Khan, who have focused on preparing a review manuscript to a top Chemistry journal with primary focus on production of hyperpolarized Xe-129. We also made plans and have six additional MsC students from the University of Nottingham after the pandemic.

Organization Name: International Tomography Center (ITC)
Location of Organization: Novosibirsk, Russia
Partner's contribution to the project:
In-kind support: Our collaborators provided their insights in the improvement of hyperpolarization practices for low-cost hyperpolarization of propane gas employing disposable polarizer.
Collaboration: We have enjoyed regular (monthly) teleconferences with the ITC team led by Prof. Igor Koptyug).

8. SPECIAL REPORTING REQUIREMENTS

Collaborative Award

This is a collaborative award with two partnering PIs. Each PI submits a copy of the identical report with face page adjusted for each report.

9. APPENDICES

Appendix 1: Original Statement of work, Years 1-3

<div align="center">

STATEMENT OF WORK – 07/03/2019
PROPOSED START DATE Apr. 01, 2020

</div>

Site 1: Wayne State University

Department of Chemistry
5101 Cass Ave
Detroit, MI 48202
PI: Dr. Chekmenev

Site 2: Southern Illinois University
Carbondale
Neckers Building,
1245 Lincoln Dr
Carbondale, IL 62901
PI: Dr. Goodson

Specific Aim 1 – To develop a clinical low-cost and high-throughput device for production and administration of HP propane contrast agent for ultimate research use in	**Timeline**	**Site 1**	**Site 2**
Major Task 1	Months		
Subtask 1: Design of the clinical propane hyperpolarizer	1-6	X	X
Milestone # 1 clinical propane polarizer is designed	6	X	X
Subtask 2: Propane hyperpolarizer construction	7-12	X	
Milestone # 2 clinical propane hyperpolarizer is constructed	12	X	
Subtask 3: Optimize propane hyperpolarizer performance	13-18	X	X
Subtask 4: Development of Good Manufacturing Practices (GMP) of hyperpolarized propane production	19-24	X	X
Milestone # 3 HP propane production GMP is developed	24	X	X
Subtask 5: Create bill of materials for propane hyperpolarizer	25-30	X	
Specific Aim 2 - To develop a safe method for HP propane gas administration and utilization, and test the purity and safety of the HP contrast agent produced by our device			
Major Task 2			
Subtask 1: Address flammability of HP propane gas in the clinical hyperpolarizer by developing inhalation procedures, using carbon filter to capture exiting propane gas	4-18	X	X
Milestone # 4 Reduction of propane content in the exhaled gas mixture to ≤1% (i.e. significantly below LEL) in 3 air inhalation/exhalation cycles after the inhalation and MRI imaging of HP propane gas; propane content in the room less than 1000 ppm (i.e. below the mandated safety level).	16-18	X	X
Subtask 2: Assess purity of produced HP propane gas by detecting the excipients	1-15	X	X
Milestone # 5 No detectable compounds except propane (>98%), H_2 (<2%), and propylene (<0.1%) in the produced contrast agent	15	X	X

Specific Aim 3 - To assess the feasibility of MRI using HP propane gas for *in vivo* functional imaging of normal lungs and in a bleomycin-induced COPD model in sheep

Major Task 3			
Subtask 1: Establish ventilation 3D ^{129}Xe MRI on a single sheep breath hold on 0.35 T using phantoms of hyperpolarized ^{129}Xe gas placed in Tedlar Bags	1-12	X	X
Milestone # 6 3D ^{129}Xe MRI imaging sequence / protocol is developed for 0.35 T MRI scanner	12	X	X
Subtask 2: Establish sub-second ventilation 3D HP propane MRI on 0.35 T using phantoms of hyperpolarized propane gas	1-12	X	
Milestone # 7 Sub-second 3D MRI imaging sequence / protocol is developed for 0.35 T MRI scanner to record MRI of propane gas ventilation	12	X	
Subtask 3: Submit documents for ACURO approval	13-16	X	X
Milestone # 8 ACURO approval obtained	18	X	X
Subtask 4: Test-retest study of HP ^{129}Xe and HP propane gas in healthy sheep [6 sheep X 4 test/re-test exams = 24 sheep scan sessions total]	19-33	X	X
Milestone # 9 Reproducibility and effectiveness of HP propane MRI to report on regional lung ventilation is demonstrated in sheep animal model	34	X	X
Subtask 3D: Bleomycin-induced lung injury detection using HP ^{129}Xe and HP propane gas in sheep [6 sheep X 2 time point exams = 12 sheep scan sessions total]	19-33	X	X
Milestone #10 Effectiveness OF HP propane MRI to detect lung injury is demonstrated in sheep animal model	34	X	X

Appendix 2: Abstracts Presented and Manuscripts Published and Accepted

9 conference abstracts and 7 published peer-reviewed publications are reported. All PDF files of 9 abstracts and 7 publications are provided below in the Appendix 2.

Clinical-Scale Production of Nearly Pure (>98.5%) Parahydrogen and Quantification by Benchtop NMR Spectroscopy

Shiraz Nantogma,[∥] Baptiste Joalland,[∥] Ken Wilkens, and Eduard Y. Chekmenev*

Read Online

ACCESS | Metrics & More | Article Recommendations | Supporting Information

ABSTRACT: Because of the extensive chemical, physical, and biomedical applications of parahydrogen, the need exists for the development of highly enriched parahydrogen in a robust and efficient manner. Herein, we present a parahydrogen enrichment equipment which substantially improves upon the previous generators with its ability to enrich parahydrogen to >98.5% and a production rate of up to 4 standard liters per minute with the added advantage of real-time quantification. Our generator employs a pulsed injection system with a 3/16 in. outside diameter copper spiral tubing filled with iron-oxide catalyst. This tubing is mated to a custom-made copper attachment to provide efficient thermal coupling to the cold head. This device allows for robust operation at high pressures up to 34 atm. Real-time quantification by benchtop NMR spectroscopy is made possible by direct coupling of the p-H$_2$ outlet from the generator to a 1.4 T NMR spectrometer using a regular 5 mm NMR tube that is continuously refilled with the exiting parahydrogen gas at ∼8 atm pressure. The use of high hydrogen gas pressure offers two critical NMR signal detection benefits: increased concentration and line narrowing. Our work presents a comprehensive description of the apparatus for a convenient and robust parahydrogen production, distribution, and quantification system, especially for parahydrogen-based hyperpolarization NMR research.
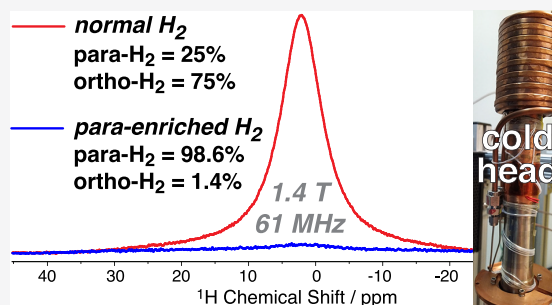
The sensitivity of nuclear magnetic resonance techniques is limited by low spin polarization P at clinically relevant conditions. One way to mitigate this limitation and increase P is to utilize NMR hyperpolarization, where nuclear spin polarization is artificially and temporarily created. Currently, there are three leading hyperpolarization methods:[1−3] spin exchange optical pumping (SEOP),[4] dissolution dynamic nuclear polarization (d-DNP),[5] and parahydrogen-induced nuclear polarization (PHIP).[6,7] The first two techniques require the use of very powerful, sophisticated, and expensive equipment together with very long turnover times to produce hyperpolarized (HP) compounds.[8,9] These techniques have advanced to clinical studies.[10,11] A higher throughput and less expensive hyperpolarization alternative is PHIP, which exploits the spin order of parahydrogen (p-H$_2$) singlet to induce nuclear spin polarization.[12,13] This can be accomplished either through hydrogenative PHIP[2,6,7] or via its non-hydrogenative variant signal amplification by reversible exchange (SABRE).[14−16] The latter relies on the simultaneous chemical exchange of p-H$_2$ and a to-be-hyperpolarized substrate on a hexacoordinate metal complex.[14] When the nuclear spin level anticrossings[17] are established, the polarization is spontaneously transferred from p-H$_2$-derived hydrides to the target nucleus of the substrate.[18] In the case of PHIP, the polarization of the nascent p-H$_2$-derived protons in PHIP can be transferred to heteronuclei via magnetic field cycling or

through the use of specially designed radio frequency (RF) pulse sequences.[19−25]

Recently, parahydrogen-hyperpolarized compounds have attracted special interest for various applications in both catalysis (reaction progress monitoring) and in biomedicine as MRI contrast agents.[1,12] Examples include HP ^{13}C-succinate to image brain cancer cells of rats ex $vivo$[26] and HP ^{13}C-pyruvate to detect metabolic dysfunction in cardiomyopathy via real-time in $vivo$ mapping of HP ^{13}C-pyruvate and ^{13}C-lactate.[27] Proton-hyperpolarized propane gas is another example for prospective use in subsecond pulmonary functional MRI.[28,29] A detailed review on bio-imaging PHIP technology can be found elsewhere.[12] Yet, despite these far-reaching applications of p-H$_2$, its enrichment to very high levels and quantification and distribution in a comprehensive manner is still a translational challenge. Therefore, there is a need to find faster, easier, efficient, and more comprehensive ways to produce and quantify p-H$_2$ in the context of biomedical applications.

The conventional route to enrich p-H_2 mixture is to shift the equilibrium state of molecular dihydrogen, which exists predominantly in the ortho-/para-state in a 3:1 ratio, toward the para-state by cryogenic cooling to very low temperatures in the presence of a suitable catalyst to accelerate the otherwise forbidden (and thus slow) transition. Up to 50% enrichment is obtained with liquid nitrogen temperature as the cooling source and activated charcoal as the catalyst.[30] Other materials were employed as hydrogen spin conversion catalysts.[31,32] Moreover, enrichment of up to 99.99% is possible with specialized cryogenic equipment, which can reduce the catalyst temperature down to 10 K.[33] For example, Hövener and co-workers have designed a continuous-flow high-throughput [4 standard liters per minute (SLM)] generator suitable for clinical settings with p-H_2 enrichment of up to 98%.[34] Prior to that, we had reported a pulsed injection method to produce up to 98% p-H_2 at a rate of 0.9 SLM.[35] The advantage of the pulsed injection method is that it provides a rather simple way to control the contact time of orthohydrogen with the catalyst without the use of specialized equipment such as a mass-flow controller.[36] However, these two previous designs employed a rather large copper chamber filled with catalyst. In our experience, this chamber covered with a copper lid with indium metal seal is highly susceptible to wear over multiple cryogenic cycles—as a result, the seal leaks, resulting in significantly reduced operating pressure.

Production of p-H_2 using liquid N_2 as a cooling source (ca. 77 K at 1 atm) is the least expensive and the least complex gateway to PHIP and SABRE hyperpolarization techniques. Such a generator can be constructed fairly easily or obtained commercially (ca. 3300 EURO, XeUS Technologies, LTD, Nicosia, Cyprus). Parahydrogen spin conversion at 77 K yields approximately 49–50% p-H_2. Indeed, a number of hyperpolarization studies have been reported using such designs.[37–40] However, it should be made abundantly clear that HP signal is reduced by a factor of 3.0 when using 50% p-H_2 as compared to near 100% p-H_2.[12,37] While this 3-fold reduction may not be an impediment for the majority of HP NMR studies, the 3-fold boost is highly advantageous when the signal-to-noise ratio (SNR) is limited. Examples of such cases include working with natural-abundance ^{13}C- and ^{15}N-compounds or *in vivo* applications.[37,41–46]

To mitigate the previous design shortcomings, we present a portable high-throughput p-H_2 generator design, which builds on the work of Feng et al.'s[35] and Tom et al.[47] Our new substantially improved design employs a spiral copper tubing filled with catalyst, which operates at high pressures of up to 34 atm. We demonstrate p-H_2 production at rates up to 4 SLM with enrichment levels greater than 98.5%. This flow rate represents a more than 4-fold improvement of Feng et al.'s[35] design and a 6-fold improvement of Tom et al.[47] and other similar designs, which demonstrated production of more than 98% p-H_2.[32,48,49] The air-cooled system employed in our device is stand-alone and semi-automated—this means that the device can be sited without the requirement of a water chilling source. Moreover, we demonstrate that the p-H_2 fraction can be conveniently quantified using a benchtop NMR spectrometer allowing for near real-time monitoring of p-H_2 production. The described p-H_2 quantification is compared to a more established high-field detection with the advantages of being substantially lower cost, more convenient, less time consuming, and very useful in longitudinal studies. The reported device has been successfully employed for a wide range of experiments

employing p-H_2 as a source of NMR hyperpolarization. Here, we also provide two illustrative utility examples of our generator to enhance nuclear spin polarization via hydrogenative and non-hydrogenative PHIP.

■ MATERIALS AND METHODS

The overall generator schematic is shown in Figure 1 and the annotated photograph is provided in Figure 2. The catalyst-
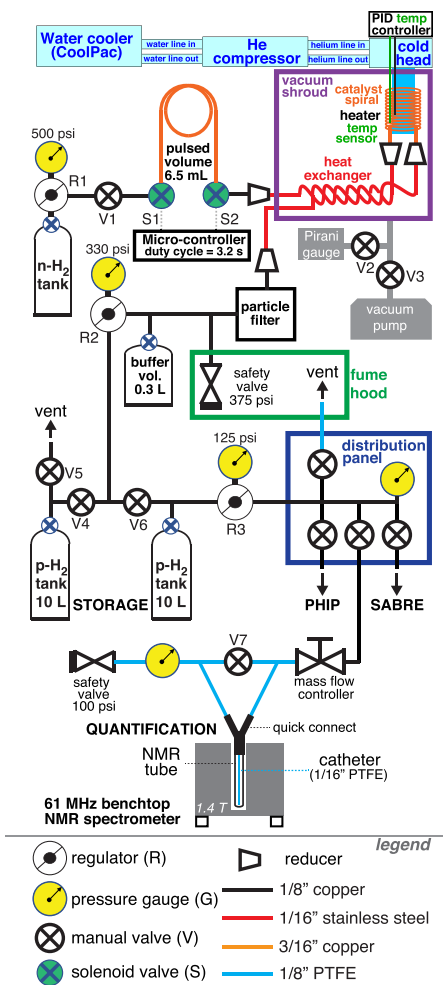

Figure 1. Schematic diagram of the parahydrogen generator. R = pressure regular; G = pressure gauge; V = manual valve; S = solenoid valve. The adapters employed are made of stainless steel for compression tubing. All tees employed with copper tubing are made of brass; V4, V5, V6 are brass ball valves.

filled copper tubing [3/16 in. (″) outer diameter (OD), 0.128″ inner diameter cleaned copper tubing, McMaster Carr 5174K2] spiral coil is made of nine turns to pack approximately 5–10 g of paramagnetic hydrated iron(III) oxide ($Fe_2O_3 \cdot H_2O$, 371254, Sigma-Aldrich, St. Louis, MO)—see the Supporting Information for details. The catalyst was washed with ethanol to eliminate microparticles. This copper tubing is tightly fitted into the helical copper core attached to a cold head to enable efficient heat transfer (Figures 3 and S1). The copper cylinder with machined hollow helical grooves was custom designed such that each winding of the copper coil tubing fits tightly into the equally spaced grooves for good
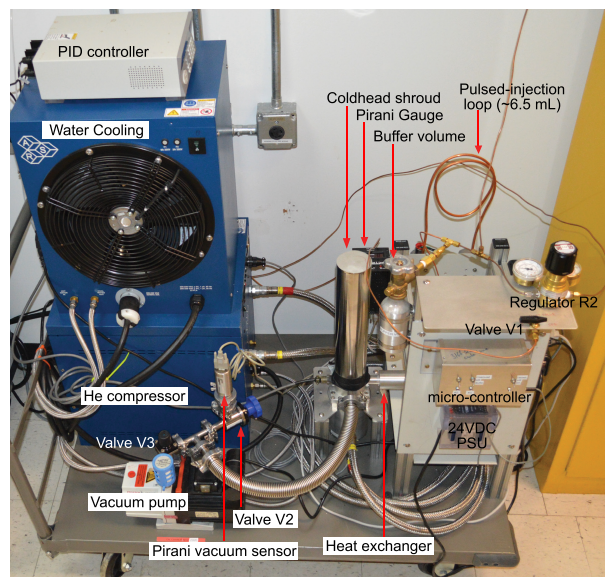
Figure 2. Annotated view of the essential components of the generator manifold without the storage tanks. These major components are connected to each other through copper and stainless-steel tubing. See the Supporting Information for more details.
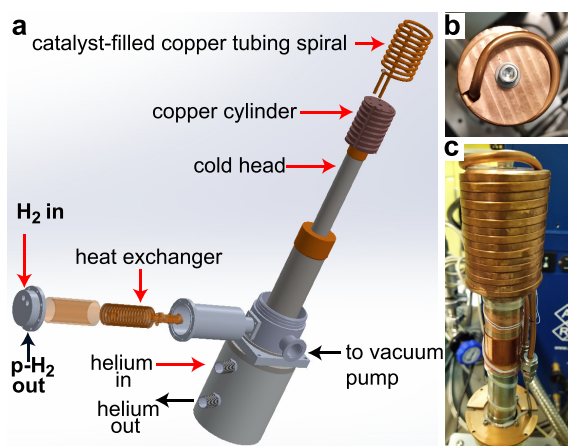

Figure 3. (a) Annotated 3D rendering of cold head assembly. (b) Top view of catalyst chamber with the top winding running along the length of copper core. (c) Side view of catalyst chamber sitting on the cold head. The tubing employed in the heat exchanger is made of stainless steel. See the Supporting Information for more details.

thermal contact between the copper spiral and the copper cylinder attached to the cold head, Figure 3. The copper cylinder mounts to the cold head using a stainless steel bolt (Figure 3b). Commercially available water-cooled helium compressor [ARS-4HW, Advances Research Systems (ARS), Macungie, PA] provides a cooling source to a cold head (model DE-204, ARS, Macungie, PA). An air-cooled cooling module (model CoolPac, ARS, Macungie, PA) provides a cooling source to the helium compressor with both devices operating using 240 VAC.

The CoolPac eliminates the need for external water cooling by recirculating water with the helium compressor. A particle filter (1/8″ Tube OD, rated to 3000 psi, Brass Housing,

McMaster Carr 9816K71) is connected to the exit line of the catalyst chamber to capture catalyst microparticles to prevent their passage to the storage tanks. A 0.3 L aluminum tank (M2, Catalina Cylinders, Garden Grove, CA, USA) is employed as temporary storage (buffer volume) with a 350−500 psi rated safety valve venting to the fume hood, Figure 1. Brass manual valves (miniature ball valves by Parker) and brass regulators are situated at various points along the generator lines to provide control and safety of hydrogen gas flow. The cold head assembly is operated under vacuum by connecting it to a vacuum pump (Duo 2.5 Rotary Vane Vacuum Pump, Pfeifer, PKD41602A) and Pirani vacuum gauge via V3 and V2 valves, respectively (Figure 1).

During operation, the normal ultrahigh purity (>99.999%) hydrogen gas is directed from the storage tank via high-pressure solenoid valves S1 and S2 (Series 20, 2-way NC, Peter Paul Electronics, New Britain, CT) to the rest of the generator manifold. These solenoid valves are controlled by an open-source Arduino microcontroller programmed to operate with a duty cycle of 3.2 s. Stainless steel adapters (Swagelok) for compression tubing were used to change the sizes and types of tubing at various stages of the generator.

■ RESULTS AND DISCUSSION

Mode of Operation. There are three phases in the p-H$_2$ enrichment process of the generator operation cycle: the generator cooling, p-H$_2$ conversion, and p-H$_2$ production phases. The first phase is the cooling phase, and to begin, the chamber surrounding the cold head must be evacuated (to minimize thermal losses), which is performed by turning on the vacuum pump and then opening valve V3 (Figure 1). Once the evacuation process starts, the main gas flow line is pressurized to approximately 460 psi using the regulator R1 followed by the opening of inlet valve V1. The pulsed injection is then switched on using the Arduino microcontroller to start the H$_2$ flow at ~4 SLM. This approach ensures that there is H$_2$ gas flow during the cooling process to purge any condensed contaminants that might have been deposited during the previous production cycle.

Generator Cooling. During the cooling phase, the hydrogen gas is vented through the safety valve. The vacuum around the cold head around the catalyst chamber is monitored by a Pirani 945 controller with a series 345 vacuum gauge (Kurt J. Lesker, Pittsburgh, PA). When the pressure reaches the range of $(2−4) \times 10^{-2}$ mbar, the helium DE-204 compressor and CoolPac (water cooler) are turned on. Once the compressor is running, the temperature controller is switched on together with the proportional−integral−derivative temperature controller, and the temperature is set at the desired point (e.g., 27 K). The generator is left on afterward for approximately 2 h and allowed to chill the catalyst chamber to the set temperature.

Parahydrogen Conversion. Parahydrogen conversion is the second phase of the p-H$_2$ enrichment process, which starts in the catalyst spiral once the desired set point is reached. Normal hydrogen is delivered to the catalyst chamber at high pressure (≥460 psi overpressure) in a pulsed cycle of 3.2 s. At the beginning of the cycle, the production rate is the highest (~4 SLM) because of the large pressure gradient between the source (460 psi overpressure) and the storage tank (0 psi overpressure). The production rate is the slowest at the end of the production cycle (*ca.* 330 psi final pressure in storage tanks): 1.4 SLM. The production rate can be adjusted via

reprogramming the cycle time of the microcontroller or varying the volume of the copper tubing between solenoid valves S1 and S2 (currently set to ~6.5 mL). Because hydrogen has a high heat capacity, formation of frost has been observed in previous generators[35] along the exit line due to atmospheric moisture condensation on the cold exit tubing. Formation of frost is the sign of substantial cooling of the outer parts of the device—this is a potential problem because the vacuum chamber surrounding the cold head may lose vacuum due to partial loss of the sealing due to shrinking O-ring seals—the partial loss in vacuum ultimately leads to operational temperatures well above the desired ≤27 K and correspondingly lower p-H$_2$ fraction. Moreover, if the moisture accumulates inside the vacuum shroud (Figure 1), a substantial downtime will be required to dry out the device. Our generator solves this shortcoming by passing the cold enriched p-H$_2$ through a heat exchanging system to establish thermal equilibrium between the entering (room temperature) normal H$_2$ and the exiting (cryogenic temperature) p-H$_2$. The heat exchanger is made of two 1/16″ stainless-steel tubes tightly coiled around each other in a helix, where one of them leads into the catalyst chamber and the other is the outlet. Consequently, cold p-H$_2$ and warm hydrogen give out negative and positive heat, respectively, when they pass over each other and a freeze out of the line is avoided.

Parahydrogen Collection. Parahydrogen collection is the last phase of the production process. After p-H$_2$ passes through the heat exchanger, it travels through the particle filter to remove any residual and unwanted particles that may be found in the exiting p-H$_2$ gas. An adapter stationed before the particle filter conveniently changes the tubing from stainless steel to copper. The temporary (buffer) storage is added to buffer the pressure jumps of the pulsed operation. It is important to note that the temporary storage tank is connected through a long tube to a safety valve rated 350−500 psi (tuned to 375 psi), which is placed in the fume hood. Overall, this prevents operation of the pressurized line above 375 psi. When the pressure inside the temporary storage is sufficiently high (and the temperature of the catalyst is low, e.g., 27K), which can be monitored using regulator R2, the manual valves V4 and V6 together with the tank valves are opened and p-H$_2$ flows into the final storage tanks. The tanks can be filled one at a time or filled simultaneously by opening both valves. Other arrangements of the storage tank filling process can be envisioned too. Alternatively, both tanks can be closed and the p-H$_2$ gas bypasses the distribution panel for either p-H$_2$ experiments or quantification. One crucial factor to note is that these storage tanks are made of aluminum to minimize wall relaxation. From these storage tanks, we feed p-H$_2$ through a custom-built distribution panel (built with copper tubing and brass Swagelok fittings and Swagelok or Parker brass ball valves) to appropriate containers for various PHIP and SABRE experiments.

Parahydrogen Quantification. Parahydrogen quantification by NMR spectroscopy is not straightaway since p-H$_2$ is NMR inactive. Several methods have been devised such as the use of Raman spectroscopy to measure the first two rotational bands of the spin isomers of normal H$_2$.[50] Matrix isolation spectroscopy, thermal conductivity, relaxation kinetics in borosilicate glass, and other para-/ortho-quantification methods exist too.[33,35,51] We utilized the indirect approach to quantify the level of enrichment by measuring the NMR signal of residual orthohydrogen using conventional high-field 9.4 T

NMR spectroscopy and also "real-time" monitoring of the exiting p-H$_2$ using bench-top 1.4 T NMR spectrometer. The spectrum obtained at 9.4 T after enrichment was compared to that of normal hydrogen to calculate the degree of enrichment. Figure 4b shows the spectra for both normal hydrogen and
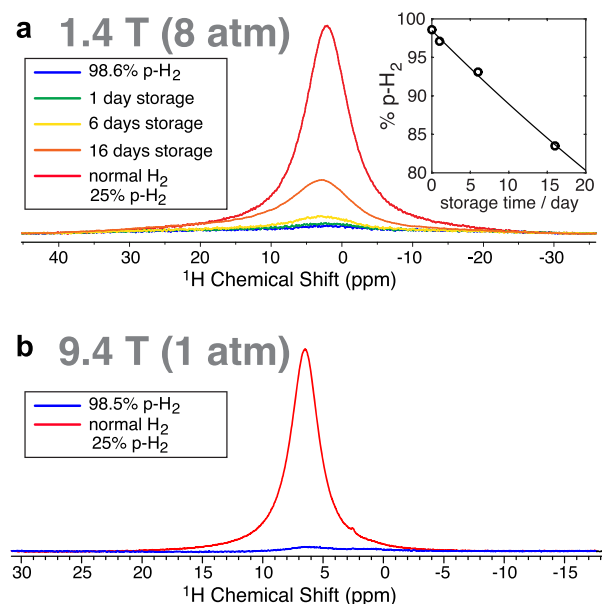

Figure 4. (a) Parahydrogen quantification using 1.4 T NMR spectrometer operating at 61 MHz proton resonance frequency using gas samples at 8 atm. Acquisition parameters: 1024 scans, 5 kHz spectral width, 52 ms acquisition time, 0.1 s repetition time, ~102 s total acquisition time, 90° excitation pulse. The inset display shows the decay of p-H$_2$ in the aluminum storage tank. (b) Parahydrogen quantification using 9.4 T Varian NMR spectrometer operating at 400 MHz proton resonance frequency using gas samples at 1 atm. Acquisition parameters: 512 scans, 20 kHz spectral width, 52 ms acquisition time, 0.1 s repetition time, ~52 s total acquisition time, 90° excitation pulse.

para-enriched hydrogen from the generator at 1 SLM$_{MAX}$ production rate. Using eq 1, the p-H$_2$ percentage was calculated to be ≥ 98.5% for 1 and 4 SLM$_{MAX}$ production rates.

However, it is important to note that in order to do high-field quantification, the NMR tube had to be carefully filled and quickly transported to the NMR spectrometer (Varian) to avoid significant relaxation due to contact with the NMR tube glass walls and other environmental variables (e.g., residual O$_2$). Thus, we demonstrate a more convenient and efficient approach to quantify the level of enrichment in real-time to avoid losses due to glass-wall relaxations and to save overall quantification time. Hence, we interfaced the outlet of the p-H$_2$ generator to an NMR tube via a Teflon tube with a mass flow controller (MFC) and pressure regulator setup described previously.[22] This setup enables direct quantification of p-H$_2$ as it exits the generator using a 1.4 T benchtop NMR spectrometer (Spinsolve ^{13}C, Magritek, New Zealand) and eliminates the need for inconvenient and time-consuming NMR tube filling and transportation for quantification. Additionally, since low-field benchtop NMR spectrometers are becoming a more common commodity and many PHIP experiments are performed with them, using them for real-time quantification offers an additional benefit. Specifically, p-H$_2$

produced is typically employed in the 5 mm NMR tube for p-H_2 bubbling experiments using PHIP or SABRE. The p-H_2 quantification is therefore performed at the point of p-H_2 utilization after it has passed through gas lines (including MFC made of stainless steel) and enters the empty 5 mm NMR tube that will be employed for the future PHIP or SABRE experiments. Here, we operate our setup at a 100 psi overpressure in economy 5 mm NMR tubes (WG-1000-8, Wilmad glass) to quantify the level of para-enrichment. It was found to be 98.6%, which is in good agreement with the value obtained using a 9.4 T NMR spectrometer. Operating at high pressure offers two critical advantages in the context of low-field detection, which is typically SNR challenged. First, the NMR line is decreased in units of Hz from ∼1.2 kHz at 1 atm (Figure 4b) to 0.6 kHz at ∼8 atm (Figure 4a). Second, the higher gas-phase concentration boosts the NMR signal by ∼8-fold. As a result, the cumulative SNR benefit of this high-pressure approach is a factor of ∼16 corresponding to a factor of ∼256 in time-saving. Therefore, it becomes possible to perform p-H_2 quantification at 1.4 T with a total scan time of less than 2 min. We anticipate that lower field NMR spectrometers can also be successfully employed for the purpose of p-H_2 quantification using eq 1

$$f = 1 - \frac{3(\text{enriched signal})}{4(\text{unenriched signal})} \qquad (1)$$

where f is the p-H_2 fraction. Note that the multipliers 3 and 4 are used to reflect the presence of 1/4 (25%) of p-H_2 in normal (unenriched) dihydrogen gas.[12] Furthermore, the p-H_2 decay curve of p-H_2 stored in an aluminum tank obtained for four data points for 16 days using a 1.4 T device showed that the percentage of enriched p-H_2 decreased by only ∼15% by the 16th day. In practical terms, this storage system enables our lab with potent p-H_2 within 2–3 weeks after the production process.

Generator Utility for Parahydrogen-Induced Polarization Experiments. Generator utility for parahydrogen-induced polarization experiments was demonstrated in a wide range of PHIP and SABRE studies since the commencement of this device in March 2019.[22,52−57]

To demonstrate the utility of ^{15}N hyperpolarization in microtesla magnetic field using SABRE in SHield Enables Alignment Transfer to Heteronuclei (SABRE-SHEATH)[58] technique (Figure 5a) with the presented p-H_2 generator, we used 2 mM of Ir(COD)(IMes)Cl [IMes = 1,3-bis(2,4,6-trimethylphenyl)imidazol-2-ylidene; COD = cyclooctadiene][59,60] as a precatalyst and 20 mM each of the substrates (isotopologues of metronidazole enriched with ^{15}N at two positions or all three nitrogen sites, Figure 5c,d). Each substrate sample was hyperpolarized in a magnetic shield operating in the microtesla regime and then transferred afterward to an NMR spectrometer for measurements. The HP signal was referenced against neat thermally polarized pyridine-^{15}N, Figure 5b. The polarization was performed by bubbling p-H_2 into an NMR tube containing the substrate and the activated polarization transfer catalyst for 50–100 s in CD$_3$OD. For metronidazole-^{15}N$_3$ (Figure 5d), where all nitrogen sites are ^{15}N-labeled, ^{15}N polarization values were up to ∼16%.[52] The ^{15}N P values were drastically decreased in metronidazole-^{15}N$_2$ (Figure 5c) yielding ^{15}N polarization values of up to 4% in otherwise identical conditions due to less favorable relaxation dynamics in microtesla magnetic field
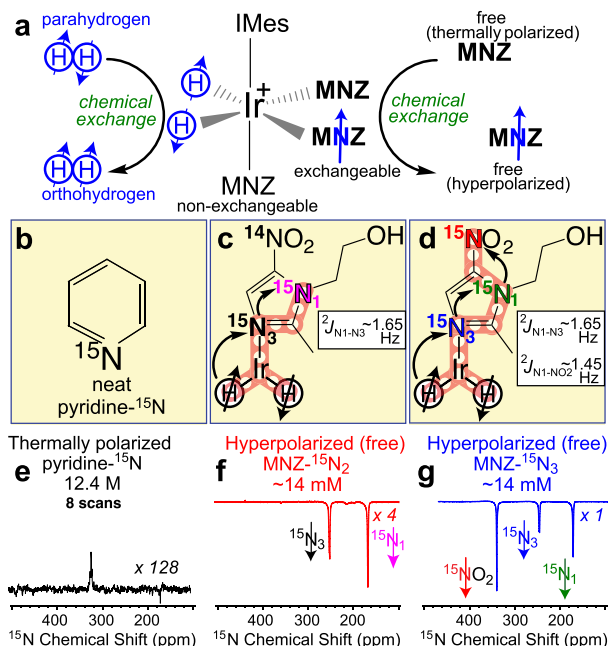

Figure 5. (a) Molecular exchange between p-H_2 and metronidazole leading to SABRE hyperpolarization. (b) Neat pyridine-^{15}N was employed as a signal reference. (c,d) Structures and polarization transfer via spin-relay between p-H_2 and ^{15}N nuclei in ^{15}N-isotopologues of metronidazole. (e) Reference ^{15}N NMR spectrum of a thermally polarized neat pyridine-^{15}N acquired with eight scans and a recovery time of 10 min. (f,g) Single-scan ^{15}N NMR spectra of SABRE-hyperpolarized metronidazole-^{15}N$_2$ and metronidazole-^{15}N$_3$. Reproduced from ref 52 with permission from The Royal Society of Chemistry.

because of the presence of ^{14}N spin in metronidazole-^{15}N$_2$.[52] This finding is important as it guides more rational design of ^{15}N-hyperpolarized contrast agents and nitro-imidazole-based drugs for future molecular imaging of hypoxia and more advanced theragnostic applications.[52,54]

Last, we demonstrate the utility of the p-H_2 generator reported here for creating of parahydrogen-induced radio amplification by stimulated emission of radiation (PHIP-RASER) effect.[53,55,61] Parahydrogen was bubbled for 10 s into a solution containing ∼200 mM ethyl vinyl substrate and 4 mM Rh-based hydrogenation catalyst in CD$_3$OD at Earth's magnetic field (Figure 6a).[53] This experiment resulted in a proton polarization of 8.4% (reference signal of thermally polarized ethyl 1-^{13}C-acetate (EA-1-^{13}C), Figure 6c,b. Spontaneous occurrence of PHIP-RASER in a 61 MHz benchtop NMR spectrometer is shown in Figure 6d.[53] These results are important because they demonstrate that PHIP can be conveniently employed to generate the RASER effect in standard NMR equipment.

■ CONCLUSIONS

In conclusion, we have presented a home-built pulse-injection p-H_2 generator employing a copper tubing spiral filled with catalyst. We estimate the cost of the components utilized on the order of 55,000 USD $ca.$ 2020. In addition, we expect that it would require approximately 4–6 months of PhD- or MS-skilled person to assemble the described equipment, make custom components, and to perform quality assurance. The
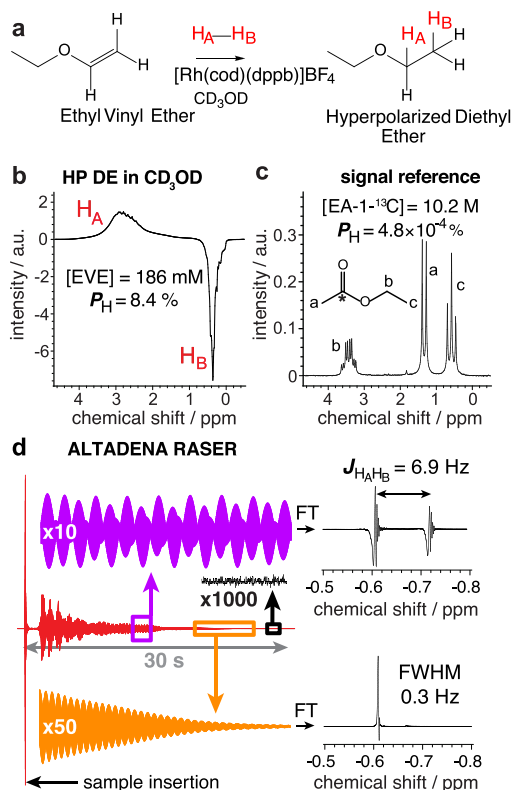
Figure 6. (a) Reaction of ethyl vinyl ether with p-H_2 (shown as H_A–H_B) in CD_3OD in the presence of Rh-based catalyst resulting in the production of HP diethyl ether (DE).[53] (b) NMR spectrum of HP protons of DE, $P_H \sim 8.4\%$. (c) NMR spectrum of thermally polarized EA-1-^{13}C as a signal reference for polarization and chemical shift comparisons. (d) FID and Fourier transformed spectra of HP DE with a resonance width of 0.3 Hz and a J-coupling of HP protons at 6.9 Hz. Acquisition parameters: NMR tube inserted 2–3 s after initiating the pulse acquisition sequence in the 61 MHz benchtop NMR spectrometer, with a pulse angle <0.1° and an opened ^{1}H detector channel for 32 s. Reprinted with permission from ref 53.

generator is portable enough to be easily transported within a building or in a vehicle. Maximum enrichment of >98.5% was achieved at a pressure of 375 psi and a set temperature of 27 K with a production rate of up to 4 SLM. Further modifications can be carried out to achieve various production targets. For instance, by increasing the size of the tubing volume between the S1 and S2 solenoid valves of the injection manifold, production rates can be further increased. Real-time p-H_2 quantification of the produced p-H_2 gas was demonstrated using a bench-top 1.4 T NMR spectrometer using pressurized exiting (∼8 atm) p-H_2 gas in real-time. High production rate and real-time quantification of p-H_2 gas bode well for biomedical translation of parahydrogen-hyperpolarized contrast agents. To that end, the utility of the generator has been successfully demonstrated for the production of several proton- and ^{15}N-hyperpolarized contrast agents. We also envision a wide range of other HP studies that can be enabled by this device ranging from biomedical HP MRI[46,54,62,63] to HP spectroscopy of reaction monitoring.[39]

ASSOCIATED CONTENT

Supporting Information

The Supporting Information is available free of charge at https://pubs.acs.org/doi/10.1021/acs.analchem.0c05129.

Additional drawings and photographs of the described equipment and operational manual for the reported device (PDF)

AUTHOR INFORMATION

Corresponding Author

Eduard Y. Chekmenev − *Department of Chemistry, Integrative Biosciences (Ibio), Wayne State University, Detroit, Michigan 48202, United States; Russian Academy of Sciences, Moscow 119991, Russia;* ⊙ orcid.org/0000-0002-8745-8801; Email: chekmenevlab@gmail.com

Authors

Shiraz Nantogma − *Department of Chemistry, Integrative Biosciences (Ibio), Wayne State University, Detroit, Michigan 48202, United States*

Baptiste Joalland − *Department of Chemistry, Integrative Biosciences (Ibio), Wayne State University, Detroit, Michigan 48202, United States;* ⊙ orcid.org/0000-0003-4116-6122

Ken Wilkens − *Department of Radiology and Radiological Sciences, Vanderbilt University Institute of Imaging Science (VUIIS), Nashville, Tennessee 37232-2310, United States*

Complete contact information is available at:
https://pubs.acs.org/10.1021/acs.analchem.0c05129

Author Contributions

‖S.N. and B.J. contributed equally.

Notes

The authors declare the following competing financial interest(s): EYC declares a stake of ownership in XeUS technologies LTD.

REFERENCES

(1) Nikolaou, P.; Goodson, B. M.; Chekmenev, E. Y. *Chem.—Eur. J.* **2015**, *21*, 3156−3166.

(2) Goodson, B. M.; Whiting, N.; Coffey, A. M.; Nikolaou, P.; Shi, F.; Gust, B. M.; Gemeinhardt, M. E.; Shchepin, R. V.; Skinner, J. G.; Birchall, J. R.; Barlow, M. J.; Chekmenev, E. Y. *Emagres* **2015**, *4*, 797−810.

(3) Kovtunov, K. V.; Pokochueva, E. V.; Salnikov, O. G.; Cousin, S. F.; Kurzbach, D.; Vuichoud, B.; Jannin, S.; Chekmenev, E. Y.; Goodson, B. M.; Barskiy, D. A.; Koptyug, I. V. *Chem.—Asian J.* **2018**, *13*, 1857−1871.

(4) Walker, T. G.; Happer, W. *Rev. Mod. Phys.* **1997**, *69*, 629−642.

(5) Ardenkjaer-Larsen, J. H.; Fridlund, B.; Gram, A.; Hansson, G.; Hansson, L.; Lerche, M. H.; Servin, R.; Thaning, M.; Golman, K. *Proc. Natl. Acad. Sci. U.S.A.* **2003**, *100*, 10158−10163.

(6) Eisenschmid, T. C.; Kirss, R. U.; Deutsch, P. P.; Hommeltoft, S. I.; Eisenberg, R.; Bargon, J.; Lawler, R. G.; Balch, A. L. *J. Am. Chem. Soc.* **1987**, *109*, 8089−8091.

(7) Bowers, C. R.; Weitekamp, D. P. *Phys. Rev. Lett.* **1986**, *57*, 2645−2648.

(8) Ardenkjaer-Larsen, J. H.; Leach, A. M.; Clarke, N.; Urbahn, J.; Anderson, D.; Skloss, T. W. *NMR Biomed.* **2011**, *24*, 927−932.

(9) Ardenkjaer-Larsen, J. H. *J. Magn. Reson.* **2016**, *264*, 3−12.

(10) Mugler, J. P.; Altes, T. A. *J. Magn. Reson. Imag.* **2013**, *37*, 313−331.

(11) Nelson, S. J.; Kurhanewicz, J.; Vigneron, D. B.; Larson, P. E. Z.; Harzstark, A. L.; Ferrone, M.; van Criekinge, M.; Chang, J. W.; Bok, R.; Park, I.; Reed, G.; Carvajal, L.; Small, E. J.; Munster, P.; Weinberg, V. K.; Ardenkjaer-Larsen, J. H.; Chen, A. P.; Hurd, R. E.; Odegardstuen, L.-I.; Robb, F. J.; Tropp, J.; Murray, J. A. *Sci. Transl. Med.* **2013**, *5*, 198ra108.

(12) Hövener, J.-B.; Pravdivtsev, A. N.; Kidd, B.; Bowers, C. R.; Glöggler, S.; Kovtunov, K. V.; Plaumann, M.; Katz-Brull, R.; Buckenmaier, K.; Jerschow, A.; Reineri, F.; Theis, T.; Shchepin, R. V.; Wagner, S.; Bhattacharya, P.; Zacharias, N. M.; Chekmenev, E. Y. *Angew. Chem., Int. Ed.* **2018**, *57*, 11140−11162.

(13) Green, R. A.; Adams, R. W.; Duckett, S. B.; Mewis, R. E.; Williamson, D. C.; Green, G. G. R. *Prog. Nucl. Magn. Reson. Spectrosc.* **2012**, *67*, 1−48.

(14) Rayner, P. J.; Duckett, S. B. *Angew. Chem., Int. Ed.* **2018**, *57*, 6742−6753.

(15) Adams, R. W.; Aguilar, J. A.; Atkinson, K. D.; Cowley, M. J.; Elliott, P. I. P.; Duckett, S. B.; Green, G. G. R.; Khazal, I. G.; Lopez-Serrano, J.; Williamson, D. C. *Science* **2009**, *323*, 1708−1711.

(16) Adams, R. W.; Duckett, S. B.; Green, R. A.; Williamson, D. C.; Green, G. G. R. *J. Chem. Phys.* **2009**, *131*, 194505.

(17) Pravdivtsev, A. N.; Yurkovskaya, A. V.; Vieth, H.-M.; Ivanov, K. L.; Kaptein, R. *ChemPhysChem* **2013**, *14*, 3327−3331.

(18) Theis, T.; Truong, M. L.; Coffey, A. M.; Shchepin, R. V.; Waddell, K. W.; Shi, F.; Goodson, B. M.; Warren, W. S.; Chekmenev, E. Y. *J. Am. Chem. Soc.* **2015**, *137*, 1404−1407.

(19) Kadlecek, S.; Emami, K.; Ishii, M.; Rizi, R. *J. Magn. Reson.* **2010**, *205*, 9−13.

(20) Kuhn, L. T.; Bommerich, U.; Bargon, J. *J. Phys. Chem. A* **2006**, *110*, 3521−3526.

(21) Plaumann, M.; Bommerich, U.; Trantzschel, T.; Lego, D.; Dillenberger, S.; Sauer, G.; Bargon, J.; Buntkowsky, G.; Bernarding, J. *Chem.—Eur. J.* **2013**, *19*, 6334−6339.

(22) Joalland, B.; Schmidt, A. B.; Kabir, M. S. H.; Chukanov, N. V.; Kovtunov, K. V.; Koptyug, I. V.; Hennig, J.; Hövener, J.-B.; Chekmenev, E. Y. *Anal. Chem.* **2020**, *92*, 1340−1345.

(23) Goldman, M.; Jóhannesson, H. *C. R. Phys.* **2005**, *6*, 575−581.

(24) Goldman, M.; Jóhannesson, H.; Axelsson, O.; Karlsson, M. *Magn. Reson. Imag.* **2005**, *23*, 153−157.

(25) Reineri, F.; Boi, T.; Aime, S. *Nat. Commun.* **2015**, *6*, 5858.

(26) Bhattacharya, P.; Chekmenev, E. Y.; Perman, W. H.; Harris, K. C.; Lin, A. P.; Norton, V. A.; Tan, C. T.; Ross, B. D.; Weitekamp, D. P. *J. Magn. Reson.* **2007**, *186*, 150−155.

(27) Cavallari, E.; Carrera, C.; Sorge, M.; Bonne, G.; Muchir, A.; Aime, S.; Reineri, F. *Sci. Rep.* **2018**, *8*, 8366.

(28) Burueva, D. B.; Romanov, A. S.; Salnikov, O. G.; Zhivonitko, V. V.; Chen, Y.-W.; Barskiy, D. A.; Chekmenev, E. Y.; Hwang, D. W.; Kovtunov, K. V.; Koptyug, I. V. *J. Phys. Chem. C* **2017**, *121*, 4481−4487.

(29) Ariyasingha, N. M.; Salnikov, O. G.; Kovtunov, K. V.; Kovtunova, L. M.; Bukhtiyarov, V. I.; Goodson, B. M.; Rosen, M. S.; Koptyug, I. V.; Gelovani, J. G.; Chekmenev, E. Y. *J. Phys. Chem. C* **2019**, *18*, 11734−11744.

(30) Gamliel, A.; Allouche-Arnon, H.; Nalbandian, R.; Barzilay, C. M.; Gomori, J. M.; Katz-Brull, R. *Appl. Magn. Reson.* **2010**, *39*, 329−345.

(31) Das, T.; Kweon, S.-C.; Nah, I. W.; Karng, S. W.; Choi, J.-G.; Oh, I.-H. *Cryogenics* **2015**, *69*, 36−43.

(32) Hövener, J.-B.; Chekmenev, E. Y.; Harris, K. C.; Perman, W. H.; Robertson, L. W.; Ross, B. D.; Bhattacharya, P. *Magn. Reson. Mater. Phys., Biol. Med.* **2009**, *22*, 111−121.

(33) Tam, S.; Fajardo, M. E. *Rev. Sci. Instrum.* **1999**, *70*, 1926−1932.

(34) Hövener, J.-B.; Bär, S.; Leupold, J.; Jenne, K.; Leibfritz, D.; Hennig, J.; Duckett, S. B.; von Elverfeldt, D. *NMR Biomed.* **2013**, *26*, 124−131.

(35) Feng, B.; Coffey, A. M.; Colon, R. D.; Chekmenev, E. Y.; Waddell, K. W. *J. Magn. Reson.* **2012**, *214*, 258−262.

(36) Birchall, J. R.; Coffey, A. M.; Goodson, B. M.; Chekmenev, E. Y. *Anal. Chem.* **2020**, *92*, 15280−15284.

(37) Golman, K.; Axelsson, O.; Jóhannesson, H.; Månsson, S.; Olofsson, C.; Petersson, J. S. *Magn. Reson. Med.* **2001**, *46*, 1−5.

(38) Zhivonitko, V. V.; Kovtunov, K. V.; Chapovsky, P. L.; Koptyug, I. V. *Angew. Chem., Int. Ed.* **2013**, *52*, 13251−13255.

(39) Chae, H.; Min, S.; Jeong, H. J.; Namgoong, S. K.; Oh, S.; Kim, K.; Jeong, K. *Anal. Chem.* **2020**, *92*, 10902−10907.

(40) Reineri, F.; Viale, A.; Giovenzana, G.; Santelia, D.; Dastrú, W.; Gobetto, R.; Aime, S. *J. Am. Chem. Soc.* **2008**, *130*, 15047−15053.

(41) Bhattacharya, P.; Chekmenev, E. Y.; Reynolds, W. F.; Wagner, S.; Zacharias, N.; Chan, H. R.; Bünger, R.; Ross, B. D. *NMR Biomed.* **2011**, *24*, 1023−1028.

(42) Salnikov, O. G.; Nikolaou, P.; Ariyasingha, N. M.; Kovtunov, K. V.; Koptyug, I. V.; Chekmenev, E. Y. *Anal. Chem.* **2019**, *91*, 4741−4746.

(43) Salnikov, O. G.; Chukanov, N. V.; Shchepin, R. V.; Manzanera Esteve, I. V.; Kovtunov, K. V.; Koptyug, I. V.; Chekmenev, E. Y. *J. Phys. Chem. C* **2019**, *123*, 12827−12840.

(44) Barskiy, D. A.; Shchepin, R. V.; Coffey, A. M.; Theis, T.; Warren, W. S.; Goodson, B. M.; Chekmenev, E. Y. *J. Am. Chem. Soc.* **2016**, *138*, 8080−8083.

(45) Barskiy, D. A.; Shchepin, R. V.; Tanner, C. P. N.; Colell, J. F. P.; Goodson, B. M.; Theis, T.; Warren, W. S.; Chekmenev, E. Y. *ChemPhysChem* **2017**, *18*, 1493−1498.

(46) Coffey, A. M.; Shchepin, R. V.; Truong, M. L.; Wilkens, K.; Pham, W.; Chekmenev, E. Y. *Anal. Chem.* **2016**, *88*, 8279−8288.

(47) Tom, B. A.; Bhasker, S.; Miyamoto, Y.; Momose, T.; McCall, B. J. *Rev. Sci. Instrum.* **2009**, *80*, 016108.

(48) Hövener, J.-B.; Chekmenev, E. Y.; Harris, K. C.; Perman, W. H.; Tran, T. T.; Ross, B. D.; Bhattacharya, P. *Magn. Reson. Mater. Phys., Biol. Med.* **2009**, *22*, 123−134.

(49) Kadlecek, S.; Vahdat, V.; Nakayama, T.; Ng, D.; Emami, K.; Rizi, R. *NMR Biomed.* **2011**, *24*, 933−942.

(50) Sutherland, L.-M.; Knudson, J. N.; Mocko, M.; Renneke, R. M. *Nucl. Instrum. Methods Phys. Res., Sect. A* **2016**, *810*, 182−185.

(51) Bradshaw, T. W.; Norris, J. O. W. *Rev. Sci. Instrum.* **1987**, *58*, 83−85.

(52) Birchall, J. R.; Kabir, M. S. H.; Salnikov, O. G.; Chukanov, N. V.; Svyatova, A.; Kovtunov, K. V.; Koptyug, I. V.; Gelovani, J. G.; Goodson, B. M.; Pham, W.; Chekmenev, E. Y. *Chem. Commun.* **2020**, *56*, 9098−9101.

(53) Ariyasingha, N. M.; Joalland, B.; Younes, H. R.; Salnikov, O. G.; Chukanov, N. V.; Kovtunov, K. V.; Kovtunova, L. M.; Bukhtiyarov, V. I.; Koptyug, I. V.; Gelovani, J. G.; Chekmenev, E. Y. *Chem.—Eur. J.* **2020**, *26*, 13621−13626.

(54) Salnikov, O. G.; Chukanov, N. V.; Svyatova, A.; Trofimov, I. A.; Kabir, M. S. H.; Gelovani, J. G.; Kovtunov, K. V.; Koptyug, I. V.; Chekmenev, E. Y. *Angew. Chem., Int. Ed.* **2020**, *60*, 2406.

(55) Joalland, B.; Ariyasingha, N. M.; Lehmkuhl, S.; Theis, T.; Appelt, S.; Chekmenev, E. Y. *Angew. Chem., Int. Ed.* **2020**, *132*, 8732−8738.

(56) Appelt, S.; Lehmkuhl, S.; Fleischer, S.; Joalland, B.; Ariyasingha, N. M.; Chekmenev, E. Y.; Theis, T. *J. Magn. Reson.* **2021**, *322*, 106815.

(57) Joalland, B.; Ariyasingha, N. M.; Younes, H. R.; Nantogma, S.; Salnikov, O. G.; Chukanov, N. V.; Kovtunov, K. V.; Koptyug, I. V.; Gelovani, J. G.; Chekmenev, E. Y. *Chem.—Eur. J.* **2020**, DOI: 10.1002/chem.202004168.

(58) Truong, M. L.; Theis, T.; Coffey, A. M.; Shchepin, R. V.; Waddell, K. W.; Shi, F.; Goodson, B. M.; Warren, W. S.; Chekmenev, E. Y. *J. Phys. Chem. C* **2015**, *119*, 8786−8797.

(59) Barskiy, D. A.; Kovtunov, K. V.; Koptyug, I. V.; He, P.; Groome, K. A.; Best, Q. A.; Shi, F.; Goodson, B. M.; Shchepin, R. V.;

Coffey, A. M.; Waddell, K. W.; Chekmenev, E. Y. *J. Am. Chem. Soc.* **2014**, *136*, 3322−3325.

(60) Cowley, M. J.; Adams, R. W.; Atkinson, K. D.; Cockett, M. C. R.; Duckett, S. B.; Green, G. G. R.; Lohman, J. A. B.; Kerssebaum, R.; Kilgour, D.; Mewis, R. E. *J. Am. Chem. Soc.* **2011**, *133*, 6134−6137.

(61) Pravdivtsev, A. N.; Sönnichsen, F. D.; Hövener, J. B. *ChemPhysChem* **2020**, *21*, 667−672.

(62) Kovtunov, K. V.; Kidd, B. E.; Salnikov, O. G.; Bales, L. B.; Gemeinhardt, M. E.; Gesiorski, J.; Shchepin, R. V.; Chekmenev, E. Y.; Goodson, B. M.; Koptyug, I. V. *J. Phys. Chem. C* **2017**, *121*, 25994−25999.

(63) Coffey, A. M.; Kovtunov, K. V.; Barskiy, D. A.; Koptyug, I. V.; Shchepin, R. V.; Waddell, K. W.; He, P.; Groome, K. A.; Best, Q. A.; Shi, F.; Goodson, B. M.; Chekmenev, E. Y. *Anal. Chem.* **2014**, *86*, 9042−9049.

LETTER - APPLICATION NOTE

WILEY

Magnetic shielding of parahydrogen hyperpolarization experiments for the masses

Baptiste Joalland[1] | **Shiraz Nantogma[1]** | **Md Raduanul H. Chowdhury[1]** |
Panayiotis Nikolaou[2] | **Eduard Y. Chekmenev[1,3]** (iD)

[1]Department of Chemistry, Integrative Biosciences (Ibio), Karmanos Cancer Institute (KCI), Wayne State University, Detroit, Michigan, USA

[2]XeUS Technologies LTD, Nicosia, Cyprus

[3]Russian Academy of Sciences (RAS), Moscow, Russia

Correspondence
Eduard Y. Chekmenev, Department of Chemistry, Integrative Biosciences (Ibio), Karmanos Cancer Institute (KCI),Wayne State University, Detroit, MI 48202, USA.
Email: chekmenevlab@gmail.com

1 | INTRODUCTION

Nuclear magnetic resonance (NMR) techniques have inherent low sensitivity due to low nuclear spin polarization (P) or the degree of alignment of nuclear spins with applied magnetic field. However, P can be transiently enhanced by several orders of magnitude via NMR hyperpolarization techniques.[1–5] Corresponding gains in signal-to-noise ratio (SNR) of hyperpolarized (HP) dilute biologically compatible compounds enable new applications: most notably, in vivo tracking of biological processes.[6–9] Parahydrogen-induced polarization (PHIP) allows for efficient and low-cost hyperpolarization of nuclear spins using parahydrogen (p-H_2).[10,11] PHIP was pioneered in 1986,[10] and the utility of p-H_2-induced hyperpolarized (HP) compounds for in vivo imaging applications was demonstrated in 2001.[6] Despite substantial developments over the past decade,[12–14] this hyperpolarization technique is certainly lagging behind compared with more established spin exchange optical pumping (SEOP)[15] and dissolution dynamic nuclear polarization (d-DNP),[2,4] which have numerous completed and pending clinical trials.[16–18] It is our opinion that successful PHIP clinical translation requires robust hyperpolarization equipment support similar to that of SEOP and d-DNP techniques. The work reported here is aimed to enable the PHIP community with an inexpensive tool to improve the robustness and precision of PHIP hyperpolarization equipment.

In PHIP, once the symmetry of nascent parahydrogen-derived protons is broken, the spin order can be transferred to X-nucleus (anything but protons, e.g., ^{13}C or ^{15}N) via spin–spin couplings through the use of nanotesla magnetic fields.[19–21] The process of polarization transfer requires precise manipulation of static magnetic fields in the range of 10–1,000 nT, where spin level anti-crossings (LAC) are created between nascent p-H_2-derived protons and to-be-hyperpolarized nucleus.[22]

In hydrogenative PHIP, p-H_2 is first added to the unsaturated precursor in a pairwise manner. Next, the magnetic field is decreased below B_{LAC} (∼100 nT). Finally, the adiabatic passage via B_{LAC} enables efficient

---

Baptiste Joalland and Shiraz Nantogma contributed equally to this study.

Institute and/or researcher Twitter usernames (https://twitter.com/waynestatechem, https://twitter.com/e_chekmenev).

polarization transfer to X-nucleus, Figure 1b.[23] This approach has been called magnetic field cycling (MFC)[19] or sweeping (MFS).[24] P_{13C} of up to 21% has been obtained[19] and P_{13C} of 5%–10% has been demonstrated for [1-^{13}C]pyruvate,[25–27] the leading ^{13}C HP contrast agent currently under evaluation in many clinical trials.

The non-hydrogenative PHIP variant called signal amplification by reversible exchange (SABRE) employs the process of simultaneous chemical exchange of p-H$_2$ and to-be-hyperpolarized molecule on a metal center.[28–31] The polarization transfer complex (PTC) containing p-H$_2$-derived hydrides and substrate containing X-nucleus (^{15}N,[32] ^{31}P,[33] ^{13}C,[21,34,35] etc.) is transiently formed. The efficient polarization transfer from p-H$_2$-derived hydrides to X-nucleus is achieved via LAC creation by matching (i) the spin–spin coupling between hydride

proton and X-nucleus, (ii) difference of gyromagnetic ratios between hydride protons and X-nucleus, (iii) and applied static magnetic field B$_{LAC}$. This condition is fulfilled at magnetic fields in the range of 0.2–1 μT,[20,36] and this approach was called SABRE-SHEATH (SABRE in SHield Enables Alignment Transfer to Heteronuclei). B$_{LAC}$ is applied throughout the SABRE-SHEATH process (Figure 1a) although alternative pulsed schemes have been developed too.[37] P_{15N} over 50%[38–40] have been demonstrated using SABRE-SHEATH for FDA-approved drug metronidazole, which can be potentially employed for hypoxia sensing applications. ^{13}C polarization exceeding 1% has been demonstrated for ^{13}C-labeled pyruvate.[41,42]

The Earth's field is approximately two orders of magnitude stronger than B$_{LAC}$ for PHIP and SABRE polarization of X-nucleus. In practice, multilayered
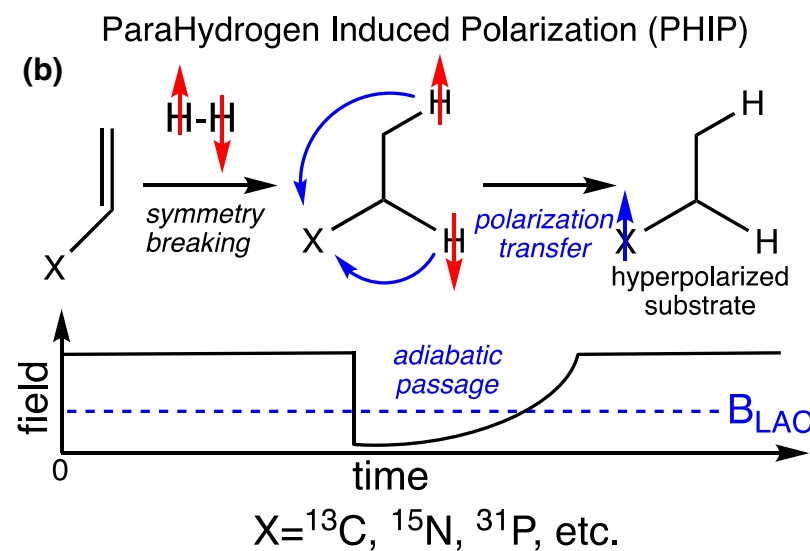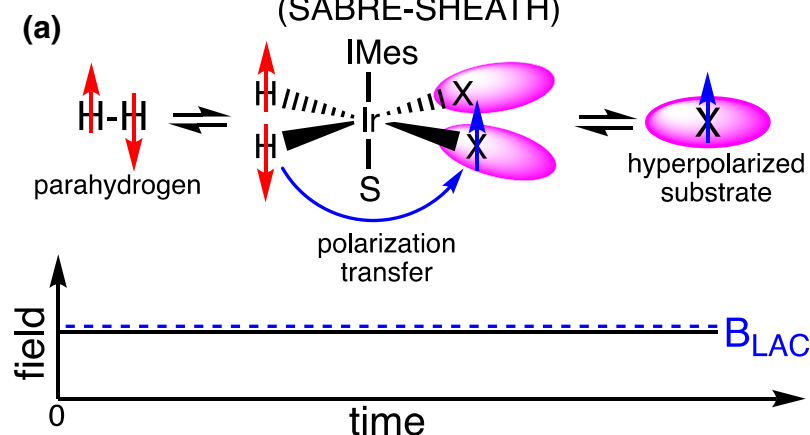

FIGURE 1 Schematics of SABRE in SHield Enables Alignment Transfer to Heteronuclei (SABRE-SHEATH) and parahydrogen-induced polarization (PHIP) magnetic field cycling (MFC) hyperpolarization techniques

mu-metal shields represent a convenient and cost-effective approach (∼$1000–5000) to attenuate the Earth's field nominally by three orders of magnitude. As a result, the desired nanotesla magnetic field can be obtained. However, mu-metal shields are susceptible to magnetization and can retain a substantial degree of residual magnetization: sometimes in excess of 1000 nT. While a small (0.1–0.2 μT) residual field can be simply treated as an offset in SABRE-SHEATH or PHIP MFC, the B_{LAC} calibration is required to account for residual static field of the magnetic shield. This is highly inconvenient at best, and it makes the daily equipment operation non-trivial.

Here, we report on simple circuitry to perform fast (2 s) automated degaussing procedure of mu-metal shields of up to 27 in. (∼0.69 m) of height with reproducible residual magnetization less than 20 nT. The degaussing process applies alternating electric current with adiabatic decay achieved by thermistors. We employ the process of ^{15}N SABRE-SHEATH hyperpolarization of $[^{15}N_3]$metronidazole as a test bed to demonstrate the utility of the reported electronics circuit.

2 | MATERIALS AND METHODS

The circuit (Figure 2a) employs 120- to 240-VAC power mains as a source of alternating current. Three thermistors (9 Ω each) are placed in parallel to boost the current carrying capacity of the circuit during the charging phase. When the switch is activated, the "charging" phase is initiated. During this phase, the current increases causing the thermistors to warm up, thus resulting in an increase of their resistance by ∼4–5 orders of magnitude. As a result, in a few hundred milliseconds, the current begins to decay adiabatically due to increasing resistance of the thermistors. The current decay is completed in less than 2 s, that is, the thermistors ensure the mains power is no longer supplied after this relatively short period of time. In practice, we employed a push-button switch, which is un-pressed after approximately 1 s. A diode is added in series with resistors to ensure the flow of power from the mains to the degaussing inductor is unidirectional. The diode output is connected to a capacitor (470 μF) and degaussing inductor, see Figure 2. In practice, we have successfully tested a wide range of degaussing
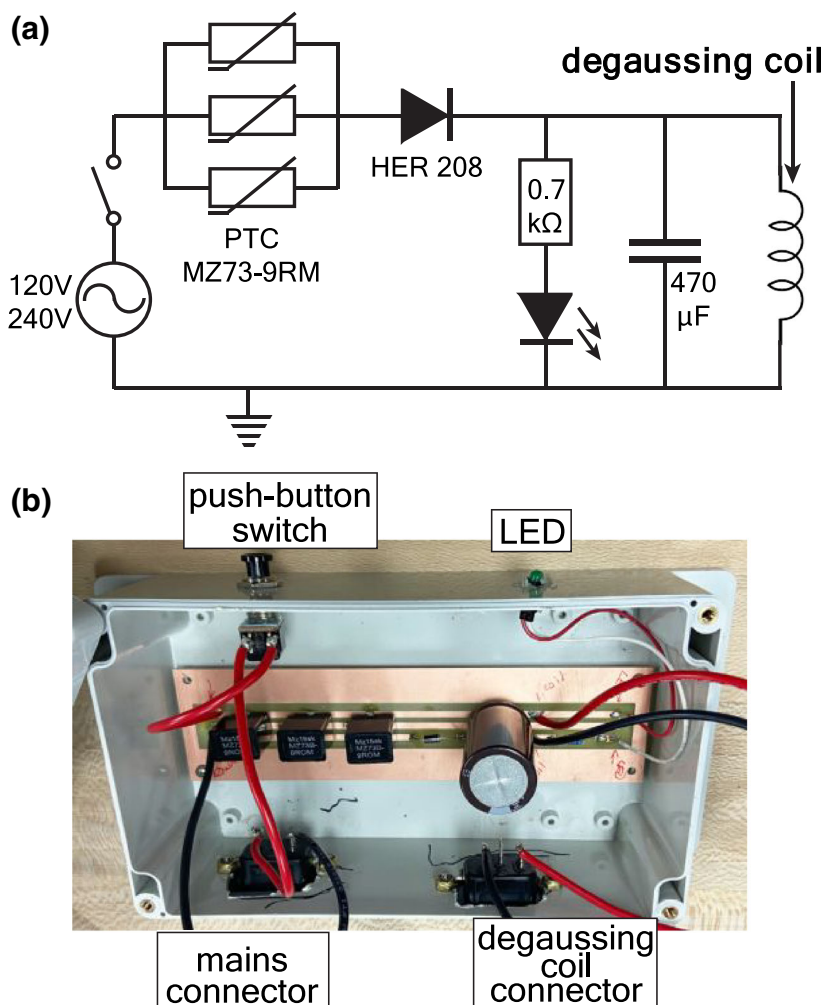

FIGURE 2 (a) Schematics of automated degaussing circuit; (b) photograph of the assembled circuit in plastic electric enclosure

inductors made in house (40.4 mH) and also supplied by the vendor for the following shields ZG-203 (4.8 mH), ZG-206 (18.1 mH), ZG-209 (105.8 mH), Magnetic Shield Corp., Bensenville, IL, USA. We have also added a light-emitting diode (LED) indicator to inform the user that the circuit was truly energized (light ON) and that the process was completed (dimming light). An ~0.7-kΩ resistor is added in series to protect the LED and to also modulate the decay rate of the electromagnetic field in the LC circuit. The complete list of part numbers, manufacturers', vendors' information, and technical drawings can be found in Figure S1. The cost of construction was $73—note that some components were purchased in bulk.

[15]N SABRE-SHEATH experiments were performed as described previously.[43–45] Briefly, Ir-IMes pre-catalyst[46] and [$^{15}N_3$]metronidazole were dissolved in CD_3OD. The prepared 0.6-ml solution contained approximately 2-mM pre-catalyst and 40-mM [$^{15}N_3$]metronidazole. The solution was placed in an economy 5-mm NMR tube jacketed with 0.25-in. (~6.35 mm) OD Teflon extension. The solution was then purged with ultra-high purity argon gas for approximately 2 min before connecting it to our p-H_2 bubbling setup via Teflon extension described in Figures 3 and S1. Once the tube was connected to the manifold, the catalyst was activated for approximately 1 h using 20 standard cubic centimeters per minute (sccm) flow rate of p-H_2 (~98%[47]) at 100 PSI (~690 kPa) overpressure. After catalyst activation, the formation of the polarization transfer complex (PTC) allows for efficient polarization transfer of nuclear spin polarization from p-H_2-derived hydrides to ^{15}N nuclei in [$^{15}N_3$]metronidazole. The details of spin-relayed polarization transfer to all three ^{15}N sites are thoroughly reviewed elsewhere.[43–45] For SABRE-SHEATH hyperpolarization, we have employed 70-sccm flow rate for p-H_2 bubbling and

ZG-203 shield equipped with degaussing solenoid coil. The coil was connected to the degaussing circuit shown in Figure 2, and degaussing was performed using 120-VAC mains. The degaussing circuit was then disconnected, and the radiofrequency (RF) solenoid coil was connected to 5-VDC power supply and current attenuation resistor bank. A residual field of less than 20 nT was measured repeatedly by a three-axis fluxgate magnetometer (Bartington Instruments, Oxford, UK) with 10-nT resolution.

For ^{15}N SABRE-SHEATH experiments, p-H_2 was bubbled in the shield at B_{LAC} (created by the RF solenoid inside the shield) for ~1 min at room temperature, 70 sccm, and 100 PSI (690 kPa) overpressure. Next, p-H_2 flow was ceased via opening the bypass valve, and the sample was quickly transferred for ^{15}N detection in 1.4-T bench-top NMR spectrometer (Nanalysis, Canada). The total delay from p-H_2 cessation to ^{15}N NMR acquisition was less than 5 s. [15]N signal enhancement and polarization levels were computed by employing external signal reference (12.4 M [^{15}N]pyridine, Figure 4b) as described in detail previously.[43]

3 | RESULTS AND DISCUSSION

The described above circuit was successfully employed for degaussing three different sizes of magnetic shields (see Methods section) ranging in size from 3″ (~7.6 cm) inner diameter (ID) and 9″ (~22.9 cm) in height to 9″ (~22.9 cm) ID and 27″ (~0.69 m) in height using four different degaussing inductor coil configurations. These shields cover a wide range of scenarios for PHIP experiments and certainly provide sufficient volume for clinical-scale production of HP contrast agents.[48] In all cases, the mu-metal shields were degaussed to ≤20-nT
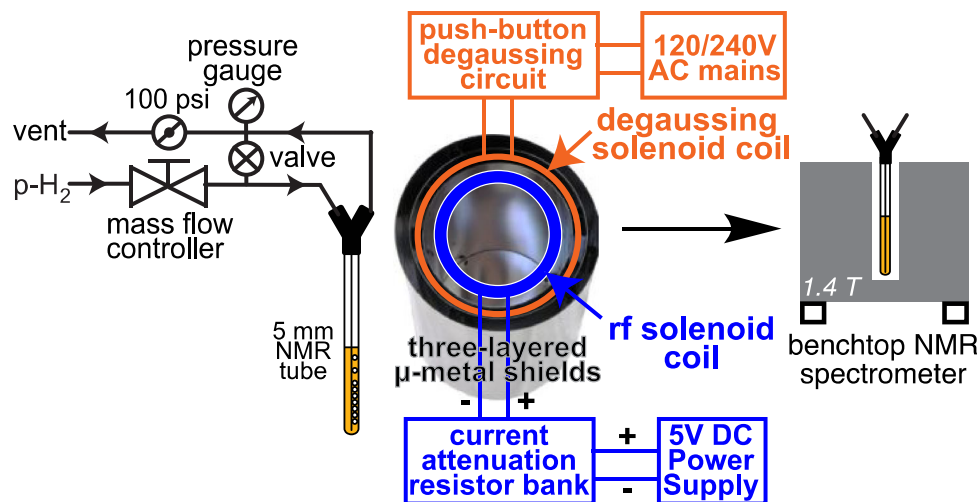

FIGURE 3 Schematic of experimental setup

FIGURE 4 (a) Simultaneous chemical exchange of p-H$_2$ and [^{15}N$_3$] metronidazole (MNZ) on activated Ir-IMes catalyst enables spontaneous polarization transfer from p-H$_2$-derived hydrides to ^{15}N$_3$ nucleus of [^{15}N$_3$] metronidazole followed by the spin-relayed spontaneous polarization transfer from ^{15}N$_3$ to ^{15}N$_1$ to ^{15}NO$_2$ sites; (b) ^{15}N nuclear magnetic resonance (NMR) spectroscopy of [^{15}N$_3$]metronidazole hyperpolarized via SHield Enables Alignment Transfer to Heteronuclei (SABRE)-SHEATH and thermally polarized [^{15}N]pyridine employed as a signal reference using 1.4-T bench-top NMR spectrometer; (b) magnetic field dependence of ^{15}N signal of HP [^{15}N$_3$]metronidazole on the residual magnetic field inside the shield after magnetic shield degaussing to less than 20-nT residual magnetic field
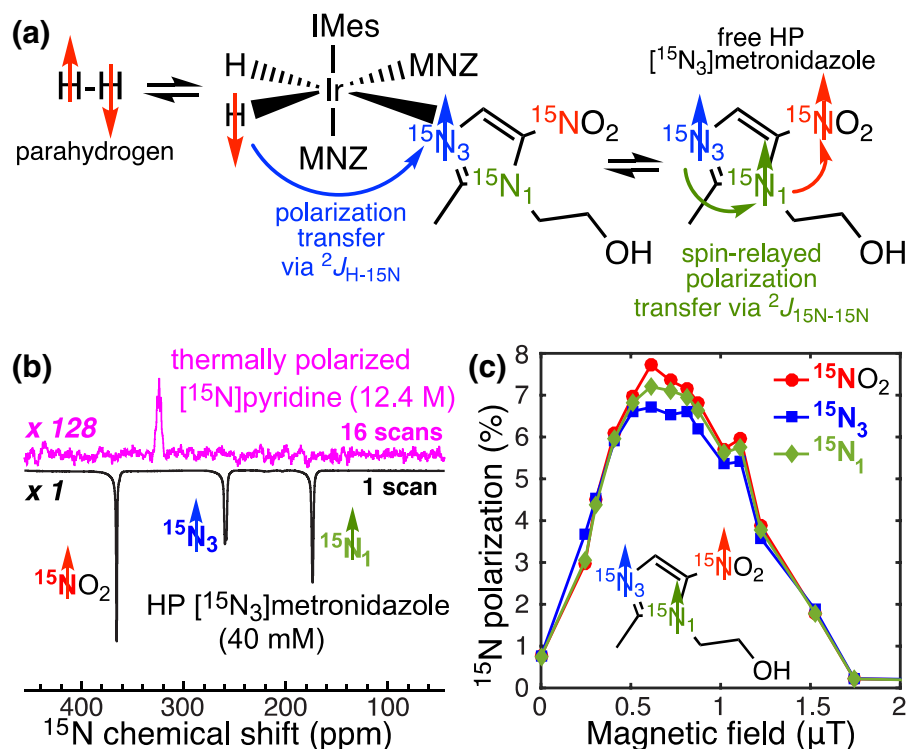
residual magnetic field, even when the shields were strongly magnetized (>2-μT residual field) prior to degaussing. The degaussing procedure was reproducible—test–retest reproducibility with back-to-back degaussing events ($N \geq 3$) spaced by at least 20 min with all three magnetic shields.

Note that the thermistors warm up during the degaussing process and therefore require a sufficiently long (20 min or more) cooling time. In cases, when such long waiting delays is not acceptable, we employed two alternatives: (i) construction of replica circuits and (ii) the use of air cooling to reduce the circuit recovery time to less than 5 min.[49] For example, we have employed one degaussing circuit with continuous air cooling to repeatedly degauss the 27-in. ($\sim$0.69-m) shield after in-situ ^{13}C NMR detection performed at $B_0 = 7.8$ mT.[49] In this study, MFC was employed to produce ^{13}C-hyperpolarized ethyl [1-^{13}C]acetate via hydrogenative PHIP approach. We therefore anticipate the circuit recovery time not to be an issue in most envisioned applications.

The utility of the reported circuit to degauss the magnetic shield to less than 20 nT is demonstrated here for application in ^{15}N SABRE-SHEATH studies. [^{15}N$_3$]metronidazole was successfully hyperpolarized using spin-relayed SABRE-SHEATH,[44] Figure 4a; Figure 4b shows ^{15}N spectrum of HP [^{15}N$_3$]metronidazole recorded using 1.4-T bench-top NMR spectrometer. The ^{15}N signal dependence on the applied magnetic field (by the

solenoid coil placed inside the shield, Figure 3b), clearly shows a maximum at $\sim$0.6 μT (Figure 4c), and ^{15}N signal reduction to nearly zero, when no additional field was applied (i.e., the residual in-shield field was <20 nT). This result is in sharp contrast with the previously published study performed without a precise magnetometer and the reported degaussing circuitry: as a result, the residual magnetic field was likely 0.2 μT resulting in two artifacts: (i) apparent maximum of ^{15}N polarization at $\sim$0.4 μT (vs. $\sim$0.6 μT in Figure 4c) applied via solenoid magnetic field and (ii) ^{15}N signal phase shift (and thus the null point) at $\sim$0.2 μT.[44] Such a residual magnetic field retained by the shield is therefore highly detrimental to SABRE-SHEATH experiments, because the actual "dialed" magnetic field of the in-shield solenoid (Figure 3) is added on top of the residual magnetic field of the shield, and may lead to systematic experimental biases. The described circuit in this Application paper mitigates these experimental challenges by conveniently fast and robust elimination of the residual in-shield field to below 20 nT.

4 | CONCLUSION

In summary, we reported on robust and inexpensive ($73 cost of parts) circuitry for fast ($\sim$2 s) degaussing of mu-metal magnetic shields for their application with hyperpolarization techniques based on parahydrogen (PHIP

and SABRE). Less than 20-nT residual field was reproducibly achieved with mu-metal shields of various sizes. The utility of degaussing was demonstrated by measuring the magnetic field profile in SABRE-SHEATH experiments with ^{15}N hyperpolarization studies of $[^{15}N_3]$metronidazole. The simple circuitry presented here may be of practical use for those working and using PHIP and/or SABRE hyperpolarization techniques.

ACKNOWLEDGEMENTS

PEER REVIEW

The peer review history for this article is available at https://publons.com/publon/10.1002/mrc.5167.

ORCID

Eduard Y. Chekmenev https://orcid.org/0000-0002-8745-8801

REFERENCES

[1] B. M. Goodson, N. Whiting, A. M. Coffey, P. Nikolaou, F. Shi, B. M. Gust, M. E. Gemeinhardt, R. V. Shchepin, J. G. Skinner, J. R. Birchall, M. J. Barlow, E. Y. Chekmenev, *Emagres* **2015**, *4*, 797.

[2] J. H. Ardenkjaer-Larsen, B. Fridlund, A. Gram, G. Hansson, L. Hansson, M. H. Lerche, R. Servin, M. Thaning, K. Golman, *Proc. Natl. Acad. Sci. U. S. A.* **2003**, *100*, 10158.

[3] B. M. Goodson, *J. Magn. Reson.* **2002**, *155*, 157.

[4] J. H. Ardenkjaer-Larsen, *J. Magn. Reson.* **2016**, *264*, 3.

[5] R. A. Green, R. W. Adams, S. B. Duckett, R. E. Mewis, D. C. Williamson, G. G. R. Green, *Prog. Nucl. Magn. Reson. Spectrosc.* **2012**, *67*, 1.

[6] K. Golman, O. Axelsson, H. Johannesson, S. Mansson, C. Olofsson, J. S. Petersson, *Magn. Reson. Med.* **2001**, *46*, 1.

[7] K. Golman, R. in't Zandt, M. Thaning, *Proc. Natl. Acad. Sci. U. S. A.* **2006**, *103*, 11270.

[8] S. E. Day, M. I. Kettunen, F. A. Gallagher, D. E. Hu, M. Lerche, J. Wolber, K. Golman, J. H. Ardenkjaer-Larsen, K. M. Brindle, *Nat. Med.* **2007**, *13*, 1382.

[9] K. M. Brindle, *J. Am. Chem. Soc.* **2015**, *137*, 6418.

[10] C. R. Bowers, D. P. Weitekamp, *Phys. Rev. Lett.* **1986**, *57*, 2645.

[11] T. C. Eisenschmid, R. U. Kirss, P. P. Deutsch, S. I. Hommeltoft, R. Eisenberg, J. Bargon, R. G. Lawler, A. L. Balch, *J. Am. Chem. Soc.* **1987**, *109*, 8089.

[12] J.-B. Hövener, A. N. Pravdivtsev, B. Kidd, C. R. Bowers, S. Glöggler, K. V. Kovtunov, M. Plaumann, R. Katz-Brull, K. Buckenmaier, A. Jerschow, F. Reineri, T. Theis, R. V. Shchepin, S. Wagner, P. Bhattacharya, N. M. Zacharias, E. Y. Chekmenev, *Angew. Chem. Int. Ed.* **2018**, *57*, 11140.

[13] P. J. Rayner, S. B. Duckett, *Angew. Chem. Int. Ed.* **2018**, *57*, 6742.

[14] F. Reineri, E. Cavallari, C. Carrera, S. Aime, *Magn. Reson. Mater. Phy.* **2021**, *34*, 25.

[15] T. G. Walker, *J. Phys. Conf. Ser.* **2011**, *294*, 012001.

[16] J. P. Mugler, T. A. Altes, *J. Magn. Reson. Imaging* **2013**, *37*, 313.

[17] J. Kurhanewicz, D. B. Vigneron, J. H. Ardenkjaer-Larsen, J. A. Bankson, K. Brindle, C. H. Cunningham, F. A. Gallagher, K. R. Keshari, A. Kjaer, C. Laustsen, D. A. Mankoff, M. E. Merritt, S. J. Nelson, J. M. Pauly, P. Lee, S. Ronen, D. J. Tyler, S. S. Rajan, D. M. Spielman, L. Wald, X. Zhang, C. R. Malloy, R. Rizi, *Neoplasia* **2019**, *21*, 1.

[18] B. Driehuys, S. Martinez-Jimenez, Z. I. Cleveland, G. M. Metz, D. M. Beaver, J. C. Nouls, S. S. Kaushik, R. Firszt, C. Willis, K. T. Kelly, J. Wolber, M. Kraft, H. P. McAdams, *Radiology* **2012**, *262*, 279.

[19] H. Johannesson, O. Axelsson, M. Karlsson, *C. R. Physique* **2004**, *5*, 315.

[20] T. Theis, M. L. Truong, A. M. Coffey, R. V. Shchepin, K. W. Waddell, F. Shi, B. M. Goodson, W. S. Warren, E. Y. Chekmenev, *J. Am. Chem. Soc.* **2015**, *137*, 1404.

[21] D. A. Barskiy, R. V. Shchepin, C. P. N. Tanner, J. F. P. Colell, B. M. Goodson, T. Theis, W. S. Warren, E. Y. Chekmenev, *ChemPhysChem* **2017**, *18*, 1493.

[22] A. N. Pravdivtsev, A. V. Yurkovskaya, H.-M. Vieth, K. L. Ivanov, R. Kaptein, *ChemPhysChem* **2013**, *14*, 3327.

[23] L. Bales, K. V. Kovtunov, D. A. Barskiy, R. V. Shchepin, A. M. Coffey, L. M. Kovtunova, A. V. Bukhtiyarov, M. A. Feldman, V. I. Bukhtiyarov, E. Y. Chekmenev, I. V. Koptyug, B. M. Goodson, *J. Phys. Chem. C* **2017**, *121*, 15304.

[24] J. Eills, J. W. Blanchard, T. Wu, C. Bengs, J. Hollenbach, D. Budker, M. H. Levitt, *J. Chem. Phys.* **2019**, *150*, 174202.

[25] E. Cavallari, C. Carrera, M. Sorge, G. Bonne, A. Muchir, S. Aime, F. Reineri, *Sci. Rep.* **2018**, *8*, 8366.

[26] O. G. Salnikov, N. V. Chukanov, R. V. Shchepin, I. V. Manzanera Esteve, K. V. Kovtunov, I. V. Koptyug, E. Y. Chekmenev, *J. Phys. Chem. C* **2019**, *123*, 12827.

[27] E. Cavallari, C. Carrera, S. Aime, F. Reineri, *J. Magn. Reson.* **2018**, *289*, 12.

[28] S. R. Muhammad, R. B. Greer, S. B. Ramirez, B. M. Goodson, A. R. Fout, *ACS Catal.* **2021**, *11*, 2011.

[29] R. W. Adams, J. A. Aguilar, K. D. Atkinson, M. J. Cowley, P. I. P. Elliott, S. B. Duckett, G. G. R. Green, I. G. Khazal, J. Lopez-Serrano, D. C. Williamson, *Science* **2009**, *323*, 1708.

[30] R. W. Adams, S. B. Duckett, R. A. Green, D. C. Williamson, G. G. R. Green, *J. Chem. Phys.* **2009**, *131*, 194505.

[31] R. E. Mewis, *Magn. Reson. Chem.* **2015**, *53*, 789.

[32] M. L. Truong, T. Theis, A. M. Coffey, R. V. Shchepin, K. W. Waddell, F. Shi, B. M. Goodson, W. S. Warren, E. Y. Chekmenev, *J. Phys. Chem. C* **2015**, *119*, 8786.

[33] V. V. Zhivonitko, I. V. Skovpin, I. V. Koptyug, *Chem. Commun.* **2015**, *51*, 2506.

[34] R. E. Mewis, R. A. Green, M. C. R. Cockett, M. J. Cowley, S. B. Duckett, G. G. R. Green, R. O. John, P. J. Rayner, D. C. Williamson, *J. Phys. Chem. B* **2015**, *119*, 1416.

[35] P. Norcott, M. J. Burns, P. J. Rayner, R. E. Mewis, S. B. Duckett, *Magn. Reson. Chem.* **2018**, *56*, 663.

[36] R. V. Shchepin, M. L. Truong, T. Theis, A. M. Coffey, F. Shi, K. W. Waddell, W. S. Warren, B. M. Goodson, E. Y. Chekmenev, *J. Phys. Chem. Lett.* **2015**, *6*, 1961.

[37] C. P. N. Tanner, J. R. Lindale, S. L. Eriksson, Z. Zhou, J. F. P. Colell, T. Theis, W. S. Warren, *J. Chem. Phys.* **2019**, *151*, 044201.

[38] D. A. Barskiy, R. V. Shchepin, A. M. Coffey, T. Theis, W. S. Warren, B. M. Goodson, E. Y. Chekmenev, *J. Am. Chem. Soc.* **2016**, *138*, 8080.

[39] B. E. Kidd, J. L. Gesiorski, M. E. Gemeinhardt, R. V. Shchepin, K. V. Kovtunov, I. V. Koptyug, E. Y. Chekmenev, B. M. Goodson, *J. Phys. Chem. C* **2018**, *122*, 16848.

[40] M. Fekete, F. Ahwal, S. B. Duckett, *J. Phys. Chem. B* **2020**, *124*, 4573.

[41] W. Iali, S. S. Roy, B. J. Tickner, F. Ahwal, A. J. Kennerley, S. B. Duckett, *Angew. Chem. Int. Ed.* **2019**, *58*, 10271.

[42] B. J. Tickner, O. Semenova, W. Iali, P. J. Rayner, A. C. Whitwood, S. B. Duckett, *Catal. Sci. Tech.* **2020**, *10*, 1343.

[43] O. G. Salnikov, N. V. Chukanov, A. Svyatova, I. A. Trofimov, M. S. H. Kabir, J. G. Gelovani, K. V. Kovtunov, I. V. Koptyug, E. Y. Chekmenev, *Angew. Chem. Int. Ed.* **2021**, *60*, 2406.

[44] J. R. Birchall, M. S. H. Kabir, O. G. Salnikov, N. V. Chukanov, A. Svyatova, K. V. Kovtunov, I. V. Koptyug, J. G. Gelovani, B. M. Goodson, W. Pham, E. Y. Chekmenev, *Chem. Commun.* **2020**, *56*, 9098.

[45] R. V. Shchepin, J. R. Birchall, N. V. Chukanov, K. V. Kovtunov, I. V. Koptyug, T. Theis, W. S. Warren, J. G. Gelovani, B. M. Goodson, S. Shokouhi, M. S. Rosen, Y.-F. Yen, W. Pham, E. Y. Chekmenev, *Chem. A Eur. J.* **2019**, *25*, 8829.

[46] M. J. Cowley, R. W. Adams, K. D. Atkinson, M. C. R. Cockett, S. B. Duckett, G. G. R. Green, J. A. B. Lohman, R. Kerssebaum, D. Kilgour, R. E. Mewis, *J. Am. Chem. Soc.* **2011**, *133*, 6134.

[47] S. Nantogma, B. Joalland, K. Wilkens, E. Y. Chekmenev, *Anal. Chem.* **2021**, *93*, 3594.

[48] S. Kadlecek, V. Vahdat, T. Nakayama, D. Ng, K. Emami, R. Rizi, *NMR Biomed.* **2011**, *24*, 933.

[49] B. Joalland, A. Schmidt, M. S. H. Kabir, N. V. Chukanov, K. V. Kovtunov, I. V. Koptyug, J. Hennig, J.-B. Hövener, E. Y. Chekmenev, *Anal. Chem.* **2020**, *92*, 1340.

SUPPORTING INFORMATION

Additional supporting information may be found online in the Supporting Information section at the end of this article.

Automated Low-Cost In Situ IR and NMR Spectroscopy Characterization of Clinical-Scale ^{129}Xe Spin-Exchange Optical Pumping

Jonathan R. Birchall,* Robert K. Irwin, Md Raduanul H. Chowdhury, Panayiotis Nikolaou, Boyd M. Goodson, Michael J. Barlow, Anton Shcherbakov, and Eduard Y. Chekmenev*

Read Online

ACCESS | Metrics & More | Article Recommendations | Supporting Information

ABSTRACT: We present on the utility of in situ nuclear magnetic resonance (NMR) and near-infrared (NIR) spectroscopic techniques for automated advanced analysis of the ^{129}Xe hyperpolarization process during spin-exchange optical pumping (SEOP). The developed software protocol, written in the MATLAB programming language, facilitates detailed characterization of hyperpolarized contrast agent production efficiency based on determination of key performance indicators, including the maximum achievable ^{129}Xe polarization, steady-state Rb−^{129}Xe spin-exchange and ^{129}Xe polarization build-up rates, ^{129}Xe spin-relaxation rates, and estimates of steady-state Rb electron polarization. Mapping the dynamics of ^{129}Xe polarization and relaxation as a function of SEOP temperature enables systematic optimization of the batch-mode SEOP process. The automated analysis of a typical experimental data set, encompassing ∼300 raw NMR and NIR spectra combined across six different SEOP temperatures, can be performed in under 5 min on a laptop computer. The protocol is designed to be robust in operation on any batch-mode SEOP hyperpolarizer device. In particular, we demonstrate the implementation of a combination of low-cost NIR and low-frequency NMR spectrometers (∼$1,100 and ∼$300 respectively, ca. 2020) for use in the described protocols. The demonstrated methodology will aid in the characterization of NMR hyperpolarization hardware in the context of SEOP and other hyperpolarization techniques for more robust and less expensive clinical production of HP ^{129}Xe and other contrast agents.
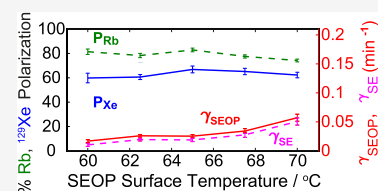
Nuclear magnetic resonance (NMR) of hyperpolarized (HP) ^{129}Xe facilitates preclinical and clinical biomedical imaging of the lungs,[1−13] brain,[14−18] and brown fat tissue.[19,20] In order to overcome the inherently poor signal-to-noise ratio (SNR) afforded by the ^{129}Xe nucleus, nuclear spin hyperpolarization is performed to increase MR signal and detection sensitivity far beyond levels observed at thermal equilibrium.[21−25] For the purposes of clinical-scale contrast agent production, ^{129}Xe hyperpolarization is typically performed by spin-exchange optical pumping (SEOP), a two-step process in which spin angular momentum is transferred from circularly polarized laser light to ^{129}Xe nuclei via gas-phase collisions, with electrons of a vaporized alkali metal such as rubidium acting as an intermediary.[26,27] A nitrogen buffer gas (N$_2$) is used to perform collisional quenching of excited Rb electrons and minimize radiative spin-relaxation[28,29] with the goal of achieving near unity ^{129}Xe polarization.

Two major approaches for clinical-scale HP ^{129}Xe contrast agent production exist. The first of these methodologies is continuous-flow production, whereby a (usually dilute) Xe-containing gas mixture is passed through the polarization vessel (termed "SEOP cell"), and the HP ^{129}Xe is collected on a cryogenically cooled coldfinger upon exit.[28,30−34] The second methodology is stopped-flow (or batch-mode), in which a fixed volume of typically Xe-rich gas mixture is hyperpolarized inside a

sealed SEOP cell for a given time period, before being ejected and the SEOP cell being refilled.[35−38] Xe-rich stopped-flow hyperpolarization negates the need for cryo-collection, but somewhat limits the contrast agent production rate relative to continuous-flow modalities.[39−41] Nevertheless, recent developments in batch-mode SEOP have enabled clinical-scale production of HP ^{129}Xe.[42,43]

For the purposes of clinical-scale HP contrast agent production, the most important considerations to account for are the maximum achievable ^{129}Xe polarization payload (i.e., the product of volume, ^{129}Xe density, and P_{Xe}) and the dose-equivalent rate of production (DE).[40] Irrespective of the production modality employed, one significant difficulty associated with evaluating hyperpolarization efficiency during the SEOP process is the complex interdependence of key performance indicators on a number of experimental factors, including SEOP cell temperature, gas mixture composition and
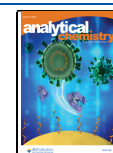
density, pump laser power (and resonant flux), Rb purity, the resulting in-cell ^{129}Xe T_1, and others. Clinical-scale HP ^{129}Xe NMR spectroscopy and imaging are emerging technologies, and although a number of studies have been performed to quantify the effect of these variables on hyperpolarization efficiency,[37,44,45] "optimal" conditions can vary substantially depending on the environment and methodologies used.

Batch-mode SEOP in particular is conducive to real-time in situ monitoring of SEOP performance via near-infrared (NIR) and low-field NMR spectroscopic techniques. Comparison of the pump laser transmission profile before, during, and after SEOP can provide valuable information on photon absorption, and by extension, Rb polarization,[29,41,42] whereas localized, low-intensity radio frequency (RF) probing of ^{129}Xe spins allows determination of the ^{129}Xe polarization, build-up rates, and relaxation rates,[46−50] which provide further insight into spin-exchange efficiency and overall SEOP cell "health".[41] The combination of these two spectroscopic techniques has been used to quantify the benefits of numerous scientific advances in the field.[41] Such advances include better optical pumping efficiency and thermal management resulting from using high-power, frequency-narrowed laser diode arrays (LDAs),[51−54] long-lived and reproducible polarization values and SEOP cell lifetimes arising from investigations into SEOP cell cleaning and preparation,[43,55−58] as well as more exotic studies into spin-exchange efficiency of hybrid alkali metal SEOP,[59,60] Rb cluster formation[44,61,62] and others. In most previous studies, NIR and NMR spectroscopic techniques have typically been performed using commercial instrumentation, which are often over-engineered for the specific purposes described here. As a consequence, these components often embody expensive solutions for relatively simple problems; for example, an HP4Pro (Ocean Insight, formerly Ocean Optics) IR spectrometer costs ~$5,300 (ca. 2020) and a low-field Kea2 NMR spectrometer (Magritek, New Zealand) costs over $20,000, thereby presenting a nontrivial cost burden to undertake studies in the field. Less expensive spectroscopic hardware would be welcomed by the hyperpolarization community to mitigate the instrumentation cost and improve access by the broader community.

In this article, we present a bimodal analysis protocol capable of fusing NMR and NIR spectroscopic data and extracting key parameters describing the SEOP process and HP ^{129}Xe production efficiency. These key performance indicator (KPI) variables include the predicted and observed ^{129}Xe polarization values, P_{Xe}, as well as the Rb−^{129}Xe spin-exchange rate, γ_{SE}, the ^{129}Xe polarization build-up and relaxation rates, γ_{SEOP} and $1/T_1$, and estimates of the Rb polarization, %P_{Rb}, all as functions of time and/or SEOP cell temperature. This protocol is written in the MATLAB programming language, offering a high degree of automation and reproducibility, as well as graphical representation of data for easier identification of trends, maxima, potential outliers, and other points of interest. Moreover, we demonstrate the utility of using low-cost NMR and NIR spectrometers to acquire the required spectroscopic data. This methodology enables a robust approach for efficient production of HP ^{129}Xe on a clinical scale, regardless of hyperpolarizer design, NMR or NIR acquisition protocols and hardware (as long as the required data output is available), or production modality utilized, which should be of practical translational importance to preclinical studies involving production and subsequent biomedical imaging of HP ^{129}Xe.

MATERIALS AND METHODS

The ^{129}Xe hyperpolarizer device used for development and testing of the MATLAB data analysis protocol was a second-generation (GEN-2) automated, clinical-scale, batch-mode XeUS device, the construction and performance of which has been presented in detail elsewhere.[41,42] A schematic representation of the SEOP process as performed on the hyperpolarizer is displayed in Figure 1.
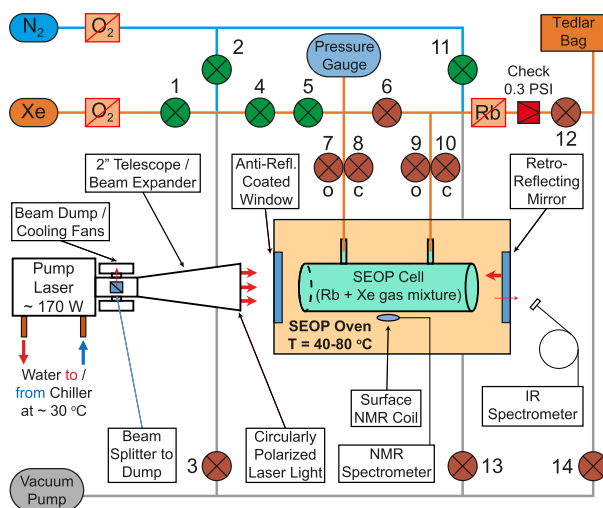

Figure 1. Schematic representation of the SEOP process as performed on the XeUS GEN-2 ^{129}Xe hyperpolarizer used in this study, illustrating the orientation and interfacing of key components necessary for acquisition of NMR and IR spectroscopic data. The central shaded area illustrates the boundaries of the forced-air SEOP oven. Numbered gas-handling manifold valves are displayed as green (normally open) and brown (normally closed) circles. Gas purifiers and filters are denoted with light brown rectangles, with a gas ejection path check valve shown as a red square.

This hyperpolarizer device features a small noise-canceling surface NMR RF coil (Figure 3d) situated directly beneath the SEOP cell containing the Xe gas mixture, which allows for in situ ^{129}Xe NMR spectroscopy via a Kea2 NMR spectrometer interfacing with Prospa v3.53 spectroscopy software (Magritek, Wellington, New Zealand). This coil arrangement is tuned to a resonance frequency of 40.8 kHz for both ^{1}H and ^{129}Xe spins.[41] Pump laser photons perform a double-pass through the SEOP cell via a retro-reflecting mirror located behind the rear of the SEOP cell, with a small proportion of these photons passing through the mirror to an HR4000 IR spectrometer via OceanView spectroscopy software (Ocean Insight Inc., Largo, FL) via a pinhole aperture and a 50 μm (o.d.) fiber optic cable. These two devices facilitate real-time monitoring of the SEOP process, and output recorded information as both raw data and graphical formats, the former of which can be readily imported into the MATLAB workspace for further processing. NMR and IR spectroscopy, along with many other hyperpolarizer functions such as ejecting HP ^{129}Xe, refilling the SEOP cell, and maintaining SEOP cell temperature, are controlled via an Arduino microcontroller and graphical user interface (GUI).

Moreover, we have also employed a custom-made low-frequency NMR spectrometer (up to 120 kHz operation range, Figure 3d) and HR1 NIR spectrometer (ASEQ Instruments, Victoria, BC, Canada, $1,100 ca. 2020) to demonstrate the
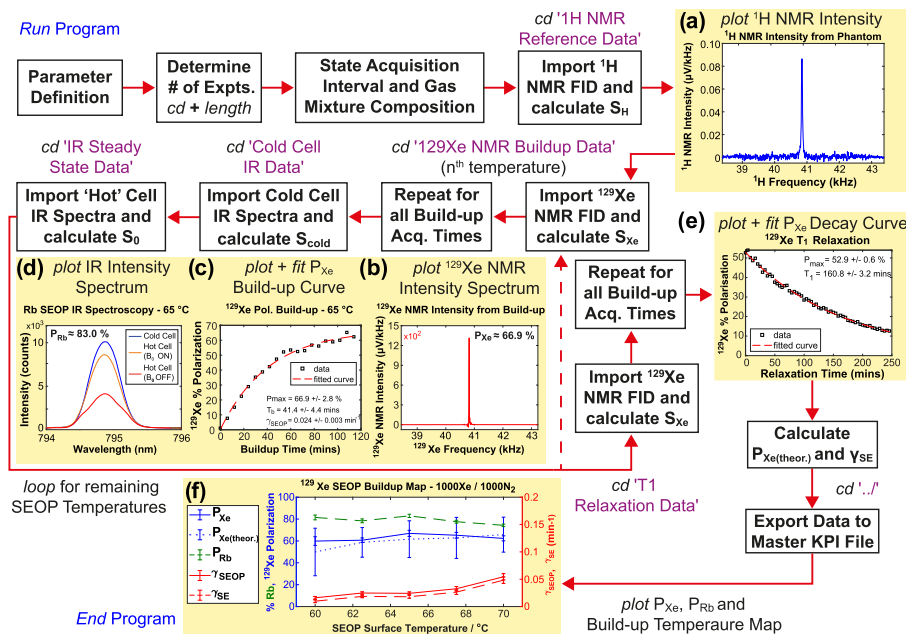
Figure 2. Flowchart depicting an overview of the automated NMR and IR spectroscopic data analysis process performed in MATLAB (cd refers to the change of directory during automated data processing). Data analyzed is used to plot a number of figures providing easier representation and trend analysis comprising (a) ^{1}H thermal reference NMR intensity; (b) HP ^{129}Xe NMR intensity; (c) ^{129}Xe NMR intensity as a function of time during SEOP build-up; (d) Pump laser NIR intensity before SEOP and after reaching steady-state polarization conditions; (e) ^{129}Xe NMR intensity as a function of time during spin-relaxation (no SEOP); (f) Key SEOP performance indicators under steady-state polarization conditions as a function of SEOP cell temperature. MATLAB file and folder architecture is indicated in purple text, see Supporting Information (SI) for more details. All figures shown are representative of their appearance as generated by MATLAB with minor postproduction editing.

feasibility of low-cost data acquisition. The total cost of the NMR spectrometer's components and assembly is less than $300. As SEOP is performed, the combination of IR and NMR spectra are collected as a series of data: (i) with inner loop as a time series to monitor SEOP polarization build-up and decay, and (ii) with outer loop as a function of SEOP cell temperature. After all desired experimentation has been performed on a given SEOP cell or gas mixture, a single execution of the MATLAB program is performed to conduct spectroscopic NMR and IR data analysis on each experiment in sequence. This protocol operates based on a predefined file architecture (see SI for more information), meaning that as long as a consistent format of naming and saving data is utilized, no significant modifications are required to ensuring that data processing can be reliably performed on other polarizer designs or experimental protocols.

RESULTS AND DISCUSSION

Program execution begins by clearing the MATLAB variable workspace of previous analyses, and definition of new constants and experiment-specific settings, including the Larmor frequency at which SEOP is performed, the number of acquired NMR data points, acquisition time delay and step size, gas mixture composition, etc. MATLAB automatically determines the number of build-up experiments and the SEOP cell temperatures at which they were performed, and begins importing free-induction decay (FID) NMR data collected during SEOP in comma-separated values (.csv) format. This operation is performed first for a specified thermal ^{1}H reference signal (typically H_2O doped with 10 mM $CuSO_4$, Figure 2a), and then for HP ^{129}Xe build-up data after changing to a second file directory (Figure 2b). P_{Xe} was computed by comparing the HP ^{129}Xe NMR signal integral (S_{Xe}, Figure 2b) to that of the

reference signal from water (S_H, Figure 2a) to determine a signal enhancement factor arising from hyperpolarization, see the Supporting Information (SI) for more details. After performing analysis of NMR data on a single SEOP build-up experiment, an exponential build-up curve of ^{129}Xe polarization (%P_{Xe}) is plotted as a function of time using MATLAB's Curve Fitting Toolbox (CFT), see Figure 2c. In addition to the maximum achievable (steady-state) ^{129}Xe polarization, the coefficients of this fit also provide the ^{129}Xe polarization monoexponential build-up time constant (T_b) and rate ($\gamma_{SEOP} = 1/T_b$). IR spectral data under various conditions for the corresponding experiment (same SEOP cell temperature) are then processed in a third directory. Trapezoidal integration and subsequent comparison of the respective cold (no optical pumping) and "hot" (steady-state polarization) pump laser NIR spectral peaks facilitates determination of the Rb electron polarization (%P_{Rb}) using Beer's Law as described previously,[41,42,45,52] see Figure 2d and SI for complete details. A series of nested loop functions is used to alternate the import and processing of NMR and IR spectroscopic data for each SEOP cell temperature in sequence. In addition to ^{129}Xe NMR build-up data, multiple spin-relaxation experiments are processed in a fourth directory, allowing for calculation of the ^{129}Xe relaxation time constant, T_1 as shown in Figure 2e.

In addition to generating figures for all of the above processed data in a widely accessible, high-resolution PDF format, the stored, steady-state variables across all SEOP cell temperatures are combined into a single array for the generation of a temperature-dependent SEOP map (Figure 2f). This plot also presents some additionally calculated key performance indicators (KPIs), such as the Rb−^{129}Xe spin-exchange rate γ_{SE} (estimated using $\gamma_{SEOP} - 1/T_1$), as well as the predicted ^{129}Xe

polarization, $P_{Xe(theor.)}$ (defined as $\%P_{Rb}\cdot\gamma_{SE}\cdot(\gamma_{SEOP})^{-1}$), see the SI for more details. This data table (with parameter values and error bars) is also saved in an easily accessible.csv format, should the user wish to perform additional analysis or figure reproduction.

These KPIs have significant practical value: $\%P_{Xe}$ is the ultimate levels of polarization attainable; γ_{SEOP} effectively reports on the overall production rate, i.e., the HP contrast agent production speed. $P_{Xe(theor.)}$ is the theoretical ^{129}Xe polarization value computed based on the measurement of % P_{Rb} (see above). All-in-all, $\%P_{Rb}$, γ_{SEOP}, and $P_{Xe(theor.)}$ provide key details about the SEOP process, and their values are important from the perspective of trouble-shooting and evaluation of overall data consistency. For example, a decrease in $\%P_{Xe}$ may be the result of lower-than-expected $\%P_{Rb}$ due to decreased photon absorption. Moreover, substantial disagreement between $\%P_{Xe}$ and $P_{Xe(theor.)}$ could be the result of other deleterious ^{129}Xe polarization losses in the SEOP cell. All-in-all, the SEOP process map shown in Figure 2f provides a detailed informational overview of the SEOP process to guide optimizing day-to-day hyperpolarizer performance, and also monitoring the SEOP process efficiency as the SEOP cell degrades with time over hundreds of production cycles.

To demonstrate the utility of the reported approach for other hyperpolarizer devices, we have also employed generation-3 XeUS hyperpolarizer[43] to probe test-retest reliability in our ongoing studies. Three ^{129}Xe polarization build-up curves were recorded during a three-day period, SI Figures S1−S3, respectively. The automated protocol for data processing yielded: $\%P_{Xe}$ values: 60.9 ± 1.5%, 60.6 ± 1.1%, and 61.7 ± 1.8%; $\%P_{Rb}$ values: 72.7 ± 1.4%, 75.7 ± 1.4%, and 70.4 ± 1.4%; γ_{SEOP} values: 0.056 ± 0.004, 0.059 ± 0.003, and 0.055 ± 0.005. These results obtained in 1000 Torr Xe and 1000 Torr N_2 mixture at 80 °C SEOP cell temperature clearly demonstrate the reproducibility of the described approach.

Finally, Figure 3 demonstrates the feasibility of low-cost NIR and NMR spectroscopy integrated with the ^{129}Xe hyperpolarizer. Figure 3a shows the example of $\%P_{Rb}$ determination using NIR spectroscopy of the cold and hot (steady-state ^{129}Xe polarization) SEOP cell using the ASEQ Instruments HR1 spectrometer. Figure 3b demonstrates the optimization plot of excitation RF pulses (0.4 ms duration) acquired using the low-cost, custom-made NMR spectrometer; a corresponding in situ low-field ^{129}Xe NMR spectrum from HP ^{129}Xe is shown in Figure 3c. A photograph of the NMR spectrometer board and the RF excitation coil is provided in Figure 3d. While other low-cost and low-frequency NMR spectrometer designs have been reported,[63−70] the design demonstrated here represents a tailored solution for integration in point-of-care products, such as our ^{129}Xe hyperpolarizer.

■ CONCLUSIONS

The MATLAB analysis protocol presented here demonstrates robust and reproducible determination of ^{129}Xe SEOP hyperpolarization efficiency that can be readily implemented in clinical research settings, irrespective of the production modality, experimental configuration, or hyperpolarizer device used (provided the necessary spectroscopic data acquisition is available). This multimodal approach combining dynamic in situ NMR spectroscopy of the ^{129}Xe-containing gas-mixture, as well as pump laser photon NIR spectroscopy of Rb electrons, facilitates the calculation of a number of factors of crucial
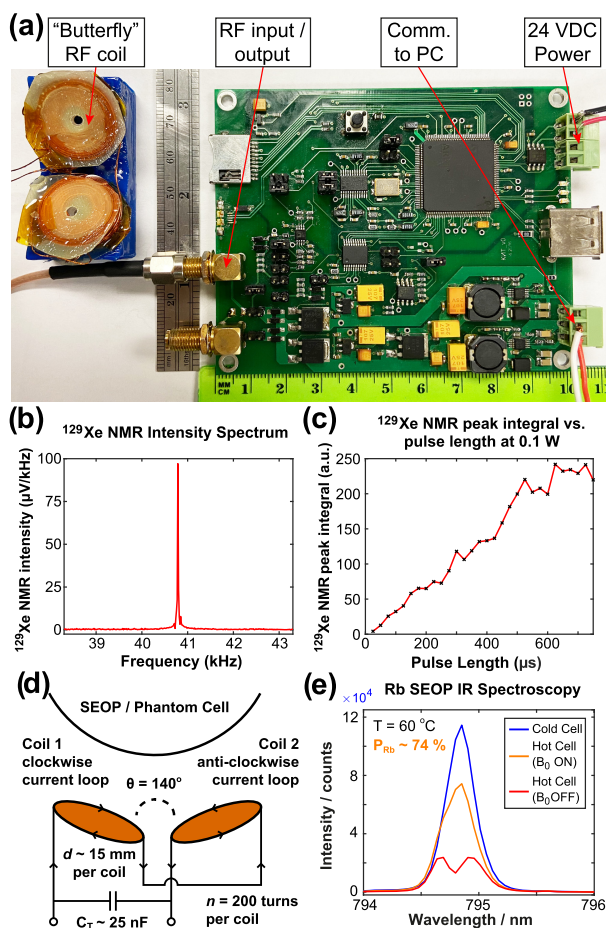

Figure 3. Low-cost NIR and NMR spectroscopy. (a) Photograph of low-cost NMR spectrometer and noise-canceling "butterfly" RF coil employed for NMR signal acquisition. (b) ^{129}Xe NMR spectroscopy of HP ^{129}Xe using low-cost NMR spectrometer. (c) Optimization of NMR signal via excitation RF pulse duration calibration for the custom-made NMR spectrometer. (d) Arrangement of SEOP cell and noise-canceling RF coil. (e) ASEQ HR-1 NIR spectra of the SEOP hyperpolarization process demonstrating the feasibility of low-cost NIR for cold SEOP cell (blue trace), hot SEOP cell with B_0 magnet on (orange trace), and hot SEOP cell with B_0 magnet off (red trace). Note the in situ NMR spectroscopy using Magritek Kea2 spectrometer (using otherwise similar parameters) is shown in Figure 2b.

importance to SEOP performance, polarization lifetime, and SEOP cell degradation on a clinical scale.

Direct comparison of thermal ^{1}H reference and HP ^{129}Xe NMR spectra via trapezoidal integration allows for quick and reliable determination of ^{129}Xe polarization enhancement during SEOP. When combined with trend and coefficient determination from MATLAB's Curve Fitting Toolbox, this allows for calculation of the ^{129}Xe polarization build-up, spin-exchange, and relaxation rates to a high degree of accuracy and precision. Comparison of ambient and steady-state SEOP pump laser photon absorption profiles via NIR spectroscopy sheds light on optical pumping efficiency and the resulting Rb polarization. Complete data analysis, including generation of all relevant figures and tables discussed previously, can be performed rapidly, on the order of 5 min for experiments comprising ∼300 combined polarization build-up and relaxation NMR and steady-state NIR spectra. The analysis protocol is also designed

with a high degree of consistency and reproducibility in mind, with spectral importing, calibration, and processing being completely automated in the directory in which the program is executed, and requiring only minimal input guidance from the user. The feasibility of simultaneous low-cost in situ NIR and NMR spectroscopy is also demonstrated. It is hoped that this methodology will provide users of ^{129}Xe hyperpolarizer devices with a better understanding of the optimal conditions for SEOP on their respective device(s), as well as facilitate further advancements in the development of lower-cost clinical-scale HP ^{129}Xe contrast agent production in the future. Finally, the approaches presented here would likely also be useful when integrated into other types of hyperpolarization devices especially those aiding from low-field in situ NMR detection.[71,72]

■ ASSOCIATED CONTENT

Ⓢ Supporting Information

The Supporting Information is available free of charge at https://pubs.acs.org/doi/10.1021/acs.analchem.0c04545.

> Complete copy of the MATLAB data analysis program for processing of NMR and IR spectra, including an example folder architecture (PDF)
>
> Additional MATLAB functions necessary for program operation (ZIP)

■ AUTHOR INFORMATION

Corresponding Authors

Jonathan R. Birchall − *Department of Chemistry, Integrative Biosciences (Ibio), Wayne State University, Karmanos Cancer Institute (KCI), Detroit, Michigan 48202, United States;* ⓞ orcid.org/0000-0003-3920-4038; Email: jonathan.birchall@outlook.com

Eduard Y. Chekmenev − *Department of Chemistry, Integrative Biosciences (Ibio), Wayne State University, Karmanos Cancer Institute (KCI), Detroit, Michigan 48202, United States; Russian Academy of Sciences, Moscow 119991, Russia;* ⓞ orcid.org/0000-0002-8745-8801; Email: chekmenevlab@gmail.com

Authors

Robert K. Irwin − *Sir Peter Mansfield Imaging Centre, University of Nottingham, Nottingham NG7 2RD, United Kingdom*

Md Raduanul H. Chowdhury − *Department of Chemistry, Integrative Biosciences (Ibio), Wayne State University, Karmanos Cancer Institute (KCI), Detroit, Michigan 48202, United States*

Panayiotis Nikolaou − *XeUS Technologies LTD, Nicosia 2312, Cyprus;* ⓞ orcid.org/0000-0002-3802-0803

Boyd M. Goodson − *Department of Chemistry and Biochemistry and Materials Technology Center, Southern Illinois University, Carbondale, Illinois 62901, United States;* ⓞ orcid.org/0000-0001-6079-5077

Michael J. Barlow − *Sir Peter Mansfield Imaging Centre, University of Nottingham, Nottingham NG7 2RD, United Kingdom*

Anton Shcherbakov − *Smart-A, Perm, Perm Region 614000, Russia; Custom Medical Systems (CMS) LTD, Nicosia 2312, Cyprus*

Complete contact information is available at:
https://pubs.acs.org/10.1021/acs.analchem.0c04545

Notes

■ REFERENCES

(1) Dregely, I.; Mugler, J. P.; Ruset, I. C.; Altes, T. A.; Mata, J. F.; Miller, G. W.; Ketel, J.; Ketel, S.; Distelbrink, J.; Hersman, F. W.; Ruppert, K. *J. Magn. Reson. Imaging* **2011**, *33* (5), 1052−1062.

(2) Mugler, J. P.; Altes, T. A.; Ruset, I. C.; Dregely, I. M.; Mata, J. F.; Miller, G. W.; Ketel, S.; Ketel, J.; Hersman, F. W.; Ruppert, K. *Proc. Natl. Acad. Sci. U. S. A.* **2010**, *107* (50), 21707−21712.

(3) Mugler, J. P., III; Driehuys, B.; Brookeman, J. R.; Cates, G. D.; Berr, S. S.; Bryant, R. G.; Daniel, T. M.; De Lange, E. E.; Downs, J. H.; Erickson, C. J.; Happer, W.; Hinton, D. P.; Kassel, N. F.; Maier, T.; Phillips, C. D.; Saam, B. T.; Sauer, K. L.; Wagshul, M. E. *Magn. Reson. Med.* **1997**, *37*, 809−815.

(4) Mugler, J. P.; Altes, T. A. *J. Magn. Reson. Imaging* **2013**, *37* (2), 313−331.

(5) Qing, K.; Mugler, J. P.; Altes, T. A.; Jiang, Y.; Mata, J. F.; Miller, G. W.; Ruset, I. C.; Hersman, F. W.; Ruppert, K. *NMR Biomed.* **2014**, *27* (12), 1490−1501.

(6) Albert, M. S.; Cates, G. D.; Driehuys, B.; Happer, W.; Saam, B.; Springer, C. S.; Wishnia, A. *Nature* **1994**, *370* (6486), 199−201.

(7) Walkup, L. L.; Woods, J. C. *NMR Biomed.* **2014**, *27* (12), 1429−1438.

(8) Matsuoka, S.; Patz, S.; Albert, M. S.; Sun, Y.; Rizi, R. R.; Gefter, W. B.; Hatabu, H. *J. Thorac. Imaging* **2009**, *24* (3), 181−188.

(9) Stewart, N. J.; Chan, H.-F.; Hughes, P. J. C.; Horn, F. C.; Norquay, G.; Rao, M.; Yates, D. P.; Ireland, R. H.; Hatton, M. Q.; Tahir, B. A.; Ford, P.; Swift, A. J.; Lawson, R.; Marshall, H.; Collier, G. J.; Wild, J. M. *J. Magn. Reson. Imaging* **2018**, *48* (3), 632−642.

(10) Mammarappallil, J. G.; Rankine, L.; Wild, J. M.; Driehuys, B. *J. Thorac. Imaging* **2019**, *34* (2), 136−150.

(11) Wang, Z.; Bier, E. A.; Swaminathan, A.; Parikh, K.; Nouls, J.; He, M.; Mammarappallil, J. G.; Luo, S.; Driehuys, B.; Rajagopal, S. *Eur. Respir. J.* **2019**, *54*, 1900831.

(12) Thomen, R. P.; Walkup, L. L.; Roach, D. J.; Cleveland, Z. I.; Clancy, J. P.; Woods, J. C. *J. Cystic Fibrosis* **2017**, *16* (2), 275−282.

(13) Ruppert, K.; Hamedani, H.; Amzajerdian, F.; Xin, Y.; Duncan, I. F.; Profka, H.; Siddiqui, S.; Pourfathi, M.; Kadlecek, S.; Rizi, R. R. *Sci. Rep.* **2018**, *8* (1), 7310.

(14) Rao, M. R.; Stewart, N. J.; Griffiths, P. D.; Norquay, G.; Wild, J. M. *Radiology* **2018**, *286* (2), 659−665.

(15) Mazzanti, M. L.; Walvick, R. P.; Zhou, X.; Sun, Y. P.; Shah, N.; Mansour, J.; Gereige, J.; Albert, M. S. *PLoS One* **2011**, *6* (7), 7.

(16) Wakai, A.; Nakamura, K.; Kershaw, J.; Kanno, I. *Int. Congr. Ser.* **2004**, *1265*, 139−143.

(17) Duhamel, G.; Choquet, P.; Grillon, E.; Lamalle, L.; Leviel, J. L.; Ziegler, A.; Constantinesco, A. *Magn. Reson. Med.* **2001**, *46*, 208−212.

(18) Swanson, S. D.; Rosen, M. S.; Agranoff, B. W.; Coulter, K. P.; Welsh, R. C.; Chupp, T. E. *Magn. Reson. Med.* **1997**, *38*, 695−698.

(19) Antonacci, M. A.; McHugh, C.; Kelley, M.; McAllister, A.; Degan, S.; Branca, R. T. *Sci. Rep.* **2019**, *9*, 14865−14876.

(20) Branca, R. T.; He, T.; Zhang, L.; Floyd, C. S.; Freeman, M.; White, C.; Burant, A. *Proc. Natl. Acad. Sci. U. S. A.* **2014**, *111* (50), 18001−18006.

(21) Goodson, B. M.; Whiting, N.; Coffey, A. M.; Nikolaou, P.; Shi, F.; Gust, B.; Gemeinhardt, M. E.; Shchepin, R. V.; Skinner, J. G.; Birchall, J. R.; Barlow, M. J.; Chekmenev, E. Y., Hyperpolarization Methods for MRS. In *eMagRes: Handbook of in Vivo Magnetic Resonance Spectroscopy;* Griffiths, J.; Bottomley, P.; Wasylishen, R. E., Eds.; John Wiley & Sons, Ltd: West Sussex, UK, 2015; Vol. 4, pp 797−810.

(22) Kovtunov, K. V.; Pokochueva, E. V.; Salnikov, O. G.; Cousin, S.; Kurzbach, D.; Vuichoud, B.; Jannin, S.; Chekmenev, E. Y.; Goodson, B. M.; Barskiy, D. A.; Koptyug, I. V. *Chem. - Asian J.* **2018**, *13* (15), 1857−1871.

(23) Nikolaou, P.; Goodson, B. M.; Chekmenev, E. Y. *Chem. - Eur. J.* **2015**, *21* (8), 3156−3166.

(24) Ardenkjaer-Larsen, J. H.; Fridlund, B.; Gram, A.; Hansson, G.; Hansson, L.; Lerche, M. H.; Servin, R.; Thaning, M.; Golman, K. *Proc. Natl. Acad. Sci. U. S. A.* **2003**, *100* (18), 10158−10163.

(25) Barskiy, D. A.; Coffey, A. M.; Nikolaou, P.; Mikhaylov, D. M.; Goodson, B. M.; Branca, R. T.; Lu, G. J.; Shapiro, M. G.; Telkki, V.-V.; Zhivonitko, V. V.; Koptyug, I. V.; Salnikov, O. G.; Kovtunov, K. V.; Bukhtiyarov, V. I.; Rosen, M. S.; Barlow, M. J.; Safavi, S.; Hall, I. P.; Schröder, L.; Chekmenev, E. Y. *Chem. - Eur. J.* **2017**, *23* (4), 725−751.

(26) Walker, T. G. *J. Phys. Conf. Ser.* **2011**, *294*, No. 012001.

(27) Walker, T. G.; Happer, W. *Rev. Mod. Phys.* **1997**, *69* (2), 629−642.

(28) Driehuys, B.; Cates, G. D.; Miron, E.; Sauer, K.; Walter, D. K.; Happer, W. *Appl. Phys. Lett.* **1996**, *69* (12), 1668−1670.

(29) Saha, I.; Nikolaou, P.; Whiting, N.; Goodson, B. M. *Chem. Phys. Lett.* **2006**, *428* (4−6), 268−276.

(30) Knagge, K.; Prange, J.; Raftery, D. *Chem. Phys. Lett.* **2004**, *397* (1−3), 11−16.

(31) Haake, M.; Pines, A.; Reimer, J. A.; Seydoux, R. *J. Am. Chem. Soc.* **1997**, *119*, 11711−11712.

(32) Ruset, I. C.; Ketel, S.; Hersman, F. W. *Phys. Rev. Lett.* **2006**, *96* (5), No. 053002.

(33) Zook, A. L.; Adhyaru, B. B.; Bowers, C. R. *J. Magn. Reson.* **2002**, *159* (2), 175−182.

(34) Norquay, G.; Collier, G. J.; Rao, M.; Stewart, N. J.; Wild, J. M. *Phys. Rev. Lett.* **2018**, *121* (15), 153201.

(35) Rosen, M. S.; Chupp, T. E.; Coulter, K. P.; Welsh, R. C.; Swanson, S. D. *Rev. Sci. Instrum.* **1999**, *70* (2), 1546−1552.

(36) Six, J. S.; Hughes-Riley, T.; Stupic, K. F.; Pavlovskaya, G. E.; Meersmann, T. *PLoS One* **2012**, *7* (11), 16.

(37) Nikolaou, P.; Coffey, A. M.; Ranta, K.; Walkup, L. L.; Gust, B.; Barlow, M. J.; Rosen, M. S.; Goodson, B. M.; Chekmenev, E. Y. *J. Phys. Chem. B* **2014**, *118* (18), 4809−4816.

(38) Pałasza, T.; Mikowskaa, L.; Głowacza, B.; Olejniczakb, Z.; Suchanekc, M.; Dohnalika, T. *Acta Phys. Pol., A* **2019**, *136*, 1008−1017.

(39) Nikolaou, P.; Coffey, A. M.; Walkup, L. L.; Gust, B. M.; Whiting, N.; Newton, H.; Barcus, S.; Muradyan, I.; Dabaghyan, M.; Moroz, G. D.; Rosen, M.; Patz, S.; Barlow, M. J.; Chekmenev, E. Y.; Goodson, B. M. *Proc. Natl. Acad. Sci. U. S. A.* **2013**, *110* (35), 14150−14155.

(40) He, M.; Robertson, S. H.; Kaushik, S. S.; Freeman, M. S.; Virgincar, R. S.; Davies, J.; Stiles, J.; Foster, W. M.; McAdams, H. P.; Driehuys, B. *Magn. Reson. Imaging* **2015**, *33* (7), 877−885.

(41) Birchall, J. R.; Irwin, R. K.; Nikolaou, P.; Pokochueva, E.; Kovtunov, K. V.; V, K. I.; Barlow, M. J.; Goodson, B. M.; Chekmenev, E. Y. *J. Magn. Reson.* **2020**, *316*, 106755.

(42) Birchall, J. R.; Irwin, R. K.; Nikolaou, P.; Coffey, A. M.; Kidd, B. E.; Murphy, M.; Molway, M.; Bales, L. B.; Ranta, K.; Barlow, M. J.; Goodson, B. M.; Rosen, M. S.; Chekmenev, E. Y. *J. Magn. Reson.* **2020**, *319*, 106813.

(43) Birchall, J. R.; Nikolaou, P.; Coffey, A. M.; Kidd, B. E.; Murphy, M.; Molway, M.; Bales, L. B.; Goodson, B. M.; Irwin, R. K.; Barlow, M. J.; Chekmenev, E. Y. *Anal. Chem.* **2020**, *92* (6), 4309−4316.

(44) Antonacci, M. A.; Burant, A.; Wagner, W.; Branca, R. T. *J. Magn. Reson.* **2017**, *279*, 8.

(45) Birchall, J. R.; Nikolaou, P.; Irwin, R. K.; Barlow, M. J.; Ranta, K.; Coffey, A. M.; Goodson, B. M.; Pokochueva, E. V.; Kovtunov, K. V.; Koptyug, I. V.; Chekmenev, E. Y. *J. Magn. Reson.* **2020**, *315*, 106739.

(46) Romalis, M.; Cates, G. D. *Phys. Rev. A: At., Mol., Opt. Phys.* **1998**, *58*, 3004.

(47) Saam, B., T₁ Relaxation of ¹²⁹Xe and How to Keep it Long. In *Hyperpolarized Xenon-129 Magnetic Resonance: Concepts, Production, Techniques and Applications*; Meersmann, T.; Brunner, E., Eds.; Royal Soc. Chem., 2015; pp 122−141.

(48) Norquay, G.; Leung, G.; Stewart, N. J.; Tozer, G. M.; Wolber, J.; Wild, J. *Magn. Reson. Med.* **2015**, *74*, 303−311.

(49) Anger, B. C.; Schrank, G.; Schoeck, A.; Butler, K. A.; Solum, M. S.; Pugmire, R. J.; Saam, B. *Phys. Rev. A: At., Mol., Opt. Phys.* **2008**, *78* (4), No. 043406.

(50) Nelson, I. A.; Walker, T. G. *Phys. Rev. A: At., Mol., Opt. Phys.* **2001**, *65*, No. 012712.

(51) Whiting, N.; Nikolaou, P.; Eschmann, N. A.; Barlow, M. J.; Lammert, R.; Ungar, J.; Hu, W.; Vaissie, L.; Goodson, B. M. *Appl. Phys. B: Lasers Opt.* **2012**, *106* (4), 775−788.

(52) Nikolaou, P.; Whiting, N.; Eschmann, N. A.; Chaffee, K. E.; Goodson, B. M. *J. Magn. Reson.* **2009**, *197* (2), 249−254.

(53) Birchall, J. R.; Whiting, N.; Skinner, J. G.; Barlow, M. J.; Goodson, B. M., Using Raman Spectroscopy to Improve Hyperpolarized Noble Gas Production for Clinical Lung Imaging Techniques. In *Raman Spectroscopy and Applications*; Maaz, K., Ed.; InTechOpen, 2017; pp 247−268.

(54) Newton, H.; Walkup, L. L.; Whiting, N.; West, L.; Carriere, J.; Havermeyer, F.; Ho, L.; Morris, P.; Goodson, B. M.; Barlow, M. J. *Appl. Phys. B: Laser Opt.* **2013**, 1−6.

(55) Wu, Z.; Happer, W.; Kitano, M.; Daniels, J. *Phys. Rev. A: At., Mol., Opt. Phys.* **1990**, *42*, 2774.

(56) Zeng, X.; Miron, E.; Van. Wijngaarden, W. A.; Schreiber, D.; Happer, W. *Phys. Lett. A* **1983**, *96* (4), 191−194.

(57) Breeze, S. R.; Lang, S.; Moudrakovski, I.; Ratcliffe, C. I.; Ripmeester, J. A.; Santyr, G.; Simard, B.; Zuger, I. *J. Appl. Phys.* **2000**, *87* (11), 8013−8017.

(58) Breeze, S. R.; Lang, S.; Moudrakovski, I.; Ratcliffe, C. I.; Ripmeester, J. A.; Simard, B.; Santyr, G. *J. Appl. Phys.* **1999**, *86* (7), 4040−4042.

(59) Singh, J. T.; Dolph, P. A. M.; Tobias, W. A.; Averett, T. D.; Kelleher, A.; Mooney, K. E.; Nelyubin, V. V.; Wang, Y.; Zheng, Y.; Cates, G. D. *Phys. Rev. C: Nucl. Phys.* **2015**, *91*, No. 055205.

(60) Babcock, E.; Nelson, I.; Kadlecek, S.; Driehuys, B.; Anderson, L. W.; Hersman, F. W.; Walker, T. G. *Phys. Rev. Lett.* **2003**, *91* (12), 4.

(61) Freeman, M. S.; Emami, K.; Driehuys, B. *Phys. Rev. A: At., Mol., Opt. Phys.* **2014**, *90* (2), No. 023406.

(62) Plummer, J. W.; Emami, K.; Dummer, A.; Woods, J. C.; Walkup, L. L.; Cleveland, Z. I. *J. Magn. Reson.* **2020**, *320*, 106845.

(63) Michal, C. A. *Meas. Sci. Technol.* **2010**, *21* (10), 105902.

(64) Kadlecek, S.; Vahdat, V.; Nakayama, T.; Ng, D.; Emami, K.; Rizi, R. *NMR Biomed.* **2011**, *24* (8), 933−942.

(65) Sarracanie, M.; LaPierre, C. D.; Salameh, N.; Waddington, D. E. J.; Witzel, T.; Rosen, M. S. *Sci. Rep.* **2015**, *5*, 15177.

(66) Chen, H.-Y.; Kim, Y.; Nath, P.; Hilty, C. *J. Magn. Reson.* **2015**, *255*, 100−105.

(67) Cooley, C. Z.; Stockmann, J. P.; Witzel, T.; LaPierre, C.; Mareyam, A.; Jia, F.; Zaitsev, M.; Wenhui, Y.; Zheng, W.; Stang, P.; Scott, G.; Adalsteinsson, E.; White, J. K.; Wald, L. L. *J. Magn. Reson.* **2020**, *310*, 106625.

(68) Song, Y.-Q.; Utsuzawa, S.; Tang, Y. *J. Magn. Reson.* **2019**, *306*, 109−111.

(69) Mao, W.; Bao, Q.; Yang, L.; Chen, Y.; Liu, C.; Qiu, J.; Ye, C. *Meas. Sci. Technol.* **2011**, *22* (2), No. 025901.

(70) Saam, B. T.; Conradi, M. S. *J. Magn. Reson.* **1998**, *134*, 67−71.

(71) Barskiy, D. A.; Kovtunov, K. V.; Koptyug, I. V.; He, P.; Groome, K. A.; Best, Q. A.; Shi, F.; Goodson, B. M.; Shchepin, R. V.; Truong, M. L.; Coffey, A. M.; Waddell, K. W.; Chekmenev, E. Y. *ChemPhysChem* **2014**, *15* (18), 4100−4107.

(72) Coffey, A. M.; Shchepin, R. V.; Truong, M. L.; Wilkens, K.; Pham, W.; Chekmenev, E. Y. *Anal. Chem.* **2016**, *88* (16), 8279−8288.

Medical Imaging

Enabling Clinical Technologies for Hyperpolarized ^129Xenon Magnetic Resonance Imaging and Spectroscopy

Alixander S. Khan, Rebecca L. Harvey, Jonathan R. Birchall, Robert K. Irwin, Panayiotis Nikolaou, Geoffry Schrank, Kiarash Emami, Andrew Dummer, Michael J. Barlow, Boyd M. Goodson, and Eduard Y. Chekmenev*

These are not the final page numbers!

*H*yperpolarization is a technique that can increase nuclear spin polarization with the corresponding gains in nuclear magnetic resonance (NMR) signals by 4–8 orders of magnitude. When this process is applied to biologically relevant samples, the hyperpolarized molecules can be used as exogenous magnetic resonance imaging (MRI) contrast agents. A technique called spin-exchange optical pumping (SEOP) can be applied to hyperpolarize noble gases such as ^{129}Xe. Techniques based on hyperpolarized ^{129}Xe are poised to revolutionize clinical lung imaging, offering a non-ionizing, high-contrast alternative to computed tomography (CT) imaging and conventional proton MRI. Moreover, CT and conventional proton MRI report on lung tissue structure but provide little functional information. On the other hand, when a subject breathes hyperpolarized ^{129}Xe gas, functional lung images reporting on lung ventilation, perfusion and diffusion with 3D readout can be obtained in seconds. In this Review, the physics of SEOP is discussed and the different production modalities are explained in the context of their clinical application. We also briefly compare SEOP to other hyperpolarization methods and conclude this paper with the outlook for biomedical applications of hyperpolarized ^{129}Xe to lung imaging and beyond.

From the Contents

1. Introduction

Magnetic resonance imaging (MRI) is a versatile and commonly used clinical imaging technique for producing highly detailed soft-tissue images. The principle of MRI relies on nuclear magnetic resonance (NMR) of nuclei within the body as a result of applied magnetic fields and radio frequency (RF) pulses. The NMR signal from the nuclei depends on the nuclear spin polarization factor, *P*, which gives a measure of the extent of alignment of the nuclei's spins. In order to obtain a greater signal, *P* must be maximized. In conventional NMR, this is given by Equation (1).

$$P \approx \frac{\hbar \gamma B_0}{2 k_B T} \tag{1}$$

Therefore, in a conventional 3 Tesla (T) clinical MRI scanner with a temperature of 300 K, the maximum polarization value for ^{1}H is $\approx 1 \times 10^{-5}$. This low *P* is the result of very few nuclei being aligned with the magnetic field, and therefore only a small number of nuclei produce a signal during NMR investigations. The low *P* poses a significant fundamental problem: only with highly abundant nuclei, such as ^{1}H of water and fat, can suitably strong signals still be obtained for imaging purposes—albeit with spatial–temporal resolution lower than that of computed tomography (CT).[1] MRI is challenging with more-dilute compounds and other magnetically active nuclei, and therefore low *P* fundamentally reduces the versatility of MRI and NMR techniques.

To overcome this limitation, a technique to enhance the nuclear spin polarization factor, called hyperpolarization, can be used to increase NMR sensitivity by 4–8 orders of magnitude.[2] The improved sensitivity occurs due to an increased level of alignment of the hyperpolarized (HP) spins, resulting in corresponding gains of the NMR signal. By increasing the signal generated, the uses of MRI can be expanded, allowing clinically useful data to be created in

[*] A. S. Khan, R. L. Harvey, R. K. Irwin, Dr. M. J. Barlow
Sir Peter Mansfield Imaging Centre, University of Nottingham
Nottingham, NG7 2RD (UK)

Dr. J. R. Birchall, Prof. E. Y. Chekmenev
Intergrative Biosciences (Ibio)
Wayne State University, Karmanos Cancer Institute (KCI)
5101 Cass Avenue, Detroit, MI 48202 (USA)
E-mail: chekmenevlab@gmail.com

Dr. P. Nikolaou
XeUS Technologies
Nicosia 2312 (Cyprus)

Dr. G. Schrank
Northrup Grumman Space Systems
45101 Warp Drive, Sterling, VA 20166 (USA)

Dr. K. Emami, Dr. A. Dummer
Polarean Inc.
Durham, NC 27713 (USA)

Prof. B. M. Goodson
Department of Chemistry and Biochemistry
Southern Illinois University
1245 Lincoln Drive, Carbondale, IL 62901 (USA),
and
Materials Technology Center, Southern Illinois University
1245 Lincoln Drive, Carbondale, IL 62901 (USA)

Prof. E. Y. Chekmenev
Russian Academy of Sciences
Leninskiy Prospekt 14, Moscow 119991 (Russia)

 The ORCID identification number(s) for the author(s) of this article can be found under:
https://doi.org/10.1002/anie.202015200.

many more scenarios. The stronger signal means investigations can be performed in lower magnetic fields with shorter scan duration times, thereby increasing the versatility of the approach. As a result of the stronger signals, HP molecules have been used for investigations into, for example, metabolism,[3] cancer,[4] lung and function[5] (Figure 1).
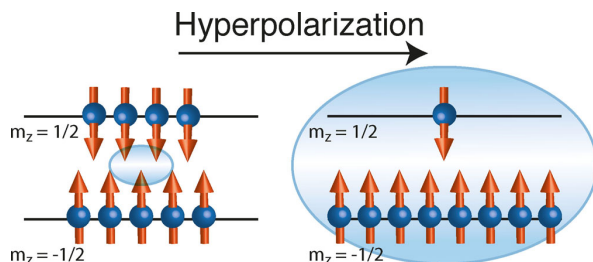

Figure 1. Thermal equilibrium polarization produces a small excess of spins in one state. When the sample undergoes hyperpolarization, a large excess of spins exists in one state producing a considerably stronger signal since more spins contribute.

An area of particular importance is the functional imaging of lungs using HP gases. This developing method offers a new clinical tool that is non-invasive and provides high-quality images and data. This technique involves using a HP noble gas such as ^{3}He and ^{129}Xe as a contrast agent. The HP gas is inhaled by the patient and diffuses within the lungs allowing for both detailed MRI images and quantitative information to be obtained.[6]

Using HP gases offers several advantages in MRI compared to traditional methods. Most notably, when an inhaled gas like ^{3}He or ^{129}Xe is imaged, there is a higher magnetization density of NMR-active molecules in the lungs compared to traditional ^{1}H imaging, which improves the MRI images that can be obtained. Moreover, unlike proton MRI which reports on anatomical features of lung tissues, HP gas MRI reports primarily on void lung compartments. This allows imaging of lung function including gas ventilation, diffusion, and perfusion (as discussed in Section 7). The functional lung images can be collected in a single breath hold, reducing the strain on the patient. This not only makes the imaging more convenient for the patient but increases the accessibility of the imaging technique. This is particularly useful for patients with pulmonary disorders who are the main target for the imaging technique as they cannot carry out long breath-holds and cannot be imaged for long periods of time. The first biological images using HP ^{129}Xe were obtained in 1994 by Albert et al.[7] and using ^{3}He in 1995 by Middleton et al.[8] Historically, MRIs of the lung were poor due to the weak signals in the ^{1}H images as a result of the low density within this organ. For this reason, HP ^{3}He was proposed as an imaging technique to produce clinically useful lung images. Since ^{3}He has the highest gyromagnetic ratio of the noble gases, γ (32.4338 MHz T^{-1}) compared to proton (42.5775 MHz T^{-1}), it was selected in order to allow for a strong signal to be produced during HP lung imaging.[9]

Despite early work on HP ^{3}He producing high spatial resolution and clinically useful images, the use of the gas was limited due to worldwide shortages,[10] resulting in cost increases that were deemed unsustainable for the envisioned use. Instead, ^{129}Xe was found to be a suitable alternative gas for clinical studies. While the gas suffers from a lower γ (11.7769 MHz T^{-1})—and therefore a lower signal—than ^{3}He, hyperpolarization is still able to impart a sufficiently strong signal for the images to be clinically useful. Moreover, the use of ^{129}Xe is advantageous compared to other gases due to its lipophilic properties, making it is soluble in barrier tissue,

Ali Khan completed his MSci in Physics at the University of Nottingham (UK) in 2020. He is currently a PhD student supervised by Prof. Ferdia Gallagher and Dr. Mary McLean at the University of Cambridge, where he is applying MR hyperpolarization technology to profile the metabolic flux of glioblastoma.

Rebecca Harvey studied Physics at the University of Nottingham, obtaining her MSc in 2020. She will be continuing her career in medical imaging at Caristo Diagnostics.

Prof. Eduard Y. Chekmenev received his PhD in Physical Chemistry (supervisor Prof. Richard J. Wittebort) in 2003 at the University of Louisville, KY (USA). He conducted postdoctoral research at the National High Magnetic Field Laboratory in Tallahassee, FL (with Prof. Timothy Cross), Caltech (Prof. Daniel P. Weitekamp) and HMRI in Pasadena, CA (USA) (with Dr. Brian D. Ross). In 2009, Dr. Chekmenev started his hyperpolarization program at Vanderbilt University (Nashville, TN) and he was tenured in 2015. In 2018, he moved to Wayne State University (Detroit, MI) to continue his research on MR hyperpolarization.

www.angewandte.org

© 2021 Wiley-VCH GmbH

Angew. Chem. Int. Ed. **2021**, *60*, 2 – 24

These are not the final page numbers!

blood,[11] and others.[12] The absorption of ^{129}Xe by various biological compartments (e.g., red blood cells) induces a frequency shift, allowing the absorbed and non-absorbed gas to be distinguished via spectroscopy.[13] This aids the clinical properties of HP ^{129}Xe, leading to not only high-quality images, but also quantitative information on lung function and gas perfusion rate.[14] As a result, ^{129}Xe has been the focus of both clinical studies and technological developments to optimize the hyperpolarization process in the HP gas production for clinical use, aiming to obtain clinical grade HP gas in a time- and cost-efficient manner.

For noble gases, the most common hyperpolarization method is spin-exchange optical pumping (SEOP).[15] While the fundamental physics of SEOP is unchanged, the approach and technologies can vary significantly depending on the production method employed. HP ^{129}Xe can be prepared via two distinct methods to hyperpolarize and collect the product. In the first method, called continuous flow, the ^{129}Xe gas flows through the SEOP cell at a fixed rate before exiting the polarizer and can be cryo-collected for subsequent use. Alternatively, in a method called batch mode (or stopped-flow), the ^{129}Xe gas is loaded into an oven where the SEOP process occurs for a set amount of time before the process is stopped and the HP gas is removed. In this Review, the development of the different production methods of SEOP will be discussed and their respective advantages and limitations explained. This will be compared with other emerging hyperpolarization production technologies. The promising biomedical outlook for the use of ^{129}Xe HP production technology will then be presented.

2. Spin-Exchange Optical Pumping (SEOP)

Optical pumping (OP) was first introduced in 1950 by Kastler, who found that an alkali metal vapor's electrons can be spin-polarized in the presence of a magnetic field and circularly polarized light.[16] While this was a pioneering discovery on its own, it was not until 1960 that it was found that the electron spin polarization possessed by the alkali metal vapor could be transferred to the nuclear spins of noble gases.[17] This finding led to the SEOP process known today, allowing the production of highly polarized noble gases through the optical pumping of alkali metals. SEOP is composed of two stages. In the first step, a vaporized alkali metal, for example, rubidium (Rb), undergoes optical pumping through the application of circularly polarized light, thereby imparting electron spin polarization to the alkali metal. In the second step, the spin polarization of the alkali metal electrons is transferred to the nuclei of the noble gas of interest (e.g., ^{129}Xe) to produce a HP noble gas over time.

2.1. Step 1: Optical Pumping of Electron Spins

To perform SEOP, the vaporized alkali metal and noble gas are contained with an optically transparent cell, often with other buffer gases to assist with the hyperpolarization process. Outside the SEOP cell, a high-power laser is used to apply the

circularly polarized light tuned to the alkali metal's D_1 resonant frequency (at ca. 794.7 nm for Rb), which when absorbed by a Rb atom within the SEOP cell, excites its outer-shell electron from the $^2S_{1/2}$ (ground) to the $^2P_{1/2}$ (excited) state. Additionally, a static magnetic field (typically a few millitesla) is applied along the beam direction of circularly polarized laser light. Within both the ground and excited states exists two sublevels denoted $m_J = \pm 1/2$ (neglecting the nuclear hyperfine splitting for simplicity). Thus, when a resonant photon is absorbed, the unpaired electron is excited into a specific m_J sublevel of the $^2P_{1/2}$ state, as dictated by the conservation of the angular momentum (Figure 2). While in the excited state, the electrons of the Rb vapor become evenly distributed between the two sublevels as a result of collisions with other gas-phase species. This equalization results in the ground state sublevels being repopulated by relaxation at roughly equal rates. If the polarized light is continually applied to the Rb, there is a build-up of the population in a single ground state sublevel, usually reaching steady state in a fraction of a second. As a result, the alkali metal becomes electronically spin polarized (Figure 2).

While most electron spins remain within the $m_J = 1/2$ sublevel of the ground state, some return to the $m_J = -1/2$ sublevel via relaxation caused by non-angular-momentum-conserving collisions with other gases in the optical cell. As a result, the steady-state polarization achieved via optical pumping is determined by the balance of these competing factors, according to Equation (2),[18]

$$P_{Rb}(z) = \frac{\gamma_{op}(z)}{\gamma_{op}(z) + \gamma_{sd}} \tag{2}$$
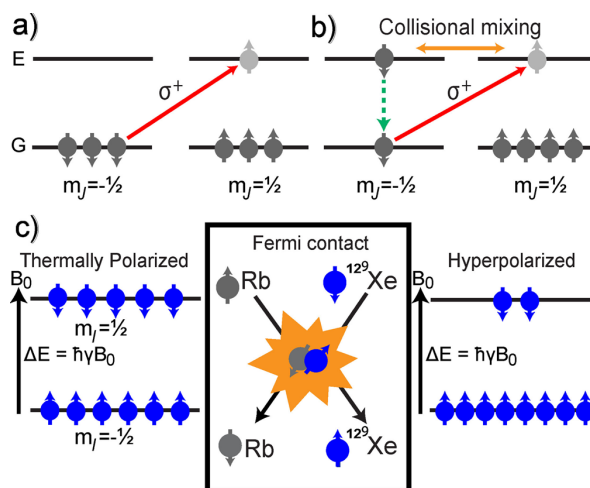

Figure 2. Optical pumping of Rb electron spins. a) Rb begins in the ground state, with electrons equally distributed between sublevels. Absorption of circularly polarized light excites electrons into the $m_J = \frac{1}{2}$ sublevel, conserving angular momentum. Collisional mixing equilibrates the excited sublevel populations and the rates at which the ground sublevels are repopulated by relaxation (b), but selective depletion of one sublevel by the laser leaves the vapor electronically spin-polarized. c) Rb/^{129}Xe spin-exchange collisions allow ^{129}Xe nuclear spin polarization to accumulate over time.

where $P_{Rb}(z)$ is the polarization of the Rb vapor at position z along the optical cell axis, $\gamma_{op}(z)$ is the optical pumping rate (which depends on the photon flux at that point in the SEOP cell), and γ_{sd} is the Rb depolarization rate (also known as "spin destruction" rate). Therefore, minimizing the spin destruction rate, and ensuring $\gamma_{op} \gg \gamma_{sd}$ allows for a near-unity Rb polarization to be achieved.

2.2. Step 2: Polarizing Xe Nuclei via Spin Exchange

The electronic polarization of the Rb atoms can be transferred to the nuclear spins of ^{129}Xe in the gas mix via two types of gas-phase collisions: binary collisions between the Rb and ^{129}Xe atoms, and tertiary collisions involving a third body that result in the formation of Rb/Xe van der Waals "molecules". When collisions occur between the two species, Fermi-contact hyperfine interactions allow the Rb electronic spins and the ^{129}Xe nuclear spins to exchange angular momentum.[19] Although only a small fraction of these collisions yield successful spin exchange, over time a bulk nuclear spin polarization accumulates in the ^{129}Xe nuclear spins, according to Equation (3),[20]

$$P_{Xe}(t) = \frac{\gamma_{se}}{\gamma_{se} + \Gamma_{Xe}} \langle P_{Rb} \rangle \left(1 - e^{-(\gamma_{se} + \Gamma_{Xe})t}\right) \tag{3}$$

where $\langle P_{Rb} \rangle$ is the average Rb polarization within the SEOP cell, Γ_{Xe} is the ^{129}Xe nuclear spin relaxation rate ($1/T_1$), for example, due to collisions with the SEOP walls, and γ_{se} is the rate of polarization transfer from the Rb to the ^{129}Xe atoms via spin-exchange collisions.

To maximize the ^{129}Xe polarization attainable via SEOP, several factors should be optimized. Most notably, the polarization of the Rb vapor can be increased by minimizing the spin destruction rate (e.g., by keeping the Xe density low), or by increasing the Rb optical pumping rate by using a higher power laser. Additionally, the ^{129}Xe polarization can be increased by mitigating ^{129}Xe relaxation in the SEOP cell.

While the fundamental physics, of course, remains unchanged, the SEOP production methods and technologies vary significantly. HP ^{129}Xe can be prepared via many ways falling within two distinct categories to hyperpolarize and collect the HP product. In the first method, called continuous flow, ^{129}Xe flows through the SEOP cell at a fixed rate before exiting the polarizer while being cryo-collected for subsequent use (Figure 3). Alternatively, in a method called batch mode or stopped-flow, the ^{129}Xe is first loaded into the SEOP cell for a set period of time before the process is stopped and the HP gas is removed. These two approaches are described in greater detail in Sections 3 and 4, respectively.

3. Continuous-Flow SEOP Production Method

3.1. CF-SEOP: Design Considerations and Initial Efforts

^{129}Xe hyperpolarizer designs based on continuous flow (CF) polarization allow for an uninterrupted stream of
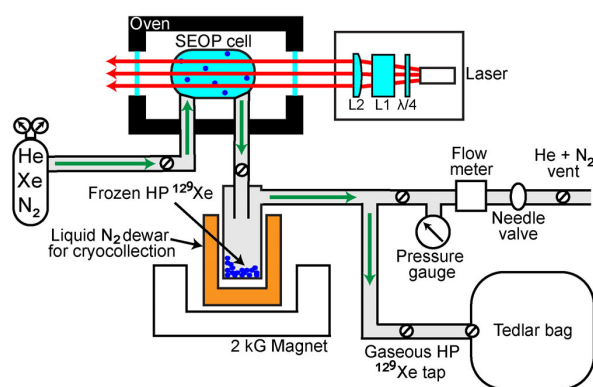

Figure 3. Overall design of the original continuous flow (CF) ^{129}Xe hyperpolarizer.[20] $\lambda/4$ refers to high-power polarizing beam splitter, and L1 and L2 lenses to other beam-expanding components of the optical train.

a xenon gas mixture to be passed through the SEOP cell.[21] A gas mixture containing ^{129}Xe and Rb vapor is flowed through the heated SEOP cell and irradiated by circularly polarized light. After passing through the SEOP cell and undergoing hyperpolarization, the ^{129}Xe gas is cryo-collected using liquid N$_2$ so that the HP ^{129}Xe is concentrated in the solid state (Figure 3). Since solid HP ^{129}Xe is stored at a low temperature and within a high magnetic field, the HP state can be retained for a long period of time due to the temperature and magnetic field dependence of the nuclear spin-lattice relaxation rate, T_1 (many hours at 77 K).[22] Furthermore, by cryo-collecting the HP ^{129}Xe, a higher density of HP product is produced since additional buffer gases included in the gas mix (e.g., N$_2$ and ^{4}He) are removed.[20,23] When sufficient quantities of HP ^{129}Xe have been accumulated, it is rapidly thawed into the gas phase and expanded into a storage vessel—such as a Tedlar bag—that can be transported to the MRI scanner (e.g., where the Xe can be inhaled by a subject). However, while the collection of the solid ^{129}Xe is useful for the removal of buffer gases, care must be taken with this step because the cryogenic separation and accumulation can otherwise lead to significant polarization losses. For example, Kuzma et al.[24] showed that Xe polarization can be lost when the solid ^{129}Xe is warmed to near its melting point (161.4 K) because the T_1 can decrease dramatically, to the order of seconds. This problem can be mitigated by moving through phase transitions rapidly, in addition to applying a magnetic field[22] during cryogenic separation to raise the T_1 of solid-state ^{129}Xe. While the relaxation rate of the HP gas is strongly dependent on the magnetic field, it was found that very little change in the T_1 occurs when a magnetic field greater than 500 G is applied[25] (using, for example, strong permanent magnets placed near the Xe cryo-collection vessel).

In order for CF production to work effectively, the flow rate must be high enough to produce a sufficiently large quantity of HP ^{129}Xe for the desired application, for example, clinical imaging in humans. However, for the ^{129}Xe polarization level to *also* be high, the spin exchange rate must be

||||
↖↖ These are not the final page numbers!

www.angewandte.org

© 2021 Wiley-VCH GmbH

Angew. Chem. Int. Ed. **2021**, *60*, 2 – 24

high enough to accommodate for the correspondingly low in-cell Xe residence times. High spin exchange rates can be achieved with high rubidium densities (i.e., at elevated SEOP cell temperature), but these high optical densities must be compensated with increased photon flux. Thus, high-power laser diode arrays (LDAs) were the primary enabling technology that led to the development of the first clinical-scale CF hyperpolarizer in 1996 by Driehuys et al. (Figure 3).[20] Indeed, this device included a laser system that could produce high power (and therefore high photon irradiance) in a lower cost, compact structure.[26] The original LDAs had a much broader spectral output than (say) Ar$^+$/Ti:sapphire lasers, as measured by the full width half maximum (FWHM). This characteristic meant a lower proportion of the incident laser flux was resonant with the Rb D1 absorption line.[25] To compensate for the spectrally broader LDA output, the early CF hyperpolarizers employed high gas pressures (up to 8–10 atm) to pressure broaden the Rb absorption line.[27] Unfortunately, the ^{129}Xe density has to be kept low to maintain high Rb polarization (the loss of Rb polarization from non-angular-momentum-conserving collisions is roughly three orders of magnitude greater for Xe than that for lighter gases such as He and N$_2$). Instead, by using a gas mixture dominated by ^{4}He, the Rb D1 resonance can be broadened,[28] allowing for a greater proportion of the incident laser light to be absorbed. In addition to the pressure broadening, the Rb atoms' photon emission needs to be quenched to allow for a high level of polarization to be retained. The optical emission from excited Rb comprises unpolarized photons, which cause a *loss* of electron polarization when absorbed by other Rb atoms. N$_2$ is often selected as the quenching gas due to its large quenching cross section and ability to absorb energy from electronically excited Rb atoms into its ro-vibrational energy levels.[29,30] By incorporating the higher power LDA (50 W with 2 nm FWHM) with the lean gas mix into the hyperpolarizer, Driehuys et al. were able to dramatically increase the rate of HP gas production. When a gas mix of 98% ^{4}He, 1% ^{129}Xe, and 1% N$_2$ was used at 10 atm, around 1 standard liter (sL) of ^{129}Xe was produced with a P_{Xe} of 5%.[20] This increase in production capacity enabled viable first-in-kind clinical studies.

3.2. Scaling Up CF-SEOP and Commercial Ventures

While a high production rate was established, the P_{Xe} level was limited by the available optical power of the LDAs at the Rb D1 wavelength. This limitation was addressed by Zook et al.[31] who used a 210 W LDA to hyperpolarize the Rb. This LDA comprised seven individual fiber array packages (FAPs) that were independently tuned to 795 nm. This approach increased the photon flux and thus P_{Rb}—and hence P_{Xe}—reached 65% using a 0.6% ^{129}Xe gas mix. While this demonstration achieved greatly increased P_{Xe}, the LDA still suffered from a rough Gaussian frequency distribution with FWHM ≈ 1.6 nm. As a result, a large proportion of the incident photons were not absorbed by the Rb vapor, despite considerable pressure broadening of the Rb D1 line.

Most early CF hyperpolarizers focused on increasing P_{Xe} by increasing LDA power while working in the high-pressure regime (3–10 bar).[20] Hersman and Ruset[15] developed a CF hyperpolarizer that works in the low-pressure regime, where three-body van der Waals interactions dominate, giving rise to higher spin exchange rates.[32] The higher spin exchange rate allows a higher flow rate, therefore improving the HP ^{129}Xe production rate. Moreover, since ^{129}Xe concentrations are kept low, high Rb polarization can be obtained with less laser absorption.[15] Operating in this regime, enabled in part by new design features described below, led to record metrics of HP ^{129}Xe production: a maximum P_{Xe} of 64% was obtained with a flow rate of 0.3 sL of Xe h^{-1}. Increasing the Xe flow rates to 1.2 sL h^{-1} and 6 sL h^{-1} gave P_{Xe} of 50% and 22% respectively.

Hersman's design[15] features an enormous (1.8-m-long) oil-heated SEOP cell optimized for the low-pressure/high-flow rate regime and employing counterflow operation for the gas mixture "against" the high-power laser beam, 90 W and spectral bandwidth of 1.5 nm. Allowing the gas mixture to flow against the laser means Rb exiting the cell should receive maximum laser flux at the front of the cell to ensure the highest P_{Rb} and by extension the highest possible P_{Xe} (Figure 4a). The large SEOP cell equipped with long-lasting Rb presaturator (25 g Rb metal) requires a complex optical setup to ensure the whole cell is uniformly illuminated by the circularly polarized light. In 2008 this polarizer was used for human-scale HP ^{129}Xe production for lung imaging studies.[33] Around three to four batches of HP ^{129}Xe could be produced daily by the hyperpolarizer in a hospital setting, ranging from 0.5 to 2 sL batch^{-1} with P_{Xe} of $\approx 15\%$, demonstrating the consistency in production of large quantities of HP ^{129}Xe, which is important for the future of clinical MRI applications. This hyperpolarizer design was later improved through
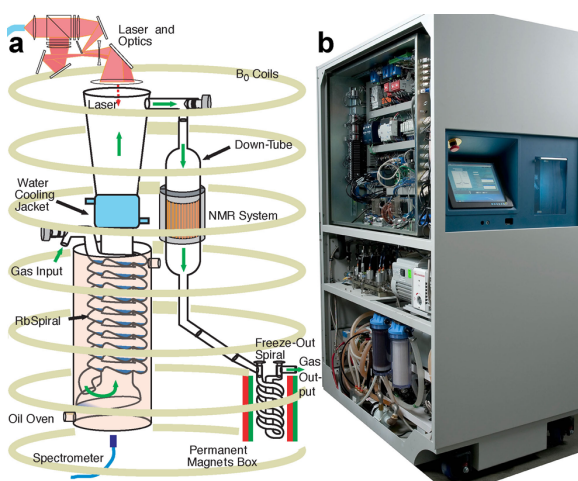

Figure 4. a) Overall design of a continuous flow (CF) ^{129}Xe hyperpolarizer developed by Hersman and co-workers. b) The most recent embodiment of the ^{129}Xe hyperpolarizer by Xemed LLC, Durham, NH (USA). Images courtesy of Dr. Iulian Ruset and Prof. William Hersman.

Angew. Chem. Int. Ed. **2021**, *60*, 2 – 24

© 2021 Wiley-VCH GmbH

www.angewandte.org

These are not the final page numbers! ↗↗

a series of additional technology advances including a significantly higher-power frequency narrowed LDA.[34]

Xemed LLC (Durham, NH (USA)) now offers its fully automated XeBox ^{129}Xe hyperpolarizer (employing ≈ 1 kW LDA), clinically ready, which does not require operator supervision other than replacing consumables (Figure 4b). The hyperpolarizer operates in a CF regime, energized by a kilowatt-scale laser with automated cryogenic separation/accumulation. This hyperpolarizer is capable of producing up to 6 sL of HP ^{129}Xe per hour, selectable by a touchscreen or remotely. In its current configuration, it can hyperpolarize up to four bags of various sizes per batch totaling up to 3 sL of HP ^{129}Xe gas. P_{Xe} reported by users routinely exceeds 50% (up to 55%) in the bag (polarizations in the flow are typically 20–25% higher). A recent laser development, SpectraLock, incorporating a novel atomic line filter in the external cavity, will allow higher power, cost reduction, and new polarizer operating regimes or designs.

Although able to produce excellent P_{Xe} values in volumes useful for a clinical setting, this hyperpolarizer has a complex design that would be difficult and expensive to build and emulate. As a result, Saam et al.[35] developed a hyperpolarizer inspired by Hersman's design, aiming to be simpler as well as to keep manufacturing costs below $100 000. This hyperpolarizer[35] made use of a large (but comparatively shorter, ca. 1 m) SEOP cell with the counterflow of the gas mixture against the laser light. However, the new hyperpolarizer utilized lower-cost options for heating, SEOP cell manufacturing, and the LDA system. Like the Hersman design, the Utah design introduced the Rb presaturator outside the main SEOP region. However, the Utah design used a forced-air heating system. Moreover, the Utah design utilized simple glass wool saturated with Rb in order to introduce the vapor into the gas stream. Finally, the Utah design used a much lower-power LDA with "only" 100 W maximum power. The average P_{Xe} obtained was 20% at a flow rate of 0.6 sL h^{-1} with 30 W laser photon flux. Although the HP ^{129}Xe production rates were lower than those demonstrated by Hersman, these values demonstrate that it is possible to achieve high P_{Xe} at lower cost and with a simplified design.

The Utah hyperpolarizer was also used to validate a numerical model for CF-SEOP (see also Section 5);[35] both the P_{Xe} and the in situ P_{Rb} were measured and compared to numerical predictions. The P_{Rb} was measured using optically detected Rb electron spin resonance spectroscopy (ESR). The relative heights of the hyperfine peaks are directly indicative of the Rb polarization (Figure 5).

High P_{Xe} of the inhaled HP gas bolus is particularly important in a clinical setting. For example, image quality comparison using signal-to-noise ratio (SNR) metrics among HP ^{129}Xe ventilation images produced by Norquay et al.[36] showed that using a smaller volume of ^{129}Xe—produced at a lower flow rate, but with higher ^{129}Xe polarization—yielded comparable images to those acquired with a larger administered dose with lower P_{Xe} (produced at a higher flow rate). Achieving comparable magnetization, and hence image quality, with a smaller administered dose can be particularly useful when there is a need to either dilute the Xe (to make it easier for patients with impaired lung function to inhale,
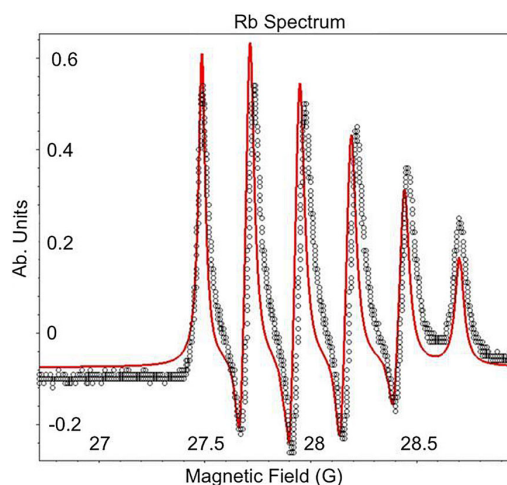

Figure 5. A ^{85}Rb ESR spectrum used to determine P_{Rb} in the SEOP cell of the Utah hyperpolarizer. Relative heights of the peaks in the hyperfine spectrum were used to calculate P_{Rb}. The spectrum represents Rb with a very low polarization. At higher P_{Rb} values, only the first two or three peaks are visible.

owing to reduced gas density) or reduce the anesthetic effects of xenon (as Xe mixtures of over 50% can give rise to anesthetic effects[37]). The hyperpolarizer used by Norquay et al. operates within the mid-pressure range, at 2 bar, compared to Hersman's hyperpolarizer that operates at <1 bar. Operating within this mid-pressure range means the molecular lifetimes are shorter and the contribution of van der Waals interactions is reduced. As this contribution is inversely proportional to the gas density, operating at high Rb density will ensure that the spin exchange rate remains high at this pressure. P_{Xe} of 12% was obtained at a flow rate of 18 L h^{-1} at 373 K and a pressure of 2 bar, using a 25 W laser with FWHM of 0.1 nm. The laser FWHM is not significantly greater than the Rb D1 linewidth at this given cell pressure (0.05 nm), ensuring high photon absorption and a high optical pumping rate. A later adaptation of this hyperpolarizer, containing a larger volume SEOP cell and higher laser power, showed it is possible to generate higher P_{Xe} of 30% at a production rate of around 4 sL of Xe h^{-1} for HP gas imaging within a clinical setting.[38] Experimental results achieved a dose equivalence (DE)[39] rate of 1.013 L of pure and 100% polarized ^{129}Xe h^{-1}—three times higher than the highest previously reached value.[15] Obtaining such high output rates suggests the possibility of performing high-resolution HP gas lung MRI with naturally abundant Xe (at high doses), which has a lower ^{129}Xe enrichment of 26.4% than the enriched (typically over 85%) ^{129}Xe usually used for these investigations.[40] Due to the much lower cost of naturally abundant Xe, this would further aid the development and clinical adaptation of this technology.

A key organization in the commercial development of Xe hyperpolarizers for clinical use is Polarean, Inc. (Durham, NC (USA)), a spinoff of GE Healthcare which is actively pursuing regulatory approval of the technology. Their clinical Xe hyperpolarizer model 9820 (Figure 6) has completed
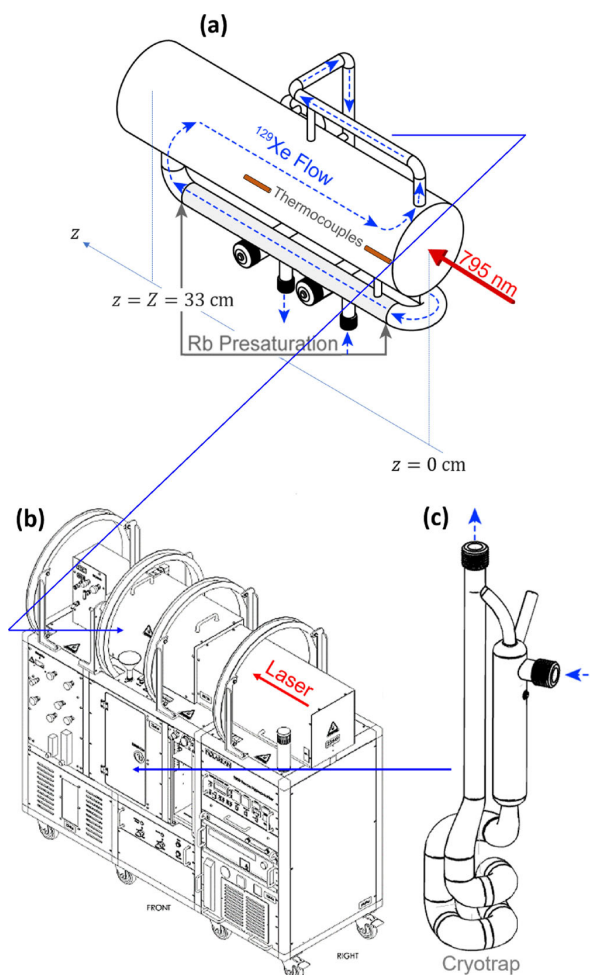
Figure 6. a) Schematic of the SEOP cell used within a Polarean 9820-A hyperpolarizer, featuring a gas flow path through a presaturated Rb chamber. b) Diagram of the overall device. c) Borosilicate cryotrap used with this polarizer. Reprinted with permission from ref. [41]. Figure courtesy of Joseph Plummer.

3.3. Other Key Developments in CF-SEOP

Meersmann and co-workers[43] showed that the product of P_{Xe} and Xe concentration increases with an increasing Xe partial pressure, and as a result it is possible to operate even at near 100% Xe mole fraction. This approach produces HP Xe gas with an in-cell SEOP Xe pressure of over 1 atm, obviating the requirement for cryo-collection of HP Xe and allowing truly continuous delivery of dense Xe gas to a sample.[44] In this method, removing the molecular nitrogen from the gas mixture initially reduces achievable signal intensities due to radiation trapping; however, at high ^{129}Xe densities, P_{Xe} is less affected by radiation trapping because the dominating source of Rb depolarization is Xe itself, due to the increased significance of spin relaxation by Rb–^{129}Xe collisions at higher xenon densities.

Other methods of CF delivery have been investigated, including operating without ^{4}He as a buffer gas[45] and using very low ^{129}Xe concentrations.[46] Fujiwara et al.[47,48] showed that possible alternatives to N_2 can be used successfully as quenching gases this way, including isobutene, furan, and butane, and Meersmann et al.[49,50] demonstrated a method of removing N_2 without the need for cryo-collection. However, due to the complexities (and potential toxicities) that such alternative methods may bring to the SEOP process, they may not be suitable for implementation in a clinical setting.

Continuous, real-time delivery of HP ^{129}Xe for gas imaging has been successfully demonstrated using "traditional" SEOP methods. Driehuys and co-workers[51] showed real-time delivery of HP ^{129}Xe to rodents, using dilute concentrations (1%) of ^{129}Xe produced on demand. Instead of performing cryo-accumulation, the xenon pressure was reduced to physiological levels and the gas mixture, with $P_{Xe} = 25\%$, could be directly delivered to the subject to enable continuous imaging within a clinical setting.

4. Stopped-Flow SEOP Production Method

4.1. SF-SEOP Fundamentals

The stopped-flow (SF) modality, alternatively called batch mode, is a technique for producing a defined quantity of HP ^{129}Xe in a desired gas mixture. In this process, the mixture of Xe and (often) N_2 gas is loaded into the SEOP cell with Rb metal and sealed; the SEOP cell is then heated and illuminated with circularly polarized laser light. Once Xe gas in hyperpolarized, the SEOP cell is opened and the gas is expanded from the SEOP cell into a storage container allowing its subsequent use. The SEOP cell is then reloaded.

Particularly in the 1980s and 1990s, a large number of groups around the world developed small-scale single-batch setups for fundamental studies of SEOP, as well as applications in chemistry/biochemistry, materials science, and physics (for reviews, see refs. [19, 52, 53]). The first ^{129}Xe HP lung MRI was performed by Albert et al. in 1994 using a small-scale SEOP device, which was employed for the imaging of a mouse lung.[7] In their single-batch SEOP polarization experiment, 1–2 Watts of circularly polarized light produced by a Ti:sap-

Phase III clinical trials and is currently under FDA review as a drug–device combination product. Polarean devices are currently in use in more than a dozen research institutes located across North America and Europe.

The 9820 Xe polarizer is by design a CF hyperpolarizer. It runs at a moderate pressure of ≈ 2 bar and has a relatively large diameter cell (≈ 85 mm), which is fully illuminated by circularly polarized light from a ≈ 170 W laser. The device delivers a polarization level exceeding 55% for 300 mL batches produced at a rate of 2 sL h^{-1}, equivalent to a DE production rate of ≈ 1 sL h^{-1} (85% isotopically enriched ^{129}Xe). For device units operating in the field, research groups have reported polarization levels up to 40% under similar conditions.[41,42]

phire laser was applied to polarize the Rb atoms' electron spins. Following 5–20 minutes of optical pumping, $P_{Xe} \approx 25\%$ was achieved, and the contrast agent was administered into the mouse's lung through the breaking of the SEOP cell to expel the HP gas. This pioneering report allowed for a high-concentration HP ^{129}Xe mix to be delivered into the lungs, permitting ultrafast (0.3 s) ^{129}Xe images to be recorded, and demonstrating the viability of the imaging technique.

Following the demonstration of very high P_{Xe} in small quantities by Jänsch and co-workers,[55] the batch/SF design was improved in 1999 by Rosen et al.,[54] who created a SEOP polarization and collection system to increase the capacity of HP ^{129}Xe production and to enable SEOP cell reloading and reuse without physical destruction of glassware—making the device a true stopped-flow system. The so-called Rosen SEOP cell (Figures 7 and 8) at the center of the device comprised an inner cylinder (75 mL, 1-inch diameter) that was contained within a larger (2-inch diameter) glass cylinder that acted as a forced-air oven, such that the inner cell could be heated to a desired temperature. The cell had two stopcocks allowing the inner cell's volume to be reproducibly loaded and unloaded as desired. The hyperpolarizer also included a cryo-collection apparatus, allowing the HP ^{129}Xe produced over multiple batches to be accumulated over time and enabling a greater overall volume to be collected for in vivo studies. The SEOP system also employed a 30 W LDA system (comprising two 15 W FAPs with FWHM of 2–3 nm) for irradiation of the SEOP cell, resulting in the increased HP ^{129}Xe gas production rate and quantity in a compact and cost-effective manner.[26]

The cryo-storage vessel was placed within a 500 G magnetic field and kept at a temperature of 77 K (by immersion in a liquid N_2 reservoir), resulting in a ^{129}Xe T_1 on the order of

Figure 8. A Rosen SEOP cell during illumination by a high-power IR laser (coming in from the left). The bright violet light emanating from the inner cylinder (containing the gas and Rb vapor) is caused by the lack of N_2 gas, intentionally absent to allow the study of radiation trapping processes. Re-emission of resonant photons gives rise to energy pooling, resulting in the population of higher-lying Rb excited states.[30,57]

1 hour. Thus, the ^{129}Xe is frozen in storage while any N_2 within the gas mixture can be pumped out, leaving the concentrated HP ^{129}Xe gas mix. Once the hyperpolarization process is completed, the SEOP cell is opened to expand the HP ^{129}Xe gas into the transportation manifold for later use. Following the HP ^{129}Xe expansion, the HP ^{129}Xe gas has a T_1 of 18 minutes.[24,56] The Rosen device marked a useful demonstration of the ability to perform SEOP using an LDA configuration, and again increase the capacity of HP ^{129}Xe production: This hyperpolarizer performed SEOP of a gas mixture containing 1700 torr of ^{129}Xe and 150 torr of N_2, producing 0.16 sL of HP ^{129}Xe gas with P_{Xe} of $\approx 7.5\%$ every 5 minutes.[54]

4.2. Enabling Advances in Laser Technology

Regardless of overall design, the performance of ^{129}Xe hyperpolarizers was clearly limited by the low quality of the light provided by the high-power LDA sources. Luckily, new methods to spectrally narrow LDA outputs were developed to mitigate the primary weakness of these light sources for ^{129}Xe SEOP. To better appreciate the technical challenge that had to be overcome, it is instructive to consider the work of Levron et al.,[58] who investigated cesium (Cs) optical pumping using a single-mode LD with a narrow spectral width of only ≈ 0.12 nm FWHM. While this LD had a suitably narrow emission bandwidth (i.e., approaching the D1 linewidth) for optical pumping, it had very limited optical power of just ≈ 0.3 W. To increase the power, more LD elements would need to be added, but such a LDA would necessarily have a broader spectral output because the output of each element has its own independent spectral profile, producing a wide
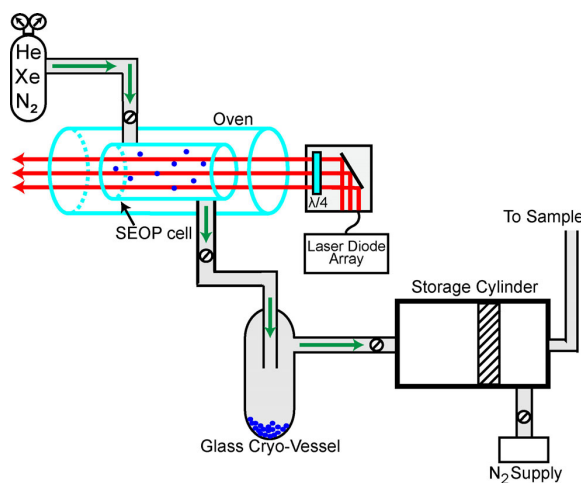

Figure 7. Rosen stopped-flow polarizer design. Once Xe is polarized through the SEOP cell, Xe is expanded into the remainder of the system for accumulation, storage, and delivery. Large quantities of HP Xe are accumulated and then frozen in the glass cryo-vessel, which is held in a 500 G magnetic field provided by a permanent magnet (not shown). Once enough Xe has been accumulated in the cryo-vessel, it is thawed and flows into the storage cylinder where it has a gas polarization lifetime of 18 minutes.[54]
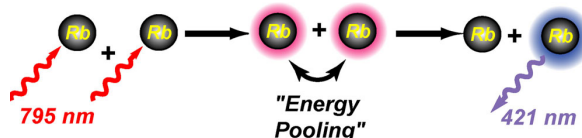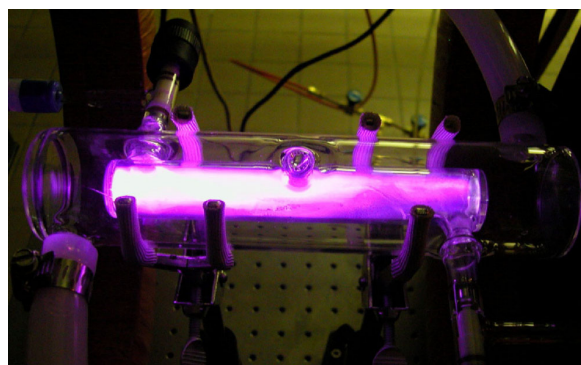
These are not the final page numbers!

distribution of frequency outputs when all the elements were used together. To reduce the frequency range and narrow the output, Walker et al.[59] employed a dispersive ruled grating (DRG) within an external cavity diode laser (ECDL) in 2000 to improve the optical pumping efficiency. The LDA used an external cavity with a diffraction grating (1800 lines mm^{-1}) to narrow the laser emissions. The diffraction grating reflects back a narrow spectral range to the LDA. This process in turn seeds the LDA's gain medium (of each element) to "lock onto" the reflected spectral wavelength resulting in a narrowed spectral width.[60] As a result, the bandwidth of the overall LDA emission (tuned to Rb D_1 frequency) was narrowed from ≈ 2 to 0.1 nm. While the DRG also decreased the power output from 4 W to 2.5 W, this reduction in total photon flux was significantly outweighed by the large increase in the fraction of light that was resonant with the Rb vapor— as demonstrated by the fact that the narrowed 2.5 W laser resulted in 1.40-fold greater P_{Xe} compared to a 15 W unnarrowed LDA.[59]

While the use of the DRG increased the proportion of laser photons that were tuned to the Rb D_1 absorption frequency, the efficiency (manifested by the decreased power output) remained a limitation. Moreover, the effectiveness of the DRG relied sensitively on the optical alignment of the system to ensure optimal efficiency and spectral quality, creating a complex arrangement that is difficult to align and maintain. However, instead of using a dispersive 2D diffraction grating as the feedback element, the narrowing can also be performed using volume holographic gratings (VHG, also referred to as a volume Bragg grating (VBG)) as proposed by Barlow et al. for use in SEOP.[61] By using VHGs, a simpler cavity feedback arrangement for spectral narrowing of the laser emission was achieved, with efficiencies up to 90%[62] being realized (compared to ≈ 40–66% efficiency with external cavity narrowing[61]), thereby providing more resonant light for SEOP.

VHGs are composed of a frequency-selective grating that can be formed in a slab of photosensitive glass. As in the ECDL design, the VHG feedback wavelength is defined by the repeat spacing of the Bragg grating to lock the diode emission and restrict the spectral width;[63] the spacing, in turn, can vary slightly with the temperature of the optic, providing a narrow tuning range (see below). This approach results in the LDA being made to lase at the required wavelength, narrowing the emissions and increasing the proportion of photons tuned to the Rb D_1 frequency.

The use of the VHGs for ^{129}Xe hyperpolarization was first demonstrated by Nikolaou et al.[61] in 2009 using a Rosen SEOP cell setup, with binary (Xe/N$_2$) gas mixtures totaling 2000 torr. Using the setup, the power output from the LDA was varied to tune the VHG and maximize polarization. When first used for ^{129}Xe SEOP, it was found that the narrowed LDA spectral output led to a large increase in absorption by Rb atoms at the front of the cell. Thus, reduced photon transmission to the back of the SEOP cell occurs due to the high optical density of the Rb vapor, resulting in "dark" regions where Rb polarization tends to zero. To correct this limitation, the laser emission was offset ≈ 0.1 nm from the center of the D1 resonance to increase the transmission

through the optically thick Rb vapor and ensure good illumination throughout the entire length of the SEOP cell. However, such attempts to tune "fixed" VHGs can present an additional problem: a dependence of the laser's wavelength on power. This issue arises from the fact that as the power is increased, the VHG heats up, which causes the spacing of the VHG's grating to increase, thereby red-shifting the wavelength at which the VHG "locks" the LDA's output. To address this issue, both the laser's power and the external temperature had to be adjusted in concert to tune the laser with respect to the D1 line, albeit at the expense of reduced LDA power (here 27 W, generating a FWHM of 0.27 nm). When SEOP was performed in this configuration, a threefold increase in P_{Xe} was achieved compared to a conventional LDA of the same power.

For most applications, it is not P_{Xe} but the magnetization "payload" (proportional to the product of P_{Xe} and the number of spins) that is the most important parameter for determining the clinical quality of the resulting images and spectra. However, while it can often be relatively easy to achieve high P_{Xe} with low in-cell Xe densities [^{129}Xe], P_{Xe} can often drop dramatically as Xe density is increased because of the inverse relation between P_{Xe} and [^{129}Xe][43] due to the non-spin conserving collisions that arise between the ^{129}Xe and the Rb atoms[27,64] (in addition to reduced contributions from more-efficient three-body collisions to the Rb/Xe spin-exchange rate,[32] as discussed above). Because of this problem, increasing [^{129}Xe] often resulted in lower (or at best, similar) overall magnetization payload. However, it was found that the decrease in polarization as a result of increasing [^{129}Xe] can be mitigated by changing the temperature at which SEOP is performed, particularly when high resonant photon flux is applied (e.g., with a high-wattage VHG-narrowed LDA): Under these conditions, an inverse relationship was found between Xe density and the optimal SEOP temperature (i.e., T_{opt}, the temperature at which the highest P_{Xe} was achieved)— a result that was well-reproduced by simulations (see below).[65] Under such conditions where the in-cell ^{129}Xe T_1 was very long (i.e., so that $1/T_1$ was much smaller than γ_{SE}), higher Xe densities require better cell illumination and a greater "photon-to-Rb ratio" (because of the increased Rb spin-destruction rate). Thus, *lowering* the cell temperature can help ensure higher P_{Rb} throughout the cell, and hence, higher overall P_{Xe} at high Xe densities, albeit built up over a longer time.[61] Indeed, temperature optimization resulted in a levelling off of polarization with increasing density.[66] Although this work was performed using single batches in smaller volumes (Rosen cells, 75 cm^3), it showed that that it was possible to use SF-SEOP and high in-cell densities to create HP Xe with much higher magnetization "payload" than previously anticipated.

4.3. Scaling SF-SEOP to Clinical Production

As a result, the hyperpolarizer developed by Nikolaou et al.[67,68] in 2012, dubbed "XeNA", aimed to increase P_{Xe} at higher densities while maintaining a high production rate. Moreover, the hyperpolarizer strived to increase accessibility

of the HP ^{129}Xe production method via open-source use of "off-the-shelf" components while introducing an automated method of production to improve ease of use. The focus of the hyperpolarizer was to maximize the magnetization at clinically useful volumes of the delivered HP product ($\approx$ 0.5–1 L at 1 atm in a Tedlar bag) at increased ^{129}Xe concentration (up to 75% content). This device utilized a $\approx$ 180 W VHG-narrowed LDA (FWHM $\approx$ 0.27 nm[69]) to compensate for the increased Rb spin destruction rate that arises due to higher [^{129}Xe]. A design advantage of using higher Xe densities is that the cryo-collection step may be entirely obviated, thus simplifying the HP ^{129}Xe production process and making the device easier to automate. With the XeNA hyperpolarizer, the 0.5-L SEOP cell operated at a total pressure of 2000 torr,[69] resulting in a production rate of approximately 1 sL of HP gas mixture per hour, with each run providing a $\approx$ 0.8 sL batch. To improve ease of use, a graphical user interface (GUI) controlled the majority of the system components, allowing for easier adoption into clinical settings. With this system, a P_{Xe} of up to 90% was achieved with an in-cell ^{129}Xe partial pressure of 300 torr. However, at higher ^{129}Xe partial pressure of 1570 torr, P_{Xe} was reduced to 30% but a greater magnetization was generated, demonstrating the benefits of the higher density polarization. Korchak et al. created a portable polarizer with a design that has many similar features, except that it is also capable of running in both CF and SF modes. This device produced P_{Xe} up to $\approx$ 40% in small SF batches, or values of $P_{Xe} = 25$% and 13% in CF mode with flow rates (and Xe partial pressures) of 6.5×10^{-3} sL min^{-1} (0.1 bar) and 26×10^{-3} sL min^{-1} (0.4 bar).[70]

An improvement to the XeNA system was introduced by Nikolaou et al. with the second-generation (GEN-2) "XeUS" system.[71] XeUS offered some notable advantages over the previous hyperpolarizer designs that improved the automation and performance of the system. One of the most important changes was the introduction of the highly integrated 3D printed oven featuring a thermo-electric cooling (TEC) module for temperature control of the SEOP cell (Figure 9).[71]

The redesigned SEOP cell uses a premixed Xe-containing gas mixture, resulting in a substantially simplified gas-handling manifold design;[73,74] operating at a constant positive pressure mitigates the potential for Rb in-cell oxidation otherwise caused by slow leaks between gas-reloading stages for the SEOP cell. Furthermore, a 2-inch-diameter laser beam expander was integrated in the LDA design, which when coupled with the mechanical aligning legs of the oven assembly, allowed for convenient alignment of the laser beam with the SEOP cell. The originally introduced LDA with FWHM of 0.20–0.30 nm was later upgraded to a LDA with FWHM of 0.154 nm.[73] Through these modifications, a maximum P_{Xe} of 83.9% $\pm$ 2.7% was achieved with a ^{129}Xe density of 1000 torr, while the highest DE values were achieved at a higher ^{129}Xe density of 1330 torr at P_{Xe} of 72.6 $\pm$ 1.4% (Figure 10).[75–77] This polarizer was also used as a testing platform for temperature-ramped SEOP, where faster initial build-up rates (γ_{SEOP}) could be achieved by *starting* with oven temperatures that would otherwise be too high to yield stable SEOP for the whole duration of the Xe
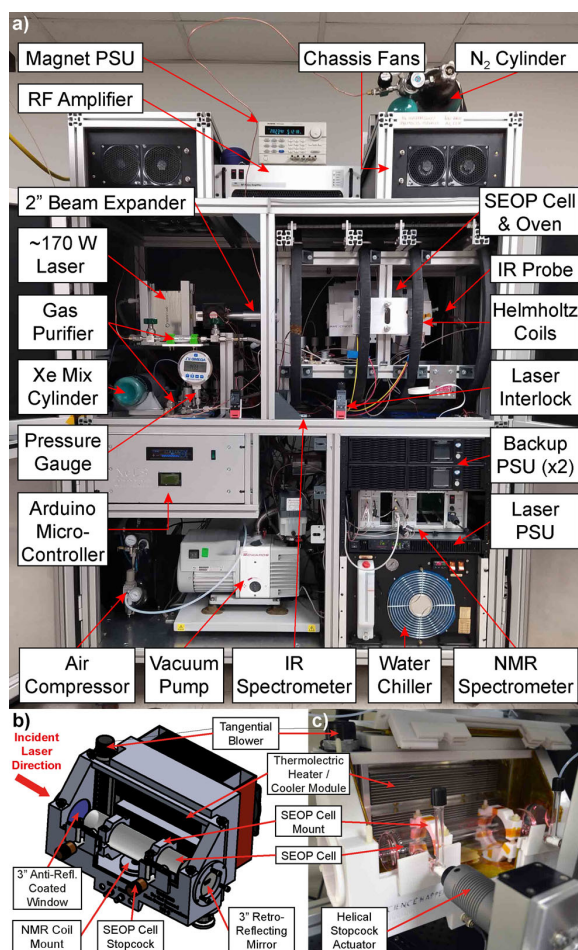

Figure 9. a) Annotated photograph of the second-generation (GEN-2) XeUS hyperpolarizer device and chassis, outlining the key components (e.g., power supply units, PSUs) and their orientation; b) 3D rendered schematic showing the GEN-2 hyperpolarizer SEOP cell and 3D-printed forced air oven interface; c) corresponding photograph. Display (a) reproduced with permission from ref. [72]; Displays (b,c) reproduced with permission from ref. [73].

polarization run; after an initial period (but before the onset of "Rb runaway"[31,75,78]), the oven temperature would then be ramped down to achieve more stable SEOP and yield a high final polarization near what would be achieved without the ramping process, but in half the time.

The presence of two nearly identical GEN-2 "XeUS" hyperpolarizers on two continents allowed the first-in-kind pilot quality assurance (QA) study of clinical-scale hyperpolarizers[72] (Figure 10c). In this study, the repeatability of SEOP in a 1000 torr Xe/900 torr N$_2$/100 torr ^{4}He (2000 torr total pressure) gas mixture was investigated over several hundred gas-loading cycles, with very little decrease in performance during the first $\approx$ 200 cycles: $P_{Xe} = 71.7 \pm 1.5$%, $\gamma_{SEOP} = 0.019 \pm 0.003$ min^{-1}, ^{129}Xe $T_1 = 90.5 \pm 10.3$ min. Although the SEOP cell in this study exhibited a detectable performance decrease after 400 cycles, the cell continued to produce potentially useable $P_{Xe} = 42.3 \pm 0.6$%
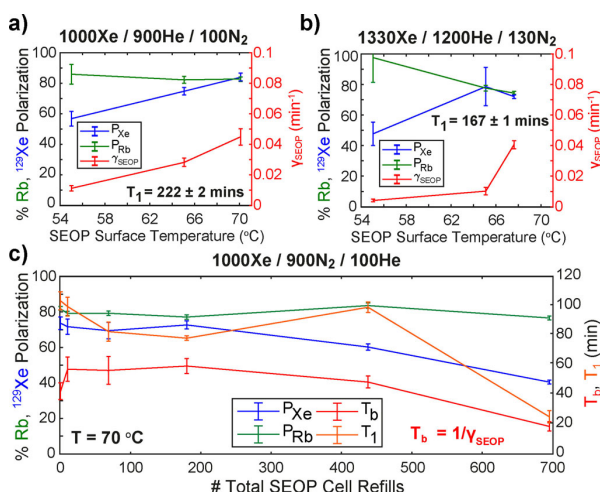
www.angewandte.org

© 2021 Wiley-VCH GmbH

Angew. Chem. Int. Ed. **2021**, 60, 2–24

Figure 10. a, b) Temperature maps of steady-state P_{Xe}, γ_{SEOP}, and P_{Rb} values following SEOP at different temperatures in a single cell using a generation-2 "XeUS" hyperpolarizer with forced air cooling/heating. Note two different color-coded y-axes for P_{Xe}, P_{Rb}, and γ_{SEOP}. c) Results comparing P_{Xe}, T_b, P_{Rb}, and T_1 from a single SEOP cell across a quality assurance study. Displays (a,b) are reproduced with permission from ref. [76]; Display (c) is reproduced with permission from ref. [72]. Gas mixture compositions are listed in units of torr.

even after nearly 700 refill cycles.[72] The ability to reproducibly achieve and maintain performance over so many refill cycles without having to replace the SEOP cell bodes well for the ultimate translation of the device to biomedical and clinical imaging applications.

A third-generation (GEN-3) SF-SEOP hyperpolarizer was introduced in 2020 by Birchall et al.[74] One of several improvements embodied by the design was replacement of the forced air oven with an aluminum jacket in direct thermal contact with the SEOP cell, offering rapid heat transfer during the temperature cycles (Figure 11). This new design resulted in a sevenfold decrease in the heating and cooling times to ≈4 minutes while also ensuring that the process is more thermally stable with the γ_{SEOP} build-up rate of up to 0.2 min^{-1} (Figure 12[74]); as a consequence, the design also allows far more nimble temperature ramping during SEOP. The GEN-3 device also offers improved in situ NMR polarimetry: Figure 12a shows a reference ^{1}H NMR spectrum from a thermally polarized water phantom (used for absolute calibration of ^{129}Xe polarization) acquired with 1024 scans in only 5 minutes. Moreover, the GEN-3 device has a small footprint, 1.2 m (width) × 1.5 m (height) × 0.6 m (depth), enabled in part by use of a compact solenoid magnet and provides a true push-button operation with advanced automation and integration over a WiFi interface.

5. Simulations of SEOP Processes

5.1. CF-SEOP Simulations

Broadly speaking, the theoretical mechanisms important in CF production of HP ^{129}Xe are well understood, and this
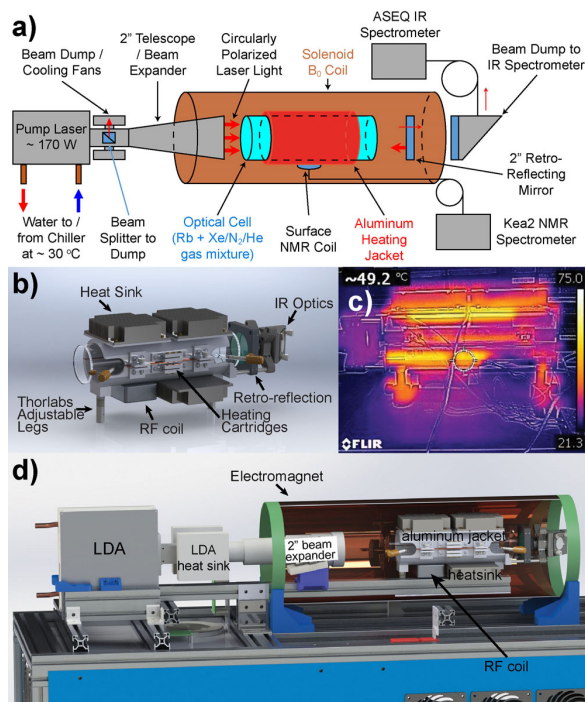

Figure 11. a) Schematic drawing of the third-generation (GEN-3) SF hyperpolarizer. The SEOP cell (blue cylinder) is encased within an aluminum heating jacket (red cylinder) to achieve the Rb vapor density necessary for efficient SEOP. The cell and heating jacket are contained within a magnetic solenoid coil (orange cylinder), which provides the homogeneous magnetic B_0 field created by a solenoid. b) 3D rendering of the GEN-3 hyperpolarizer SEOP cell and aluminum heating jacket design. c) Thermal photo taken during hyperpolarizer operation. d) 3D rendering of the upper chassis with solenoid magnet coil shown as a cut-away to depict SEOP cell and other internal components. The images are adopted with permission from ref. [74] (copyright 2020, American Chemical Society).

insight allows quantitative modeling of CF-SEOP processes. Such computational models generally belong to one of two categories: finite difference models (FDMs)[79,80] or finite element models (FEMs).[81–86] Although these descriptions refer to the computational methods that are used, the important distinction between these types is the *complexity* of the physical model employed: For modeling SEOP, FDMs generally use one spatial dimension to approximate laser-light propagation through the SEOP cell, and one- or two-dimensional (2D) uniform or laminar-flow approximations. Nuances of SEOP cell geometry are often ignored, along with effects such as laser heating, alkali density inhomogeneities, and convection. In contrast, FEMs typically use 2D or 3D geometries; moreover, as both commercial and open-source "multiphysics" packages using FEMs are relatively common, thermal, diffusion, and convective-flow effects can easily be incorporated. Additionally (and in contrast to most FDMs), FEMs typically include the frequency distribution of the laser light, often approximated as Gaussian.

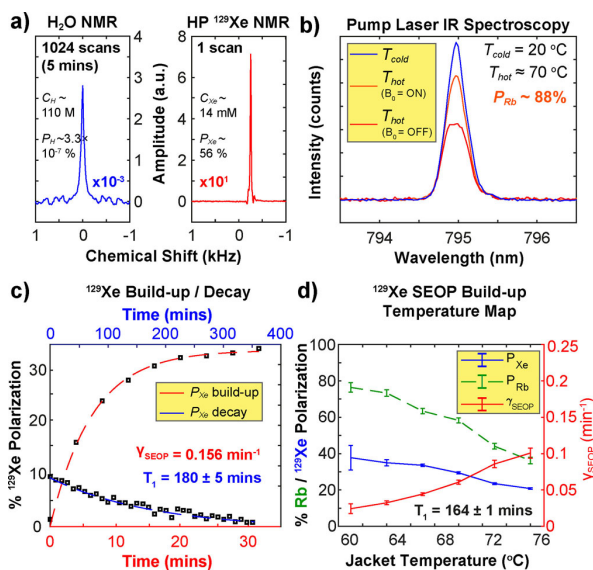For CF systems that use large SEOP cells (such as the Hersman design[15,35]), simple 2D laminar-flow FDMs predict

Angew. Chem. Int. Ed. **2021**, *60*, 2–24

© 2021 Wiley-VCH GmbH

www.angewandte.org

These are not the final page numbers! ↗↗

Figure 12. a) ^{1}H (blue) and ^{129}Xe (red) NMR measurements of thermally polarized water (doped with 10 mM CuSO$_4$, 1024 scans over 5 minutes, and a HP Xe gas mixture, 1 scan, respectively to determine ^{129}Xe nuclear spin polarization (P_{Xe}). b) IR spectroscopic measurements of the SEOP pump laser to estimate Rb electron polarization (P_{Rb}). c) Typical SEOP ^{129}Xe polarization build-up (red, P_{Xe}-(max) = 34.3 ± 0.9%) and decay (blue) to determine polarization build-up rate (γ_{SEOP}) and ^{129}Xe relaxation decay constant (T_1). (d) Temperature-dependent SEOP map of steady-state P_{Xe}, γ_{SEOP}, and P_{Rb}, P_{Xe}-(max) = 37.9 ± 6.7% at a jacket temperature of 60°C. All data acquired from various SEOP cells and Xe-containing gas mixtures using the GEN-3 XeUS hyperpolarizer.[74]

the observed P_{Xe} relatively well.[79] In addition to good agreement with P_{Xe}, Schrank et al. also observed relatively good agreement between such models and the in situ Rb polarization.[35] Further, Fink et al.[82] used an FEM to simulate a geometry similar to that used by Ruset et al.,[15] and found good agreement between their model's predictions and the available experimental results at the time. Fink et al. made several recommendations for CF polarizer construction based on the results of their model. They determined that it was best practice to presaturate the Rb vapor in the gas stream and to preheat the gas stream before flowing it to the SEOP region. They also recommended flowing the gas antiparallel to the laser beam. Finally, they recommended orienting the SEOP cell vertically, supporting many of the design features present in the Hersman design.

However, for CF systems that use smaller SEOP cells, there is an apparent discrepancy between the modelled and observed P_{Xe} values, especially when high-power pumping lasers are used. For example, Freeman et al. characterized this disagreement by examining P_{Xe} in 100, 200, and 300-cm^3 SEOP cells and compared those observations with predictions of a 2D FDM model using uniform flow.[87] The observed P_{Xe} differed from the model by as much as a factor of 4. A few approaches have been attempted to resolve this large disagreement. For example, Plummer and co-workers simulated[41] the entire CF-SEOP process (including ^{129}Xe cryo-

collection) and found that when Rb density and solid-state ^{129}Xe T_1 were allowed to be freely floating parameters fit to experimental data, both values tended to be significantly less than literature expectations—potentially explaining much of the perceived underperformance of certain CF-SEOP designs. Earlier, Freeman et al. suggested that the discrepancy was a result of a novel form of contamination in the SEOP cell manifested by Rb cluster formation. This hypothesis originated from the fact that small SEOP cells coupled with high-powered pump lasers give rise to very high power densities. Researchers who study alkali metal molecular clusters frequently use heated tubes containing bulk alkali metal with coupled plasma to form the clusters; thus, the apparatus used to produce the molecular clusters share a number of similarities with small SEOP setups. Freeman et al. added terms associated with theoretical clusters to their simulation, affecting it in three ways: 1) a decreased optical pumping rate, owing to reduced photon flux caused by light scattering off of clusters; 2) an increased Rb spin-destruction rate, under the expectation that cluster–Rb collisions would randomize the Rb electron spin-polarization; and 3) an increased ^{129}Xe spin-relaxation rate, for similar reasons. By including these additional terms for the clusters, Freeman et al. were able to fit an FDM with the available data to find estimates for the scattering cross-section, spin-destruction cross-section, and spin-relaxation cross-section due to the clusters of 1×10^{-12} cm^2, 4×10^{-7} cm^3 s^{-1}, and 4×10^{-13} cm^3 s^{-1}, respectively. The estimates assumed a metal cluster density that was 1/1000 of the Rb atomic vapor density. Using those fit parameters and assumptions, the FDM had much better agreement with the observed experimental data.

Flower et al. later disassembled used SEOP cells from a CF apparatus and examined them using scanning electron microscopy and transmission electron microscopy.[88] This study found hemispherical particles on the interior surface of the optical pumping cells ranging in diameter from 200 nm to 10 μm. Additionally, the study found pits on the interior glass surface of the cells. Researchers ascribed the existence of the particles and the glass pitting to be related to Rb cluster formation. Nevertheless, to date, Rb metal clusters have not been detected in situ in active SEOP cells.[80]

FEM models also have had success reproducing the behavior of CF-SEOP hyperpolarizers. Fink et al.[82] examined small-cell systems and reported relatively good agreement with data from Shah et al.,[89] who used a SEOP cell with a cross-section of 13 cm^2 and a modest laser power of 50 W. More recent FEM models of CF-SEOP created by Burant and Schrank[83–85] are currently under development with the goal of better capturing all phenomena of CF-SEOP hyperpolarizers, including complexities of mass and thermal transport within different regions of CF-SEOP cells.[65]

5.2. SF-SEOP Simulations

As with CF-SEOP, simulations of SF-SEOP can also be useful to both gain insight into underlying phenomena and to help devise practical guidance for hyperpolarizer design and operation. SF-SEOP modeling requires several simplifying

▮▮▮▮
↖↖ These are not the final page numbers!

www.angewandte.org

© 2021 Wiley-VCH GmbH

Angew. Chem. Int. Ed. **2021**, *60*, 2–24

modifications, such as the omission of the gas flow terms and Rb clusters (which, if relevant, are thought to occur only in certain CF regimes).[90] Two such simulations of SF-SEOP were implemented by Skinner et al.[65] and validated against two experimental datasets[75,91] from the high-Xe-density, high resonant-photon-flux regime. Both simulations provided excellent qualitative and quantitative reproduction of the Xe-rich SF-SEOP datasets, including the inverse relationship between the optimal cell temperature (T_{opt}) and [Xe]. Furthermore, under certain conditions the simulations trended towards a "universally optimal" laser absorption when P_{Xe} is maximized—which may help provide 1) an explanation for the experimentally observed interplay of laser linewidth, T_{opt}, and [Xe], in the context of optimizing the photon-to-[Rb] ratio (mentioned above), and 2) a new way to optimize SF hyperpolarizer operation. The simulations also studied the design and operation of such hyperpolarizers, considering cell temperature, cell geometry, laser linewidth, laser power, gas mixture, and gas pressure, to help further improve performance, including the prediction that reduction of laser linewidth improves P_{Xe} disproportionately at higher [Xe], and the potential utility of ternary gas mixtures containing ^{4}He (for improved temperature stability owing to higher thermal conductivity), which was recently realized in a second-generation clinical-scale hyperpolarizer.[65]

Finally, very recently Branca and co-workers[92,93] published simulation work that aimed to improve previous efforts by going against assumptions that may lead to underestimation of Rb/Xe spin-exchange cross-sections but significant *over*estimatation of Rb vapor densities (particularly in CF polarizers) and Xe cell residence times (exclusively in CF polarizers). The resulting simulations showed good quantitative reproduction of experimental polarization values and dynamics in both CF-SEOP and SF-SEOP, without considerations of contributions to spin exchange or relaxation beyond those considered in established theory.[19,29,32] Future experimental observations (including careful measurements of spin exchange contributions under relevant conditions, position-dependent Rb polarization and density, light and heat transport, presence or absence of Rb clusters, etc.) may help shed light on differences among the various approaches.

6. Other Emerging Technologies for HP ^{129}Xe Production

6.1. Alternative SEOP-Based Methods for Xe Hyperpolarization

While CF- and SF-SEOP-based designs have dominated the production of HP ^{129}Xe over the years, a number of alternative approaches have been also developed. One such approach stems from an otherwise "traditional" CF-SEOP design where the flow of the produced HP ^{129}Xe gas mixture is re-directed back into the SEOP cell.[94,95] Raftery and co-workers investigated the use of such a recirculating SEOP setup for long-term acquisition of enhanced NMR spectra of materials' surfaces. The ^{129}Xe is circulated through the hyperpolarizer multiple times, allowing higher P_{Xe} to be achieved compared to a single-pass through system. This

system proved to be surprisingly effective, producing P_{Xe} as high as 69% after only 5 minutes of recirculation with two 40 W coupled lasers.[96]

Saam and co-workers introduced a different SEOP hyperpolarizer design with the goal of creating large quantities of liquid HP ^{129}Xe[97] with a relatively small device. In their method, ^{129}Xe is still hyperpolarized in the gas phase via SEOP; however, once polarized, the gas undergoes phase exchange (facilitated by convection) with a column of liquid xenon, allowing polarization to accumulate in the liquid phase. Using just an 8-mL spherical SEOP cell and 15 W LDA, the apparatus provided 8% P_{Xe} in 0.1 mL of liquid Xe in 15 min.

To dramatically decrease the size of the hyperpolarization equipment, a microdevice can be employed to perform ^{129}Xe SEOP. In the device by Jimenez-Martınez et al.,[98] a gas mixture of ^{129}Xe and N$_2$ flows from an external gas manifold into the chip's pump chamber. Rb is deposited in the microdevice chamber (via the reaction of barium azide and RbCl) and is illuminated by circularly polarized light in the "pump" chamber, where the ^{129}Xe entering the chamber is hyperpolarized by SEOP. The ^{129}Xe polarization is then measured optically in the adjacent (downstream) "probe" chamber via an independently controlled laser beam using the response from the polarized ^{87}Rb to perform optical magnetometry.[99,100] The pump and probe chambers, embedded within a 1-mm-thick chip measuring 1×3 cm^2, are only 5×5 mm^2 and 3×3 mm^2, respectively. In principle, the HP ^{129}Xe gas could then be allowed to flow out of the chip for use in investigations. This first-generation on-chip SEOP device demonstrated the viability of the overall approach; however, ^{129}Xe polarization was limited ($\approx 0.5\%$). Collaboration with the Pines group and optimization of the chip design led to a significantly improved device (Figure 13). Kennedy et al. reported an on-chip SEOP device with lateral dimensions of 4×4 mm^2 for pump and probe chambers; the device could
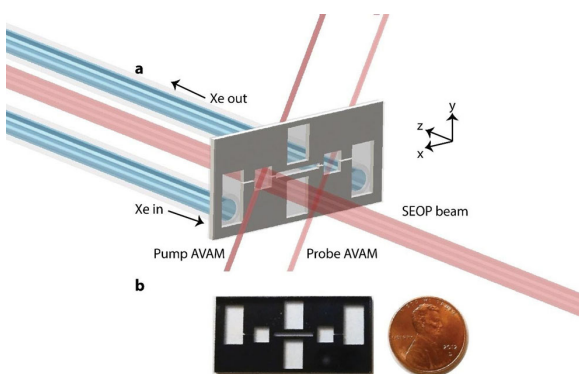

Figure 13. The optimized "on-chip" ^{129}Xe hyperpolarizer.[101] a) A mixture of Xe and N$_2$ gas flows from an external gas manifold into the chip, where laser light (795 nm) optically pumps the electron spins of Rb vapor atoms; ^{129}Xe that flows through this pump chamber is hyperpolarized via SEOP. Additional 795 nm laser beams are used to perform optical magnetometry in both pump and probe chambers. b) Photo of the device. Courtesy of V. Bajaj and A. Pines, reprinted with permission.

employ a gas flow rate of $\approx 5\ \mu L\,s^{-1}$ while also achieving P_{Xe} levels of 7% with a ^{129}Xe polarization lifetime of $\approx 6\ s$.[101] While the HP Xe production capacity of such on-chip devices may be limited, the small device size (39×19 mm^2) allows direct integration into other microfluidic devices.[102]

6.2. Non-SEOP-Based Approaches for Hyperpolarizing ^{129}Xe

Non-SEOP hyperpolarization techniques for the production of HP ^{129}Xe have also been developed. So-called "brute force" polarization is one such technique; it instead relies on the dependence that the *equilibrium* P_{Xe} has on temperature and applied magnetic field [Eq. (1)]. To induce large P_{Xe}, the temperature is reduced to milli-kelvin values, while the sample is subjected to a large magnetic field.[103–106] However, when such low temperatures are applied to the sample, the ^{129}Xe T_1 increases dramatically, meaning that the sample needs to be kept in the "brute force" conditions for a long period of time—an issue that can be mitigated by the addition of paramagnetic substances. For example, molecular oxygen can be mixed into the sample to further reduce the ^{129}Xe T_1, and thus reduce the time that "brute force" polarization needs to be applied from 65 to 9.5 hours.[107] Although P_{Xe} levels of up to 40% have been achieved,[108] the extraction of the HP ^{129}Xe gas can also be challenging without losing a substantial fraction of polarization during the phase-transition process.

Finally, in dynamic nuclear polarization (DNP),[109,110] a sample is mixed with a free radical and then cooled to $\leq 1\ K$ while it is subjected to a high magnetic field (between 3–7 T).[111,112] Under these conditions, the electron spins gain near-unity polarization,[113] and microwaves tuned to the electron spin resonance are applied to drive electron polarization to nearby nuclei in the lattice. When the hyperpolarization process is completed, the sample is rapidly heated with a solvent, allowing the dissolved HP substance to be removed and used for HP NMR or MRI; this variant is known as dissolution DNP (d-DNP).[113] Although d-DNP is most commonly applied for hyperpolarization of liquid ^{13}C-labelled molecules, there has also been success in producing HP ^{129}Xe via DNP[114,115] including HP ^{129}Xe gas via sublimation (dubbed s-DNP),[114] with clinically useful P_{Xe} levels as high as 30% achieved[114] (Figure 14). Currently, s-DNP is limited by a number of factors. First, the effectiveness of the s-DNP process relies upon the homogeneity of the sample, which can be hard to achieve for solid-state ^{129}Xe mixtures. Second, P_{Xe} can be limited by a "spin bottleneck", in which the electrons cannot efficiently transfer polarization to ^{129}Xe (the permanent magnetic moment of the paramagnetic dopants can shift the frequencies of ^{129}Xe spins near the dopants from those farther away, slowing the spread of polarization into the bulk lattice). Third, to date, s-DNP provides limited quantities of HP ^{129}Xe (ca. 0.015 sL), which is not yet sufficient for clinical applications. Current s-DNP efforts aim to overcome these limitations.
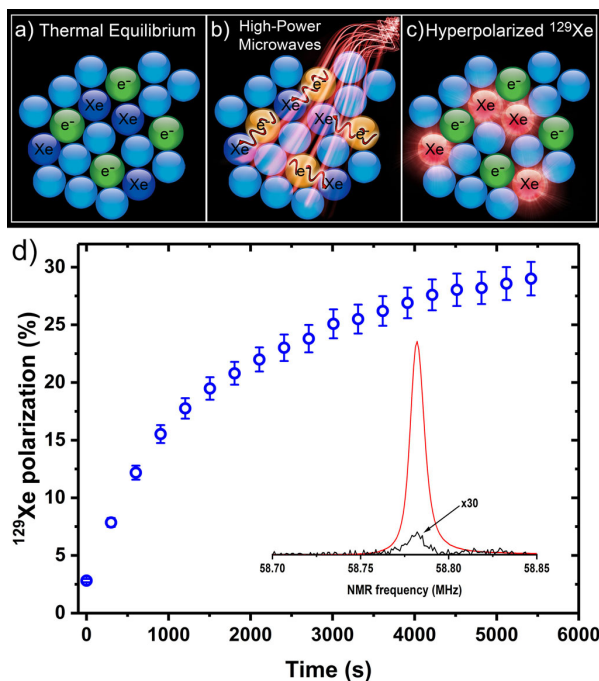

Figure 14. a) Schematic of thermal equilibrium of Xe nuclei in the solid state. b) Application of high-power microwaves to hyperpolarize electron spins at cryogenic temperature to near-unity polarization followed by polarization transfer to nearby Xe nuclear spins. c) Bulk HP ^{129}Xe states is created over time. d) Sublimation DNP hyperpolarization of ^{129}Xe: ^{129}Xe polarization build-up curve measured at 5 T and 1.15 ± 0.05 K in a 1.5 M xenon sample dissolved in d$_6$-ethanol containing 50 mM TEMPO. Inset: DNP-enhanced (red) and thermal equilibrium (black) ^{129}Xe NMR spectra measured to determine P_{Xe}. Display (d) Reprinted from ref. [114] (copyright 2015, American Chemical Society); image courtesy of Dr. Arnaud Comment.

7. Outlook for Biomedical Applications

The inherent properties of Xe such as diffusivity, blood solubility, and frequency shifts in different environments,[116] can be collectively exploited to directly probe Xe transport and distribution through various biological tissues and organs. In the case of the lungs, in addition to the straightforward imaging of HP ^{129}Xe gas in pulmonary airways, referred to as "ventilation imaging", it provides the unique capability of essentially imaging the gas exchange pathway followed by inhaled O$_2$.[117] More specifically, once ^{129}Xe is inhaled and enters into the alveolar space, it diffuses across the alveolar–capillary barrier membrane, where it exhibits a 197.8 ppm shift in its resonant frequency[118] relative to ^{129}Xe atoms remaining in the airspaces, corresponding to a shift of ≈ 3.5 kHz at 1.5 T. Xe then passes into the local capillary network and enters into the red blood cells (RBCs)[119] where it exhibits an even larger frequency shift of 217.6 ppm.[120] These two compartments, barrier and RBC, are collectively referred to as the "dissolved phase" (see Figure 15).

The inherent challenge of imaging dissolved-phase ^{129}Xe, with a more than 50-fold smaller signal than the gas phase (because the absorbed faction is substantially lower than that
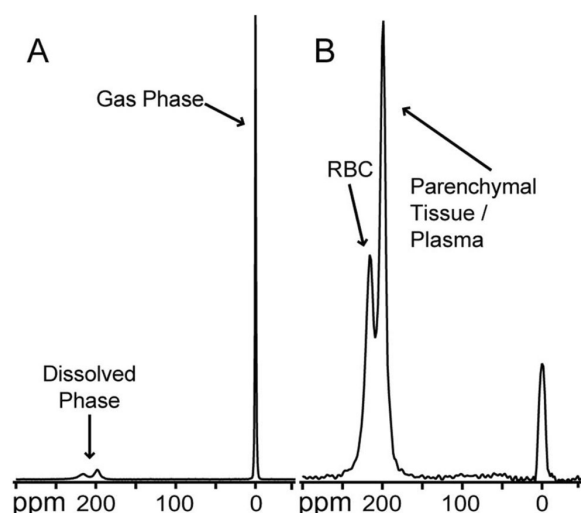
Figure 15. ^{129}Xe MRS showing signal intensity in human lungs at 1.5 T. A) NMR spectrum obtained when the gas- and dissolved-phase ^{129}Xe is excited equally, showing that the dissolved-phase ^{129}Xe signal is only 1–2% as large as the gas-phase. B) When the dissolved phase is selectively excited, the barrier and RBC spectral peaks are better appreciated. Reprinted with permission from ref. [121].

of the gas phase), is overcome by continuous replenishment of HP ^{129}Xe diffusing in from the airspaces, which allows one to use a much larger flip angle excitation than that typically used for ventilation imaging.[121] This property permits imaging of dissolved and gas-phase ^{129}Xe during the same breath-hold,[122] which is critical for quantitative analysis of gas transfer. ^{129}Xe images are typically processed into quantitative binning maps of all three compartments using thresholds based on the mean and standard deviations of distributions derived from the healthy reference cohort, subsequently analyzed to derive quantitative measures of ventilation, barrier uptake, and RBC transfer. In the following sections, we briefly review HP ^{129}Xe biomedical applications in various organs and diseases, where it provides a unique competitive advantage over other diagnostic imaging methods.

7.1. Idiopathic Pulmonary Fibrosis

Idiopathic pulmonary fibrosis (IPF) is a progressive scarring disease of the lungs of unknown cause, and this disease is ultimately fatal. IPF affects 13 to 20 people per 100 000 population worldwide. While IPF diagnosis has been revolutionized by high-resolution computed tomography (HRCT), this imaging modality still exhibits significant limitations, particularly in assessing disease progression and therapy response. The need for non-invasive assessment of regional lung function has become more acute in light of recently introduced and in-the-pipeline novel therapies. Thus, it will likely be valuable to complement 3D imaging of lung structure with 3D regional assessment of function. This challenge is well addressed by HP ^{129}Xe MRI, exploiting the unique properties of this inert gas to image its distribution,

not only in the airspaces, but also in the interstitial barrier tissues and red blood cells (RBCs). This single-breath imaging exam could ultimately become the ideal, non-invasive tool to assess pulmonary gas-exchange impairment in IPF. Here, we detail the evolution of HP ^{129}Xe MRI from its early development to its current state as a clinical research platform. The key imaging biomarkers generated from the ^{129}Xe MRI exam for potential utility in IPF diagnosis, prognosis, and assessment of therapeutic response. We conclude by discussing the types of studies that must be performed for HP ^{129}Xe MRI to be incorporated into the IPF clinical algorithm and begin to positively impact IPF disease diagnosis and management.

HP ^{129}Xe MRI permits the evaluation of the heterogeneous, fibrotic thickening of the interstitial barrier tissue and alveolar collapse that collectively impair gas exchange.[123] A reliable method for concurrent mapping of all three Xe compartments utilizes thoracic ^{1}H/^{129}Xe MRI with one-point Dixon decomposition of multiple tissue resonances to obtain separate images of ^{129}Xe in airspaces, barrier tissue, and RBCs.[120] In a recent study, HP ^{129}Xe MRI depicted functional impairment in patients with IPF, whose mean barrier uptake increased by 188% compared with the healthy reference population.[118] ^{129}Xe MRI metrics correlated poorly and insignificantly with CT fibrosis scores but the RBC:barrier ratio correlated strongly with diffusing capacity of the lungs for carbon monoxide (DLCO), indicating a potentially better imaging metric of the disease progression.

In a study investigating the spatial effects of antifibrotic drugs, an IPF patient who started on antifibrotic treatment one month before baseline MRI, returned five months later for a follow-up scan.[124] At baseline, the patient presented with 49% of their lung volume exhibiting high barrier uptake, while focal RBC transfer defects at the lung bases accounted for low RBC transfer in 35% of the lung. When the patient returned five months later, the percentage of lung exhibiting high barrier uptake had improved to encompass only 30% of the lung, while the RBC transfer defects remained stable at 35% of lung volume (Figure 16). Thus, the HP ^{129}Xe MRI provided feedback on drug efficacy.

7.2. Cystic Fibrosis

Cystic fibrosis (CF) is a genetic disease that carries high morbidity and mortality from lung-function decline. Monitoring disease progression and treatment response in young patients is desirable, but serial imaging via CT is often considered prohibitive. HP ^{129}Xe MRI has demonstrated regional ventilation defects in mild CF lung disease with normal FEV_1 (i.e., the amount of air one can force from the lungs in 1 s) and more effectively discriminated CF from controls than FEV_1.[125] The feasibility, safety, and tolerability of HP ^{129}Xe MRI has been demonstrated in children as young as six years old.[126] O_2 saturation (SpO_2) changes in these young patients are consistent with the expected physiological effects of a short anoxic breath-hold and known anesthetic properties of xenon. In addition to single-breath HP ^{129}Xe MRI scans, multibreath washout protocols have been reported to be feasible in pediatric CF patients, making it
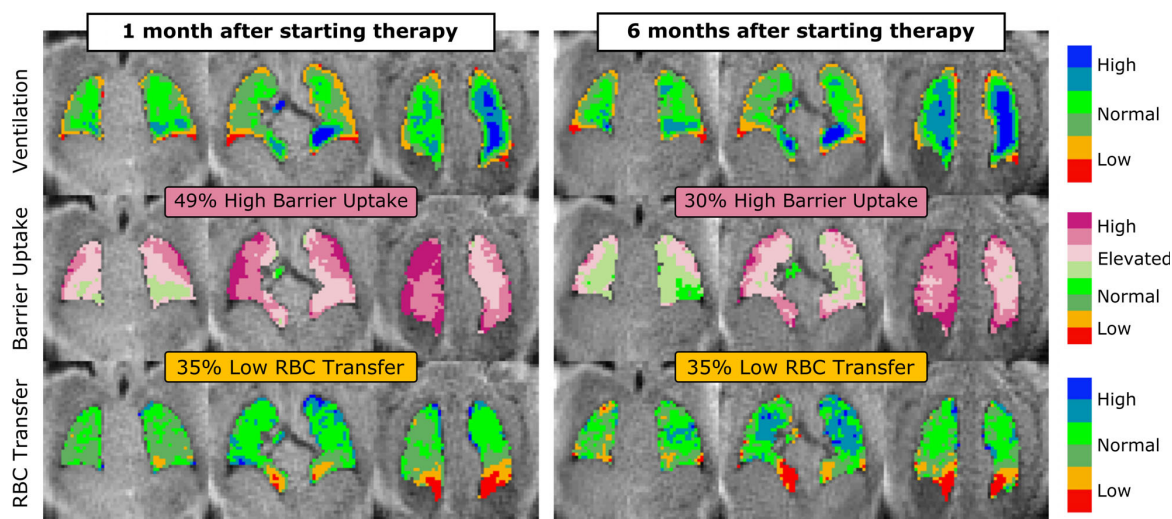
Angew. Chem. Int. Ed. **2021**, *60*, 2 – 24

© 2021 Wiley-VCH GmbH

www.angewandte.org

These are not the final page numbers! ↗↗

Figure 16. Observed improvement of ^{129}Xe gas-exchange metrics for an IPF patient on current therapy. This patient started anti-fibrotic therapy one month prior to baseline MRI and presented with 49% high barrier uptake, and focal RBC transfer defects at the lung bases resulting in 35% low RBC transfer. Upon return 5 months later, the percentage of lung exhibiting high barrier uptake had decreased to 30%, while the RBC transfer defects remained stable at 35% of lung volume. Reprinted with permission from ref. [124].

possible to measure fractional ventilation in this population.[127] In a more recent study, the size and extent of regional ventilation defects in pediatric CF were quantified by HP ^{129}Xe MRI and associated with the presence of specific structural abnormalities identified by ultrashort echo time (UTE) ^{1}H MRI: bronchiectasis (a lung condition where the bronchial tubes are permanently damaged, widened, and thickened), bronchial wall thickening, mucus plugs, and ground glass opacities.[128]

7.3. Pulmonary Arterial Hypertension and Cardiopulmonary Diseases

A significant subset of patients exhibiting concurrent cardiac and pulmonary diseases are most adversely affected by standard diagnosis and management methods. HP ^{129}Xe MRI and MRS methods can provide valuable information to help with diagnostic challenges in cardiopulmonary disease, such as left heart failure (LHF) and pulmonary arterial hypertension (PAH), and increase understanding of regional lung function and hemodynamics at the alveolar–capillary level. In addition to spectral parameters of HP ^{129}Xe described above, dynamic ^{129}Xe MRS provides additional insight, with particular focus on quantifying cardiogenic oscillations in the RBC resonance. Decoupling the spectral parameters and temporal dynamics of the airspace, interstitial barrier, and RBCs confirms that in addition to altered the RBC:barrier ratio, all three ^{129}Xe resonances are affected by the breathing maneuver, with several RBC spectral parameters exhibiting prominent oscillations at the cardiac frequency.[129] A study utilizing this methodology demonstrated that Chronic Obstructive Pulmonary Disease (COPD), IPF, LHF, and PAH each exhibit unique ^{129}Xe MRI and dynamic spectroscopy signatures.[130] COPD patients demonstrated the

most ventilation and barrier defects, whereas IPF patients demonstrated elevated barrier uptake, increased RBC amplitude, and shift oscillations compared to healthy controls. Patients with COPD and PAH both exhibited decreased RBC amplitude oscillations, and LHF was distinguishable from PAH by enhanced RBC amplitude oscillations (see Figure 17).

A more recent study extended this methodology by 3D mapping of the magnitude of cardiogenic dynamics using radial MRI to assess regional blood volume fluctuations within the pulmonary microvasculature throughout the cardiac cycle.[131] The regional heterogeneity of oscillations was found to be sensitive to disease state in PAH and IPF patients, with greater percentages of lungs exhibiting low-amplitude oscillations in PAH patients, and high-amplitude oscillations increasing significantly over time in IPF patients. Other emerging pulmonary applications of HP ^{129}Xe MRI include localized measurement of lung function impairment caused by COVID-19[132, 133]—currently the subject of clinical trials in Europe and North America (see for example, refs. [133,134]).

7.4. Brain Imaging

After inhalation, HP ^{129}Xe dissolves in pulmonary blood and is transferred to the brain through systemic circulation. Uptake of inhaled Xe gas into extravascular brain tissue compartment across the blood–brain barrier provides an opportunity to probe regional cerebrovascular physiology. The contrast mechanism of HP ^{129}Xe in brain, beyond regional microvascular perfusion, is a function of gas exchange, T_1 relaxation, and RF depolarization history of the dissolved signal on route to the brain tissue.

Imaging dissolved HP ^{129}Xe in the brain was first demonstrated in healthy humans after the imaging RF coil
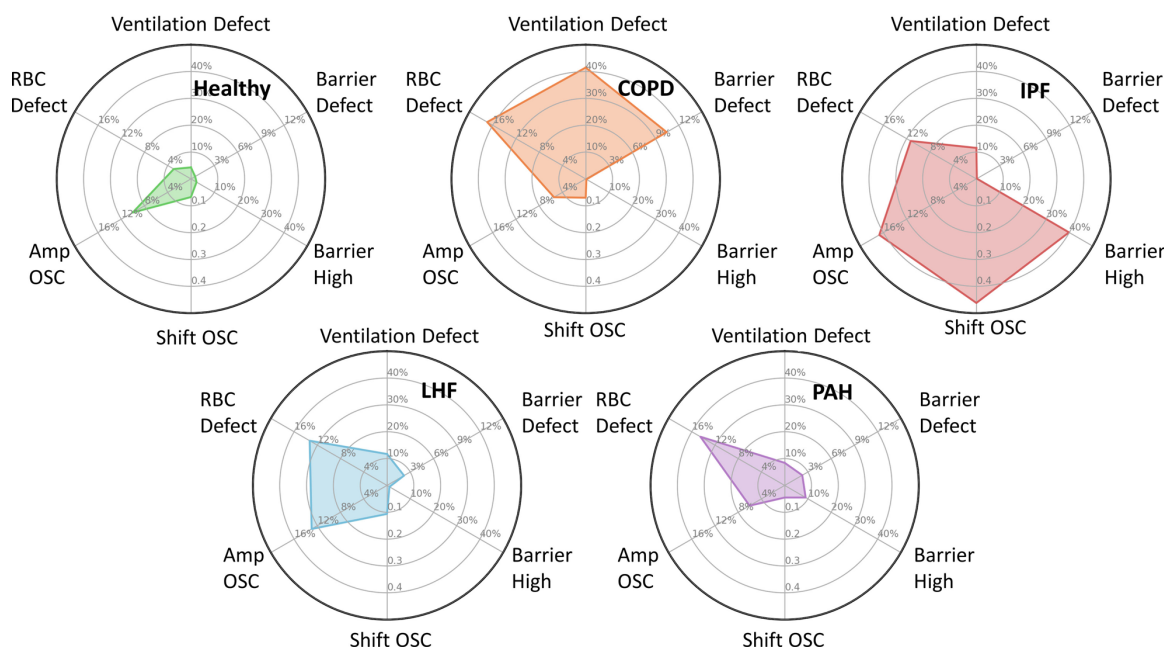
||||
↖↖ These are not the final page numbers!

www.angewandte.org

© 2021 Wiley-VCH GmbH

Angew. Chem. Int. Ed. 2021, 60, 2 – 24

Figure 17. Radar plots to display the primary ^{129}Xe MRI and spectroscopic signatures associated with a) healthy volunteers and patients with b) COPD, c) IPF, d) LHF, and e) PAH. The mean cohort values of the key markers are plotted on one of the six radials: ventilation defect, barrier defect, barrier high, and RBC defect percentages derived from imaging, and RBC shift oscillation (SO) and amplitude oscillation (AO) from MRS. Reprinted with permission from ref. [130].

and pulse sequences were optimized to achieve 20–40 SNR after inhalation of 1 sL of HP ^{129}Xe.[136] Similar results were subsequently reported in subjects with established stroke.[137] HP ^{129}Xe washout rate has been explored as a biomarker for Alzheimer's disease (AD).[138] Xe washout parameter is influenced by cerebral perfusion, T_1 relaxation of ^{129}Xe, and the associated partition coefficient, which all are in turn influenced by AD. Xe washout parameter was extracted by fitting the HP ^{129}Xe data to a pharmacokinetic model, showing that Xe washout rate in white and gray matters in AD patients were approximately half of that in healthy controls. In a recent study, quantitative maps of regional perfusion in healthy human brains were acquired by using time-resolved depolarization of HP ^{129}Xe (SNR ≈ 10) and subsequently evaluated to detect changes in cerebral blood flow (CBF) due to a hemodynamic response in response to brain stimuli (Figure 18).[135]

7.5. Other Applications in Tissues

The exquisite sensitivity of the ^{129}Xe chemical shift[53] can be exploited in other applications, for example, HP MRI of brown fat, as demonstrated by Branca and co-workers.[139] However, in other cases resonances of ^{129}Xe dissolved in tissues may be too weak or nonspecific to provide desired biomolecular insights. Pines and co-workers[140] showed that the specificity of Xe could be enhanced by "functionalizing" it with analyte-binding molecular cages (e.g., cryptophanes,[141]

cucurbiturils,[142] gas-binding protein nanostructures,[143] etc.[144, 145]), giving rise to unique analyte-bound ^{129}Xe resonances.[144, 145] By implementing chemical exchange saturation transfer (Hyper-CEST)[146] the strong "bulk" ^{129}Xe signal can be encoded with the much-weaker response of the analyte-bound Xe biosensor, greatly improving the detection sensitivity. In vivo HyperCEST using Xe-binding molecular cages has now been demonstrated (Figures 19 and 20).[147] The approach offers great promise for extending HP ^{129}Xe MRI to molecular imaging of a wide range of biomarkers.

8. Conclusions

Hyperpolarization of ^{129}Xe via SEOP on a clinical scale has been achieved by CF and SF approaches, which have matured and transitioned to the commercialization of the corresponding instrumentation technologies. A number of clinical studies and trials have already demonstrated the efficacy of HP ^{129}Xe MRI and MRS for diagnosis, prognosis, and monitoring response to treatment of several diseases. We envision that the regulatory approval for diagnostic use of HP ^{129}Xe MRI will be in place in the USA, EU, UK, and other countries in the near future for this game-changing diagnostic modality. While much work remains to be done for this technology to translate from the leading pioneering sites to the clinical realm to make it available for the general population, the production technologies are certainly ready to support production of HP ^{129}Xe at clinical scale.
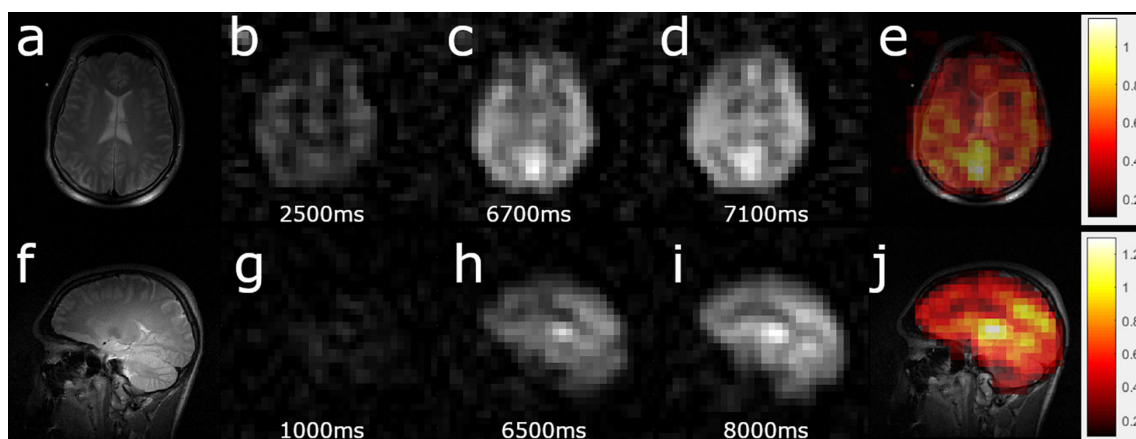
Figure 18. ^{129}Xe perfusion maps acquired in human brain: a,f) High-resolution, T_2-weighted ^{1}H scans for brain localization. b–d) Three dynamic HP ^{129}Xe images acquired 2.5 s, 6.8 s, and 7.1 s after the application of a depolarization RF pulse in the axial projection. e) The perfusion map in mL of blood per mL of tissue per min. g–i) Three dynamic images acquired after 1 s, 6.5 s, and 8 s in the sagittal view. j) Perfusion map in the sagittal view. Reprinted with permission from ref. [135].
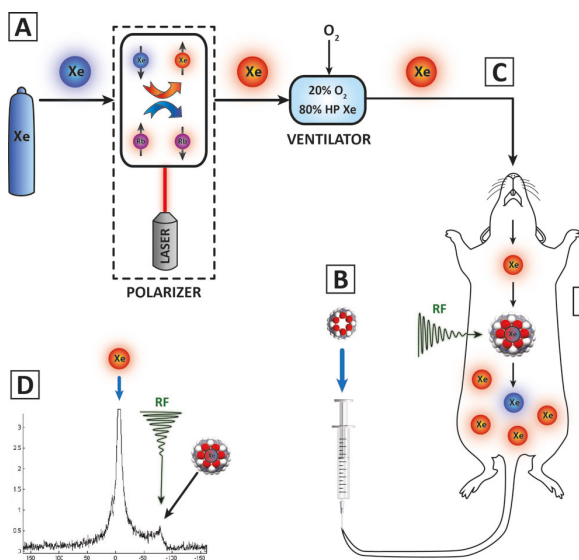
Figure 19. a) HP ^{129}Xe is mixed with O_2; b) HyperCEST agent is administered via tail-vein injection; c) HP ^{129}Xe is administered via inhalation; d) model "Analyte-bound" ^{129}Xe resonance is selectively irradiated; e) corresponding MRI image is encoded. Image courtesy of Prof. M. Albert, reproduced with permission from ref. [147].
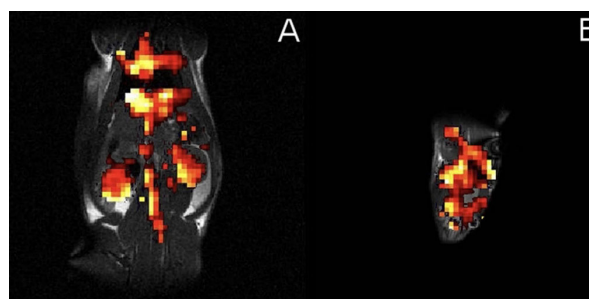

Figure 20. a) HyperCEST saturation map of a rat abdomen zoomed in and overlaid on a ^{1}H MRI showing the location of the CB6 cage contrast agent. b) Same as (a) but of the rat brain. Image courtesy of Prof. M. Albert, reproduced with permission from ref. [147].

Prof. W. Hersman for images provided for Figure 4, Dr. V. Bajaj and Prof. A. Pines for Figure 13, Dr. A. Comment for Figure 14, and Prof. M. Albert for Figures 19 and 20. B.M.G., P.N., and E.Y.C. declare a stake of ownership in XeUS Technologies LTD. K.E. and A.D. are employees of Polarean Inc.

Conflict of interest

B.M.G., P.N., and E.Y.C. declare a stake of ownership in XeUS Technologies LTD. K.E. and A.D. are employees of Polarean Inc.

[1] J. F. Heidenreich, A. M. Weng, C. Metz, T. Benkert, J. Pfeuffer, H. Hebestreit, T. A. Bley, H. Köstler, S. Veldhoen, *Radiology* **2020**, *296*, 191–199.

[2] C. Witte, L. Schroder, *NMR Biomed.* **2013**, *26*, 788–802.

▐▌▐▌ **www.angewandte.org**
◤◤ These are not the final page numbers!

© 2021 Wiley-VCH GmbH

Angew. Chem. Int. Ed. **2021**, *60*, 2–24

[3] M. A. Schroeder, H. J. Atherton, L. E. Cochlin, K. Clarke, G. K. Radda, D. J. Tyler, *Magn. Reson. Med.* **2009**, *61*, 1007–1014.

[4] A. Viale, S. Aime, *Curr. Opin. Chem. Biol.* **2010**, *14*, 90–96.

[5] J. P. Mugler, T. A. Altes, *J. Magn. Reson. Imaging* **2013**, *37*, 313–331.

[6] S. B. Fain, F. R. Korosec, J. H. Holmes, R. O'Halloran, R. L. Sorkness, T. M. Grist, *J. Magn. Reson. Imaging* **2007**, *25*, 910–923.

[7] M. S. Albert, G. D. Cates, B. Driehuys, W. Happer, B. Saam, C. S. Springer, A. Wishnia, *Nature* **1994**, *370*, 199–201.

[8] H. Middleton, R. D. Black, B. Saam, G. D. Cates, G. P. Cofer, R. Guenther, W. Happer, L. W. Hedlund, G. Alan Johnson, K. Juvan, *Magn. Reson. Med.* **1995**, *33*, 271–275.

[9] E. J. R. van Beek, J. M. Wild, *Proc. Am. Thorac. Soc.* **2005**, *2*, 528–532.

[10] D. A. Shea, D. Morgan, (Ed.: C. r. Service), CRS, **2010**.

[11] L. Ebner, J. Kammerman, B. Driehuys, M. L. Schiebler, R. V. Cadman, S. B. Fain, *Eur. J. Radiol.* **2017**, *86*, 343–352.

[12] R. T. Branca, T. He, L. Zhang, C. S. Floyd, M. Freeman, C. White, A. Burant, *Proc. Natl. Acad. Sci. USA* **2014**, *111*, 18001–18006.

[13] K. Qing, K. Ruppert, Y. Jiang, J. F. Mata, G. W. Miller, Y. M. Shim, C. Wang, I. C. Ruset, F. W. Hersman, T. A. Altes, *J. Magn. Reson. Imaging* **2014**, *39*, 346–359.

[14] K. Ruppert, J. F. Mata, J. R. Brookeman, K. D. Hagspiel, J. P. Mugler III, *Magn. Reson. Med.* **2004**, *51*, 676–687.

[15] I. C. Ruset, S. Ketel, F. W. Hersman, *Phys. Rev. Lett.* **2006**, *96*, 053002.

[16] A. Kastler, *J. Phys. Radium* **1950**, *11*, 255–265.

[17] M. A. Bouchiat, T. R. Carver, C. M. Varnum, *Phys. Rev. Lett.* **1960**, *5*, 373–375.

[18] W. Happer, W. A. Van Wijngaarden, *Hyperfine Interact.* **1987**, *38*, 435–470.

[19] T. G. Walker, W. Happer, *Rev. Mod. Phys.* **1997**, *69*, 629–642.

[20] B. Driehuys, G. D. Cates, E. Miron, K. Sauer, D. K. Walter, W. Happer, *Appl. Phys. Lett.* **1996**, *69*, 1668–1670.

[21] B. Goodson, N. Whiting, A. Coffey, P. Nikolaou, F. Shi, B. Gust, M. Gemeinhardt, R. Shchepin, J. Skinner, J. Birchall, M. Barlow, E. Chekmenev, *Emagres.* **2015**, *4*, 797–810.

[22] M. Gatzke, G. D. Cates, B. Driehuys, D. Fox, W. Happer, B. Saam, *Phys. Rev. Lett.* **1993**, *70*, 690–693.

[23] F. W. Hersman, I. C. Ruset, S. Ketel, I. Muradian, S. D. Covrig, J. Distelbrink, W. Porter, D. Watt, J. Ketel, J. Brackett, A. Hope, S. Patz, *Acad. Radiol.* **2008**, *15*, 683–692.

[24] N. N. Kuzma, B. Patton, K. Raman, W. Happer, *Phys. Rev. Lett.* **2002**, *88*, 147602.

[25] W. J. Cummings, O. Häusser, W. Lorenzon, D. R. Swenson, B. Larson, *Phys. Rev. A* **1995**, *51*, 4842.

[26] M. E. Wagshul, T. E. Chupp, *Phys. Rev. A* **1989**, *40*, 4447.

[27] M. A. Bouchiat, J. Brossel, L. C. Pottier, *J. Chem. Phys.* **1972**, *56*, 3703–3714.

[28] M. V. Romalis, E. Miron, G. D. Cates, *Phys. Rev. A* **1997**, *56*, 4569.

[29] W. Happer, *Rev. Mod. Phys.* **1972**, *44*, 169.

[30] I. Saha, P. Nikolaou, N. Whiting, B. M. Goodson, *Chem. Phys. Lett.* **2006**, *428*, 268–276.

[31] A. L. Zook, B. B. Adhyaru, C. R. Bowers, *J. Magn. Reson.* **2002**, *159*, 175–182.

[32] W. Happer, E. Miron, S. Schaefer, D. Schreiber, W. A. Van Wijngaarden, X. Zeng, *Phys. Rev. A.* **1984**, *29*, 3092–3110.

[33] F. W. Hersman, I. C. Ruset, S. Ketel, I. Muradian, S. D. Covrig, J. Distelbrink, W. Porter, D. Watt, J. Ketel, J. Brackett, A. Hope, S. Patz, *Acad. Radiol.* **2008**, *15*, 683–692.

[34] F. W. Hersman, J. Distelbrink, J. Ketel, S. Ketel, S. Bryn, D. W. Watt, W. C. Porter, J. F. Mata, I. C. Ruset, in *XVth International Workshop on Polarized Sources, Targets and Polarimetry*, Charlottesville, Virginia, USA, **2013**.

[35] G. Schrank, Z. Ma, A. Schoeck, B. Saam, *Phys. Rev. A* **2009**, *80*, 063424.

[36] G. Norquay, S. R. Parnell, X. J. Xu, J. Parra-Robles, J. M. Wild, *J. Appl. Phys.* **2013**, *113*, 044908.

[37] B. Lachmann, S. Armbruster, W. Schairer, M. Landstra, A. Trouwborst, G. J. Van Daal, A. Kusuma, W. Erdmann, *Lancet* **1990**, *335*, 1413–1415.

[38] G. Norquay, G. J. Collier, M. Rao, N. J. Stewart, J. M. Wild, *Phys. Rev. Lett.* **2018**, *121*, 153201.

[39] M. He, S. H. Robertson, S. S. Kaushik, M. S. Freeman, R. S. Virgincar, J. Davies, J. Stiles, W. M. Foster, H. P. McAdams, B. Driehuys, *Magn. Reson. Imaging* **2015**, *33*, 877–885.

[40] N. J. Stewart, G. Norquay, P. D. Griffiths, J. M. Wild, *Magn. Reson. Med.* **2015**, *74*, 346–352.

[41] J. W. Plummer, K. Emami, A. Dummer, J. C. Woods, L. L. Walkup, Z. I. Cleveland, *J. Magn. Reson.* **2020**, *320*, 106845.

[42] K. Qing, N. J. Tustison, J. P. Mugler III, J. F. Mata, Z. Lin, L. Zhao, D. Wang, X. Feng, J. Y. Shin, S. J. Callahan, *Acad. Radiol.* **2019**, *26*, 326–334.

[43] M. G. Mortuza, S. Anala, G. E. Pavlovskaya, T. J. Dieken, T. Meersmann, *J. Chem. Phys.* **2003**, *118*, 1581.

[44] T. Hughes-Riley, J. S. Six, D. M. L. Lilburn, K. F. Stupic, A. C. Dorkes, D. E. Shaw, G. E. Pavlovskaya, T. Meersmann, *J. Magn. Reson.* **2013**, *237*, 23–33.

[45] H. Imai, J. Fukutomi, A. Kimura, H. Fujiwara, *Concepts Magn. Reson. Part B* **2008**, *33*, 192–200.

[46] T. Wakayama, M. Kitamoto, T. Ueyama, H. Imai, M. Narazaki, A. Kimura, H. Fujiwara, *J. Magn. Reson. Imaging* **2008**, *27*, 777–784.

[47] H. Fujiwara, H. Imai, S. Iguchi, H. Yoshimura, A. Kimura, (Ed.: USPTO), Osaka University NUC, **2014**.

[48] S. Hodono, H. Imai, Y. Yamauchi, A. Kawamura, H. Matsumoto, S. Okumura, H. Fujiwara, A. Kimura, *NMR Biomed.* **2016**, *29*, 1414–1419.

[49] N. J. Rogers, F. Hill-Casey, K. F. Stupic, J. S. Six, C. Lesbats, S. P. Rigby, J. Fraissard, G. E. Pavlovskaya, T. Meersmann, *Proc. Natl. Acad. Sci. USA* **2016**, *113*, 3164–3168.

[50] J. S. Six, T. Hughes-Riley, K. F. Stupic, G. E. Pavlovskaya, T. Meersmann, *PLoS One* **2012**, *7*, e49927.

[51] B. Driehuys, J. Pollaro, G. P. Cofer, *Magn. Reson. Med.* **2008**, *60*, 14–20.

[52] D. A. Barskiy, A. M. Coffey, P. Nikolaou, D. M. Mikhaylov, B. M. Goodson, R. T. Branca, G. J. Lu, M. G. Shapiro, V.-V. Telkki, V. V. Zhivonitko, I. V. Koptyug, O. G. Salnikov, K. V. Kovtunov, V. I. Bukhtiyarov, M. S. Rosen, M. J. Barlow, S. Safavi, I. P. Hall, L. Schröder, E. Y. Chekmenev, *Chem. Eur. J.* **2017**, *23*, 725–751.

[53] B. M. Goodson, *J. Magn. Reson.* **2002**, *155*, 157–216.

[54] M. S. Rosen, T. E. Chupp, K. P. Coulter, R. C. Welsh, S. D. Swanson, *Rev. Sci. Instrum.* **1999**, *70*, 1546–1552.

[55] H. J. Jänsch, T. Hof, U. Ruth, J. Schmidt, D. Stahl, D. Fick, *Chem. Phys. Lett.* **1998**, *296*, 146–150.

[56] S. D. Swanson, M. S. Rosen, K. P. Coulter, R. C. Welsh, T. E. Chupp, *Magn. Reson. Med.* **1999**, *42*, 1137–1145.

[57] L. Barbier, M. Cheret, *J. Phys. B* **1983**, *16*, 3213.

[58] D. Levron, D. K. Walter, S. Appelt, R. J. Fitzgerald, D. Kahn, S. E. Korbly, K. L. Sauer, W. Happer, T. L. Earles, L. J. Mawst, *Appl. Phys. Lett.* **1998**, *73*, 2666–2668.

[59] I. A. Nelson, B. Chann, T. G. Walker, *Appl. Phys. Lett.* **2000**, *76*, 1356–1358.

[60] H. Zhu, I. C. Ruset, F. W. Hersman, *Opt. Lett.* **2005**, *30*, 1342–1344.

[61] P. Nikolaou, N. Whiting, N. A. Eschmann, K. E. Chaffee, B. M. Goodson, *J. Magn. Reson.* **2009**, *197*, 249–254.

[62] A. Gourevitch, G. Venus, V. Smirnov, D. A. Hostutler, L. Glebov, *Opt. Lett.* **2008**, *33*, 702–704.

[63] B. L. Volodin, S. V. Dolgy, E. D. Melnik, E. Downs, J. Shaw, V. S. Ban, *Opt. Lett.* **2004**, *29*, 1891–1893.

[64] I. A. Nelson, T. G. Walker, *Phys. Rev. A* **2001**, *65*, 012712.

[65] J. G. Skinner, K. Ranta, N. Whiting, A. M. Coffey, P. Nikolaou, M. S. Rosen, E. Y. Chekmenev, P. G. Morris, M. J. Barlow, B. M. Goodson, *J. Magn. Reson.* **2020**, *312*, 106686.

[66] B. M. Goodson, N. Whiting, H. Newton, J. G. Skinner, K. Ranta, P. Nikolaou, M. J. Barlow, E. Y. Chekmenev, in *Hyperpolarized Xenon-129 Magnetic Resonance: Concepts, Production, Techniques and Applications*, The Royal Society of Chemistry, Cambridge, **2015**, pp. 96–121.

[67] P. Nikolaou, A. M. Coffey, L. L. Walkup, B. M. Gust, N. Whiting, H. Newton, I. Muradyan, M. Dabaghyan, K. Ranta, G. D. Moroz, M. S. Rosen, S. Patz, M. J. Barlow, E. Y. Chekmenev, B. M. Goodson, *Magn. Reson. Imaging* **2014**, *32*, 541–550.

[68] P. Nikolaou, A. M. Coffey, L. L. Walkup, B. M. Gust, N. Whiting, H. Newton, S. Barcus, I. Muradyan, M. Dabaghyan, G. D. Moroz, M. Rosen, S. Patz, M. J. Barlow, E. Y. Chekmenev, B. M. Goodson, *Proc. Natl. Acad. Sci. USA* **2013**, *110*, 14150–14155.

[69] N. Whiting, P. Nikolaou, N. A. Eschmann, M. J. Barlow, R. Lammert, J. Ungar, W. Hu, L. Vaissie, B. M. Goodson, *Appl. Phys. B* **2012**, *106*, 775–788.

[70] S. E. Korchak, W. Kilian, L. Mitschang, *Appl. Magn. Reson.* **2013**, *44*, 65–80.

[71] P. Nikolaou, A. M. Coffey, L. L. Walkup, B. Gust, C. LaPierre, E. Koehnemann, M. J. Barlow, M. S. Rosen, B. M. Goodson, E. Y. Chekmenev, *J. Am. Chem. Soc.* **2014**, *136*, 1636–1642.

[72] J. R. Birchall, R. K. Irwin, P. Nikolaou, E. V. Pokochueva, K. V. Kovtunov, I. V. Koptyug, M. J. Barlow, B. M. Goodson, E. Y. Chekmenev, *J. Magn. Reson.* **2020**, *316*, 106755.

[73] J. R. Birchall, R. K. Irwin, P. Nikolaou, A. M. Coffey, B. E. Kidd, M. Murphy, M. Molway, L. B. Bales, K. Ranta, M. J. Barlow, B. M. Goodson, M. S. Rosen, E. Y. Chekmenev, *J. Magn. Reson.* **2020**, *319*, 106813.

[74] J. R. Birchall, P. Nikolaou, A. M. Coffey, B. E. Kidd, M. Murphy, M. Molway, L. B. Bales, B. M. Goodson, R. K. Irwin, M. J. Barlow, *Anal. Chem.* **2020**, *92*, 4309–4316.

[75] P. Nikolaou, A. M. Coffey, K. Ranta, L. L. Walkup, B. M. Gust, M. J. Barlow, M. S. Rosen, B. M. Goodson, E. Y. Chekmenev, *J. Phys. Chem. B* **2014**, *118*, 4809–4816.

[76] J. R. Birchall, P. Nikolaou, R. K. Irwin, M. J. Barlow, K. Ranta, A. M. Coffey, B. M. Goodson, E. V. Pokochueva, K. V. Kovtunov, I. V. Koptyug, *J. Magn. Reson.* **2020**, *315*, 106739.

[77] P. Nikolaou, A. M. Coffey, M. J. Barlow, M. S. Rosen, B. M. Goodson, E. Y. Chekmenev, *Anal. Chem.* **2014**, *86*, 8206–8212.

[78] C. Witte, M. Kunth, F. Rossella, L. Schröder, *J. Chem. Phys.* **2014**, *140*, 084203.

[79] I. Ruset, PhD Dissertation, University of New Hampshire **2005**, https://scholars.unh.edu/dissertation/282/.

[80] M. S. Freeman, PhD Dissertation, Duke University **2015**, https://dukespace.lib.duke.edu/dspace/handle/10161/9907.

[81] A. Fink, D. Baumer, E. Brunner, *Phys. Rev. A* **2005**, *72*, 053411.

[82] A. Fink, E. Brunner, *Appl. Phys. B* **2007**, *89*, 65–71.

[83] G. M. Schrank, *arXiv preprint arXiv:1911.01574*, **2019**.

[84] G. M. Schrank, *arXiv preprint arXiv:2005.08404*, **2020**.

[85] A. B. Burant, PhD Dissertation, The University of North Carolina at Chapel Hill **2018**, https://doi.org/10.17615/036f-ng45.

[86] M. G. Larson, F. Bengzon, *The Finite Element Method: Theory, Implementation, and Applications*, Springer-Verlag, Berlin, Heidelberg, **2013**.

[87] M. S. Freeman, K. Emami, B. Driehuys, *Phys. Rev. A* **2014**, *90*, 023406.

[88] C. Flower, M. S. Freeman, M. Plue, B. Driehuys, *J. Appl. Phys.* **2017**, *122*, 024902.

[89] N. J. Shah, T. Unlü, H. P. Wegener, H. Halling, K. Zilles, S. Appelt, *NMR Biomed.* **2000**, *13*, 214–219.

[90] J. Skinner, PhD Dissertation, University of Nottingham **2017**, http://eprints.nottingham.ac.uk/41416/.

[91] N. Whiting, P. Nikolaou, N. A. Eschmann, M. J. Barlow, B. M. Goodson, *J. Magn. Reson.* **2011**, *208*, 298–304.

[92] M. Kelley, A. Burant, R. T. Branca, *J. Appl. Phys.* **2020**, *128*, 144901.

[93] M. Kelley, R. T. Branca, *J. Appl. Phys.* **2021**, *129*, 154901.

[94] M. Haake, A. Pines, J. A. Reimer, R. Seydoux, *J. Am. Chem. Soc.* **1997**, *119*, 11711–11712.

[95] R. Seydoux, A. Pines, M. Haake, J. A. Reimer, *J. Phys. Chem. B* **1999**, *103*, 4629–4637.

[96] K. Knagge, J. Prange, D. Raftery, *Chem. Phys. Lett.* **2004**, *397*, 11–16.

[97] T. Su, G. L. Samuelson, S. W. Morgan, G. Laicher, B. Saam, *Appl. Phys. Lett.* **2004**, *85*, 2429–2431.

[98] R. Jiménez-Martínez, D. J. Kennedy, M. Rosenbluh, E. A. Donley, S. Knappe, S. J. Seltzer, H. L. Ring, V. S. Bajaj, J. Kitching, *Nat. Commun.* **2014**, *5*, 3908.

[99] S. R. Schaefer, G. D. Cates, T.-R. Chien, D. Gonatas, W. Happer, T. G. Walker, *Phys. Rev. A* **1989**, *39*, 5613.

[100] Z. L. Ma, E. G. Sorte, B. Saam, *Phys. Rev. Lett.* **2011**, *106*, 193005.

[101] D. J. Kennedy, S. J. Seltzer, R. Jiménez-Martínez, H. L. Ring, N. S. Malecek, S. Knappe, E. A. Donley, J. Kitching, V. S. Bajaj, A. Pines, *Sci. Rep.* **2017**, *7*, 43994.

[102] G. M. Whitesides, *Nature* **2006**, *442*, 368–373.

[103] T. Masayoshi, K. Takayuki, F. Mamoru, K. Hideki, O. Takeshi, U. Masahiko, Y. Masaru, O. Satoshi, F. Kohji, T. Kunihiko, U. Kunihiro, P. D. Jean, P. Giorgio, W. Arlette de, *J. Phys. Conf. Ser.* **2011**, *295*, 012167.

[104] G. Frossati, *J. Low Temp. Phys.* **1998**, *111*, 521–532.

[105] J. D. O'Neill, E. V. Krjukov, J. R. Owers-Bradley, Y. Xia, *J. Low Temp. Phys.* **2007**, *146*, 563–579.

[106] E. V. Krjukov, J. D. O'Neill, J. R. Owers-Bradley, *J. Low Temp. Phys.* **2005**, *140*, 397–408.

[107] J. D. O'Neill, University of Nottingham **2008**.

[108] J. D. O'Neill, E. V. Krjukov, J. R. Owers-Bradley, Y. Xia, *J. Low Temp. Phys.* **2007**, *146*, 563–579.

[109] K. V. Kovtunov, E. V. Pokochueva, O. G. Salnikov, S. Cousin, D. Kurzbach, B. Vuichoud, S. Jannin, E. Y. Chekmenev, B. M. Goodson, D. A. Barskiy, I. V. Koptyug, *Asian J. Chem.* **2018**, *13*, 1857–1871.

[110] U. L. Günther, in *Modern NMR Methodology*, Springer, Berlin, **2011**, pp. 23–69.

[111] P. Nikolaou, B. M. Goodson, E. Y. Chekmenev, *Chem. Eur. J.* **2015**, *21*, 3156–3166.

[112] J. H. Ardenkjaer-Larsen, *J. Magn. Reson.* **2016**, *264*, 3–12.

[113] J. H. Ardenkjaer-Larsen, B. Fridlund, A. Gram, G. Hansson, L. Hansson, M. H. Lerche, R. Servin, M. Thaning, K. Golman, *Proc. Natl. Acad. Sci. USA* **2003**, *100*, 10158–10163.

[114] A. Capozzi, C. Roussel, A. Comment, J. N. Hyacinthe, *J. Phys. Chem. C* **2015**, *119*, 5020–5025.

[115] M. Pourfathi, J. Clapp, S. J. Kadlecek, C. D. Keenan, R. K. Ghosh, N. N. Kuzma, R. R. Rizi, *Magn. Reson. Med.* **2016**, *76*, 1007–1014.

[116] R. Y. Chen, F.-C. Fan, S. Kim, K. M. Jan, S. Usami, S. Chien, *J. Appl. Physiol.* **1980**, *49*, 178–183.

[117] J. E. Roos, H. P. McAdams, S. S. Kaushik, B. Driehuys, *Magn. Reson. Imaging Clin. N. Am.* **2015**, *23*, 217–229.

[118] J. M. Wang, S. H. Robertson, Z. Wang, M. He, R. S. Virgincar, G. M. Schrank, R. M. Smigla, T. G. O'Riordan, J. Sundy, L. Ebner, *Thorax* **2018**, *73*, 21–28.

www.angewandte.org

© 2021 Wiley-VCH GmbH

Angew. Chem. Int. Ed. **2021**, *60*, 2–24

These are not the final page numbers!

[119] A. Bifone, Y. Q. Song, R. Seydoux, R. E. Taylor, B. M. Goodson, T. Pietrass, T. F. Budinger, G. Navon, A. Pines, *Proc. Natl. Acad. Sci. USA* **1996**, *93*, 12932–12936.

[120] Z. Wang, S. H. Robertson, J. Wang, M. He, R. S. Virgincar, G. M. Schrank, E. A. Bier, S. Rajagopal, Y. C. Huang, T. G. O'Riordan, *Med. Phys.* **2017**, *44*, 2415–2428.

[121] Z. I. Cleveland, G. P. Cofer, G. Metz, D. Beaver, J. Nouls, S. S. Kaushik, M. Kraft, J. Wolber, K. T. Kelly, H. P. McAdams, *PloS one* **2010**, *5*, e12192.

[122] J. P. Mugler, T. A. Altes, I. C. Ruset, I. M. Dregely, J. F. Mata, G. W. Miller, S. Ketel, J. Ketel, F. W. Hersman, K. Ruppert, *Proc. Natl. Acad. Sci. USA* **2010**, *107*, 21707–21712.

[123] N. W. Todd, S. P. Atamas, I. G. Luzina, J. R. Galvin, *Expert Rev. Respir. Med.* **2015**, *9*, 411–418.

[124] J. G. Mammarappallil, L. Rankine, H.-F. Chan, N. Weatherley, J. Wild, B. Driehuys, *J. Thorac Imaging* **2019**, *34*, 136.

[125] R. P. Thomen, L. L. Walkup, D. J. Roach, Z. I. Cleveland, J. P. Clancy, J. C. Woods, *J. Cystic Fibrosis* **2017**, *16*, 275–282.

[126] L. L. Walkup, R. P. Thomen, T. G. Akinyi, E. Watters, K. Ruppert, J. P. Clancy, J. C. Woods, Z. I. Cleveland, *Pediatr. Radiol.* **2016**, *46*, 1651–1662.

[127] M. J. Couch, F. Morgado, N. Kanhere, K. Kowalik, J. H. Rayment, F. Ratjen, G. Santyr, *Magn. Reson. Med.* **2020**, *84*, 304–311.

[128] R. P. Thomen, L. L. Walkup, D. J. Roach, N. Higano, A. Schapiro, A. Brody, J. P. Clancy, Z. I. Cleveland, J. C. Woods, *Am. J. Respir. Crit. Care Med.* **2020**, *202*, 290–292.

[129] E. A. Bier, S. H. Robertson, G. M. Schrank, C. Rackley, J. G. Mammarappallil, S. Rajagopal, H. P. McAdams, B. Driehuys, *NMR Biomed.* **2019**, *32*, e4029.

[130] Z. Wang, E. A. Bier, A. Swaminathan, K. Parikh, J. Nouls, M. He, J. G. Mammarappallil, S. Luo, B. Driehuys, S. Rajagopal, *Eur. Respir. J.* **2019**, *54*, 1900831.

[131] P. J. Niedbalski, E. A. Bier, Z. Wang, M. M. Willmering, B. Driehuys, Z. I. Cleveland, *J. Appl. Physiol.* **2020**, *129*, 218–229.

[132] H. Li, X. Zhao, Y. Wang, X. Lou, S. Chen, H. Deng, L. Shi, J. Xie, D. Tang, J. Zhao, L.-S. Bouchard, L. Xia, X. Zhou, *Sci. Adv.* **2021**, *7*, eabc8180.

[133] J. T. Grist, M. Chen, G. J. Collier, B. Raman, G. AbuEid, A. McIntyre, V. Matthews, E. Fraser, L.-P. Ho, J. M. Wild, F. Gleeson, *Radiology* **2021**, https://doi.org/10.1148/radiol.2021210033.

[134] P. J. Niedbalski, *Hyperpolarized 129Xe MRI of Survivors of COVID-19* **2020**, ClinicalTrials.gov Identifier: NCT04659707.

[135] Y. Shepelytskyi, F. T. Hane, V. Grynko, T. Li, A. Hassan, M. S. Albert, *Diagnostics* **2020**, *10*, 630.

[136] M. R. Rao, N. J. Stewart, P. D. Griffiths, G. Norquay, J. M. Wild, *Radiol.* **2018**, *286*, 659–665.

[137] M. R. Rao, G. Norquay, N. Stewart, N. Hoggard, P. Griffiths, J. Wild, *J. Magn. Reson. Imaging* **2019**, *50*, 1002–1004.

[138] F. T. Hane, T. Li, J.-A. Plata, A. Hassan, K. Granberg, M. S. Albert, *Diagnostics* **2018**, *8*, 41.

[139] M. A. Antonacci, C. McHugh, M. Kelley, A. McCallister, S. Degan, R. T. Branca, *Sci. Rep.* **2019**, *9*, 14865.

[140] M. M. Spence, S. M. Rubin, I. E. Dimitrov, E. J. Ruiz, D. E. Wemmer, A. Pines, S. Q. Yao, F. Tian, P. G. Schultz, *Proc. Natl. Acad. Sci. USA* **2001**, *98*, 10654–10657.

[141] T. Brotin, J. P. Dutasta, *Chem. Rev.* **2009**, *109*, 88–130.

[142] J. Lagona, P. Mukhopadhyay, S. Chakrabarti, L. Isaacs, *Angew. Chem. Int. Ed.* **2005**, *44*, 4844–4870; *Angew. Chem.* **2005**, *117*, 4922–4949.

[143] M. G. Shapiro, R. M. Ramirez, L. J. Sperling, G. Sun, J. Sun, A. Pines, D. V. Schaffer, V. S. Bajaj, *Nat. Chem.* **2014**, *6*, 629–634.

[144] L. Schröder, *Phys. Med.* **2013**, *29*, 3–16.

[145] Y. Wang, I. J. Dmochowski, *Acc. Chem. Res.* **2016**, *49*, 2179–2187.

[146] L. Schroder, T. J. Lowery, C. Hilty, D. E. Wemmer, A. Pines, *Science* **2006**, *314*, 446–449.

[147] F. T. Hane, T. Li, P. Smylie, R. M. Pellizzari, J. A. Plata, B. DeBoef, M. S. Albert, *Sci. Rep.* **2017**, *7*, 41027.
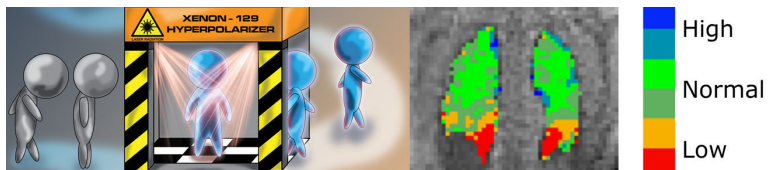
Reviews

Medical Imaging

A. S. Khan, R. L. Harvey, J. R. Birchall,
R. K. Irwin, P. Nikolaou, G. Schrank,
K. Emami, A. Dummer, M. J. Barlow,
B. M. Goodson,
E. Y. Chekmenev* ————— ▮▮▮▮–▮▮▮▮

Enabling Clinical Technologies for
Hyperpolarized ^{129}Xenon Magnetic
Resonance Imaging and Spectroscopy

The use of hyperpolarized ^{129}Xe has the potential to revolutionize clinical imaging, offering a non-ionizing contrast of organ function complementary to that of CT imaging and conventional MRI. In this Review, the physics of spin-exchange optical pumping (SEOP) is discussed, production modalities of hyperpolarized ^{129}Xe are explained, and biomedical applications to lung imaging and beyond are described.

▮▮▮▮
↖↖ These are not the final page numbers!

www.angewandte.org

© 2021 Wiley-VCH GmbH

Angew. Chem. Int. Ed. **2021**, *60*, 2 – 24

Article

Low-Cost High-Pressure Clinical-Scale 50% Parahydrogen Generator Using Liquid Nitrogen at 77 K

Benjamin Chapman, Baptiste Joalland, Collier Meersman, Jessica Ettedgui, Rolf E. Swenson, Murali C. Krishna, Panayiotis Nikolaou, Kirill V. Kovtunov, Oleg G. Salnikov, Igor V. Koptyug, Max E. Gemeinhardt, Boyd M. Goodson, Roman V. Shchepin, and Eduard Y. Chekmenev*

Read Online

ACCESS | Metrics & More | Article Recommendations

ABSTRACT: We report on a robust and low-cost parahydrogen generator design employing liquid nitrogen as a coolant. The core of the generator consists of catalyst-filled spiral copper tubing, which can be pressurized to 35 atm. Parahydrogen fraction >48% was obtained at 77 K with three nearly identical generators using paramagnetic hydrated iron oxide catalysts. Parahydrogen quantification was performed on the fly via benchtop NMR spectroscopy to monitor the signal from residual orthohydrogen—parahydrogen is NMR silent. This real-time quantification approach was also used to evaluate catalyst activation at up to 1.0 standard liter per minute flow rate. The reported inexpensive device can be employed for a wide range of studies employing parahydrogen as a source of nuclear spin hyperpolarization. To this end, we demonstrate the utility of this parahydrogen generator for hyperpolarization of concentrated sodium $[1-^{13}C]$pyruvate, a metabolic contrast agent under investigation in numerous clinical trials. The reported pilot optimization of SABRE-SHEATH (signal amplification by reversible exchange—shield enables alignment transfer to heteronuclei) hyperpolarization yielded ^{13}C signal enhancement of over 14,000-fold at a clinically relevant magnetic field of 1 T corresponding to approximately 1.2% ^{13}C polarization—if near 100% parahydrogen would have been employed, the reported value would be tripled to ^{13}C polarization of 3.5%.
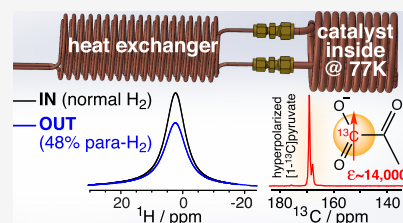
INTRODUCTION

NMR hyperpolarization techniques enhance the detection sensitivity of NMR spectroscopy and imaging by several orders of magnitude.[1−4] These tremendous gains in detection sensitivity enable new applications, including molecular imaging of exogenous contrast agents.[5−7] The nuclear spins of these new contrast agents are hyperpolarized (HP) using a wide range of techniques.[1,8−10] Some hyperpolarization techniques have been successfully employed in clinical trials.[11−14] Despite the major successes in clinical research, none of these methods have enjoyed widespread or routine clinical use so far, in part because of high instrumentation cost and low hyperpolarization throughput.[14]

Parahydrogen-induced polarization (PHIP) is a simple, fast, and low-cost hyperpolarization approach[15,16] that has the potential to revolutionize the production of HP contrast agents for clinical use. Canonical PHIP requires pairwise para-hydrogen (p-H₂) addition to an unsaturated molecular substrate.[17,18] More recently, the nonhydrogenative variant called signal amplification by reversible exchange (SABRE) has emerged:[19,20] the latter method employs chemical exchange of p-H₂ and to-be-hyperpolarized substrates on metal complexes.[21,22] Both PHIP and SABRE approaches have produced a range of HP contrast agents with some validation success in

cellular and preclinical models[23−29] as also described in recent reviews.[10,30,31]

Parahydrogen, employed as the source of nuclear spin order in PHIP,[15,32,33] is produced by transient exposure of normal dihydrogen gas (with its ambient 1:3 para-to-ortho-state distribution) to a low temperature.[26,34−38] Because p-H₂ is a lower energy state, the equilibrium shifts to the para-state at sufficiently low temperatures;[39] nearly 100% p-H₂ can be obtained at ≤20 K.[2,40] When pure p-H₂ is employed for PHIP, near-unity proton polarization can be unlocked after the magnetic equivalence of the nascent p-H₂-derived protons is broken.[15,17,41] Moreover, in both hydrogenative PHIP and its nonhydrogenative variant SABRE, it has been demonstrated that the polarization of nascent p-H₂-derived protons can be transferred via the network of spin−spin couplings to other spin-1/2 nuclei including ^{13}C,[24,42−45] ^{15}N,[46−48] ^1H,[21] ^{31}P,[49] ^{19}F,[50,51] and so forth.[52] Nuclear spin polarization (P) values in
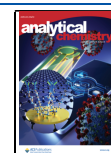
excess of 50% have been demonstrated[53−55] when polarization transfer is optimized using pure p-H_2 gas.

Once one has a supply of p-H_2 in hand, the remaining hardware required to accomplish polarization transfer in PHIP and SABRE is relatively straightforward and low-cost (e.g., approximately $10k for a setup employing a mass-flow controller and mu-metal shields for SABRE[56] or PHIP field cycling studies[57] at micro-tesla fields) because no cryogenic or high-field hardware is required. However, the ostensible need for pure p-H_2 would require the use of cryogenic equipment in the range of $50,000−125,000 (e.g., Bruker or ARS generators),[26,29,34,36,58] representing a substantial investment and a barrier for those working in (or desiring to enter) the field of p-H_2-based hyperpolarization. Moreover, the quantification of the p-H_2 fraction is often required to ensure reproducible results in PHIP and SABRE. In the NMR hyperpolarization community, the measurement is typically performed using high-field NMR spectroscopic quantification of the residual orthohydrogen fraction—because p-H_2 is NMR silent[59]—although other methods have been demonstrated.[60−62] Once created, the p-H_2 gas can then be stored in pressurized aluminum cylinders for weeks.[34,36,63] The requirement of a high-field NMR spectrometer adds additional complexity and cost to the infrastructure for the robust and reproducible operation of a p-H_2-based hyperpolarization facility. As an alternative, we have recently demonstrated that the residual orthohydrogen fraction in near 100% p-H_2 gas can be monitored in real-time using low-field benchtop NMR spectroscopy.[64] Benchtop NMR spectrometers have a substantially lower cost than high-field NMR devices; they are also portable, have a small footprint, require no cryogens to operate, and are increasingly becoming a standard "workhorse" in routine hyperpolarization studies.[65−67]

To mitigate the cost and complexity of cryogenic hardware, p-H_2 production can be conducted at liquid N_2 temperature (ca. 77 K at 1 atm) resulting in an approximately 50% p-H_2 fraction.[38] Moreover, liquid He can also be employed as a chilling source resulting in a 97.5% p-H_2 fraction.[63] The key disadvantage of using 50% (vs near 100%) p-H_2 is the reduction of the resulting hyperpolarization effect by a factor of ∼3. Such substantial polarization decrease can be unforgiving for many signal-to-noise ratio-challenged applications, for example, most notably in vivo studies.[27,68] However, many other applications—including the development phase of PHIP- and SABRE-based contrast agents—can be accomplished with this "lower" p-H_2 grade, which is much easier and cheaper to achieve in practice.[69−71]

Several parahydrogen converter/generator designs employing a wide range of ortho-to-para conversion catalysts have been reported for operation at liquid N_2 temperature.[38,62,71−73] Moreover, very recently, a liquid He-based system has been employed in the production of nearly pure p-H_2 using an inexpensive design ($1,200 in parts),[63] although the design relies on liquid He (which may impose a substantial additional running cost and infrastructure), which requires a ∼90 min cool-down time and has limited production capacity at maximum specs [200 standard cubic centimeters per minute (sccm)].

Here, we report a robust and inexpensive design of a p-H_2 generator for operation with liquid N_2 at a tested pressure of up to 35 atm. The reported design is based on more than 10 years of experience in our laboratories. The produced compressed H_2 gas is quantified by "real-time" NMR

spectroscopy of exiting p-H_2 using a benchtop 1.4 T NMR spectrometer. The design reproducibility has been evaluated with three separately constructed devices. Moreover, we have also investigated ortho−para catalyst activation by catalyst exposure to >100 °C to achieve a production rate of 1,000 sccm with a ∼49% p-H_2 fraction. The utility of the reported device has been tested in the feasibility demonstration of [1-^{13}C]pyruvate hyperpolarization via SABRE, following the work of Duckett and coworkers.[74] HP [1-^{13}C]pyruvate is a leading HP contrast agent employed for tracking metabolism in vivo[7,11,12,14] and is currently being evaluated in many clinical trials and preclinical models of numerous human diseases.[13,14,75] Taken together, the reported design augmented by real-time p-H_2 quantification using benchtop NMR spectroscopy will hopefully be of interest not only to those already working in the field of NMR hyperpolarization in general (and p-H_2-based hyperpolarization in particular) but also to those seeking a low-barrier entryway into NMR hyperpolarization techniques.

■ MATERIALS AND METHODS

Generator Design. The core component employs copper tubing (0.25 in. outer diameter, OD; 0.03 in. wall; 0.19 in. inner diameter, ID, McMaster-Carr, P/N 5174K21; and ∼115 cm length) that was filled with ∼21 g of hydrated iron(III)oxide ($Fe_2O_3 \cdot H_2O$, 371254, Sigma-Aldrich, St. Louis, MO)—this material is produced as Ionex Type OP Catalyst (https://www.molecularproducts.com/products/ionex-type-op-catalyst Molecular Products, Louisville, Colorado, USA). Prior to loading, the catalyst material was purged of microparticles by mechanical filtration via ABN strainer cone funnels with disposable 190 μm mesh https://www.amazon.com/gp/product/B01H7PEHEK/. Each funnel was filled to ∼1/5 of its capacity, and the catalyst was washed with ethanol or isopropanol until the washing liquid passing through it became practically colorless. The alcohol-washed catalyst was further washed with hexane until the washing liquid became colorless as well. The washed catalyst was placed in a glass beaker and dried overnight in an oven at ∼60 °C. If not removed, microparticles can degrade p-H_2 generator performance if they escape downstream of the cryogenic region. The catalyst-filled copper tube was wound into a spiral with a ∼2.36 in. (6 cm) OD consisting of approximately six turns [∼2.75 in. (7 cm) height], Figure 1. The ends of the copper tubing were filled with glass wool to ensure the catalyst remains in the 0.25 in. copper tubing segment. Next, each end of the catalyst-filled 0.25 in. spiral tubing segment was adapted to a heat exchange 0.125 in. OD copper tubing spiral (0.03 in. wall and 0.065 in. OD, McMaster-Carr, P/N 5174K1) using brass Yor-Lok reducers (McMaster-Carr, P/N 5272K214). The two hollow spirals (∼20 turns of similar diameter) made of 0.125 in. copper tubing are designed to serve two purposes. The 0.125 in. copper tubing spiral is reinforced by aluminum brackets (Figure 1) to enhance structural rigidity. In case the liquid N_2 level is above the heat exchangers, the inlet heat exchanger allows for precooling of the incoming H_2 gas. Alternatively, if the liquid N_2 level is below the heat exchangers, heat exchange between incoming and exiting hydrogen gas flows allows for precooling of the incoming H_2 gas while warming exiting para-enriched H_2, as shown in Figure 1.

Experimental Setup for "Real-Time" Benchtop NMR Spectroscopy of Hydrogen Gas. To monitor the p-H_2
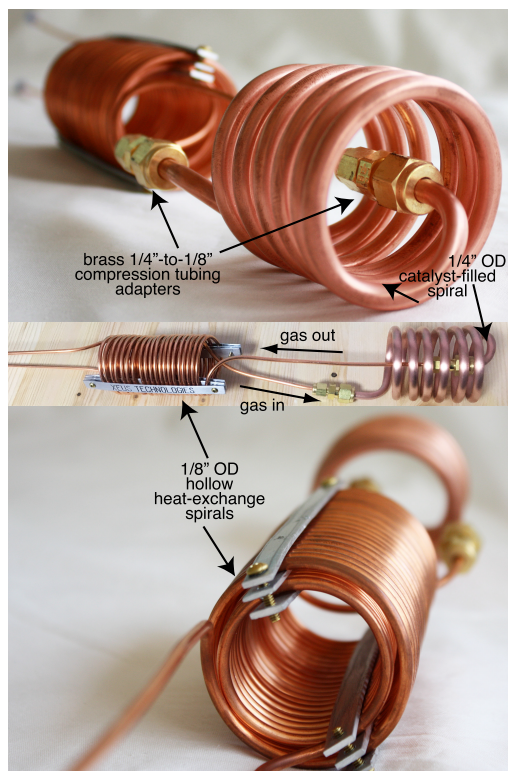
Figure 1. Annotated photographs of the p-H_2 generator device core, outlining the orientations and interfaces of key components.

enrichment on the fly, we have employed the setup described previously,[64] which was adapted for operation with the present generator, as shown in Figure 2. A high-pressure tank equipped
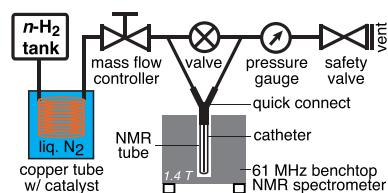

Figure 2. Experimental setup schematic employed for p-H_2 quantification studies using real-time benchtop 1.4 T NMR spectroscopy. The safety valve allows for 100 PSI overpressure, and the normal hydrogen (n-H_2) pressure of the main hydrogen tank was set to 125 PSI. Switching the valve to the "OFF" position directs hydrogen gas to an NMR tube via a 0.065 in. OD Teflon catheter.

with a dual-stage pressure regulator and containing ultrahigh-purity (>99.999%) hydrogen was connected to the input port of the generator using a Yor-Lok brass coupling. The other end of the generator was connected directly to the input of a mass flow controller (MFC; Sierra Instruments Inc., Monterey, California, USA, P/N C100L-DD-1-OV1-SV1-PV2-V1-S0, 1000 sccm model). The hydrogen tank pressure was set to ~125 PSI. The flexible 0.125 in. copper lines allow for easy maneuvering of the generator core to insert into/remove from the liquid N_2 bath (in a Styrofoam container) or exposing the catalyst-filled section to a heat gun for catalyst activation studies (see below). Parahydrogen quantification was performed using a 1.4 T NMR spectrometer operating at 61 MHz

proton resonance frequency with gas samples at 8 atm (100 PSI overpressure) employing the following acquisition parameters: 1024 scans, 5 kHz spectral width, 52 ms acquisition time, 0.1 s repetition time, ~102 s total acquisition time, and 90° excitation pulse of ~10 μs duration.

Parahydrogen Quantification. Parahydrogen quantification was performed using the previously described method,[64] which was adapted for operation with the described generator. Briefly, on the day of the operation, the setup (Figure 2) was first operated at room temperature, that is, without a liquid N_2 bath. The MFC flow rate was set to 150 sccm, and the safety valve was set to 100 PSI overpressure (as confirmed by the pressure gauge, Figure 2). The valve was placed in the "OFF" position, and normal hydrogen was allowed to pass through the catheter and run through a standard 5 mm NMR tube equipped with a "Y" connector for 10 min. This "purge" stage was required to remove any residual air and moisture from the setup and to fill the NMR tube to 100 PSI overpressure with normal H_2 gas (containing 75% o-H_2).

Next, the valve is switched to the "ON" position and the gas flow is directed via bypass rather than through the NMR tube. As a result, normal hydrogen (25% para-H_2 and 75% ortho-H_2) in the tube was not flowing during NMR acquisition (instead, the flow was directed via bypass). Next, an NMR spectrum of normal H_2 gas was acquired using the acquisition parameters listed above. The signal (integrated area under the curve, AUC) was computed using SpinSolve Expert software supplied by the vendor (Magritek, New Zealand). The corresponding signal from an empty NMR tube was also acquired and subtracted from each NMR measurement to account for any background signal using the same spectral processing parameters.

The generator's catalyst-filled spiral was then submerged into a liquid N_2 bath and allowed to equilibrate at cryogenic temperature for 10 min with a continuous H_2 flow at 150 sccm. The valve was switched to the "OFF" position to direct the gas flow through the NMR tube for ~2 min. Next, the valve is switched "ON". As a result, para-enriched hydrogen in the tube was not flowing during NMR acquisition (instead, the flow was directed via bypass). Next, an NMR spectrum of the para-enriched H_2 gas was acquired using the acquisition parameters listed in the caption of Figure 3. The NMR signal was processed in the same fashion as for normal H_2 as described
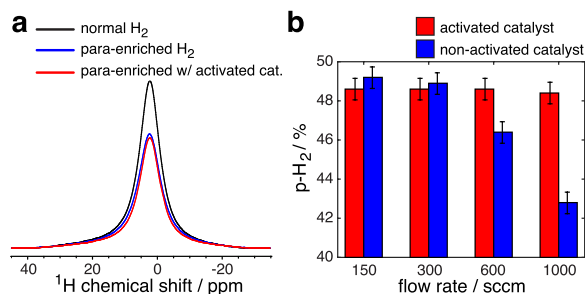

Figure 3. (a) Parahydrogen quantification using a 1.4 T NMR spectrometer operating at 61 MHz proton resonance frequency using gas samples at 8 atm (100 PSI overpressure). Acquisition parameters: 1024 scans, 5 kHz spectral width, 52 ms acquisition time, 0.1 s repetition time, ~102 s total acquisition time, and 90° excitation pulse (~10 μs long). (b) Dependence of the p-H_2 fraction on the flow rate for the activated and nonactivated catalyst.

above. All measurements for the p-H$_2$-enriched and normal H$_2$ gas were repeated three times and averaged. The p-H$_2$ fraction (f) was computed using eq 1

$$f = 1 - \frac{3 \times S_{\text{enriched}}}{4 \times S_{\text{normal}}} \tag{1}$$

where S_{enriched} and S_{normal} are the corresponding NMR signals for p-H$_2$-enriched and normal (i.e., nonenriched) hydrogen gas samples, respectively. Note that multipliers 3 and 4 are used to reflect 75% o-H$_2$ in normal (unenriched) H$_2$ gas.[30] Three p-H$_2$ generators were tested for test-retest reproducibility.

Catalyst Activation. Catalyst activation was performed by heating the catalyst-containing spiral using a heat gun to >100 °C for ~15 min under a continuous 150 sccm flow of H$_2$ gas.

^{13}C SABRE Hyperpolarization of [1-^{13}C]pyruvate. ^{13}C SABRE hyperpolarization of [1-^{13}C]pyruvate was performed using SABRE in SHield enables alignment transfer to heteronuclei (SABRE−SHEATH)[47,48] tailored for the ^{13}C nucleus[45,76] using the DMSO-coligand approach developed by Duckett and coworkers.[74] Sodium [1-^{13}C]-pyruvate and deuterated methanol-d_4 solvent were purchased from Sigma-Aldrich and used without any further purification. The [IrCl(COD)(IMes)] SABRE catalyst precursor was synthesized according to a literature procedure.[21] The sample was prepared with a fixed ratio of substrate to Ir-IMes SABRE precatalyst and DMSO in 0.6 mL of methanol-d_4 in a 5 mm NMR tube with a typical ratio of substrate, catalyst (12 mM), and DMSO as 7:1:10. Ultrahigh-purity H$_2$ gas (Airgas) was fed into a p-H$_2$ generator and enriched to about 50% para-fraction using liquid N$_2$ as described above. The p-H$_2$ flow is directed via Polytetrafluoroethylene (PTFE) tubing using the MFC (Sierra Instruments SmartTrak 100 series) set at 80 sccm flow rate and directed to a conventional 5 mm NMR tube (Norell) to allow for p-H$_2$ bubbling through the sample. The entire p-H$_2$ line was pressurized to 40 PSI overpressure unless otherwise noted. SABRE−SHEATH requires the use of microtesla or submicrotesla magnetic fields to enable efficient polarization transfer from p-H$_2$-derived hydrides to heteronuclei (e.g., ^{13}C targeted here). In practice, these fields are achieved by attenuating the Earth's magnetic field and creating a minute magnetic field inside the shield using electromagnets. Here, magnetic fields near or below ~1 μT were achieved with a home-built apparatus consisting of a solenoid coil placed inside a mu-metal shield (Magnetic Shield Corporation, model no. ZG-206). This solenoid is 41 mm in diameter: 40 mm core, 20 cm long windings with 220 turns of AWG20 (0.9 mm) Cu wire and with 220 Ω resistor in series. The solenoid coil was driven by commercial 1.5 V batteries with a variable resistance decade box in series to provide finer control of the internal magnetic field of the shield, which is monitored using a Lakeshore Cryotronics Gaussmeter (model no. 475 DSP with HMMA-2512-VR Hall probe). NMR experiments were performed using a 1 T Magritek Spinsolve benchtop NMR spectrometer. All ^{13}C NMR spectra were taken without ^{1}H decoupling throughout the duration of the experiment. The time required to manually transfer the sample from the shield region to the magnet for low-field NMR acquisition was usually <5 s. The ^{13}C signal enhancement was computed by comparing the HP signal AUC to the external ^{13}C signal thermal signal reference (4 M sodium [1-^{13}C]acetate) using eq 2

$$\varepsilon(^{13}\text{C}) = \frac{S_{\text{HP}}}{S_{\text{REF}}} \cdot \frac{C_{\text{REF}}}{C_{\text{HP}}} \cdot \frac{A_{\text{REF}}}{A_{\text{HP}}} \tag{2}$$

where S_{HP} and S_{REF} are ^{13}C signals from HP [1-^{13}C]pyruvate and thermal signal reference [1-^{13}C]acetate, respectively, C_{REF} and C_{HP} are concentrations of thermal signal reference [1-^{13}C]acetate (4 M) and HP [1-^{13}C]pyruvate, respectively, and A_{REF} and A_{HP} are effective cross sections of the NMR tubes for thermal signal reference [1-^{13}C]acetate and HP [1-^{13}C]pyruvate samples, respectively.

■ RESULTS AND DISCUSSION

Parahydrogen Enrichment. Three identical copies of the generator were employed for quality assurance prior to catalyst activation. Under conditions of liquid N$_2$ and 150 sccm p-H$_2$ flow rate, the benchtop NMR quantification yielded the following p-H$_2$ enrichment fractions: 48.4 ± 0.5, 48.1 ± 0.5, and 48.2 ± 0.5%, demonstrating the robustness of the design in the context of reproducible generator construction. A representative NMR quantification of the p-H$_2$ fraction at 150 sccm flow rate is shown in Figure 3a. The remaining p-H$_2$ quantification studies were performed with one of the three devices. The flow rate was then varied from 150 to 1000 sccm (Figure 3b, blue bars) clearly demonstrating the reduction of the p-H$_2$ fraction with increased flow rate. This finding is rationalized as follows: the nonactivated catalyst has some potency for ortho ↔ para conversion, which is sufficient for slow-flowing H$_2$ gas. When the flow rate is fast (i.e., 1000 sccm), the slow ortho ↔ para conversion rate is no longer sufficient to allow the system to reach an equilibrium conversion while the gas moves along the catalyst-filled copper spiral, thus yielding a lower than expected p-H$_2$ fraction.

Catalyst Activation by Heating under H$_2$ Atmosphere. After catalyst activation in the copper spiral as described above, the performance of the same generator was evaluated at various flow rates (Figure 3b, red bars). The results clearly indicate that catalyst activation is indeed important in order to maximize the ortho ↔ para conversion, allowing the system to achieve full conversion at high flow rates up to 1,000 sccm. Although higher hydrogen flow rates were not tested due to limitations of the MFC, we expect the generator to perform well at substantially higher flow rates of at least 4000 sccm. Our expectation is based on the performance of a recently published cryogenic design, which employs catalyst-filled copper tubing filled with half the quantity of the catalyst (10 g vs 21 g employed here) in smaller ID/OD copper tubing.[64] This recently published design performed well at flow rates of up to 4000 sccm.[64]

Utility of the Parahydrogen Generator for ^{13}C SABRE−SHEATH Hyperpolarization. Hyperpolarization of [1-^{13}C]pyruvate was evaluated using another copy of the generator at a different site. It was employed for SABRE hyperpolarization studies of [1-^{13}C]pyruvate using SABRE−SHEATH. The simultaneous exchange of p-H$_2$ and [1-^{13}C]-pyruvate on the activated Ir-IMes catalyst leads to a buildup of ^{13}C hyperpolarization, as shown in Figure 4a. Figure 4b shows a representative spectrum of ^{13}C-hyperpolarized [1-^{13}C]-pyruvate with signal enhancement ε of over 14,000-fold, corresponding to P_{13C} of 1.2% obtained via comparison of the NMR signal intensity with a reference sample, as shown in Figure 4c.

If near 100% p-H$_2$ would have been employed, P_{13C} would be tripled to P_{13C} = 3.5%.[30] We note that P_{13C} strongly
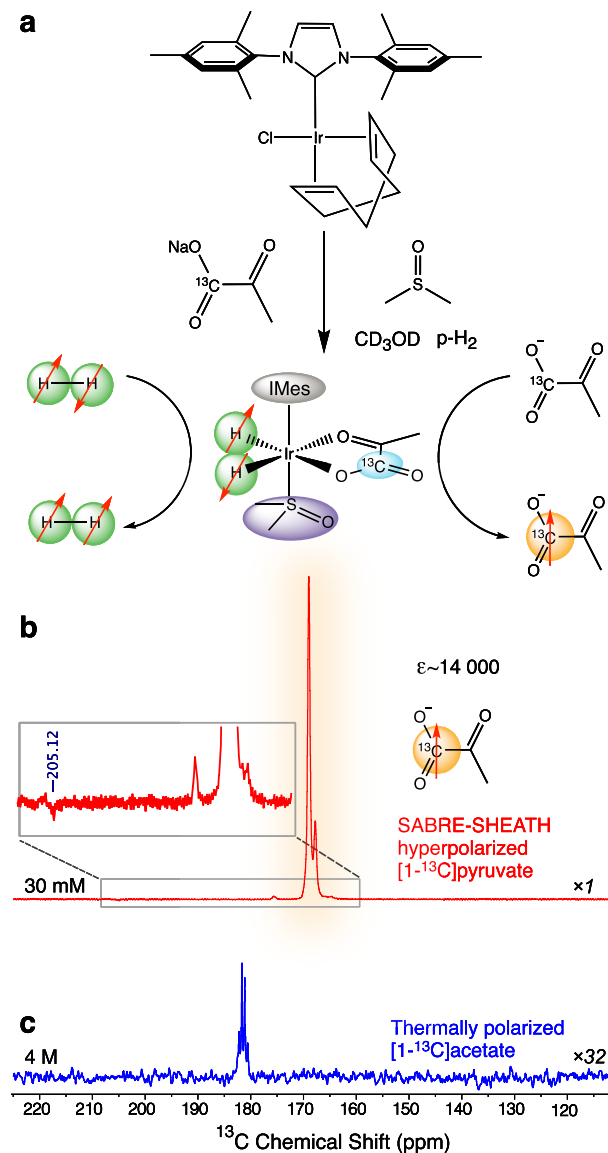
Figure 4. (a) Schematic of the catalytic system for SABRE−SHEATH hyperpolarization. The activated Ir complex catalyst, $[\text{Ir}(\text{H}_2)(\eta^2\text{-pyruvate})(\text{DMSO})(\text{IMes})]$, transfers magnetization from p-H$_2$ to $[1\text{-}^{13}\text{C}]$pyruvate through a J-coupled spin network. Both p-H$_2$ and pyruvate have weak, transient binding to the iridium complex. (b) Single-scan HP ^{13}C spectrum selected from SABRE−SHEATH experiments; enhancement $\varepsilon \approx 14{,}000$. Sample: 30 mM sodium $[1\text{-}^{13}\text{C}]$pyruvate, 20 mM DMSO, and 7.8 mM Ir-IMes catalyst in methanol-d_4; the spectrum was acquired immediately following manual sample transfer to 1 T after 55 s p-H$_2$ bubbling at $B_T = -0.7\ \mu\text{T}$. The inset of (b) shows a close-up of the ^{13}C spectrum. (c) Single-scan thermally polarized ^{13}C signal from 4 M sodium $[1\text{-}^{13}\text{C}]$acetate using similar acquisition parameters. All experiments were performed with p-H$_2$ (∼50% para-) at 1.0 T and overpressure (Magritek SpinSolve ^{13}C).

advancement for HP $[1\text{-}^{13}\text{C}]$pyruvate production via the SABRE−SHEATH technique.

The pilot optimization of ^{13}C SABRE−SHEATH conditions reveal ^{13}C signal dependence on the microtesla magnetic field (Figure 5a), temperature (Figure 5b), polarization buildup
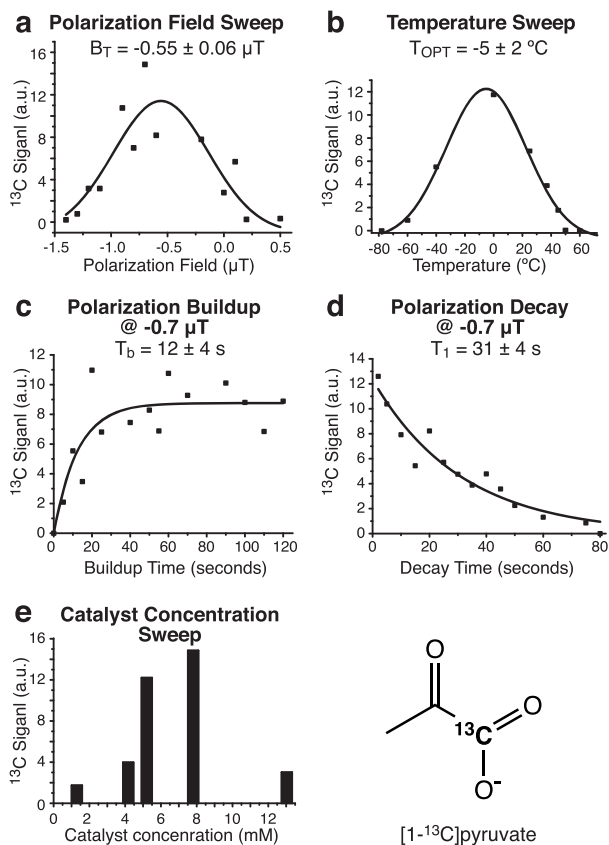

Figure 5. Pilot optimization of SABRE−SHEATH hyperpolarization of $[1\text{-}^{13}\text{C}]$pyruvate: (a) magnetic field sweep of a sample of $[\text{Ir(COD)(IMes)}]$ (13 mM) with sodium $[1\text{-}^{13}\text{C}]$pyruvate (90 mM) and DMSO (120 mM) in 0.6 mL of methanol-d_4 at room temperature; (b) temperature sweep of a sample of $[\text{Ir(COD)-(IMes)}]$ (7.8 mM) with sodium $[1\text{-}^{13}\text{C}]$pyruvate (30 mM) and DMSO (20 mM) in 0.6 mL of methanol-d_4 at $B_T = -0.7\ \mu\text{T}$; (c) p-H$_2$ bubbling duration sweep using a sample of $[\text{Ir(COD)(IMes)}]$ (7.8 mM) with sodium $[1\text{-}^{13}\text{C}]$pyruvate (30 mM) and DMSO (20 mM) in 0.6 mL of methanol-d_4 at $B_T = -0.7\ \mu\text{T}$; (d) in-shield ^{13}C T_1 signal decay using a sample of $[\text{Ir(COD)(IMes)}]$ (7.8 mM) with sodium $[1\text{-}^{13}\text{C}]$pyruvate (30 mM) and DMSO (20 mM) in 0.6 mL of methanol-d_4 at $B_T = -0.7\ \mu\text{T}$; and (e) SABRE catalyst concentration sweep using samples of 30 mM sodium $[1\text{-}^{13}\text{C}]$pyruvate and 20 mM DMSO in 0.6 mL of methanol-d_4 at $B_T = -0.7\ \mu\text{T}$. All experiments were performed with 100 PSI p-H$_2$ (∼50% para-) overpressure at ∼100 sccm flow rate at 1.0 T (Magritek SpinSolve ^{13}C).

time (i.e., the duration of p-H$_2$ bubbling, Figure 5c), and catalyst concentration (Figure 5e). The ^{13}C T_1 in-shield relaxation value of 31 ± 4 s at [catalyst] = 7.8 mM is substantially longer than ^{15}N T_1 of ca. 12−15 s of $[^{15}\text{N}_3]$metronidazole at [catalyst]∼2 mM[78] despite the fact that the ^{13}C gyromagnetic ratio is 2.5 times greater than that of the ^{15}N one; and therefore, the ^{13}C spin would be more prone to the catalyst-induced relaxation. We rationalize this observation by the greater distance of the ^{13}C1 nucleus from

depends on the experimental conditions. To the best of our knowledge, the extrapolated P_{13C} value reported here exceeds the highest reported value (P_{13C} of 1.0% for $[1\text{-}^{13}\text{C}]$pyruvate and P_{13C} of 1.85% for $[1,2\text{-}^{13}\text{C}]$pyruvate[74,77] by threefold and nearly twofold respectively), representing a substantial

Ir due to the presence of bridging oxygen (i.e., Ir−O=^{13}C) *versus* direct Ir interaction with the ^{15}N nucleus (i.e., Ir−^{15}N). This observation is important because longer in-shield ^{13}C T_1 at the microtesla magnetic field effectively results in greater P_{13C}.[78]

We envision that additional future improvements for ^{13}C pyruvate polarization can be made through the increase of p-H$_2$ pressure and flow rate[79] and the use of recently reported hardware for more precise calibration of the in-shield nanotesla magnetic field.[80]

The reported results clearly demonstrate the utility of our generator to produce a HP state that can be easily detectable, even when using a benchtop NMR spectrometer operating at 1 T. We note that although [1-^{13}C]-labeled pyruvate was employed, the resonance at 205 ppm corresponds to the natural ^{13}C abundance signal from ^{13}C2 locked in a singlet state with ^{13}C1.[77] Thus, we anticipate that our generator can enable a wide range of p-H$_2$-based hyperpolarization studies in the context of development, optimization, and quality assurance of HP ^{13}C compounds and biocompatible contrast agents even at the natural abundance ^{13}C level. We also anticipate that other nuclei (^{15}N, ^{19}F, ^{1}H, etc.) can also be readily studied using our low-cost and easy-to-maintain p-H$_2$ generator in combination with a benchtop NMR spectrometer. Such a combination should provide a straightforward gateway for HP studies with p-H$_2$ for a wide range of laboratories.

CONCLUSIONS

In summary, we report a robust design of a p-H$_2$ generator developed for operation at liquid N$_2$ temperature based on many years of experience in our laboratories. We employed near real-time benchtop NMR spectroscopy for quantification of the p-H$_2$ fraction, indicating p-H$_2$ enrichment of ∼48% (three separately constructed devices) at flow rates of up to 1000 sccm; moreover, it is expected that flow rates of up to 4000 sccm should be attainable without performance loss. Catalyst activation by heat under the H$_2$ atmosphere was shown to be important for efficient operation at high flow rates. The utility of the generator has been investigated for SABRE−SHEATH ^{13}C-hyperpolarization of [1-^{13}C]pyruvate, the leading metabolic ^{13}C contrast agent under investigation in clinical trials. Despite the low p-H$_2$ fraction resulting in ∼threefold signal reduction (*vs* near 100% p-H$_2$), it was possible to successfully hyperpolarize [1-^{13}C]pyruvate for detection using a 1 T benchtop NMR spectrometer ($\varepsilon \approx$ 14,000, $P_{13C} \approx$ 1.2%). We anticipate that the reported generator design will be useful for those working on the development of p-H$_2$-based hyperpolarization technologies (e.g., PHIP and SABRE), and particularly those working on developing new biocompatible compounds that can be employed as exogenous HP contrast agents. Taken together, the combination of the described p-H$_2$ generator and a benchtop NMR spectrometer embodies a low-cost and robust gateway to the field of p-H$_2$ hyperpolarization without substantial investment in complex infrastructure. Although on-demand p-H$_2$ production for utility in SABRE hyperpolarization was demonstrated here, the produced p-H$_2$ gas can also be stored in an aluminum tank for weeks because p-H$_2$ back conversion to normal hydrogen is slow.[36,64]

AUTHOR INFORMATION

Corresponding Author

Eduard Y. Chekmenev − *Department of Chemistry, Integrative Biosciences (Ibio), Wayne State University, Karmanos Cancer Institute (KCI), Detroit, Michigan 48202, United States; Russian Academy of Sciences, Moscow 119991, Russia;* orcid.org/0000-0002-8745-8801; Email: chekmenevlab@gmail.com

Authors

Benjamin Chapman − *Department of Materials and Metallurgical Engineering, South Dakota School of Mines and Technology, Rapid City, South Dakota 57701, United States;* orcid.org/0000-0002-8173-2195

Baptiste Joalland − *Department of Chemistry, Integrative Biosciences (Ibio), Wayne State University, Karmanos Cancer Institute (KCI), Detroit, Michigan 48202, United States;* orcid.org/0000-0003-4116-6122

Collier Meersman − *Department of Chemistry, Biology, and Health Sciences, South Dakota School of Mines and Technology, Rapid City, South Dakota 57701, United States*

Jessica Ettedgui − *Chemistry and Synthesis Center, National Heart, Lung, and Blood Institute, Bethesda, Maryland 20850, United States*

Rolf E. Swenson − *Chemistry and Synthesis Center, National Heart, Lung, and Blood Institute, Bethesda, Maryland 20850, United States*

Murali C. Krishna − *Center for Cancer Research, National Cancer Institute, National Institutes of Health, Bethesda, Maryland 20814, United States*

Panayiotis Nikolaou − *XeUS Technologies Limited, Lakatamia 2312, Nicosia, Cyprus;* orcid.org/0000-0002-3802-0803

Kirill V. Kovtunov − *International Tomography Center, SB RAS, Novosibirsk 630090, Russia; Novosibirsk State University, Novosibirsk 630090, Russia;* orcid.org/0000-0001-7577-9619

Oleg G. Salnikov − *International Tomography Center, SB RAS, Novosibirsk 630090, Russia; Novosibirsk State University, Novosibirsk 630090, Russia; Boreskov Institute of Catalysis SB RAS, Novosibirsk 630090, Russia;* orcid.org/0000-0003-2266-7335

Igor V. Koptyug − *International Tomography Center, SB RAS, Novosibirsk 630090, Russia;* orcid.org/0000-0003-3480-7649

Max E. Gemeinhardt − *Department of Chemistry and Biochemistry, Southern Illinois University, Carbondale, Illinois 62901, United States*

Boyd M. Goodson − *Department of Chemistry and Biochemistry and Materials Technology Center, Southern Illinois University, Carbondale, Illinois 62901, United States;* orcid.org/0000-0001-6079-5077

Roman V. Shchepin − *Department of Chemistry, Biology, and Health Sciences, South Dakota School of Mines and Technology, Rapid City, South Dakota 57701, United States;* orcid.org/0000-0001-9135-3036

Complete contact information is available at:
https://pubs.acs.org/10.1021/acs.analchem.1c00716

Notes

The authors declare the following competing financial interest(s): EYC, PN, and BMG declare a stake of ownership in XeUS Technologies, LTD.

■ REFERENCES

(1) Nikolaou, P.; Goodson, B. M.; Chekmenev, E. Y. *Chem.—Eur. J.* **2015**, *21*, 3156−3166.

(2) Goodson, B. M.; Whiting, N.; Coffey, A. M.; Nikolaou, P.; Shi, F.; Gust, B. M.; Gemeinhardt, M. E.; Shchepin, R. V.; Skinner, J. G.; Birchall, J. R.; Barlow, M. J.; Chekmenev, E. Y. *Emagres* **2015**, *4*, 797−810.

(3) Ardenkjaer-Larsen, J. H.; Fridlund, B.; Gram, A.; Hansson, G.; Hansson, L.; Lerche, M. H.; Servin, R.; Thaning, M.; Golman, K. *Proc. Natl. Acad. Sci. U.S.A.* **2003**, *100*, 10158−10163.

(4) Ardenkjaer-Larsen, J. H. *J. Magn. Reson.* **2016**, *264*, 3−12.

(5) Golman, K.; Axelsson, O.; Jóhannesson, H.; Månsson, S.; Olofsson, C.; Petersson, J. S. *Magn. Reson. Med.* **2001**, *46*, 1−5.

(6) Golman, K.; Ardenkjaer-Larsen, J. H.; Petersson, J. S.; Månsson, S.; Leunbach, I. *Proc. Natl. Acad. Sci. U.S.A.* **2003**, *100*, 10435−10439.

(7) Golman, K.; in 't Zandt, R.; Thaning, M. *Proc. Natl. Acad. Sci. U.S.A.* **2006**, *103*, 11270−11275.

(8) Mugler, J. P.; Altes, T. A. *J. Magn. Reson. Imag.* **2013**, *37*, 313−331.

(9) Kovtunov, K. V.; Pokochueva, E. V.; Salnikov, O. G.; Cousin, S. F.; Kurzbach, D.; Vuichoud, B.; Jannin, S.; Chekmenev, E. Y.; Goodson, B. M.; Barskiy, D. A.; Koptyug, I. V. *Chem.−Asian J.* **2018**, *13*, 1857−1871.

(10) Rayner, P. J.; Duckett, S. B. *Angew. Chem., Int. Ed.* **2018**, *57*, 6742−6753.

(11) Brindle, K. M. *J. Am. Chem. Soc.* **2015**, *137*, 6418−6427.

(12) Kurhanewicz, J.; Vigneron, D. B.; Brindle, K.; Chekmenev, E. Y.; Comment, A.; Cunningham, C. H.; DeBerardinis, R. J.; Green, G. G.; Leach, M. O.; Rajan, S. S.; Rizi, R. R.; Ross, B. D.; Warren, W. S.; Malloy, C. R. *Neoplasia* **2011**, *13*, 81−97.

(13) Nelson, S. J.; Kurhanewicz, J.; Vigneron, D. B.; Larson, P. E. Z.; Harzstark, A. L.; Ferrone, M.; van Criekinge, M.; Chang, J. W.; Bok, R.; Park, I.; Reed, G.; Carvajal, L.; Small, E. J.; Munster, P.; Weinberg, V. K.; Ardenkjaer-Larsen, J. H.; Chen, A. P.; Hurd, R. E.; Odegardstuen, L.-I.; Robb, F. J.; Tropp, J.; Murray, J. A. *Sci. Transl. Med.* **2013**, *5*, 198ra108.

(14) Kurhanewicz, J.; Vigneron, D. B.; Ardenkjaer-Larsen, J. H.; Bankson, J. A.; Brindle, K.; Cunningham, C. H.; Gallagher, F. A.; Keshari, K. R.; Kjaer, A.; Laustsen, C.; Mankoff, D. A.; Merritt, M. E.; Nelson, S. J.; Pauly, J. M.; Lee, P.; Ronen, S.; Tyler, D. J.; Rajan, S. S.; Spielman, D. M.; Wald, L.; Zhang, X.; Malloy, C. R.; Rizi, R. *Neoplasia* **2019**, *21*, 1−16.

(15) Bowers, C. R.; Weitekamp, D. P. *Phys. Rev. Lett.* **1986**, *57*, 2645−2648.

(16) Eisenschmid, T. C.; Kirss, R. U.; Deutsch, P. P.; Hommeltoft, S. I.; Eisenberg, R.; Bargon, J.; Lawler, R. G.; Balch, A. L. *J. Am. Chem. Soc.* **1987**, *109*, 8089−8091.

(17) Bowers, C. R.; Weitekamp, D. P. *J. Am. Chem. Soc.* **1987**, *109*, 5541−5542.

(18) Koptyug, I. V.; Kovtunov, K. V.; Burt, S. R.; Anwar, M. S.; Hilty, C.; Han, S.-I.; Pines, A.; Sagdeev, R. Z. *J. Am. Chem. Soc.* **2007**, *129*, 5580−5586.

(19) Adams, R. W.; Aguilar, J. A.; Atkinson, K. D.; Cowley, M. J.; Elliott, P. I. P.; Duckett, S. B.; Green, G. G. R.; Khazal, I. G.; Lopez-Serrano, J.; Williamson, D. C. *Science* **2009**, *323*, 1708−1711.

(20) Adams, R. W.; Duckett, S. B.; Green, R. A.; Williamson, D. C.; Green, G. G. R. *J. Chem. Phys.* **2009**, *131*, 194505.

(21) Cowley, M. J.; Adams, R. W.; Atkinson, K. D.; Cockett, M. C. R.; Duckett, S. B.; Green, G. G. R.; Lohman, J. A. B.; Kerssebaum, R.; Kilgour, D.; Mewis, R. E. *J. Am. Chem. Soc.* **2011**, *133*, 6134−6137.

(22) Muhammad, S. R.; Greer, R. B.; Ramirez, S. B.; Goodson, B. M.; Fout, A. R. *ACS Catal.* **2021**, *11*, 2011−2020.

(23) Goldman, M.; Jóhannesson, H.; Axelsson, O.; Karlsson, M. *Magn. Reson. Imag.* **2005**, *23*, 153−157.

(24) Goldman, M.; Johannesson, H.; Axelsson, O.; Karlsson, M. *Compt. Rendus Chem.* **2006**, *9*, 357−363.

(25) Bhattacharya, P.; Chekmenev, E. Y.; Perman, W. H.; Harris, K. C.; Lin, A. P.; Norton, V. A.; Tan, C. T.; Ross, B. D.; Weitekamp, D. P. *J. Magn. Reson.* **2007**, *186*, 150−155.

(26) Hövener, J.-B.; Chekmenev, E. Y.; Harris, K. C.; Perman, W. H.; Robertson, L. W.; Ross, B. D.; Bhattacharya, P. *Magn. Reson. Mater. Phys., Biol. Med.* **2009**, *22*, 111−121.

(27) Bhattacharya, P.; Chekmenev, E. Y.; Reynolds, W. F.; Wagner, S.; Zacharias, N.; Chan, H. R.; Bünger, R.; Ross, B. D. *NMR Biomed.* **2011**, *24*, 1023−1028.

(28) Perman, W. H.; Bhattacharya, P.; Leupold, J.; Lin, A. P.; Harris, K. C.; Norton, V. A.; Hoevener, J.-B.; Ross, B. D. *Magn. Reson. Imag.* **2010**, *28*, 459−465.

(29) Kadlecek, S.; Vahdat, V.; Nakayama, T.; Ng, D.; Emami, K.; Rizi, R. *NMR Biomed.* **2011**, *24*, 933−942.

(30) Hövener, J.-B.; Pravdivtsev, A. N.; Kidd, B.; Bowers, C. R.; Glöggler, S.; Kovtunov, K. V.; Plaumann, M.; Katz-Brull, R.; Buckenmaier, K.; Jerschow, A.; Reineri, F.; Theis, T.; Shchepin, R. V.; Wagner, S.; Bhattacharya, P.; Zacharias, N. M.; Chekmenev, E. Y. *Angew. Chem., Int. Ed.* **2018**, *57*, 11140−11162.

(31) Kovtunov, K. V.; Koptyug, I. V.; Fekete, M.; Duckett, S. B.; Theis, T.; Joalland, B.; Chekmenev, E. Y. *Angew. Chem., Int. Ed.* **2020**, *59*, 17788−17797.

(32) Green, R. A.; Adams, R. W.; Duckett, S. B.; Mewis, R. E.; Williamson, D. C.; Green, G. G. R. *Prog. Nucl. Magn. Reson. Spectrosc.* **2012**, *67*, 1−48.

(33) Kovtunov, K. V.; Zhivonitko, V. V.; Skovpin, I. V.; Barskiy, D. A.; Koptyug, I. V. *Top. Curr. Chem.* **2013**, *338*, 123−180.

(34) Hövener, J.-B.; Bär, S.; Leupold, J.; Jenne, K.; Leibfritz, D.; Hennig, J.; Duckett, S. B.; von Elverfeldt, D. *NMR Biomed.* **2013**, *26*, 124−131.

(35) Tom, B. A.; Bhasker, S.; Miyamoto, Y.; Momose, T.; McCall, B. J. *Rev. Sci. Instrum.* **2009**, *80*, 016108.

(36) Feng, B.; Coffey, A. M.; Colon, R. D.; Chekmenev, E. Y.; Waddell, K. W. *J. Magn. Reson.* **2012**, *214*, 258−262.

(37) Birchall, J. R.; Coffey, A. M.; Goodson, B. M.; Chekmenev, E. Y. *Anal. Chem.* **2020**, *92*, 15280−15284.

(38) Gamliel, A.; Allouche-Arnon, H.; Nalbandian, R.; Barzilay, C. M.; Gomori, J. M.; Katz-Brull, R. *Appl. Magn. Reson.* **2010**, *39*, 329−345.

(39) Farkas, A. *Orthohydrogen, Parahydrogen, and Heavy Hydrogen*; Cambridge University Press: Cambridge, 1935.

(40) Bowers, C. R. Sensitivity Enhancement Utilizing Parahydrogen. *eMagRes*; John Wiley & Sons, Ltd, 2007.

(41) Goldman, M.; Johannesson, H. *Compt. Rendus Chem.* **2005**, *6*, 575−581.

(42) Kadlecek, S.; Emami, K.; Ishii, M.; Rizi, R. *J. Magn. Reson.* **2010**, *205*, 9−13.

(43) Bär, S.; Lange, T.; Leibfritz, D.; Hennig, J.; von Elverfeldt, D.; Hoevener, J.-B. *J. Magn. Reson.* **2012**, *225*, 25−35.

(44) Cai, C.; Coffey, A. M.; Shchepin, R. V.; Chekmenev, E. Y.; Waddell, K. W. *J. Phys. Chem. B* **2013**, *117*, 1219−1224.

(45) Barskiy, D. A.; Shchepin, R. V.; Tanner, C. P. N.; Colell, J. F. P.; Goodson, B. M.; Theis, T.; Warren, W. S.; Chekmenev, E. Y. *ChemPhysChem* **2017**, *18*, 1493−1498.

(46) Bales, L. B.; Kovtunov, K. V.; Barskiy, D. A.; Shchepin, R. V.; Coffey, A. M.; Kovtunova, L. M.; Bukhtiyarov, A. V.; Feldman, M. A.; Bukhtiyarov, V. I.; Chekmenev, E. Y.; Koptyug, I. V.; Goodson, B. M. *J. Phys. Chem. C* **2017**, *121*, 15304−15309.

(47) Theis, T.; Truong, M. L.; Coffey, A. M.; Shchepin, R. V.; Waddell, K. W.; Shi, F.; Goodson, B. M.; Warren, W. S.; Chekmenev, E. Y. *J. Am. Chem. Soc.* **2015**, *137*, 1404−1407.

(48) Truong, M. L.; Theis, T.; Coffey, A. M.; Shchepin, R. V.; Waddell, K. W.; Shi, F.; Goodson, B. M.; Warren, W. S.; Chekmenev, E. Y. *J. Phys. Chem. C* **2015**, *119*, 8786−8797.

(49) Zhivonitko, V. V.; Skovpin, I. V.; Koptyug, I. V. *Chem. Commun.* **2015**, *51*, 2506−2509.

(50) Shchepin, R. V.; Goodson, B. M.; Theis, T.; Warren, W. S.; Chekmenev, E. Y. *ChemPhysChem* **2017**, *18*, 1961−1965.

(51) Plaumann, M.; Bommerich, U.; Trantzschel, T.; Lego, D.; Dillenberger, S.; Sauer, G.; Bargon, J.; Buntkowsky, G.; Bernarding, J. *Chem.—Eur. J.* **2013**, *19*, 6334−6339.

(52) Olaru, A. M.; Burt, A.; Rayner, P. J.; Hart, S. J.; Whitwood, A. C.; Green, G. G. R.; Duckett, S. B. *Chem. Commun.* **2016**, *52*, 14482−14485.

(53) Rayner, P. J.; Burns, M. J.; Olaru, A. M.; Norcott, P.; Fekete, M.; Green, G. G. R.; Highton, L. A. R.; Mewis, R. E.; Duckett, S. B. *Proc. Natl. Acad. Sci. U.S.A.* **2017**, *114*, E3188−E3194.

(54) Fekete, M.; Ahwal, F.; Duckett, S. B. *J. Phys. Chem. B* **2020**, *124*, 4573−4580.

(55) Korchak, S.; Mamone, S.; Glöggler, S. *ChemistryOpen* **2018**, *7*, 672−676.

(56) Shchepin, R. V.; Birchall, J. R.; Chukanov, N. V.; Kovtunov, K. V.; Koptyug, I. V.; Theis, T.; Warren, W. S.; Gelovani, J. G.; Goodson, B. M.; Shokouhi, S.; Rosen, M. S.; Yen, Y.-F.; Pham, W.; Chekmenev, E. Y. *Chem.—Eur. J.* **2019**, *25*, 8829−8836.

(57) Reineri, F.; Boi, T.; Aime, S. *Nat. Commun.* **2015**, *6*, 5858.

(58) Hövener, J.-B.; Chekmenev, E. Y.; Harris, K. C.; Perman, W. H.; Tran, T. T.; Ross, B. D.; Bhattacharya, P. *Magn. Reson. Mater. Phys., Biol. Med.* **2009**, *22*, 123−134.

(59) Bhattacharya, P.; Harris, K; Lin, A. P.; Mansson, M.; Norton, V. A.; Perman, W. H.; Weitekamp, D. P.; Ross, B. D. *Magn. Reson. Mater. Phys., Biol. Med.* **2005**, *18*, 245−256.

(60) Tam, S.; Fajardo, M. E. *Rev. Sci. Instrum.* **1999**, *70*, 1926−1932.

(61) Knopp, G.; Kirch, K.; Beaud, P.; Mishima, K.; Spitzer, H.; Radi, P.; Tulej, M.; Gerber, T. *J. Raman Spectrosc.* **2003**, *34*, 989−993.

(62) Parrott, A. J.; Dallin, P.; Andrews, J.; Richardson, P. M.; Semenova, O.; Halse, M. E.; Duckett, S. B.; Nordon, A. *Appl. Spectrosc.* **2019**, *73*, 88−97.

(63) Du, Y.; Zhou, R.; Ferrer, M.-J.; Chen, M.; Graham, J.; Malphurs, B.; Labbe, G.; Huang, W.; Bowers, C. R. *J. Magn. Reson.* **2020**, *321*, 106869.

(64) Nantogma, S.; Joalland, B.; Wilkens, K.; Chekmenev, E. Y. *Anal. Chem.* **2021**, *93*, 3594−3601.

(65) Semenova, O.; Richardson, P. M.; Parrott, A. J.; Nordon, A.; Halse, M. E.; Duckett, S. B. *Anal. Chem.* **2019**, *91*, 6695−6701.

(66) Joalland, B.; Schmidt, A. B.; Kabir, M. S. H.; Chukanov, N. V.; Kovtunov, K. V.; Koptyug, I. V.; Hennig, J.; Hövener, J.-B.; Chekmenev, E. Y. *Anal. Chem.* **2020**, *92*, 1340−1345.

(67) Chae, H.; Min, S.; Jeong, H. J.; Namgoong, S. K.; Oh, S.; Kim, K.; Jeong, K. *Anal. Chem.* **2020**, *92*, 10902−10907.

(68) Zacharias, N. M.; McCullough, C. R.; Wagner, S.; Sailasuta, N.; Chan, H. R.; Lee, Y.; Hu, J.; Perman, W. H.; Henneberg, C.; Ross, B. D.; Bhattacharya, P. *J. Mol. Imag. Dynam.* **2016**, *6*, 123.

(69) Shchepin, R. V.; Barskiy, D. A.; Coffey, A. M.; Manzanera Esteve, I. V.; Chekmenev, E. Y. *Angew. Chem., Int. Ed.* **2016**, *55*, 6071−6074.

(70) Reineri, F.; Viale, A.; Giovenzana, G.; Santelia, D.; Dastrù, W.; Gobetto, R.; Aime, S. *J. Am. Chem. Soc.* **2008**, *130*, 15047−15053.

(71) Reineri, F.; Viale, A.; Dastrù, W.; Gobetto, R.; Aime, S. *Contrast Media Mol. Imaging* **2011**, *6*, 77−84.

(72) Emmett, P. H.; Harkness, R. W. *J. Am. Chem. Soc.* **1935**, *57*, 1624−1631.

(73) Das, T.; Kweon, S.-C.; Nah, I. W.; Karng, S. W.; Choi, J.-G.; Oh, I.-H. *Cryogenics* **2015**, *69*, 36−43.

(74) Iali, W.; Roy, S. S.; Tickner, B. J.; Ahwal, F.; Kennerley, A. J.; Duckett, S. B. *Angew. Chem., Int. Ed.* **2019**, *58*, 10271−10275.

(75) Merritt, M. E.; Harrison, C.; Storey, C.; Jeffrey, F. M.; Sherry, A. D.; Malloy, C. R. *Proc. Natl. Acad. Sci. U.S.A.* **2007**, *104*, 19773−19777.

(76) Gemeinhardt, M. E.; Limbach, M. N.; Gebhardt, T. R.; Eriksson, C. W.; Eriksson, S. L.; Lindale, J. R.; Goodson, E. A.; Warren, W. S.; Chekmenev, E. Y.; Goodson, B. M. *Angew. Chem., Int. Ed.* **2020**, *59*, 418−423.

(77) Tickner, B. J.; Semenova, O.; Iali, W.; Rayner, P. J.; Whitwood, A. C.; Duckett, S. B. *Catal. Sci. Technol.* **2020**, *10*, 1343−1355.

(78) Birchall, J. R.; Kabir, M. S. H.; Salnikov, O. G.; Chukanov, N. V.; Svyatova, A.; Kovtunov, K. V.; Koptyug, I. V.; Gelovani, J. G.; Goodson, B. M.; Pham, W.; Chekmenev, E. Y. *Chem. Commun.* **2020**, *56*, 9098−9101.

(79) Salnikov, O. G.; Chukanov, N. V.; Svyatova, A.; Trofimov, I. A.; Kabir, M. S. H.; Gelovani, J. G.; Kovtunov, K. V.; Koptyug, I. V.; Chekmenev, E. Y. *Angew. Chem., Int. Ed.* **2021**, *60*, 2406−2413.

(80) Joalland, B.; Nantogma, S.; Chowdhury, M. R. H.; Nikolaou, P.; Chekmenev, E. Y. *Magn. Reson. Chem.* **2021**, DOI: 10.1002/mrc.5167.

Check for updates

Europe
European Chemical
Societies Publishing

■ Imaging Agents | *Hot Paper* |

Low-Flammable Parahydrogen-Polarized MRI Contrast Agents

Baptiste Joalland,[a] Nuwandi M. Ariyasingha,[a] Hassan R. Younes,[a] Shiraz Nantogma,[a] Oleg G. Salnikov,[b, c, d] Nikita V. Chukanov,[b, c] Kirill V. Kovtunov,[b, c] Igor V. Koptyug,[b, c] Juri G. Gelovani,[a, e] and Eduard Y. Chekmenev*[a, f]

Abstract: Many MRI contrast agents formed with the para-hydrogen-induced polarization (PHIP) technique exhibit biocompatible profiles. In the context of respiratory imaging with inhalable molecular contrast agents, the development of nonflammable contrast agents would nonetheless be highly beneficial for the biomedical translation of this sensitive, high-throughput and affordable hyperpolarization technique. To this end, we assess the hydrogenation kinetics, the polarization levels and the lifetimes of PHIP hyperpolarized products (acids, ethers and esters) at various degrees of fluorine substitution. The results highlight important trends as a function of molecular structure that are instrumental for the design of new, safe contrast agents for in vivo imaging applications of the PHIP technique, with an emphasis on the highly volatile group of ethers used as inhalable anesthetics.

Introduction

NMR and MRI represent a set of powerful techniques to provide diagnostic information through molecular characterization, yet their signal intensity is directly proportional to the nuclear spin polarization (P) that is only about 10^{-5} for protons in physiologically and clinically relevant conditions.[1] Hyperpolarization techniques aim at increasing P through the manipulation of the population difference between nuclear spin levels, resulting in several orders of magnitude gains in sensitivity.[2–5] One of these, parahydrogen-induced polarization (PHIP) converts the singlet spin order of parahydrogen (p-H$_2$) into a large P via the pairwise addition of p-H$_2$ to an unsaturated substrate.[6–8] The high magnetization of the hyperpolarized (HP) pool of p-H$_2$-derived protons induces the occurrence of RASER (radiofrequency amplification by stimulated emission radiation), a quantum effect in which the radiofrequency modes of the inductive detector of an NMR spectrometer are enslaved by the proton nuclear spin evolution. Proton RASER allows for determining J-coupling constants and chemical shift differences while surpassing the nominal spectroscopic resolution and uncovering nonlinear effects in coupled spin oscillators, for example, frequency combs, line collapse, chaos, etc.[9–12]

PHIP and other hyperpolarization techniques such as dissolution dynamic nuclear polarization (d-DNP)[13] and spin-exchange optical pumping (SEOP)[14] have attracted much attention for their potential for in vivo applications.[15–23] Hyperpolarized (HP) compounds can indeed be employed as injectable or inhalable contrast agents.[24,25] Currently, in vivo applications of hyperpolarization methods use ^{13}C and ^{129}Xe nuclei because of the greater lifetimes of their HP states compared to those of protons (> 10 s for ^{13}C and ^{129}Xe vs. ~ 1–2 s for ^{1}H).[17,26–28] However, despite major successes of HP ^{13}C and ^{129}Xe contrast agents in a number of biomedical studies and clinical trials, ^{13}C and ^{129}Xe detection is not available on clinical MRI scanners. As a result, costly ($\sim$ \$0.5M) and bulky hardware upgrades and custom MRI sequences must be implemented on a clinical MRI scanner to enable these functionalities. Even though the ^{129}Xe and ^{13}C-based contrast agents are ready for prime time biomedical applications, the MRI scanner availability is clearly a substantial translational barrier.

The unveiling of long-lived spin states (LLS) by M. H. Levitt and colleagues, with T_{LLS} values significantly greater than corresponding spin-lattice relaxation time constant T_1, has revived the interest in imaging of proton-hyperpolarized contrast agents.[29–32] Interestingly, we have recently demonstrated the existence of LLS in HP propane and HP diethyl ether in the gas

[a] Dr. B. Joalland, N. M. Ariyasingha, H. R. Younes, S. Nantogma, Prof. J. G. Gelovani, Prof. E. Y. Chekmenev
Department of Chemistry, Integrative Biosciences (Ibio)
Karmanos Cancer Institute (KCI), Wayne State University
Detroit, Michigan 48202 (USA)
E-mail: chekmenev@wayne.edu

[b] Dr. O. G. Salnikov, Dr. N. V. Chukanov, Dr. K. V. Kovtunov, Prof. I. V. Koptyug
International Tomography Center SB RAS
Institutskaya St. 3A, 630090 Novosibirsk (Russia)

[c] Dr. O. G. Salnikov, Dr. N. V. Chukanov, Dr. K. V. Kovtunov, Prof. I. V. Koptyug
Department of Natural Sciences, Novosibirsk State University
Pirogova St. 2, 630090 Novosibirsk (Russia)

[d] Dr. O. G. Salnikov
Boreskov Institute of Catalysis SB RAS
Acad. Lavrentiev Prospekt 5, 630090 Novosibirsk (Russia)

[e] Prof. J. G. Gelovani
United Arab Emirates University, Al Ain (United Arab Emirates)

[f] Prof. E. Y. Chekmenev
Russian Academy of Sciences, Leninskiy Prospekt 14
Moscow, 119991 (Russia)

Supporting information and the ORCID identification numbers for the authors of this article can be found under:
https://doi.org/10.1002/chem.202004168.

Chemistry–A European Journal

Full Paper
doi.org/10.1002/chem.202004168

**Chemistry
Europe**
European Chemical
Societies Publishing

phase using homogeneous and heterogeneous (HET) PHIP;[33–37] HET-PHIP is particularly promising since it allows production of pure catalyst-free HP hydrocarbon gas. Two compounds (propane and diethyl ether) with anesthetic features showed promising enough polarization levels and lifetimes (T_{LLS} of 3–4 s at physiologically relevant conditions) to envision testing them as inhalable contrast agents in our up-and-coming preclinical laboratory. It should be stressed that this gain in the HP state lifetime is substantial—for example, HP propane would retain less than 15% of its potency during 2 s long inhalation if stored using T_1 versus retaining over 50% of its potency during 2 s long inhalation if stored in accord to T_{LLS} under physiologically relevant conditions.[33–37] The key benefits of proton-hyperpolarized inhalable contrast agents are the low cost of their precursors, low cost of hyperpolarization process and high production throughput. Moreover, unlike HP ^{129}Xe, proton-hyperpolarized contrast agents can be readily detected on already installed clinical MRI scanners thereby making this new technology available to the doctors and patients.

Pulmonary functional imaging is a substantial unmet medical need: there is currently no widespread clinical imaging modality to perform high-resolution functional lung imaging: computed tomography (CT), conventional MRI, and X-ray can only provide structural images of dense tissues—informing about pathologies like tumors and pneumonia—but yielding little or no information about lung ventilation, perfusion, alveoli size, gas-exchange efficiency, etc. Deadly diseases such as chronic obstructive pulmonary disease (COPD), asthma, constrictive bronchiolitis, lung injury, and pulmonary fibrosis affect > 300 million people worldwide and cause ~3 million annual deaths (5% of all deaths worldwide).[38] These diseases do not have any clinical imaging marker, especially in the early disease stages when intervention can be potentially curative. This state of affairs is in contrast with that of cancer imaging, which includes a wide range of imaging modalities with their own merits, such as MRI, CT, ultrasound, mammography, positron emission tomography (PET), and others—collectively enabling early diagnosis by population screening and monitoring response to treatment. Furthermore, CT scans (2D and 3D X-ray) expose the body to ionizing radiation, and thus cannot be performed frequently due to increased risk associated with cancer-inducing radiation. On the other hand, MRI involves no ionizing radiation, and is effectively non-invasive. Inhalable HP contrast agents can provide 3D functional lung imaging information on a single breath hold;[17, 21] thus, the use of proton-hyperpolarized contrast agents[23] has a potential to revolutionize pulmonary health care.

In our recent work, we have demonstrated the feasibility of clinical-scale production of HP propane gas and its high-resolution (0.3 × 0.3 mm^2 pixel size) MRI.[39] The feasibility of pulmonary imaging even when using non-hyperpolarized propane has been demonstrated by Hane and co-workers in rats.[40] Feasibility of HP diethyl ether MRI has also been demonstrated.[41]

Although diethyl ether is approved for medical use in some countries including Russia, the development of a new, gas-phase, inhalable proton-hyperpolarized contrast agent de-
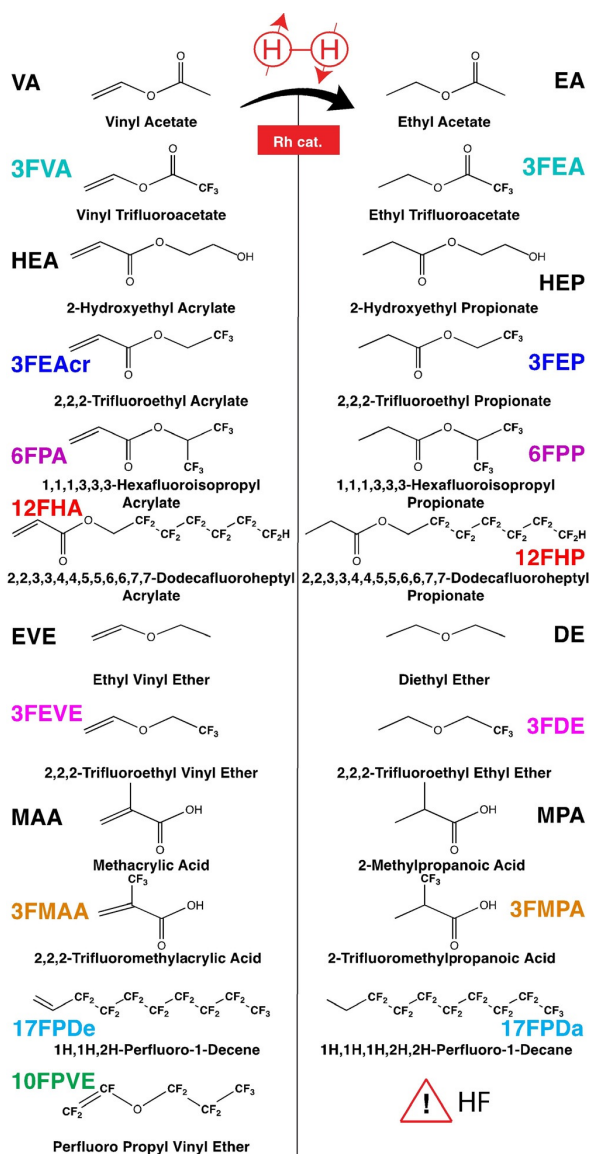
mands to address flammability concerns specifically. For example, the use of the first commercially developed anesthetic (diethyl ether) has been phased out in many developed countries and WHO removed it from the list of essential medications after 2003.[42] In this context, we report here on the chemical conversion and proton polarization build-up, maxima and lifetimes of PHIP products fluorinated to various extents, revealing trends as a function of structure and bonding patterns that are essential to tackle with the development of efficient and low-flammable PHIP contrast agents. Fluorinated hydrocarbons hyperpolarized via the PHIP technique have been reported previously, showing possibility for inducing polarization transfer from ^{1}H to ^{19}F by magnetic field cycling[43–45] or for taking advantage of the lipophilic propensity of fluorocarbons in in vivo imaging,[46] both examples illustrating valuable advantages in using HP fluorinated compounds other than non-flammability. However, previous works have focused on materials intended for the use in the liquid state. As the medical field of anesthesiology employs nowadays a group of highly volatile, halogenated, and non-flammable ethers as inhalable anesthetics, such as isoflurane $CF_3CHClOCHF_2$, sevoflurane $(CF_3)_2CHOCH_2CH_2F$, and desflurane $CF_3CHFOCHF_2$, this work examines alternative scenarios for PHIP, which could eventually provide novel in vivo molecular contrast agents combining inhalable, anesthetic and non-flammable properties with the high detection sensitivity and simplicity of the PHIP hyperpolarization technique.

Results and Discussion

The hydrogenation reactions studied here are shown in Scheme 1. The fluorinated molecules include:

1) Vinyl trifluoroacetate (3FVA) leading to ethyl trifluoroacetate (3FEA);
2) Trifluoroethyl acrylate (3FEAcr), hexafluoroisopropyl acrylate (6FPA), and dodecafluoroheptyl acrylate (12FHA), leading to trifluoroethyl propionate (3FEP), hexafluoroisopropyl propionate (6FPP), and dodecafluoroheptyl propionate (12FHP), respectively;
3) Trifluoroethyl vinyl ether (3FEVE), the first halogenated hydrocarbon anesthetic to be produced (a.k.a. fluroxene), leading to trifluoroethyl ethyl ether (3FDE);
4) Trifluoromethyl acrylic acid (3FMAA) leading to 2-trifluoromethyl propanoic acid (3FMPA).

The results are compared to those obtained with corresponding non-fluorinated molecules: vinyl acetate (VA) leading to ethyl acetate (EA), hydroxyethyl acrylate (HEA) to hydroxyethyl propionate (HEP), ethyl vinyl ether (EVE) to diethyl ether (DE), and methacrylic acid (MAA) to 2-methyl propanoic acid (MPA). Note that two other fluorinated precursors were tentatively hydrogenated: $1H,1H,2H$-perfluoro-1-decene (17FPDe) and perfluoro propyl vinyl ether (10FPVE). For alkene 17FPDe, the chemical conversion toward alkane 17FPDa (~15–20% after 30 s reaction) and the ^{1}H polarization of 17FPDa (~0.1% at 10 s reaction) were low and 17FPDe was poorly soluble in solvent [D_4]MeOH, aborting further experiments with this mol-

Chemistry–A European Journal

Full Paper
doi.org/10.1002/chem.202004168

Chemistry Europe
European Chemical
Societies Publishing

Scheme 1. PHIP reactions reported in the present study. Pairwise addition of parahydrogen in CD$_3$OD is found efficient for all unsaturated substrates, with the exception of 17FPDe, which dissolves poorly in methanol, and 10FPVE, for which the reaction with H$_2$ leads to the formation of hydrofluoric acid (HF).

ecule. For ether 10FPVE, the hydrogenation reaction was found hazardous due to the formation of hydrofluoric acid (HF) revealed as glass NMR tube melting.

All measurements were performed with standard high-throughput 5 mm NMR tubes filled under argon atmosphere. The solutions contained ~40 mM of substrates and ~4 mM of rhodium catalyst ((1,4-bis(diphenylphosphino)butane)(1,5-cyclooctadiene)rhodium(I) tetrafluoroborate) dissolved in CD$_3$OD, with the exception of the EVE + p-H$_2$ → DE reaction for which 186 mM of EVE were used in a recent study.[37] The samples were pressurized at 8 bar with p-H$_2$ (~98%) and heated at

80 °C for 30 s. Note that all studied compounds are volatile liquids under normal pressure—as a result, the depressurization of the HP liquid renders the expansion of HP proton-hyperpolarized gas. However, this depressurization would lead to unwanted polarization losses and make the comparison and quantitative studies of reaction kinetics rather challenging. Therefore, the NMR detection of proton-hyperpolarized compounds was performed in the liquid state in 5 mm NMR tubes.

The hydrogenation reaction was achieved by bubbling p-H$_2$ though the solution at a flow rate of 150 standard cubic centimeters per minute (sccm) in the Earth's magnetic field (50 µT), corresponding to ALTADENA conditions[47]—the sample transfer took less than 2 seconds from cessation of p-H$_2$ flow to spectrum acquisition unless noted otherwise. The chemical conversion was evaluated for each sample from the thermal spectra acquired before and after the reaction, as well as the residual concentration of the products in CD$_3$OD (liquid fraction) in the case of highly volatile ethers. ^{1}H polarization levels were corrected accordingly (see Supporting Information for details).

We note that no HP resonances were observed before p-H$_2$ bubbling. Moreover, once p-H$_2$ bubbling stops, the chemical reaction is effectively ceased under our conditions.[48]

^{1}H NMR spectra were measured with a benchtop NMR spectrometer (Spinsolve Carbon 60, Magritek, 61 MHz/1.4 T) and polarization levels were calibrated against reference spectra of neat ^{13}C-labeled ethyl acetate (Figure 1 a, b). RASER activity,
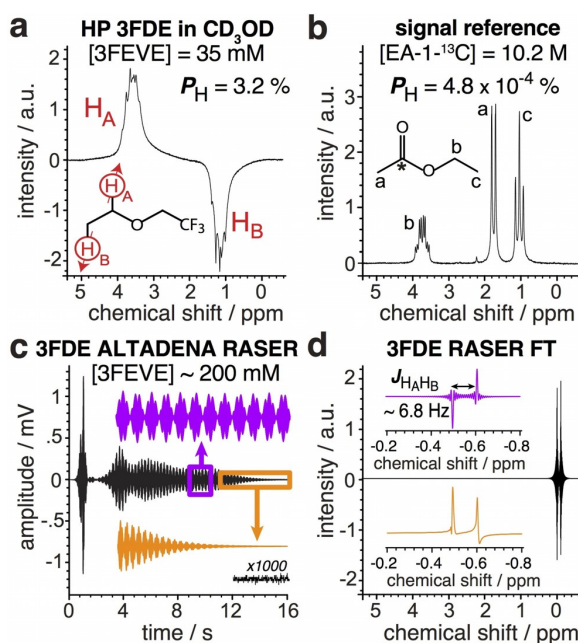

Figure 1. a) ^{1}H NMR spectrum of HP 3FDE in CD$_3$OD solution acquired using 8° flip angle. Polarization of 3.2% was measured after correction for evaporation and the Earth's field relaxation. b) Corresponding NMR spectrum of neat thermally polarized ethyl-acetate-1-^{13}C. c) ALTADENA RASER signal of HP 3FDE recorded without excitation pulse. d) Fourier transform (FT) spectra of the RASER signal for the regions outlined by purple and orange boxes in panel c (H$_A$/H$_B$ two-mode RASER).

Chemistry–A European Journal

Full Paper
doi.org/10.1002/chem.202004168

Chemistry
Europe
European Chemical
Societies Publishing

which prevents the measurement of polarization levels just as the reaction is completed, is only briefly observed with 40 mM solutions after full polarization build-up for the most strongly hyperpolarized molecules, that is, ethyl acetate and propionates. Therefore, a delay of only 5 seconds in the Earth's magnetic field before inserting the samples in the bore of the spectrometer was necessary to avoid RASER. The polarization levels were back-calculated to account for the corresponding relaxation. Significant RASER activity can however be easily observed at higher concentrations, that is even for HP molecules with relatively modest polarization levels of a few percent, such as shown in Figure 1c and d for 3FDE where a two-mode RASER is induced without any radiofrequency excitation pulse.

Figure 2 shows the ^{1}H polarization levels P_H measured as a function of reaction (bubbling) time t and fitted to Equation (1):

$$P_H(t) = \frac{P_{max}}{T_{cat}/T_{LLS} - 1}\left(\exp\left(-\frac{t-t_0}{T_{cat}}\right) - \exp\left(-\frac{t-t_0}{T_{LLS}}\right)\right) \quad (1)$$

In order to derive P_{max}, the theoretical maximum polarization neglecting relaxation, and T_{cat}, the time constant for the catalytic reaction (or polarization build-up), while leaving t_0 fixed to 1 s and T_{LLS} fixed to the average of H_A and H_B values of relaxation decay constant measured independently in the Earth's magnetic field (~50 μT, see Figure S2). Figure 3 compiles P_{max}, T_{cat}, T_{LLS}, and T_1 (measured at 1.4 T, see Figure S2) values for all compounds shown in Figure 2, with the exception of 3FEA for which the measured P_H were too low.

For 3FVA/3FEA, it is clear that the presence of the CF$_3$ group on the carboxylic side induces deleterious effects: the ^{1}H polarization reaches a maximum of about 0.1% and the chemical conversion is less than 40% after 10 s of reaction, whereas in the non-fluorinated case (VA/EA) the chemical conversion is complete after 10 s of reaction with P_{max} = 25% and T_{cat} ~1 s. These results are in sharp contrast with those obtained for the series of acrylates/propionates. We find that the replacement of —CH$_2$OH by —CF$_3$ or even —(CF$_2$)$_5$CF$_2$H does not affect much the speed and specificity of the catalytic pairwise addition reaction, with P_{max} on the order of 20%, T_{cat} ~1 s and full chemical conversion after 10 s of reaction. In the case of the branched 6FPP, P_{max} and T_{cat} are equal to 14% and ~1 s, respectively, and the chemical conversion is also completed after 10 s of p-H$_2$ supply. The negative inductive effect of the electron-accepting fluorinated group, which affects the electron density at the C=C double bond through the conjugated π-system involving the CO carbonyl group, is thus only deleterious at a short distance; in 3FEP, 6FPP and 12FHP the fluorinated groups and the conjugated systems are separated by an aliphatic carbon so that little effects on the hydrogenation reaction outcomes are observed. On the other hand, expectedly, the larger the carbon framework is the shorter is the relaxation constant (both T_{LLS} in the strong coupling regime and T_1 in the weak coupling regime), with a clear 3FEP > 6FPP > 12FHP trend.

In the case of highly volatile ethers EVE/DE, substituting the methyl group with —CF$_3$ induces a decrease of polarization by a factor of ~2.5. However, the hydrogenation reaction remains
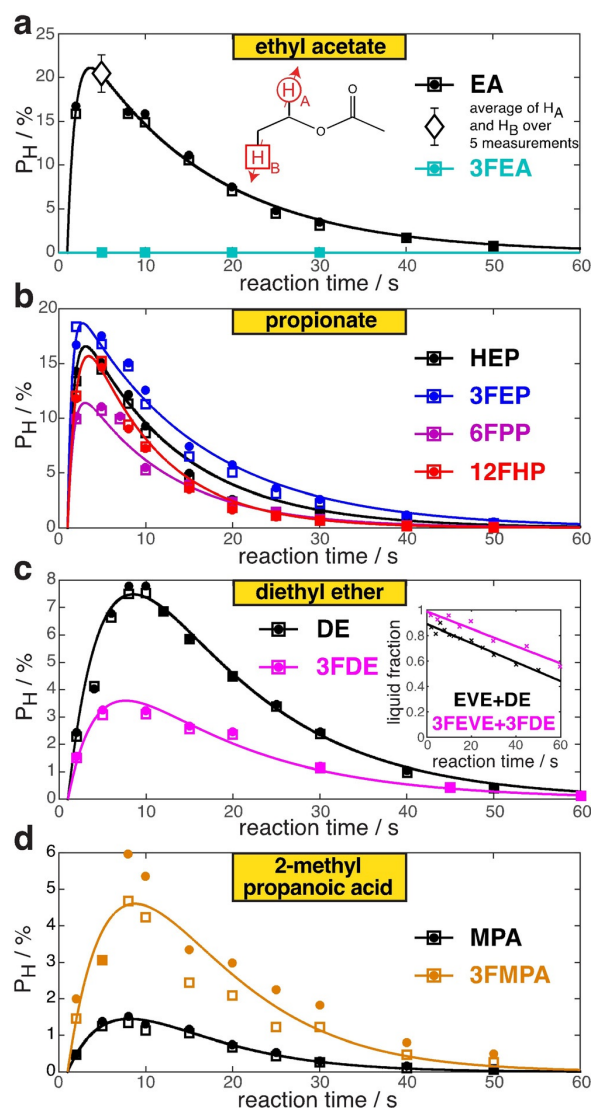

Figure 2. PHIP kinetics for hydrogenation reactions in CD$_3$OD at 8 bar and 80 °C. All reactions were studied with ~40 mM solutions, with the exception of the EVE + p-H$_2$ → DE reaction ([EVE] = 186 mM). Solid circles correspond to polarization of H_A protons (methine CH group of 2-methylpropanoic acid (MPA) and 2-trifluoromethylpropanoic acid (3FMPA), methylene CH$_2$ group in all other cases) and empty squares correspond to polarization of H_B protons (methyl CH$_3$ group). H_A and H_B polarizations were averaged in the fit. a) ^{1}H polarization of ethyl acetate and ethyl trifluoroacetate (EA and 3FEA) as a function of reaction time. b) ^{1}H polarization of propionates (HEP, 3FEP, 6FPP and 12FHEP) as a function of reaction time. c) ^{1}H polarization of diethyl ether and 2,2,2-trifluoroethyl ethyl ether (DE and 3FDE) as a function of reaction time. The inset represents the liquid fraction of EVE/DE and 3FEVE/3FDE, which decreases with reaction time due to evaporation. d) ^{1}H polarization of 2-MPA and 3FMPA as a function of reaction time.

fast with 100% conversion reached after 10 s of reaction, and neither the relaxation nor the buildup time are affected by the presence of F atoms. Nonspecific interactions in the catalytic hydrogenation reaction are therefore more pronounced for HP ethers than HP propionates, but remain far from deleterious.
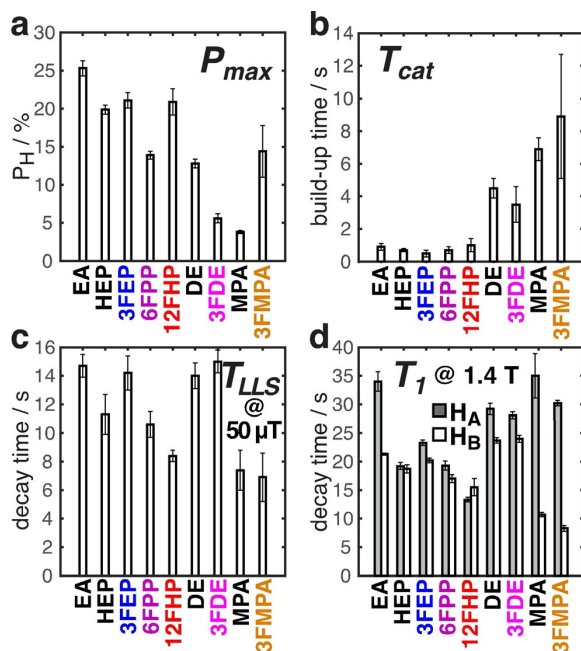
Chemistry–A European Journal

Full Paper
doi.org/10.1002/chem.202004168

Chemistry Europe
European Chemical
Societies Publishing

Figure 3. a) Maximum polarization without relaxation P_{max}. b) Build-up time T_{cat}. c) Earth's field relaxation time constant T_{LLS}. d) High field (1.4 T) relaxation time constant T_1. H_A and H_B polarizations are averaged to derive P_{max} (a), T_{cat} (b) and T_{LLS} (c). H_A notation corresponds to HP protons of CH group (in case of MPA and 3FMPA) or CH_2 group (in all other cases) and H_B notation corresponds to HP protons of CH_3 group.

Methacrylic acid represents a test case for F substitution on a methyl group that forms a branch adjacent to the double bond hosting the pairwise addition of p-H_2. For both MPA and 3FMPA hydrogenated products, the chemical conversion is found similar, i.e., 79% and 75% after 10 s of reaction, respectively, and the buildup time constants are significantly longer (7 to 9 s) than for the other compounds studied here. Interestingly, the effective P_H of 3FMPA is found about three times higher than the one of MPA, even though HP MPA and 3FMPA show similar relaxation constants at both Earth's field and high field. Note that methine (H_A) and methyl (H_B) groups exhibit a pronounced difference in T_1 at high field, with values >30 s for methine and <10 s for methyl. This is also manifested in the strong coupling regime (at Earth's magnetic field), with methyl group polarization values inferior by about 20% when compared to methine group values. This effect is not due to the presence of F atoms in the vicinity of the HP protons, as it is observed similarly for MPA and 3FMPA.

We now turn the discussion toward designing an effective, nonflammable and inhalable PHIP contrast agent. As the flammability limits for most of the molecules studied here (PHIP substrates and products) are yet unknown, we invoke the empirical model developed by Kondo et al. to predict the lower (L) and upper (U) flammability limits (in vol%) of partially fluorinated and perfluorinated compounds.[49,50] This model is based on experimental values measured for 74 alkanes, alkenes, ethers, and esters following the ASHRAE criteria.[51] The experi-

mental values of L and U can be predicted with an average relative deviation of 10% and 36%, respectively, as shown in Figure 4 for a selection of 42 benchmark molecules along with the PHIP substrates and hydrogenated products. Although the predicted upper flammability limit of non-fluorinated ethers such as EVE and DE are underestimated, this model reproduces fairly well the subtle differences in partially fluorinated ethers and esters that are closely related to the molecules studied here.

By comparing the chemical structures, F rates, and experimental and predicted flammability limits within this ensemble
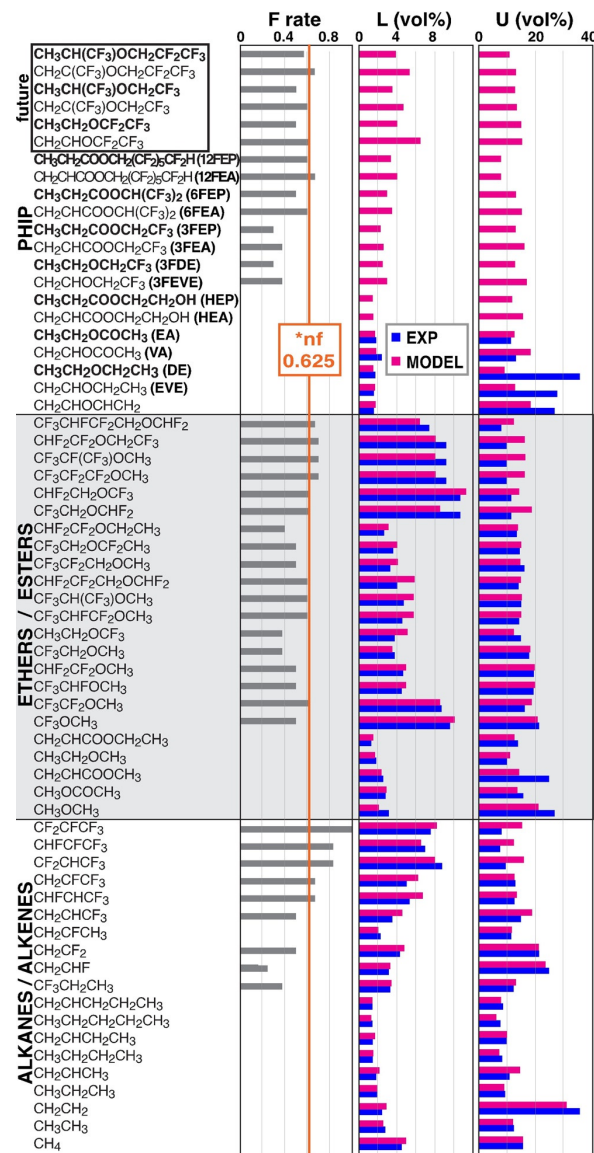

Figure 4. Fluorine substitution rate F and predicted lower (L)/upper (U) flammability limits in vol% of the PHIP substrates (regular font) and products (bold font) compared to a representative set of experimental measurements obtained with non-fluorinated and fluorinated alkanes, alkenes, ethers and esters used to model L/U.[50] The orange line in the F rate column represents the minimal F substitution degree to allow for non-flammability (F = 0.625).

Chemistry–A European Journal

Full Paper
doi.org/10.1002/chem.202004168

Chemistry Europe
European Chemical
Societies Publishing

of molecules, one can derive the following general trends in terms of flammability:

1) The larger the F substitution rate is, the less flammable the compound is. Compounds with $F > 0.625$ are mostly non-flammable.
2) Flammability further decreases when F atoms are attached to C atoms adjacent to double bonds, whereas $-C-CF_3$ group has no diminishing effect on flammability other than increasing the F rate.
3) In ethers, $-O-CF_3$ group significantly decreases flammability while $-O-CF=$ and $-O-CF_2-$ groups have no particular effect.

Another important dimension that must be accounted for in the development of PHIP inhalable contrast agents concerns the normal boiling points (b.p.) of the hydrogenation products. Overall, perfluorination and partial fluorination tend to decrease the boiling point, which is desirable to ensure an efficient vaporization at atmospheric pressure of the HP PHIP products. To estimate these values, we refer to the modified Joback group contribution method developed by Devotta and Pendyala.[52,53] In this empirical model originally developed for the screening of alternatives to chlorofluorocarbons (CFCs), halogens are treated differently from other functional groups—because of halogen–halogen and halogen–hydrogen nonbonding interactions—so that isomeric features are taken into account. The boiling point of 3FDE is estimated to be 15 °C lower than the one of DE (35 °C), bringing it to room temperature. Consequently, this partially fluorinated ether exhibits rather ideal properties for engineering a simple vaporizer with no condensation issues. The moderate fluorinated content of 3FDE ($F = 0.3$) does not however imply non-flammability.

Increasing F substitution rate while keeping intact the carbon framework and the hydrogen atoms on the hydrogenated arm of diethyl ether leads to $CH_3CH_2OCF_2CF_3$ (5FDE), with $F = 0.5$, $L = 4.0$, $U = 15.2$, and a boiling point of 19 °C. This molecule certainly lies near the nonflammability boundary, if not in the nonflammable group. We plan to test it with PHIP once its precursor $CH_2CHOCF_2CF_3$ (5FEVE) is available. Alternatives exist with larger systems to further reduce flammability while allowing for an effective PHIP process, as our results with propionates and acids suggest. For instance, we envision studying the following two candidates:

1) $CH_3CH(CF_3)OCH_2CF_3$ ($F = 0.5$, $L = 3.5$ vol%, $U = 12.4$ vol%, and b.p. $= 50$ °C)
2) $CH_3CH(CF_3)OCH_2CF_2CF_3$ ($F = 0.57$, $L = 3.5$ vol%, $U = 12.4$ vol%, b.p. $= 71$ °C)

These compounds are of interest especially because of the threefold increase in polarization measured in the case of 3FMPA, that is, where a branched CF_3 group is attached to the methine carbon. This effect could possibly compensate for the polarization loss observed when partial fluorination is used on the non-hydrogenated arm of an ether. The potential flamma-

bility should be assessed experimentally, because the fluorine content of these systems is close to the elusive $F = 0.625$ non-flammability limit. Further increasing F substitution rate with larger carbon backbones would certainly guarantee non-flammability, yet at the expense of increasing the boiling point.

Imaging studies in the gas-phase is the next logical step of this work in order to demonstrate the feasibility of functional MRI using proton-hyperpolarized fluorinated hydrocarbons. It should be noted that future HP gas imaging studies would greatly benefit from MRI detection of long-lived spin states in the gas phase as they enable a much longer readout time window. These LLS persist in low magnetic field in the strongly coupled regime, i.e., when the spin–spin coupling is greater than the chemical shift difference of the nascent parahydrogen derived protons. In practice, such field is achieved below 0.4 T for propane and below 0.1 T for other less symmetric hydrocarbons. A number of suitable low-field MRI scanning platforms is becoming increasingly available: for example, Time Medical PICA MRI scanner and Hyperfine MRI scanner to name a few. Our ongoing efforts are currently focused on establishing the dedicated low-field MRI imaging facility with the goal of feasibility studies in phantoms, excised lungs and large animal model (e.g., sheep) hopefully in 2021–2023.

Conclusions

A consistent series of ^1H NMR spectroscopy experiments were introduced to compare the yields, polarization levels, build-up times and lifetimes of parahydrogen-induced polarization (PHIP) reaction products involving fluorinated molecules. The results show evidence that, depending on the F-substituted functional groups, fluorination can have no effect on the hyperpolarized states or nearly completely suppress them, as the partially fluorinated, hyperpolarized molecules studied here exhibit a broad range of polarization levels (with measured P_H maxima ranging from 0.1% to about 20%). The cross analysis of these results enable us to rationalize the following trends:

For esters, F substitution on the carbon adjacent to the carbonyl group (α-carbon) is highly deleterious, both in terms of reaction efficiency (poor chemical conversion) and specificity (maximum polarization level < 0.1%). However, F substitution within the $-O$-alkyl (alkoxy) group does not affect the efficiency and specificity of the reaction when the α-carbon is not bound to F atoms.

For highly volatile ether such as diethyl ether, which represents a promising class of PHIP molecules to be used as inhalable anesthetics, the polarization levels are lowered by a factor of ~ 2.5 with the F substitution of the methyl group. The results are still deemed suitable for biomedical applications with highly desirable reduced flammability.

A branched CF_3 group directly attached to the methine group of the $C=C$ double bond hosting the addition of parahydrogen seems promising for reaching high fluorine content, because the measured polarization levels are found significantly higher than those in the non-fluorinated case. This effect could possibly mitigate the polarization decrease observed with linear, partially fluorinated ethers.

In conclusion, all the hydrogenation reactions studied here were intentionally catalyzed with the same Rh complex for comparison purposes; nevertheless each reaction could also benefit from the more rational design of a targeted catalyst.

Acknowledgements

Conflict of interest

E.Y.C. declares a stake of ownership in XeUS Technologies Ltd.

Keywords: flammability · fluorine · hyperpolarization · inhalable anesthetics · parahydrogen

[1] D. I. Hoult, R. E. Richards, *J. Magn. Reson.* **1976**, *24*, 71–85.
[2] P. Nikolaou, B. M. Goodson, E. Y. Chekmenev, *Chem. Eur. J.* **2015**, *21*, 3156–3166.
[3] B. M. Goodson, N. Whiting, A. M. Coffey, P. Nikolaou, F. Shi, B. M. Gust, M. E. Gemeinhardt, R. V. Shchepin, J. G. Skinner, J. R. Birchall, M. J. Barlow, E. Y. Chekmenev, *Emagres* **2015**, *4*, 797–810.
[4] K. V. Kovtunov, E. V. Pokochueva, O. G. Salnikov, S. Cousin, D. Kurzbach, B. Vuichoud, S. Jannin, E. Y. Chekmenev, B. M. Goodson, D. A. Barskiy, I. V. Koptyug, *Chem. Asian J.* **2018**, *13*, 1857–1871.
[5] J. Kurhanewicz, D. B. Vigneron, K. Brindle, E. Y. Chekmenev, A. Comment, C. H. Cunningham, R. J. DeBerardinis, G. G. Green, M. O. Leach, S. S. Rajan, R. R. Rizi, B. D. Ross, W. S. Warren, C. R. Malloy, *Neoplasia* **2011**, *13*, 81–97.
[6] C. R. Bowers, D. P. Weitekamp, *Phys. Rev. Lett.* **1986**, *57*, 2645–2648.
[7] C. R. Bowers, D. P. Weitekamp, *J. Am. Chem. Soc.* **1987**, *109*, 5541–5542.
[8] T. C. Eisenschmid, R. U. Kirss, P. P. Deutsch, S. I. Hommeltoft, R. Eisenberg, J. Bargon, R. G. Lawler, A. L. Balch, *J. Am. Chem. Soc.* **1987**, *109*, 8089–8091.
[9] M. Suefke, S. Lehmkuhl, A. Liebisch, B. Blümich, S. Appelt, *Nature Phys.* **2017**, *13*, 568–572.
[10] S. Appelt, A. Kentner, S. Lehmkuhl, B. Blümich, *Prog. Nucl. Magn. Reson. Spectrosc.* **2019**, *114*, 1–32.
[11] A. N. Pravdivtsev, F. D. Sönnichsen, J. B. Hövener, *ChemPhysChem* **2020**, *21*, 667–672.
[12] B. Joalland, N. M. Ariyasingha, S. Lehmkuhl, T. Theis, S. Appelt, E. Y. Chekmenev, *Angew. Chem. Int. Ed.* **2020**, *59*, 8654–8660; *Angew. Chem.* **2020**, *132*, 8732–8738.
[13] J. H. Ardenkjaer-Larsen, A. M. Leach, N. Clarke, J. Urbahn, D. Anderson, T. W. Skloss, *NMR Biomed.* **2011**, *24*, 927–932.
[14] T. G. Walker, *J. Phys. Conf. Ser.* **2011**, *294*, 012001.
[15] S. J. Nelson, J. Kurhanewicz, D. B. Vigneron, P. E. Z. Larson, A. L. Harzstark, M. Ferrone, M. van Criekinge, J. W. Chang, R. Bok, I. Park, G. Reed, L. Carvajal, E. J. Small, P. Munster, V. K. Weinberg, J. H. Ardenkjaer-Larsen, A. P. Chen, R. E. Hurd, L. I. Odegardstuen, F. J. Robb, J. Tropp, J. A. Murray, *Sci. Transl. Med.* **2013**, *5*, 198ra108.
[16] K. M. Brindle, *J. Am. Chem. Soc.* **2015**, *137*, 6418–6427.
[17] J. P. Mugler, T. A. Altes, *J. Magn. Reson. Imaging* **2013**, *37*, 313–331.
[18] L. L. Walkup, J. C. Woods, *NMR Biomed.* **2014**, *27*, 1429–1438.
[19] M. He, S. H. Robertson, S. S. Kaushik, M. S. Freeman, R. S. Virgincar, J. Davies, J. Stiles, W. M. Foster, H. P. McAdams, B. Driehuys, *Magn. Reson. Imaging* **2015**, *33*, 877–885.
[20] R. T. Branca, T. He, L. Zhang, C. S. Floyd, M. Freeman, C. White, A. Burant, *Proc. Natl. Acad. Sci. USA* **2014**, *111*, 18001–18006.
[21] D. A. Barskiy, A. M. Coffey, P. Nikolaou, D. M. Mikhaylov, B. M. Goodson, R. T. Branca, G. J. Lu, M. G. Shapiro, V.-V. Telkki, V. V. Zhivonitko, I. V. Koptyug, O. G. Salnikov, K. V. Kovtunov, V. I. Bukhtiyarov, M. S. Rosen, M. J. Barlow, S. Safavi, I. P. Hall, L. Schröder, E. Y. Chekmenev, *Chem. Eur. J.* **2017**, *23*, 725–751.
[22] G. Norquay, G. J. Collier, M. Rao, N. J. Stewart, J. M. Wild, *Phys. Rev. Lett.* **2018**, *121*, 153201.
[23] K. V. Kovtunov, I. V. Koptyug, M. Fekete, S. B. Duckett, T. Theis, B. Joalland, E. Y. Chekmenev, *Angew. Chem. Int. Ed.* **2020**, *59*, 17788–17797.
[24] K. Golman, J. H. Ardenkjær-Larsen, J. S. Petersson, S. Månsson, I. Leunbach, *Proc. Natl. Acad. Sci. USA* **2003**, *100*, 10435–10439.
[25] K. Golman, R. in't Zandt, M. Thaning, *Proc. Natl. Acad. Sci. USA* **2006**, *103*, 11270–11275.
[26] J. Kurhanewicz, D. B. Vigneron, J. H. Ardenkjaer-Larsen, J. A. Bankson, K. Brindle, C. H. Cunningham, F. A. Gallagher, K. R. Keshari, A. Kjaer, C. Laustsen, D. A. Mankoff, M. E. Merritt, S. J. Nelson, J. M. Pauly, P. Lee, S. Ronen, D. J. Tyler, S. S. Rajan, D. M. Spielman, L. Wald, X. Zhang, C. R. Malloy, R. Rizi, *Neoplasia* **2019**, *21*, 1–16.
[27] M. S. Albert, V. D. Schepkin, T. F. Budinger, *J. Comput. Assist. Tomogr.* **1995**, *19*, 975–978.
[28] P. Choquet, J.-N. Hyacinthe, G. Duhamel, E. Grillon, J.-L. Leviel, A. Constantinesco, A. Ziegler, *Magn. Reson. Med.* **2003**, *49*, 1014–1018.
[29] M. Carravetta, O. G. Johannessen, M. H. Levitt, *Phys. Rev. Lett.* **2004**, *92*, 153003.
[30] M. Carravetta, M. H. Levitt, *J. Am. Chem. Soc.* **2004**, *126*, 6228–6229.
[31] G. Pileio, M. H. Levitt, *J. Chem. Phys.* **2009**, *130*, 214501.
[32] J. Eills, J. W. Blanchard, T. Wu, C. Bengs, J. Hollenbach, D. Budker, M. H. Levitt, *J. Chem. Phys.* **2019**, *150*, 174202.
[33] K. V. Kovtunov, M. L. Truong, D. A. Barskiy, O. G. Salnikov, V. I. Bukhtiyarov, A. M. Coffey, K. W. Waddell, I. V. Koptyug, E. Y. Chekmenev, *J. Phys. Chem. C* **2014**, *118*, 28234–28243.
[34] K. V. Kovtunov, M. L. Truong, D. A. Barskiy, I. V. Koptyug, A. M. Coffey, K. W. Waddell, E. Y. Chekmenev, *Chem. Eur. J.* **2014**, *20*, 14629–14632.
[35] D. A. Barskiy, O. G. Salnikov, A. S. Romanov, M. A. Feldman, A. M. Coffey, K. V. Kovtunov, I. V. Koptyug, E. Y. Chekmenev, *J. Magn. Reson.* **2017**, *276*, 78–85.
[36] N. M. Ariyasingha, O. G. Salnikov, K. V. Kovtunov, L. M. Kovtunova, V. I. Bukhtiyarov, B. M. Goodson, M. S. Rosen, I. V. Koptyug, J. G. Gelovani, E. Y. Chekmenev, *J. Phys. Chem. C* **2019**, *18*, 11734–11744.
[37] N. M. Ariyasingha, B. Joalland, H. R. Younes, O. G. Salnikov, N. V. Chukanov, K. V. Kovtunova, V. I. Bukhtiyarov, I. V. Koptyug, J. G. Gelovani, E. Y. Chekmenev, *Chem. Eur. J.* **2020**, *26*, 13621–13626.
[38] World-Health-Organization. Ten threats to global health in 2019. https://www.who.int/emergencies/ten-threats-to-global-health-in-2019.
[39] O. G. Salnikov, P. Nikolaou, N. M. Ariyasingha, K. V. Kovtunov, I. V. Koptyug, E. Y. Chekmenev, *Anal. Chem.* **2019**, *91*, 4741–4746.
[40] A. Kopanski, F. Hane, T. Li, M. Albert in *25th ISMRM Conference, April 22–27*, Honolulu, Hawaii, **2017**, p.2162.
[41] O. G. Salnikov, A. Svyatova, L. M. Kovtunova, N. V. Chukanov, V. I. Bukhtiyarov, K. V. Kovtunov, E. Y. Chekmenev, I. V. Koptyug, *Chem. Eur. J.* **2020**, https://doi.org/10.1002/chem.202003638.
[42] *Essential Medicines WHO Model List (revised April 2003)*, 13th ed., World Health Organization, Geneva, **2003**.
[43] L. T. Kuhn, U. Bommerich, J. Bargon, *J. Phys. Chem. A* **2006**, *110*, 3521–3526.
[44] U. Bommerich, T. Trantzschel, S. Mulla-Osman, G. Buntkowsky, J. Bargon, J. Bernarding, *Phys. Chem. Chem. Phys.* **2010**, *12*, 10309–10312.
[45] M. Plaumann, U. Bommerich, T. Trantzschel, D. Lego, S. Dillenberger, G. Sauer, J. Bargon, G. Buntkowsky, J. Bernarding, *Chem. Eur. J.* **2013**, *19*, 6334–6339.
[46] P. Bhattacharya, E. Y. Chekmenev, W. F. Reynolds, S. Wagner, N. Zacharias, H. R. Chan, R. Bünger, B. D. Ross, *NMR Biomed.* **2011**, *24*, 1023–1028.
[47] M. G. Pravica, D. P. Weitekamp, *Chem. Phys. Lett.* **1988**, *145*, 255–258.
[48] O. G. Salnikov, N. V. Chukanov, R. V. Shchepin, I. V. Manzanera Esteve, K. V. Kovtunov, I. V. Koptyug, E. Y. Chekmenev, *J. Phys. Chem. C* **2019**, *123*, 12827–12840.
[49] S. Kondo, Y. Urano, K. Takizawa, A. Takahashi, K. Tokuhashi, A. Sekiya, *Fire Saf. J.* **2006**, *41*, 46–56.

[50] S. Kondo, K. Takizawa, A. Takahashi, K. Tokuhashi, J. Mizukado, A. Sekiya, *J. Hazard. Mater.* **2009**, *171*, 613–618.

[51] A. Standard, *Ansi/Ashrae Standard* **2010**, 34–2007.

[52] K. G. Joback, R. C. Reid, *Chem. Eng. Commun.* **1987**, *57*, 233–243.

[53] S. Devotta, V. R. Pendyala, *Ind. Eng. Chem. Res.* **1992**, *31*, 2042–2046.

▌**Imaging Agents** |*Hot Paper*|

Heterogeneous Parahydrogen-Induced Polarization of Diethyl Ether for Magnetic Resonance Imaging Applications

Oleg G. Salnikov,*[a, b, c] Alexandra Svyatova,[a, c] Larisa M. Kovtunova,[a, b, c] Nikita V. Chukanov,[a, c] Valerii I. Bukhtiyarov,[b, c] Kirill V. Kovtunov†,[a, c] Eduard Y. Chekmenev,[d, e] and Igor V. Koptyug[a, c]

Dedicated to the memory of Kirill V. Kovtunov (1983–2020), friend, colleague, and mentor.

Chemistry–A European Journal

Full Paper
doi.org/10.1002/chem.202003638

Chemistry Europe
European Chemical
Societies Publishing
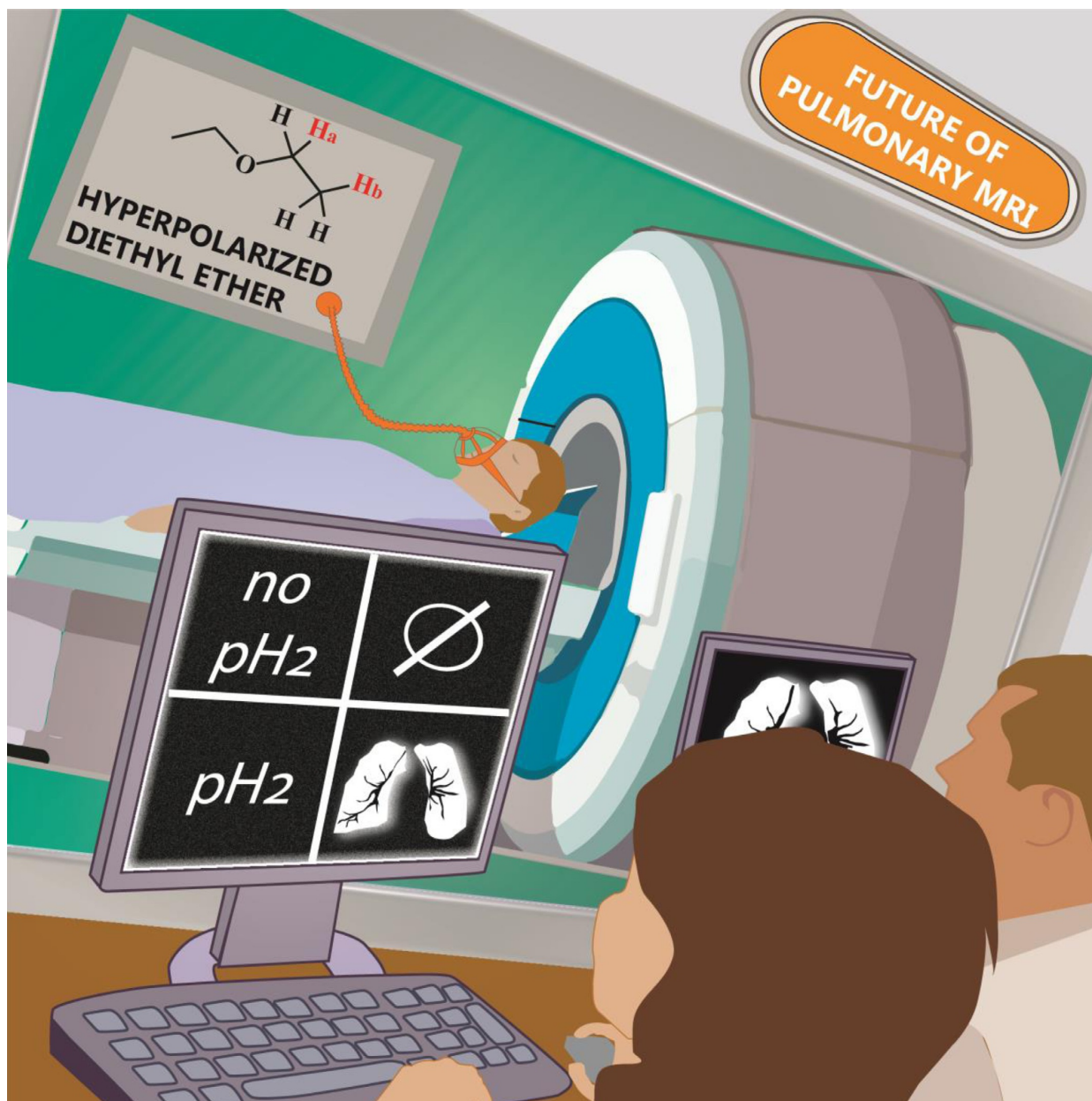
Abstract: Magnetic resonance imaging (MRI) with the use of hyperpolarized gases as contrast agents provides valuable information on lungs structure and function. While the technology of ^{129}Xe hyperpolarization for clinical MRI research is well developed, it requires the expensive equipment for production and detection of hyperpolarized ^{129}Xe. Herein we present the ^{1}H hyperpolarization of diethyl ether vapor that can be imaged on any clinical MRI scanner. ^{1}H nuclear spin polarization of up to 1.3% was achieved using heterogene-

ous hydrogenation of ethyl vinyl ether with parahydrogen over Rh/TiO$_2$ catalyst. Liquefaction of diethyl ether vapor proceeds with partial preservation of hyperpolarization and prolongs its lifetime by $\approx$10 times. The proof-of-principle 2D ^{1}H MRI of hyperpolarized diethyl ether was demonstrated with 0.1×1.1 mm^2 spatial and 120 ms temporal resolution. The long history of use of diethyl ether for anesthesia is expected to facilitate the clinical translation of the presented approach.

Introduction

Magnetic resonance imaging (MRI) is a widely used clinical imaging technique employed for diagnostics of various pathologies and monitoring of their medical treatment. In spite of its vast functionality, MRI suffers from an inherently low detection sensitivity due to low polarization of nuclear spins. For example, at 3 T (magnetic field of a modern high-field clinical MRI scanner) ^{1}H nuclear spin polarization (P_{1H}) is only ca. 10^{-5} meaning that only one nucleus out of ca. 100 000 contributes to the detected signal.[1–3] The sensitivity issue is especially critical for pulmonary MRI due to a low spin density of lung tissues. Therefore, non-NMR imaging techniques such as computed tomography and chest radiography are usually employed for pulmonary imaging of COPD and other lung diseases including COVID-19.[4,5] However, these techniques employ ionizing radiation. Moreover, they report on the structure of lung tissue and do not provide functional information on gas ventilation, diffusion and perfusion, which is vitally needed to evaluate organ's regional performance.

The possible way to deal with low sensitivity of MRI is to use inert ^{19}F-containing gases, for example, SF$_6$ or perfluoropropane, as contrast agents.[6,7] This approach benefits from very short ^{19}F T_1 of fluorinated gases (ca. 1–20 ms) which enables rapid signal accumulation. The alternative way to boost MRI sensitivity is the use of hyperpolarization techniques,[2,3,8,9] allowing for increase of nuclear spin polarization by several orders of magnitude. For pulmonary MRI, a gas should be hyperpolarized, inhaled by a patient and imaged before its enhanced magnetization relaxes to thermal equilibrium. Spin-exchange optical pumping (SEOP) technique can be employed for hyperpolarization of noble gases such as ^{129}Xe or ^{3}He.[2,10–12] This approach benefits from high levels of polarization (close to unity in cell and tens of percent out of the cell) and long lifetime (ca. 2 hours) of hyperpolarized (HP) gases,[13,14] which are also safe for inhalation. As a result, HP noble gases have been successfully employed for pulmonary MRI in clinical research.[2,15–17] However, currently this technology is limited only to several sites worldwide due to the need of complex and expensive equipment for hyperpolarization (for example, high-power lasers). More importantly, heteronuclear (i.e., any non-proton nucleus) detection capabilities are required for ^{129}Xe MRI that are not available on standard clinical MRI scanners.

Another technique that can be employed for the production of hyperpolarized gases is parahydrogen-induced polarization (PHIP).[3,18] In this approach, parahydrogen (p-H$_2$) is added to a double or triple chemical bond of an unsaturated substrate in a pairwise manner with retention of nuclear spins correlation.[19] Pairwise p-H$_2$ addition can be mediated by either homogeneous[20,21] or heterogeneous[22–26] catalysts, and both these approaches can be utilized for hyperpolarization of gases.[27–31] While homogeneous catalysts provide higher polarization levels for reaction products in liquid phase (up to 50–60%),[32,33] less than 1% polarization is typically achieved for HP gases produced using this approach.[27] Heterogeneous catalysts usually provide similar P_{1H} of $\approx$1%; however, recent advances in catalysis may potentially enable substantially greater P_{1H} values.[26,34] Moreover, heterogeneous catalysts are robust and allow production of HP gases on a larger scale in a catalyst-free manner,[30] and in a continuous-flow mode, if required.[35]

Currently the best candidate for a PHIP-hyperpolarized gas suitable for pulmonary MRI is propane. The feasibility of MRI of thermally polarized propane has been demonstrated in rats[36]—moreover, efforts are ongoing in our labs to demonstrate feasibility of imaging in large animals. Propane is a non-toxic asphyxiant gas[37,38] which can be easily hyperpolarized

[a] Dr. O. G. Salnikov, A. Svyatova, Dr. L. M. Kovtunova, Dr. N. V. Chukanov, Dr. K. V. Kovtunov, Prof. I. V. Koptyug
International Tomography Center SB RAS
3A Institutskaya St., 630090 Novosibirsk (Russia)
E-mail: salnikov@tomo.nsc.ru

[b] Dr. O. G. Salnikov, Dr. L. M. Kovtunova, Prof. V. I. Bukhtiyarov
Boreskov Institute of Catalysis SB RAS
5 Acad. Lavrentiev Pr., 630090 Novosibirsk (Russia)

[c] Dr. O. G. Salnikov, A. Svyatova, Dr. L. M. Kovtunova, Dr. N. V. Chukanov, Prof. V. I. Bukhtiyarov, Dr. K. V. Kovtunov, Prof. I. V. Koptyug
Department of Natural Sciences, Novosibirsk State University
2 Pirogova St., 630090 Novosibirsk (Russia)

[d] Prof. E. Y. Chekmenev
Department of Chemistry, Integrative Biosciences (Ibio)
Karmanos Cancer Institute (KCI), Wayne State University
Detroit, Michigan 48202 (USA)

[e] Prof. E. Y. Chekmenev
Russian Academy of Sciences (RAS)
14 Leninskiy Prospekt, 119991 Moscow (Russia)

[†] Deceased 19.05.2020

📄 Supporting information and the ORCID identification number(s) for the
ⓘ author(s) of this article can be found under:
https://doi.org/10.1002/chem.202003638.

Chemistry–A European Journal

Full Paper
doi.org/10.1002/chem.202003638

Chemistry Europe
European Chemical
Societies Publishing

via heterogeneous gas phase hydrogenation of propylene with *p*-H₂.[29,30] Importantly, this approach enables polarization of protons which can be imaged on any clinical MRI scanner, in contrast to HP noble gases produced by SEOP. The use of Rh/TiO₂ hydrogenation catalyst provided ≈1% ^1H polarization of the HP propane gas produced in the reaction, which was employed for a proof-of-principle 3D MRI of model phantoms with high spatial and temporal resolution.[29,39] Scale-up of this approach resulted in the construction of a propane polarizer able to produce more than 0.3 standard L of HP propane in just 2 s, maintaining P_{1H} of ≈1% and an almost complete conversion of propylene.[30] Another possibility is to employ cyclopropane as an alternative precursor for HP propane, which possesses an advantage over propylene due to its previous use as an anesthetic.[40] Hydrogenation of cyclopropane with *p*-H₂ was shown to produce HP propane with $P_{1H}=2.4\%$, though at a low reaction yield (<3%).[41]

Recently, we have demonstrated the feasibility of producing HP diethyl ether (DE) using homogeneous PHIP with P_{1H} reaching 8.4%.[42] Diethyl ether is a highly volatile compound which has been utilized as a first commercial inhalable anesthetic for a long time[43] and was in the World Health Organization model list of essential medicines until 2005. Moreover, diethyl ether is still clinically employed in many countries including Russia. Therefore, in some countries the use of HP diethyl ether as an inhalable contrast agent is anticipated to enjoy easier biomedical translation than that of HP propane. Since the precursor ethyl vinyl ether (EVE) had been also utilized as an anesthetic (trade name Vinamar), the residual traces of EVE not completely converted to DE should not impact clinical utilization of HP DE. While heterogeneous PHIP approach for production of HP DE was attempted in our previous work,[42] the estimated P_{1H} value was below 0.1%. The polarization process was not optimized because the main emphasis of the previous studies was to demonstrate the long-lived spin states in the created HP DE, which served as a motivation for our studies described here. Herein we investigate the efficiency of diethyl ether parahydrogen-induced polarization over the heterogeneous Rh/TiO₂ catalyst, and also show the feasibility of its ^1H MRI visualization—a critical milestone for future in vivo applications.

Results and Discussion

Hyperpolarization of DE was performed by passing the mixture of EVE vapor and a 6–7-fold excess of *p*-H₂ gas through the reactor filled with heterogeneous 1 wt.% Rh/TiO₂ catalyst. This catalyst was chosen based on the previous demonstration of the highest efficiency for production of HP propane.[29] The resultant HP gas mixture was directed to the 5 mm NMR tube located inside the high-resolution NMR spectrometer for detection. The representative ^1H NMR spectra of HP and thermally polarized DE produced by hydrogenation of EVE with *p*-H₂ over heterogeneous Rh/TiO₂ catalyst are presented in Figure 1. The highest observed signal enhancements were 520–570-fold at 7.05 T magnetic field. This value corresponds to P_{1H} of 1.2–1.3%, which is similar to that obtained previously for HP pro-
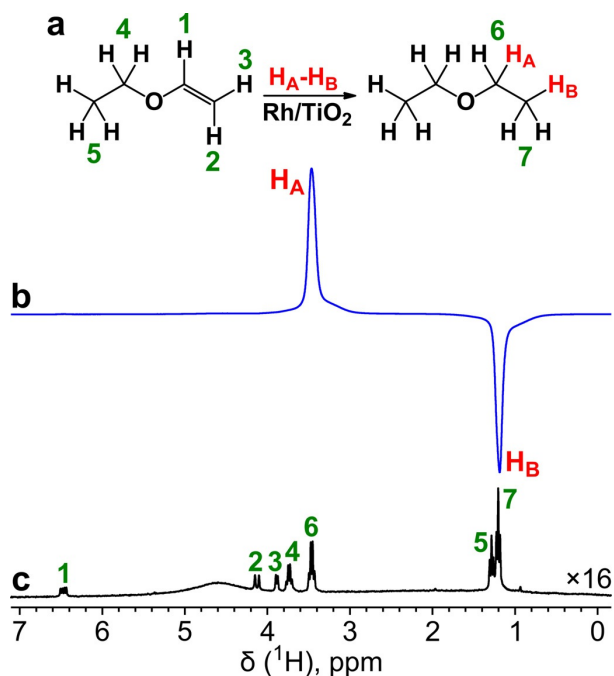

Figure 1. (a) The scheme of pairwise addition of *p*-H₂ to EVE with the formation of HP DE over Rh/TiO₂ catalyst. (b) ^1H NMR spectrum of gaseous HP DE acquired while the gas mixture was flowing at 4.3 mL s⁻¹ gas flow rate. (c) ^1H NMR spectrum of thermally polarized gaseous DE scaled by a factor of 16. The spectra were acquired with 8 signal accumulations. Hydrogenation of EVE with 6.5-fold excess of *p*-H₂ was performed at 200 °C and 2.7 bar. Signal enhancement calculated using the signal of DE CH₃ group was 570, which corresponds to $P_{1H}=1.3\%$.

pane.[29,30] It was found that apparent polarization grows with the pressure and flow rate of the gas (see Table S1 in the Supporting Information). The relaxation measurements explaining these trends are reported below. Importantly, adjustment of the gas flow rate allows us to obtain $P_{1H}\approx1.2\%$ at different pressures ranging from 1.0 to 3.9 bar (Figure S1). This is a valuable finding for the development of HP DE production on a clinical scale, because this means that certain variations of reaction conditions may not be detrimental to polarization levels. The chemical conversion of EVE to DE was 64–68% at 3.9 bar, 52–55% at 2.7 bar and 42–44% at 1.0 bar (Table S1). These rather high conversion levels along with the high levels of polarization provide strong NMR signals of HP DE.

A non-equilibrium nuclear spin polarization created by hyperpolarization techniques relaxes to a thermal equilibrium level, leading to the decrease of observable NMR signal with time. For small molecules in a gas phase, nuclear spin relaxation is governed by the spin-rotation mechanism[44] and is rather fast. For example, the spin-lattice relaxation time (T_1) of protons in propane gas is less than 1 s at atmospheric pressure and a magnetic field of a typical NMR spectrometer.[45–47] Such rapid relaxation is an important obstacle for practical applications of HP gases (except the HP noble gases which possess long relaxation times due to their atomic nature and, therefore, the lack of rotational motion). The results of T_1 measure-

Chemistry–A European Journal

Full Paper
doi.org/10.1002/chem.202003638

Chemistry Europe
European Chemical
Societies Publishing

ments for DE vapor in its mixture with parahydrogen at 7.05 T magnetic field are presented in Table S2. It was found that T_1 of DE increases with pressure, reaching 2.6 ± 0.5 s and 2.4 ± 0.2 s for CH_2 and CH_3 groups, respectively, at 3.9 bar. This explains the increase of the observed DE polarization with pressure reported in Table S1. The increase of $([EVE]+[DE])/[p\text{-}H_2]$ ratio from 0.17 to 3.2 at 1.0 bar total pressure results in increase of T_1 values from 1.0 ± 0.2 s and 1.0 ± 0.1 s for CH_2 and CH_3 sites, respectively, to 1.41 ± 0.09 s and 1.11 ± 0.07 s. Both trends have been previously observed for the spin-lattice relaxation of propane,[45] and are associated with more frequent collisions of DE molecules at higher pressures and higher fractions of larger ether molecules in a gas mixture; these findings indicate that relaxation of ^{1}H-hyperpolarized gases follows a general trend.

Next, we carried out hydrogenation of propylene with p-H_2 under the same reaction conditions in order to compare the efficiency of DE hyperpolarization with that of propane. It was found that in the case of propane the polarization levels are ca. 2 times lower (see Table S3). A plausible explanation for this result is a faster relaxation of HP propane compared to HP DE, leading to a more efficient polarization decay during the transfer of the HP reaction products from the reactor to the NMR probe. The corresponding T_1 data for propane/hydrogen mixtures at the pressures under study are presented in Table S4 and Figure S2 (the comprehensive T_1 measurements for propane in a wide range of pressures and propane fractions in its mixture with H_2 can be found elsewhere[45]).

Recently, Ariyasingha et al. have demonstrated that hyperpolarization lifetime for liquefied HP propane reaches 14.7 s at 47.5 mT, which is greater than in the gas phase at any pressure studied to date.[48] Therefore, condensation may be used for a temporary storage of HP propane polarization. Here we explore the same approach for HP diethyl ether. Since DE is liquid at standard conditions, its liquefaction is much easier than that of propane. In our study, collection of liquid DE was performed just by cooling the NMR tube to 0 °C inside the NMR spectrometer while the mixture of ether vapor and p-H_2 was flowing through. We found that it is feasible to liquefy HP DE with a partial preservation of polarization (P_{1H} up to 0.15%, Figure 2). It should be noted that this polarization level is underestimated because the amount of liquefied DE in the NMR tube is constantly increasing during this non-optimized experiment. Therefore, by the time the NMR spectrum presented in Figure 2b was acquired, part of DE molecules have already relaxed to thermal equilibrium while they were still hyperpolarized right after condensation. Thus, we speculate that actual polarization levels of liquefied DE are several times greater than our estimation. Moreover, we expect that the additional several-fold gain of polarization would be possible in case of faster condensation process. ^{1}H T_1 measurements for neat liquid DE at 7.05 T yielded 9.90 ± 0.04 s for the CH_2 group and 9.12 ± 0.03 s for the CH_3 group, meaning that liquefaction indeed can be a valuable approach for prolongation of HP DE lifetime. The use of an appropriate magnetic field may further increase the relaxation time. For example, at 47.5 mT HP DE (as well as HP propane[39,48,49]) exhibits a long-lived spin state with
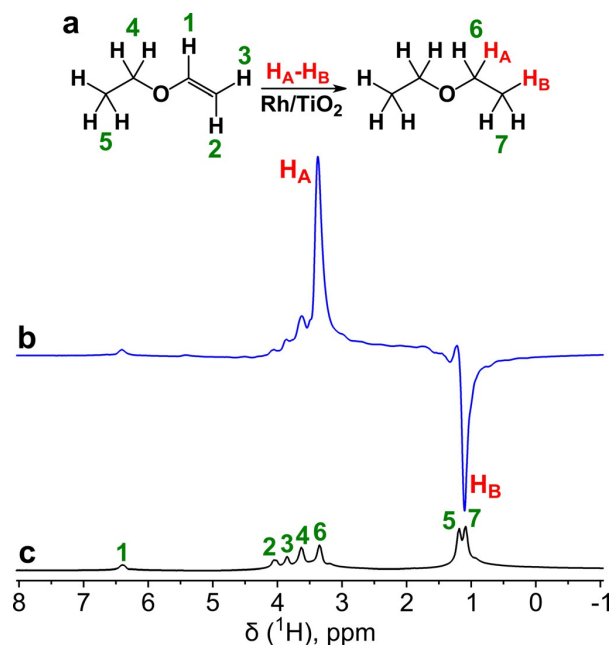

Figure 2. (a) The scheme of pairwise addition of p-H_2 to EVE with the formation of HP DE over Rh/TiO$_2$ catalyst. (b) ^{1}H NMR spectrum of liquid HP DE obtained via condensation of gaseous HP DE at 0 °C. The spectrum was acquired while the gas was bubbling through the liquid. (c) ^{1}H NMR spectrum of thermally polarized liquid DE acquired after interruption of the gas flow and relaxation of hyperpolarization. The spectra are presented on the same vertical scale. Hydrogenation of EVE with 6.5-fold excess of p-H_2 was performed at 200 °C, 4.2 mL s^{-1} gas flow rate and 2.7 bar pressure. Signal enhancement calculated using the signal of DE CH_2 group was 67, which corresponds to $P_{1H}=0.15$%.

an estimated relaxation time of 4.0 ± 0.7 s at 3.3 bar total pressure and ≈17% DE fraction in its mixture with p-H_2.[42]

To show the viability of diethyl ether for MR imaging applications, we performed ^{1}H MRI of gaseous HP DE in a 5 mm NMR tube at 9.4 T (Figure 3). It was possible to obtain images with a high spatial resolution of 0.1×1.1 mm^2/pixel and a tem-
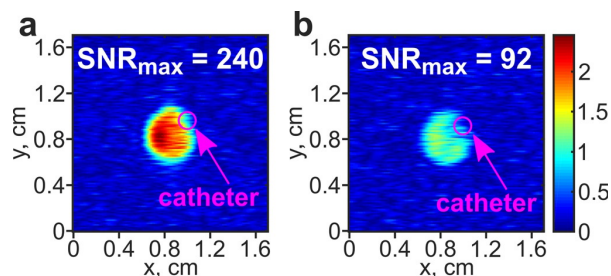

Figure 3. ^{1}H FLASH MRI of diethyl ether vapor in a 5 mm NMR tube (axial view): (a) continuously flowing (5.1 mL s^{-1} gas flow rate) hyperpolarized DE and (b) thermally polarized DE under stopped-flow conditions. The gas pressure was 3.9 bar. The images were acquired at 9.4 T. Frequency offset was adjusted to the signal of CH_3 group. The FLASH imaging parameters were: flip angle = 6°, number of averages = 2, acquisition time = 120 ms, matrix size = 128×16 (zero-filled to 128×128), FOV = 1.7 cm×1.7 cm, spatial resolution = 0.1×1.1 mm^2/pixel.

Chemistry–A European Journal

Full Paper
doi.org/10.1002/chem.202003638

Chemistry Europe
European Chemical
Societies Publishing

poral resolution of 120 ms. Moreover, we acquired a series of MR images over a period of several seconds after interruption of gas flow which show the gradual relaxation of HP DE to thermal equilibrium (Figure S3).

Conclusions

We demonstrated the hyperpolarization of diethyl ether vapor with P_{1H} of up to 1.3 % using heterogeneous hydrogenation of ethyl vinyl ether with parahydrogen over the Rh/TiO$_2$ catalyst. Polarization of diethyl ether partially survives its liquefaction, and this approach can be employed to prolong the lifetime of hyperpolarization. The feasibility of ^{1}H MRI of HP diethyl ether was also demonstrated. We envision that HP DE vapor can be employed as an inhalation contrast agent for pulmonary MRI. Diethyl ether surpasses propane in polarization levels and the HP state lifetime (under otherwise similar conditions and catalysts employed), and its long history of use for anesthesia will likely facilitate its clinical implementation. On the other hand, recent developments in HP propane production[30] and preservation[49] may be potentially extended to HP diethyl ether as well as to other ^{1}H-hyperpolarized gases. Comparing the presented approach to SEOP, one should note that at the same polarization level proton detection has ca. 6.9-fold greater sensitivity than that of ^{129}Xe due to higher gyromagnetic ratio.[50] Additional 3.8-fold sensitivity gain is provided by difference in natural abundance of corresponding nuclei, and 2-fold gain is obtained because HP DE molecule contains two HP nuclei. Therefore, HP DE with P_{1H} of 1.3 % will give as intense NMR signal as Xe gas with ≈68 % polarization; note that optimization of catalyst and polarizer setup may allow to further increase P_{1H}. Rapid relaxation of ^{1}H-hyperpolarized gases is translational challenge for clinical applications, but the fact that only several (2–3) seconds are required for inhalation[51] makes this approach viable especially in the context of long-lived spins states with lifetime of 3–4 s at physiologically relevant conditions. Flammability of DE (versus chemically inert HP ^{129}Xe) is a clear disadvantage of the presented method especially in the countries where DE has been phased out by halogenated inhalable anesthetics. Utilization of structurally similar partially fluorinated compounds in HP form which are potentially less flammable or even completely non-flammable is currently being investigated to mitigate this translational disadvantage.[52]

Experimental Section

The procedure for preparation of Rh/TiO$_2$ catalyst can be found in the Supporting Information. Ethyl vinyl ether (Sigma–Aldrich, 99 %), propylene and hydrogen were used as received. Hydrogen gas was enriched up to 85 % with the use of Bruker parahydrogen generator BPHG 90. The Scheme of experimental setup is presented in Figure 4. The mixture of ethyl vinyl ether vapor (or propylene) and 6.5-fold excess of H$_2$ was prepared in a tank. Gas flow rate was controlled using an Aalborg flow meter. The gas mixture passed through the 1/4 inch outer diameter (OD) stainless steel reactor containing 50 mg of Rh/TiO$_2$ catalyst between two pieces of fiberglass tissue. The reactor was heated to 200 °C using tubular fur-
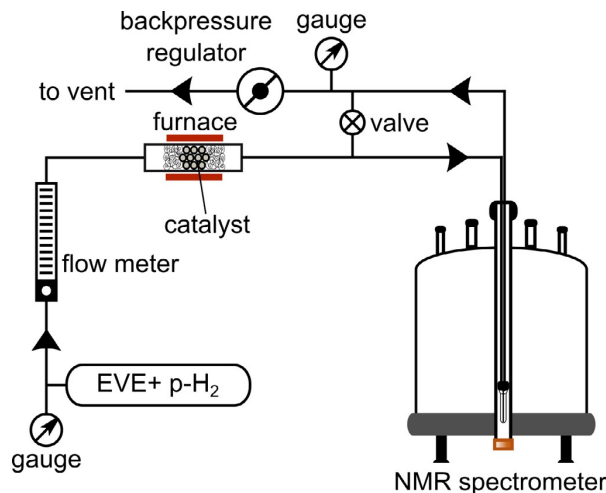

Figure 4. Scheme of the experimental setup used for hyperpolarization of diethyl ether via heterogeneous hydrogenation of ethyl vinyl ether with p-H$_2$ over Rh/TiO$_2$ catalyst.

nace. The resultant gas mixture was headed to a standard Wilmad 5 mm NMR tube tightly connected with 1/4 inch OD Teflon tubing via an Y-shape push-and-pull connector and located inside the NMR spectrometer. The NMR tube was heated to 50 °C in order to prevent condensation of diethyl ether (except for the liquefaction experiments in which the NMR tube was cooled to 0 °C). Thus, hydrogenation reaction occurred at the Earth's magnetic field and then the reaction products were transferred to the high magnetic field for detection, corresponding to ALTADENA experiment.[53] The resultant gas mixture was headed over to vent either directly or through a backpressure regulator set to 2.7 or 3.9 bar. All lines between the reactor and the NMR tube had the minimally required length and 1/32 inch inner diameter in order to minimize travel time of HP gas and subsequent losses of hyperpolarization due to relaxation phenomena. The by-pass valve was employed to rapidly interrupt the gas flow through the NMR tube.

NMR spectra were acquired on a 7.05 T Bruker AV 300 NMR spectrometer using a single 90° radiofrequency (rf) pulse. For acquisition of thermal spectra a 10 s delay between scans was introduced allowing for the relaxation of ^{1}H spins after each rf pulse. In case of acquisition of PHIP NMR spectra, such a long delay is not needed because these spectra were acquired under continuous flow conditions with the rapid and continuous replacement of gas in the NMR tube. Acquisition of thermal spectra under flow conditions leads to significant underestimation of thermal signal and hence overestimation of NMR signal enhancement.[24] Therefore, we used thermal spectra accumulated under stopped-flow conditions to calculate signal enhancements.

^{1}H MRI experiments were performed using the same experimental setup and the same procedure except that the reactor was heated using a heat gun set to 300 °C instead of the tubular furnace. The gas flow rate was 5.1 mL s^{-1}, the pressure was 3.9 bar. MR images were acquired on a 9.4 T Bruker NMR spectrometer with microimaging capabilities using FLASH (fast low angle shot) rf pulse sequence. The repetition time (TR) was 3 ms and the echo time (TE) was 1 ms. The number of averages was 2, the receiver gain (RG) was 2050. The acquisition spectral width (SW) was 10 kHz, and the spatial resolution was 0.1×1.1 mm^2/pixel, with the field of view of 1.7×1.7 cm^2. The 128×16 acquisition matrix was zero-filled to the

Chemistry–A European Journal

Full Paper
doi.org/10.1002/chem.202003638

Chemistry Europe
European Chemical
Societies Publishing

matrix size of 128×128. The phase encoding gradient had 3 G cm^{-1} strength of maximal value and 400 µs duration; the read-out gradient had 6 G cm^{-1} strength and 2 ms duration. The flip angle was 6°. No k-space filter was applied.

NMR spectra and MR images were acquired using TopSpin 2.1 and TopSpin 3.0 software, respectively. NMR spectra were analyzed using TopSpin 3.6.1. MR images were processed using MATLAB R2016b.

Conflict of interest

EYC declares a stake of ownership in XeUS Technologies LTD.

[1] N. J. Stewart, S. Matsumoto, *Magn. Reson. Med. Sci.* **2019**, https://doi.org/10.2463/mrms.rev.2019-0094.

[2] D. A. Barskiy, A. M. Coffey, P. Nikolaou, D. M. Mikhaylov, B. M. Goodson, R. T. Branca, G. J. Lu, M. G. Shapiro, V.-V. Telkki, V. V. Zhivonitko, I. V. Koptyug, O. G. Salnikov, K. V. Kovtunov, V. I. Bukhtiyarov, M. S. Rosen, M. J. Barlow, S. Safavi, I. P. Hall, L. Schröder, E. Y. Chekmenev, *Chem. Eur. J.* **2017**, *23*, 725–751.

[3] J.-B. Hövener, A. N. Pravdivtsev, B. Kidd, C. R. Bowers, S. Glöggler, K. V. Kovtunov, M. Plaumann, R. Katz-Brull, K. Buckenmaier, A. Jerschow, F. Reineri, T. Theis, R. V. Shchepin, S. Wagner, P. Bhattacharya, N. M. Zacharias, E. Y. Chekmenev, *Angew. Chem. Int. Ed.* **2018**, *57*, 11140–11162; *Angew. Chem.* **2018**, *130*, 11310–11333.

[4] C. Hani, N. H. Trieu, I. Saab, S. Dangeard, S. Bennani, G. Chassagnon, M. P. Revel, *Diagn. Interv. Imaging* **2020**, *101*, 263–268.

[5] M. El Homsi, M. Chung, A. Bernheim, A. Jacobi, M. J. King, S. Lewis, B. Taouli, *Eur. J. Radiol. Open* **2020**, *7*, 100239.

[6] M. J. Couch, I. K. Ball, T. Li, M. S. Fox, B. Biman, M. S. Albert, *J. Magn. Reson. Imaging* **2019**, *49*, 343–354.

[7] M. J. Couch, A. V. Ouriadov, M. S. Albert, *Hyperpolarized Inert Gas MRI From Technol. to Appl. Res. Med.* (Eds.: M. S. Albert, F. T. Hane), Academic Press, **2017**, pp. 279–292.

[8] P. Nikolaou, B. M. Goodson, E. Y. Chekmenev, *Chem. Eur. J.* **2015**, *21*, 3156–3166.

[9] C. Witte, L. Schröder, *NMR Biomed.* **2013**, *26*, 788–802.

[10] T. G. Walker, W. Happer, *Rev. Mod. Phys.* **1997**, *69*, 629–642.

[11] B. M. Goodson, *J. Magn. Reson.* **2002**, *155*, 157–216.

[12] D. M. L. Lilburn, G. E. Pavlovskaya, T. Meersmann, *J. Magn. Reson.* **2013**, *229*, 173–186.

[13] P. Nikolaou, A. M. Coffey, L. L. Walkup, B. M. Gust, N. Whiting, H. Newton, S. Barcus, I. Muradyan, M. Dabaghyan, G. D. Moroz, M. S. Rosen, S. Patz, M. J. Barlow, E. Y. Chekmenev, B. M. Goodson, *Proc. Natl. Acad. Sci. USA* **2013**, *110*, 14150–14155.

[14] P. Nikolaou, A. M. Coffey, L. L. Walkup, B. M. Gust, C. D. LaPierre, E. Koehnemann, M. J. Barlow, M. S. Rosen, B. M. Goodson, E. Y. Chekmenev, *J. Am. Chem. Soc.* **2014**, *136*, 1636–1642.

[15] J. P. Mugler, T. A. Altes, *J. Magn. Reson. Imaging* **2013**, *37*, 313–331.

[16] A. Ouriadov, A. Farag, M. Kirby, D. G. McCormack, G. Parraga, G. E. Santyr, *Magn. Reson. Med.* **2015**, *74*, 1726–1732.

[17] J. Xie, H. Li, H. Zhang, X. Zhao, L. Shi, M. Zhang, S. Xiao, H. Deng, K. Wang, H. Yang, X. Sun, G. Wu, C. Ye, X. Zhou, *NMR Biomed.* **2019**, *32*, e4068.

[18] C. R. Bowers, D. P. Weitekamp, *J. Am. Chem. Soc.* **1987**, *109*, 5541–5542.

[19] C. R. Bowers, D. P. Weitekamp, *Phys. Rev. Lett.* **1986**, *57*, 2645–2648.

[20] R. A. Green, R. W. Adams, S. B. Duckett, R. E. Mewis, D. C. Williamson, G. G. R. Green, *Prog. Nucl. Magn. Reson. Spectrosc.* **2012**, *67*, 1–48.

[21] S. B. Duckett, N. J. Wood, *Coord. Chem. Rev.* **2008**, *252*, 2278–2291.

[22] K. V. Kovtunov, I. E. Beck, V. I. Bukhtiyarov, I. V. Koptyug, *Angew. Chem. Int. Ed.* **2008**, *47*, 1492–1495; *Angew. Chem.* **2008**, *120*, 1514–1517.

[23] I. V. Koptyug, K. V. Kovtunov, S. R. Burt, M. S. Anwar, C. Hilty, S.-I. Han, A. Pines, R. Z. Sagdeev, *J. Am. Chem. Soc.* **2007**, *129*, 5580–5586.

[24] K. V. Kovtunov, V. V. Zhivonitko, I. V. Skovpin, D. A. Barskiy, I. V. Koptyug, *Top. Curr. Chem.* **2012**, *338*, 123–180.

[25] R. Zhou, E. W. Zhao, W. Cheng, L. M. Neal, H. Zheng, R. E. Quiñones, H. E. Hagelin-Weaver, C. R. Bowers, *J. Am. Chem. Soc.* **2015**, *137*, 1938–1946.

[26] E. W. Zhao, R. Maligal-Ganesh, C. Xiao, T. W. Goh, Z. Qi, Y. Pei, H. E. Hagelin-Weaver, W. Huang, C. R. Bowers, *Angew. Chem. Int. Ed.* **2017**, *56*, 3925–3929; *Angew. Chem.* **2017**, *129*, 3983–3987.

[27] K. V. Kovtunov, V. V. Zhivonitko, I. V. Skovpin, D. A. Barskiy, O. G. Salnikov, I. V. Koptyug, *J. Phys. Chem. C* **2013**, *117*, 22887–22893.

[28] K. V. Kovtunov, D. A. Barskiy, R. V. Shchepin, A. M. Coffey, K. W. Waddell, I. V. Koptyug, E. Y. Chekmenev, *Anal. Chem.* **2014**, *86*, 6192–6196.

[29] K. V. Kovtunov, D. A. Barskiy, A. M. Coffey, M. L. Truong, O. G. Salnikov, A. K. Khudorozhkov, E. A. Inozemtseva, I. P. Prosvirin, V. I. Bukhtiyarov, K. W. Waddell, E. Y. Chekmenev, I. V. Koptyug, *Chem. Eur. J.* **2014**, *20*, 11636–11639.

[30] O. G. Salnikov, P. Nikolaou, N. M. Ariyasingha, K. V. Kovtunov, I. V. Koptyug, E. Y. Chekmenev, *Anal. Chem.* **2019**, *91*, 4741–4746.

[31] K. V. Kovtunov, I. V. Koptyug, M. Fekete, S. B. Duckett, T. Theis, B. Joalland, E. Y. Chekmenev, *Angew. Chem. Int. Ed.* **2020**, *59*, 17788–17797; *Angew. Chem.* **2019**, *132*, 17940–17949.

[32] S. Korchak, S. Mamone, S. Glöggler, *ChemistryOpen* **2018**, *7*, 672–676.

[33] S. Korchak, M. Emondts, S. Mamone, B. Blümich, S. Glöggler, *Phys. Chem. Chem. Phys.* **2019**, *21*, 22849–22856.

[34] D. B. Burueva, K. V. Kovtunov, A. V. Bukhtiyarov, D. A. Barskiy, I. P. Prosvirin, I. S. Mashkovsky, G. N. Baeva, V. I. Bukhtiyarov, A. Y. Stakheev, I. V. Koptyug, *Chem. Eur. J.* **2018**, *24*, 2547–2553.

[35] D. A. Barskiy, O. G. Salnikov, K. V. Kovtunov, I. V. Koptyug, *J. Phys. Chem. A* **2015**, *119*, 996–1006.

[36] A. Kopanski, F. Hane, T. Li, M. Albert, *Proc. Intl. Soc. Mag. Reson. Med.* **2017**, *25*, 2162.

[37] R. D. Stewart, P. E. Newton, E. D. Baretta, *Environ. Health Perspect.* **1978**, *26*, 275–285.

[38] R. H. McKee, D. Herron, M. Saperstein, P. Podhasky, G. M. Hoffman, L. Roberts, *Int. J. Toxicol.* **2014**, *33*, 28S–51S.

[39] K. V. Kovtunov, M. L. Truong, D. A. Barskiy, I. V. Koptyug, A. M. Coffey, K. W. Waddell, E. Y. Chekmenev, *Chem. Eur. J.* **2014**, *20*, 14629–14632.

[40] J. Boyd, *Ulster Med. J.* **1946**, *15*, 58–77.

[41] O. G. Salnikov, K. V. Kovtunov, P. Nikolaou, L. M. Kovtunova, V. I. Bukhtiyarov, I. V. Koptyug, E. Y. Chekmenev, *ChemPhysChem* **2018**, *19*, 2621–2626.

[42] N. M. Ariyasingha, B. Joalland, H. R. Younes, O. G. Salnikov, N. V. Chukanov, K. V. Kovtunov, L. M. Kovtunova, V. I. Bukhtiyarov, J. G. Gelovani, E. Y. Chekmenev, *Chem. Eur. J.* **2020**, *26*, 13621–13626.

[43] J. Schüttler, H. Schwilden, Eds., *Modern Anesthetics*, Springer, Heidelberg **2008**.

[44] R. E. D. McClung, *Encycl. Magn. Reson.* **1961**, https://doi.org/10.1002/9780470034590.emrstm0524.

[45] D. A. Barskiy, K. V. Kovtunov, E. Y. Gerasimov, M. A. Phipps, O. G. Salnikov, A. M. Coffey, L. M. Kovtunova, I. P. Prosvirin, V. I. Bukhtiyarov, I. V. Koptyug, E. Y. Chekmenev, *J. Phys. Chem. C* **2017**, *121*, 10038–10046.

[46] I. V. Skovpin, V. V. Zhivonitko, R. Kaptein, I. V. Koptyug, *Appl. Magn. Reson.* **2013**, *44*, 289–300.

[47] K. V. Kovtunov, M. L. Truong, D. A. Barskiy, O. G. Salnikov, V. I. Bukhtiyarov, A. M. Coffey, K. W. Waddell, I. V. Koptyug, E. Y. Chekmenev, *J. Phys. Chem. C* **2014**, *118*, 28234–28243.

[48] N. M. Ariyasingha, O. G. Salnikov, K. V. Kovtunov, L. M. Kovtunova, V. I. Bukhtiyarov, B. M. Goodson, M. S. Rosen, I. V. Koptyug, J. G. Gelovani, E. Y. Chekmenev, *J. Phys. Chem. C* **2019**, *123*, 11734–11744.

[49] D. A. Barskiy, O. G. Salnikov, A. S. Romanov, M. A. Feldman, A. M. Coffey, K. V. Kovtunov, I. V. Koptyug, E. Y. Chekmenev, *J. Magn. Reson.* **2017**, *276*, 78–85.

[50] J. H. Lee, Y. Okuno, S. Cavagnero, *J. Magn. Reson.* **2014**, *241*, 18–31.

[51] M. Chen, O. Doganay, T. Matin, A. McIntyre, N. Rahman, D. Bulte, F. Gleeson, *Eur. J. Radiol.* **2020**, *30*, 1145–1155.

[52] B. Joalland, N. M. Ariyasingha, H. R. Younes, S. Nantogma, O. G. Salnikov, N. V. Chukanov, K. V. Kovtunov, I. V. Koptyug, J. G. Gelovani, E. Y. Chekmenev, *Chem. Eur. J.* **2020**, https://doi.org/10.1002/chem.202004168.

[53] M. G. Pravica, D. P. Weitekamp, *Chem. Phys. Lett.* **1988**, *145*, 255–258.

Toward clinical-scale heterogeneous hyperpolarization of propane gas at 1 atm

Nuwandi M. Ariyasingha[1], Anna Samoilenko,[1] Larisa Kovtunova,[2] Igor V. Koptyug,[2] Eduard Y. Chekmenev[1,2]

[1]Department of Chemistry, Ibio, Karmanos Cancer Institute, Wayne State University, Detroit, MI 48202, USA
[2]International Tomography Center, SB RAS, Institutskaya St. 3A, 630090 Novosibirsk, Russia
[3]Russian Academy of Sciences, Leninskiy Prospekt 14, Moscow 119991, Russia

Our long-term goal is to develop *proton*-hyperpolarized (HP) propane as inhalable contrast agent for ultrafast pulmonary imaging. In this work, we study the feasibility of HP propane production at physiologically relevant condition of 1 atm total pressure via heterogeneous parahydrogen addition to propylene substrate (Figure 1a) using fast pseudo 2D signal acquisition method and 1.4 T bench-top NMR spectrometer (Nanalysis NMR Pro60), Figure 1b, and 87% parahydrogen generator.

The effect of the gas flow of the mixture of propylene and parahydrogen was studied over a wide range of flow rates from 620 standard cubic centimeters (sccm) – 8800 sccm using a gas phase heterogeneous hydrogenation reaction carried out at outer reactor temperature of 100 °C. We observe substantial dependence of proton signal enhancement (SE) of Ha and Hb protons on the gas flow rate, Figure 1c, with SE increasing at higher flow rates.

Figure 1. a) PHIP reaction to produce HP propane via heterogeneous hydrogenation. b) Pseudo 2D acquisition of HP propane signal. c) and d) HP propane signal enhancement dependence on gas flow rate and flow duration respectively.

HP propane SE dependence on total reactor pressure was studied with respect to different reactor pressure values for a 1:1 gas mixture of propylene and parahydrogen. However, reactor pressure does not seem to have a significant effect in the range of the pressure values studied in this work, Figure 1d. A detailed study of pressure dependence for variable gas compositions will be presented. These findings bode well for developing disposable clinical-scale hyperpolarizer operating at 1 atm (physiological condition).

References: (1) Ariyasingha, N.M.; Salnikov, O.G.; et al, Relaxation Dynamics of Nuclear Long-Lived Spin States in Propane and Propane-d$_6$ Hyperpolarized by Parahydrogen. *J. Phys. Chem. C* **2019**, *18* (123), 11734–11744.
(2) Birchall, J. R.; Irwin, R. K.; Chowdhury, M. R. H.; et al, Automated Low-Cost In Situ IR and NMR Spectroscopy Characterization of Clinical-Scale ^{129}Xe Spin-Exchange Optical Pumping. *Anal. Chem.* **2021**, *93* (8), 3883-3888

Low-cost High-Pressure Clinical-Scale Parahydrogen Generator Using Liquid Nitrogen at 77 K

Benjamin Chapman,[a,b] Baptiste Joalland,[c] Collier Meersman,[b] Jessica Ettedgui,[d] Rolf E. Swenson,[d] Murali C. Krishna,[e] Panayiotis Nikolaou,[f] Kirill V. Kovtunov,[g,h] Oleg G. Salnikov,[g,h,i] Igor V. Koptyug,[g,h] W. Michael Snow,[j] Max E. Gemeinhardt,[k] Boyd M. Goodson,[k,l] Roman V. Shchepin,[b] and Eduard Y. Chekmenev[c,m]

[a] Department of Materials and Metallurgical Engineering, [b] Department of Chemistry, Biology, and Health Sciences, South Dakota School of Mines and Technology, Rapid City, SD USA; [c] Department of Chemistry, Integrative Biosciences, Wayne State University, Karmanos Cancer Institute, Detroit, MI USA; [d] Chemistry and Synthesis Center, National Heart, Lung, and Blood Institute, Rockville, MD USA; [e] Center for Cancer Research, National Cancer Institute, National Institutes of Health, Bethesda, MD USA; [f] XeUS Technologies LTD, Nicosia, Cyprus; [g] International Tomography Center, [h] Novosibirsk State University, [i] Boreskov Institute of Catalysis SB RAS, Novosibirsk, Russia; [j] Department of Physics, Indiana University, Bloomington, IN USA; [k] Department of Chemistry and Biochemistry, [l] Materials Technology Center, Southern Illinois University, Carbondale, IL USA; [m] Russian Academy of Sciences, Moscow, Russia.

Parahydrogen Induced Polarization (PHIP) is a simple and fast hyperpolarization approach, which has the potential to revolutionize clinical production of HP contrast agents. Parahydrogen (p-H_2) is employed as a source of polarization by PHIP. P-H_2 is produced by transient exposure of normal dihydrogen gas (25% para- and 75% ortho- states) to a low-temperature in the presence of a suitable catalyst. Because p-H_2 is a lower energy state, the equilibrium shifts to para-state at sufficiently cold temperatures. Nearly 100% p-H_2 can be obtained at $\leq$20 K. When the pure p-H_2 is employed for PHIP, near unity proton polarization can be unlocked after the magnetic symmetry of the nascent p-H_2-derived protons is broken. Moreover, in both hydrogenative PHIP and its non-hydrogenative variant SABRE, it has been demonstrated that the polarization of nascent p-H_2-derived protons can be transferred via the network of spin-spin couplings to other spin-1/2 nuclei including ^{13}C, ^{15}N, ^1H, ^{31}P, ^{19}F, and others. Nuclear spin polarization (P) values in excess of 50% have been demonstrated, when polarization transfer is optimized using pure p-H_2 gas. A wide range of biologically relevant compounds have been hyperpolarized via PHIP and SABRE.

The hardware required to accomplish polarization transfer in PHIP and SABRE is relatively straightforward and low cost (ca. $10,000), because no cryogenic- and high-field hardware is required. However, the requirement of pure p-H_2 necessitates the use of cryogenic equipment in the range of $50,000-125,000 (e.g., Bruker or ARS generators), representing a substantial investment and a barrier for those working in or entering the field of p-H_2-based hyperpolarization. To mitigate the cost and complexity of cryogenic hardware, p-H_2 production can be conducted at liquid N_2 temperature (ca. 77 K at 1 atm) resulting in ~50% p-H_2 fraction. The key disadvantage of using 50% (versus near 100%) p-H_2 is the reduction of the resulting hyperpolarization effect by a factor of ~3.0. Such substantial polarization decrease is unforgiving for in vivo studies. However, many other applications including the development phase of PHIP and SABRE-based contrast agents can be accomplished with this 'lower' p-H_2 grade.

We report on robust and inexpensive design of p-H_2 generator (o-p catalyst-filled copper tubing spiral, Figure 1a) for operation at up to 35 atm with liquid N_2. The produced exiting p-H_2 gas is quantified by 'real-time' NMR spectroscopy using bench-top 1.4 T NMR spectrometer (Figure 1b-c). The design reproducibility has been evaluated with N=3 devices. Moreover, we have also investigated ortho-para catalyst activation using exposure to high temperature to achieve production rate of 1,000 sccm with ~48% p-H_2 fraction. We anticipate the reported design can be employed
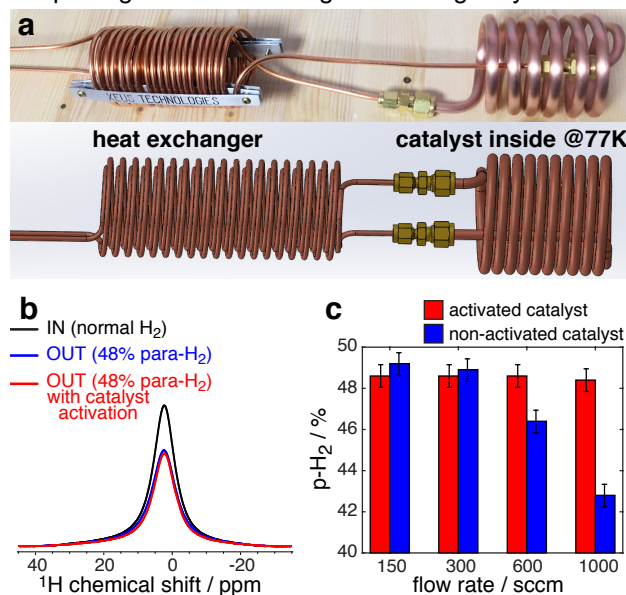

Figure 1. a) Annotated photo and CAD of p-H_2 generator for operation in liquid N_2 bath (77 K); b) Hyperpolarizer front panel; c) Parahydrogen quantification using 1.4 T bench-top NMR spectrometer using 8 atm gas samples: 1024 scans, SW=5 kHz, t_{acq}=52 ms, ~102 s experimental time. c) p-H_2 enrichment dependence on flow rate.

for p-H_2 production at higher flow rates of up to 4,000 sccm (1). The utility of the reported device has been tested in the feasibility demonstration of [1-^{13}C]pyruvate hyperpolarization using SABRE-SHEATH hyperpolarization technique.

Taken together the reported design augmented by real time p-H_2 quantification using benchtop NMR spectroscopy will be of interest to those working in the field of NMR hyperpolarization and p-H_2-based hyperpolarization.

REFERENCES: **1)** Nantogma et al. Anal. Chem. **2021**, 10.1021/acs.analchem.0c05129. **2)** Chapman et al. in preparation.

Pilot Quality Assurance Study of Batch-Mode Clinical-Scale Automated Generation-3 Xenon-129 Hyperpolarizer

Md Raduanul H. Chowdhury,[1] Jonathan R. Birchall,[1] Peter Nikolaou,[2] Michael J. Barlow,[3] Anton Shcherbakov,[4,5] Boyd M. Goodson,[6] Eduard Y. Chekmenev[1,7]

[1] Department of Chemistry, Ibio, Karmanos Cancer Institute, Wayne State University, Detroit, MI 48202, USA
[2] XeUS Technologies LTD, Nicosia, Cyprus
[3] Sir Peter Mansfield Imaging Centre, University of Nottingham, Nottingham, NG7 2RD, United Kingdom
[4] Smart-A, Perm, Perm Region, 614000, Russia, [5] Custom Medical Systems (CMS) LTD, Nicosia, Cyprus
[6] Department of Chemistry and Biochemistry, Southern Illinois University, Carbondale, Illinois 62901, USA
[7] Russian Academy of Sciences, Moscow, 119991, Russia

Assessing lung tissue structure and function has been challenging by using conventional methods like CT and X-ray. They provide only the structural morphology of the lungs and employ ionizing radiation. Low proton density of the lung tissues and B_0 susceptibility artifacts make conventional pulmonary MRI challenging. Hyperpolarized (HP) noble gases such as ^{3}He, ^{83}Kr and ^{129}Xe have been successfully employed in various MR lung applications, *e.g.*, ventilation, diffusion and gas exchange. NMR hyperpolarization increases the nuclear spin polarization well above the thermal equilibrium levels, offering the advantages of improved signal-to-noise ratio (SNR) in the context of HP nuclear spin detection. ^{129}Xe hyperpolarization is typically performed via the two-step Spin-Exchange Optical Pumping (SEOP) process. Firstly, Rb electrons are polarized by the laser beam at the gaseous stage by absorbing photon in the Rb absorption line (D_1~795nm). Second, Rb electronic spin polarization (P_{Rb}) is transferred to ^{129}Xe nuclear spins. SEOP can be performed using continuous-flow or stopped-flow (a.k.a. batch-mode) approaches. Here, we employ the process of stopped-flow SEOP, where a 0.5 L cell is filled with a 2000 Torr mixture containing 50% natural-abundance Xe and 50% N_2 buffer gas to produce 0.8 L of HP ^{129}Xe-containing mixture after ejection in a Tedlar bag (1-3).

Rb acting as spin-exchange intermediary metal is hardly consumed during the SEOP process, but it is slowly degraded during the SEOP cell refill process by residual oxygen and moisture resulting in a decrease of the HP ^{129}Xe in-cell T_1 over time. The reduced T_1 dramatically alters HP ^{129}Xe build-up time (T_b) and decreases the achievable steady-state maximum ^{129}Xe polarization ($\%P_{max}$). Eventually, HP gas starts relaxing too fast to provide any meaningful data, and a cell replacement with new metal and gas mixture is required. For the application of HP ^{129}Xe for clinical purposes, consistency from one production cycle to another is a significant factor, as clinical setup demands a high level of reproducibility to be effective and robust. Therefore, it is required that the SEOP cell can be refilled numerous times without substantial loss in performance. Moreover, replacing the SEOP cell is time-consuming, involves the cost of chemicals and labor, and interrupts daily operations.

Here, we report a pilot Quality Assurance (QA) study in our third generation XeUS (GEN-3) ^{129}Xe hyperpolarizer, Figure 1a-c. First, we employ device calibration to evaluate the robust device performance range. We have systematically studied the robust device operation via frequency sweep, electromagnet current sweep, RF pulse duration sweep, SEOP jacket temperature sweep and others. Moreover, following polarization build-up on the initial gas mixture fill, the SEOP cell was refilled with interleaved N_2 and Xe/N_2 gas mixtures. When polarization build-up was repeated, we observed no substantial deterioration of SEOP cell performance even with ~600 gas mixture refills of the SEOP cell (in first fill $\%P_{max}$ = 63.9±2.1%, T_b = 23.1±2.1 mins and after 600 refills $\%P_{max}$ = 49.4±1.6%, T_b = 22.8±1.9 mins), Figure 1d. The reproducibility of HP ^{129}Xe contrast agent production with excellent $\%P_{max}$, and fast polarization buildup rates will be instrumental for our future *in vivo* studies.
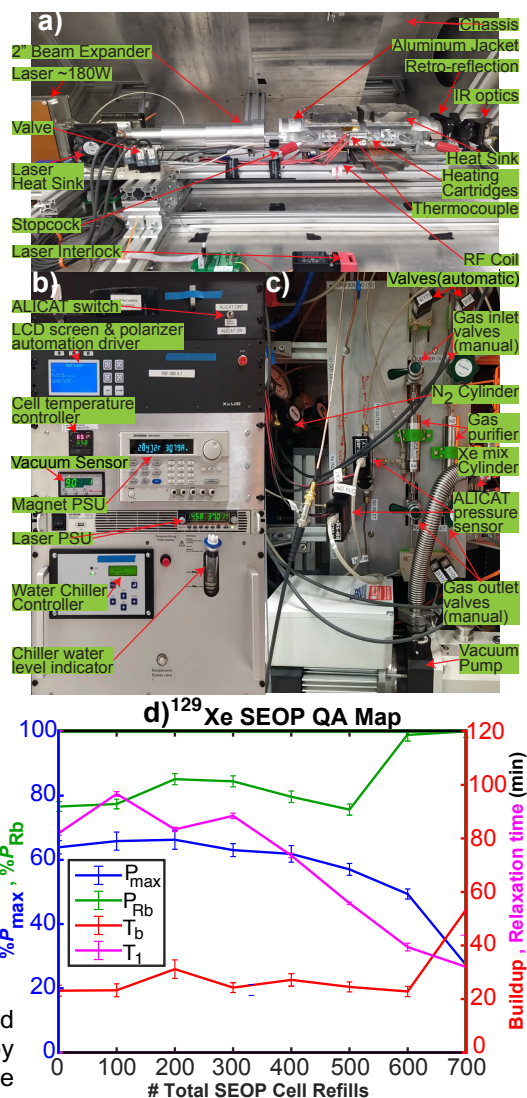

Figure 1. a) Annotated photo of open upper chassis of GEN-3 hyperpolarizer; b) Hyperpolarizer front panel; c) Internal hyperpolarizer gas-handling manifold; d) QA study data of ^{129}Xe polarization ($\%P_{max}$), Rb polarization (P_{Rb}), buildup time-constant (T_b) and relaxation time (T_1) as a function of the SEOP cell refill cycle count at 75 °C.

REFERENCES: (1) Birchall, J.R., et al., *J. Mag. Reson.* **2020**, *316*, 106755. **(2)** Birchall, J.R., et al., *Anal. Chem.* **2021**, DOI 10.1021/acs.analchem.0c04545h. **(3)** Birchall, J. R.; et al. *Anal. Chem.* **2020**, *92*, 4309-4316.

Automated Low-Cost *in situ* IR and NMR Spectroscopy for Clinical-Scale ^{129}Xe Spin-Exchange Optical Pumping

Jonathan Birchall,[1] Robert K. Irwin,[2] Md Raduanul H. Chowdhury,[1] Panayiotis Nikolaou,[3] Boyd M. Goodson,[4,5] Michael J. Barlow,[2] Anton Shcherbakov,[6,7] and Eduard Y. Chekmenev[1,8]

[1]Dept. Chemistry, Integrative Biosciences, Karmanos Cancer Institute, Wayne State University, Detroit, MI 48202, USA
[2]Sir Peter Mansfield Imaging Centre, University of Nottingham, Nottingham, NG7 2RD, United Kingdom
[3]XeUS Technologies LTD, Nicosia, Cyprus
[4]Dept. Chemistry and Biochemistry, [5]Materials Technology Center, Southern Illinois University, Carbondale, IL 62901, USA
[6]Smart-A, Perm, Perm Region, 614000, Russia, [7]Custom Medical Systems (CMS) LTD, Nicosia, Cyprus
[8]Russian Academy of Sciences, Leninskiy Prospekt 14, Moscow, 119991, Russia

Hyperpolarized (HP) ^{129}Xe Nuclear Magnetic Resonance (NMR) facilitates pre-clinical and clinical biomedical imaging within the lungs, brain and brown fat tissue. Spin-Exchange Optical Pumping (SEOP) is employed to overcome the inherently poor signal-to-noise ratio (SNR) afforded by the low natural abundance and gyromagnetic ratio of the ^{129}Xe nucleus, significantly increasing the net nuclear spin polarization above that found at thermal equilibrium. This technique combines the processes of optical pumping, involving spin angular momentum transfer from circularly polarized laser photons to electronic spins of rubidium vapor, and spin-exchange via Fermi contact interactions with ^{129}Xe nuclei (1,2). Many parameters define the SEOP process efficiency, including temperature, gas mixture composition, pump laser power and frequency, constituent purity and others, and there is substantial difficulty in precisely monitoring and optimizing these many interdependent variables.

Hyperpolarization via "batch-mode" SEOP—utilizing a fixed volume of typically Xe-rich gas mixture inside a sealed vessel for a specific time frame before ejection and refill—in particular is conducive to real-time, *in situ* monitoring of SEOP performance via near-infrared (NIR) and low-field NMR spectroscopic techniques. Previous studies have highlighted the potential for high ^{129}Xe polarization (P_{Xe}) levels and fast polarization build-up rates (γ_{SEOP}) at high Xe densities and partial pressures on a clinical production scale.(3) Comparison of the pump laser transmission profile before, during, and after SEOP can provide valuable information on photon absorption and Rb polarization,(3,4) whereas localized, low-frequency NMR sensing allows determination of the ^{129}Xe nuclear spin polarization, build-up rate, and relaxation rate.(5) The combination of these two spectroscopic techniques has been used to quantify the benefits of numerous scientific advances in the field and provide an estimation of SEOP cell "health".(3)

Here, we present two recent advances in performing low-cost, automated NMR and NIR spectroscopy for monitoring clinical scale HP ^{129}Xe contrast agent production efficiency in our second- and third-generation XeUS hyperpolarizers.(6) Firstly, we describe low-cost NMR (**Figure 1a**) and NIR spectrometers to acquire spectroscopic data at a total investment of less than $1,500—more than an order of magnitude lower than previous hyperpolarizer designs. This methodology enables a robust and accessible approach for quantifying efficient production of HP ^{129}Xe (**Figure 1b,c**) on a clinical scale for various hyperpolarizer designs. Additionally, we describe an automated, bi-modal data analysis protocol capable of extracting key parameters describing the SEOP process and HP ^{129}Xe production efficiency, such as predicted and observed ^{129}Xe polarization values (P_{Xe}), Rb-^{129}Xe spin-exchange rate, γ_{SE}, ^{129}Xe polarization build-up and relaxation rates, γ_{SEOP} and $1/T_1$, and estimates of Rb polarization, P_{Rb}, all as functions of time and/or SEOP cell temperature. This protocol is written in the open-source MATLAB code, offering a high degree of automation and reproducibility, as well as graphical representation (**Figure 1d**) for easier identification of trends, maxima, outliers, and other points of interest, irrespective of hardware or production modality utilized. When combined, these advances should be of practical translational importance to pre-clinical and clinical studies involving production and subsequent biomedical imaging of HP ^{129}Xe.
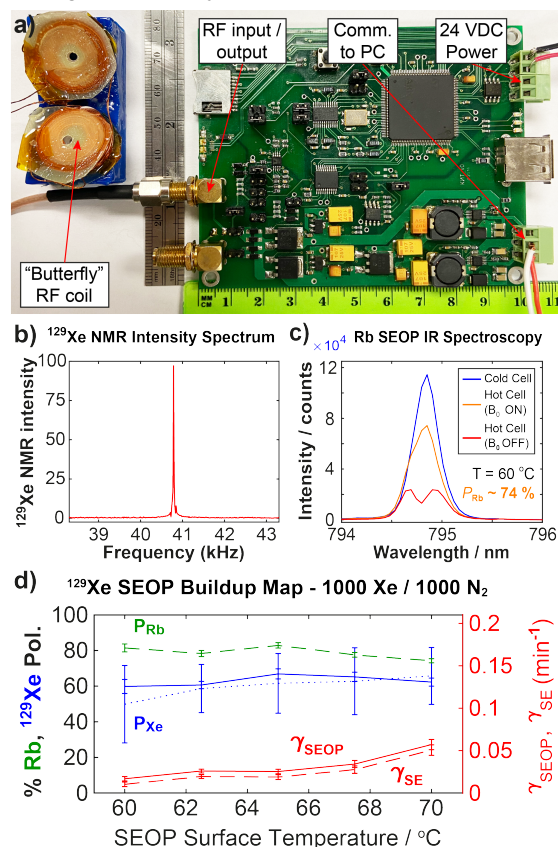

Figure 1. a) Low-cost NMR spectrometer and noise-canceling "butterfly" RF coil; b,c) HP ^{129}Xe NMR spectrum and NIR spectra from low-cost NMR and NIR spectrometers; d) MATLAB-generated plot of key steady-state SEOP parameters observed as a function of SEOP cell temperature via automated analysis protocol.(6)

REFERENCES: (**1**) Walker, T.G., Happer, W., *Rev. Mod. Phys.* **1997,** *69* (2), 629-642. (**2**) Walker, T.G., *J. Phys. Conf. Ser.* **2011,** *294*, 012001. (**3**) Birchall, J.R., et al., *J. Mag. Reson.* **2020,** *316*, 106755. (**4**) Saha, I., et al., *Chem. Phys. Lett.* **2006,** *428* (4-6), 268–276. (**5**) Romalis, M., Cates, G. D., *Phys. Rev. A* **1998**, 58, 3004 (**6**) Birchall, J.R., et al., *Anal. Chem.* **2021**, ac-2020-04545h.R1 under review.

Next-Generation Equipment for Parahydrogen-Based Hyperpolarization Experiments

Shiraz Nantogma,[a] Baptiste Joalland,[a] Ken Wilkens[b] and Eduard Y. Chekmenev[a,c]

[a] Department of Chemistry, Integrative Biosciences (Ibio), Wayne State University, Detroit, Michigan, 48202, United States
[b] Vanderbilt University Institute of Imaging Science (VUIIS), Nashville, Tennessee 37232-2310, United States
[c] Russian Academy of Sciences, Leninskiy Prospekt 14, Moscow, 119991, Russia

Parahydrogen-based polarization (PHIP) methods lead to enhancement of NMR signals by several orders of magnitude and have significant potential for translation to biomedical imaging. The effectiveness of parahydrogen-based hyperpolarization experiments depends on the level of parahydrogen enrichment and the manipulation of reaction conditions such as temperature, magnetic field, sample shuttling and sample detection times. Here, we present equipment for the clinical-scale production of >98.5% enriched parahydrogen (up to 4 standard liters per min) and its quantification by benchtop NMR spectroscopy. We also present an integrated polarizer (mark 2.2) for PHIP experiments via p-H_2 bubbling and the use microtesla magnetic fields.

Parahydrogen Generator: We employed a 3/16 in. outside diameter cleaned copper spiral tubing filled with iron-oxide catalyst and coiled in 9 turns (1). This tubing is attached to a copper cylinder which is mated to a cold head (Fig. 1a-c). The cold head is cooled by a helium compressor with a self-contained cooling system without the need of the external water-cooling source. This setup together with a pulsed injection of normal hydrogen through a loop of copper tubing (6.5 mL) produces >98.5% p-H_2 at a maximum rate of 4 standard liters per minute. Moreover, by the direct coupling of the exiting p-H_2 to a benchtop NMR spectrometer at a pressure of 8 bar, parahydrogen is easily and conveniently quantified using nearly real-time NMR spectroscopy without the need for sample preparation and transportation to high-field NMR spectrometers.

Integrated Microtesla PHIP Polarizer: To optimize the performance, reproducibility and convenience of our ongoing multi-nuclear PHIP studies, we integrated all critical components needed to perform a wide range of SABRE and hydrogenative PHIP experiments in microtesla magnetic fields ranging from fixed magnetic field needed for some SABRE-SHEATH experiments to complex magnetic field profiles employed in magnetic field sweeping/cycling experiments (2). The device dimensions are 24" (depth), 18" (width), and 18" (height). The system consists of the following critical components: mu-metal shield (ZG-203 or ZG-206) equipped with homogeneous solenoid magnet; non-magnetic variable-temperature module: 20-60 °C; automated ultrafast (<3 s) robust degaussing unit: 10 nT residual field; pressure regulator; mass flow controller for parahydrogen flow regulation; gas manifold for parahydrogen bubbling in a wide range of containers including standard 5-mm NMR tubes at 8 bar. Electromagnet is operated in series with calibrated variable resistor bank for control the field inside the magnetic shied using internal (fixed) or external (wave-form generator) power sources. The utility of the device is expanded by adjacent bench-top NMR spectrometer (SpinSolve by Magritek or NMRPro by Nanalysis) for quantification of produced hyperpolarized states, Fig. 1d.
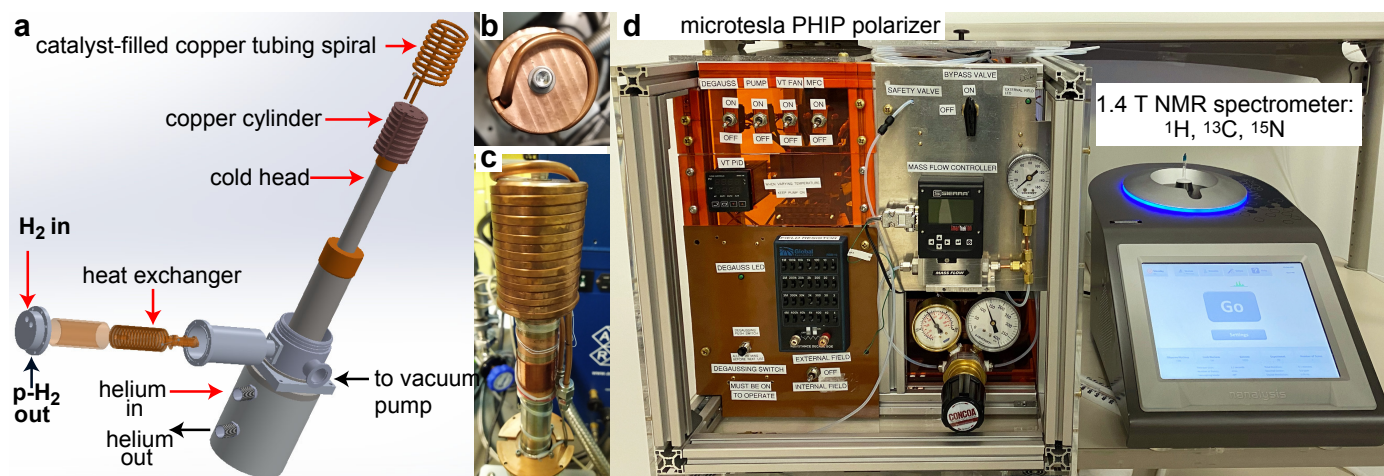

Figure 1. a) Annotated 3D rendering of cold head assembly; b) Top view of catalyst chamber with the top winding running along the length of copper core; c) Side view of catalyst chamber sitting on the cold head. The tubing employed in the heat exchanger is made of stainless steel; d) Integrated microtesla PHIP polarizer (mark 2.2) and a benchtop 1.4 T ^{1}H/^{13}C/^{15}N NMR spectrometer on a portable laboratory bench.

REFERENCES: **(1)** Nantogma, S.; Joalland, B.; Wilkens, K.; Chekmenev, E. Y., *Anal. Chem.* **2021**, DOI 10.1021/acs.analchem.0c05129. **(2)** Nantogma, S.; et al., manuscript in preparation.

Parahydrogen hyperpolarized diethyl ether for MRI

Nuwandi M. Ariyasingha[1], Oleg G. Salnikov[2,3,4], Baptiste Joalland[1], Hassan R. Younes[1] Nikita V. Chukanov[2,3], Kirill V. Kovtunov[2,3], Larisa M. Kovtunova[3,4], Valerii I. Bukhtiyarov[3,4], Igor V. Koptyug[2,3], Juri G. Gelovani[1,5] and Eduard Y. Chekmenev[1,6]

[1]Department of Chemistry, Ibio, Karmanos Cancer Institute, Wayne State University, Detroit, MI 48202, USA.
[2]International Tomography Center SB RAS, Novosibirsk, Russia.
[3]Department of Natural Sciences, Novosibirsk State University, Novosibirsk, Russia.
[4] Boreskov Institute of Catalysis SB RAS, Novosibirsk, Russia.
[5] United Arab Emirates University, Al Ain, United Arab Emirates.
[6] Russian Academy of Sciences, Leninskiy Prospekt 14, Moscow 119991, Russia.

We report successful preparation of hyperpolarized (HP) diethyl ether (DE) anesthetic using a fast and simple approach via Parahydrogen Induced Polarization (PHIP) experiments [1,2]. The existence of long-lived spin states (LLS) in HP DE was also investigated using Spin-Lock Induced Crossing (SLIC) [3].

HP DE was prepared using homogeneous hydrogenation reaction of parahydrogen gas and ethyl vinyl ether precursor and was characterized using ^{1}H NMR spectroscopy at 1.4 T and 47.5 mT magnetic fields. High proton polarization value (>8 %) of HP DE is reported with complete chemical conversion in the weakly coupled regime thus giving rise to radio amplification by stimulated emission of radiation (RASER [5]) conditions. A systematic study of HP DE hydrogenation kinetics and a relaxation study were also performed under homogeneous catalysis. T_1 values were recorded for HP DE in both liquid and vapor phases and the reported lifetimes range are 20-29 s and 1.2 s respectively. Creation of LLS of HP DE gas at the low field (47.5 mT) was successfully achieved with approximately 3-fold increase in the lifetime ($T_S \sim 4$ s) of the HP molecule at clinically relevant conditions resulting in promising application of HP DE as an inhalable contrast agent for pulmonary imaging in the future.

Although HP DE displays promising results as a good candidate for HP MRI (Figure 1) [2], a key issue preventing it from being used as a contrast agent is its flammability. We also demonstrate the use of fluorination to address the flammability in HP DE and many other structurally similar motifs amenable to PHIP in a recent study where fluorination lowered the flammability levels of the contrast agents while retaining the polarization levels [4]. DE has a long-standing history of inhalable anesthetic utility (still approved in many countries) and we envision the use of HP DE as inhalable contrast agent for functional pulmonary MRI. We thank our funders: NSF CHE-1904780, DOD CDMRP W81XWH-15-1-0271 and W81XWH-20-1-0576.
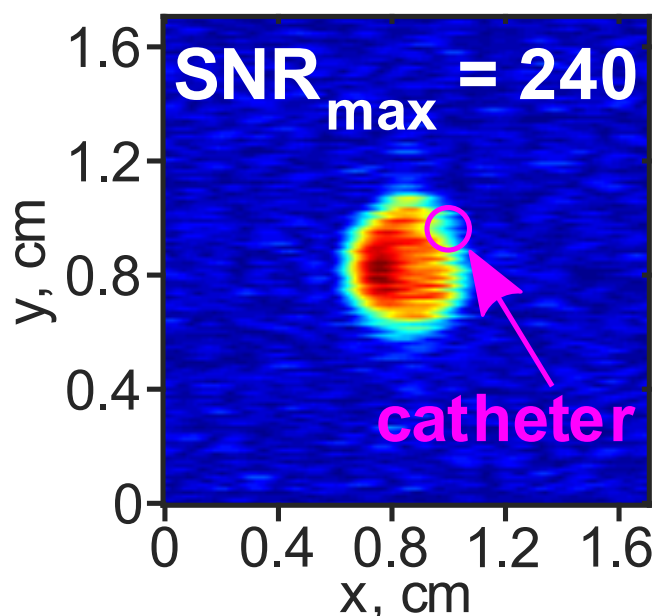
Figure 1. ^{1}H FLASH MRI of diethyl ether vapor in a 5 mm NMR tube (axial view): continuously flowing (5.1 mL/s gas flow rate) hyperpolarized DE. The gas pressure was 3.9 bar. The images were acquired at 9.4 T. Frequency offset was adjusted to the HP signal of CH_3 group. The FLASH imaging parameters were: flip angle = 6˚, number of averages = 2, acquisition time = 120 ms, matrix size = 128×16 (zero-filled to 128×128), FOV = 1.7 cm × 1.7 cm, spatial resolution = 0.1×1.1 mm^2/pixel.

References
(1) Ariyasingha, N. M.; Joalland, B.; Younes, H. R.; Salnikov, O. G.; Chukanov, N. V.; Kovtunov, K. V.; Kovtunova, L. M.; Bukhtiyarov, V. I.; Koptyug, I. V.; Gelovani, J. G.; Chekmenev, E. Y., *Chem. -Eur. J.* 2020. doi 10.1002/chem.202002528. (2) Salnikov, O. G.; et al. *Chem. Eur. J.* **2020**, DOI 10.1002/chem.202003638. (3) DeVience, S.J.; Walsworth, R.L.; Rosen, M.S. *Phys. Rev. Lett.* **2013,** *111*, 173002. (4) Joalland, B.; Ariyasingha, N. M.; Younes, H. R.; Salnikov, O. G.; Chukanov, N. V.; Kovtunov, K. V.; Kovtunova, L. M.; Bukhtiyarov, V. I.; Koptyug, I. V.; Gelovani, J. G.; Chekmenev, E. Y., *Chem. -Eur. J.* 2020. Accepted. (5) Joalland, B.; et al. *Angew. Chem. Int. Ed.* **2020,** *132* (22), 8732-8738

SABRE Hyperpolarization of Sodium [1-^{13}C]Pyruvate Using Our Low-cost High-Pressure Clinical-Scale Liquid Nitrogen-Based Parahydrogen Generator

Benjamin Chapman[1,2], Baptiste Joalland[3], Collier Meersman[2], Jessica Ettedgui[4], Rolf E. Swenson[4], Murali C. Krishna[5], Panayiotis Nikolaou[6], Kirill V. Kovtunov[7,8], Oleg G. Salnikov[7,8,9], Igor V. Koptyug[7,8], Max E. Gemeinhardt[10], Boyd M. Goodson[10,11], Roman V. Shchepin[2] and Eduard Y. Chekmenev[3,11]

[1]Department of Materials and Metallurgical Engineering, South Dakota School of Mines & Technology, Rapid City, SD USA
[2]Department of Chemistry, Biology, and Health Sciences, South Dakota School of Mines & Technology, Rapid City, SD USA
[3]Department of Chemistry, Integrative Biosciences, Wayne State University, Karmanos Cancer Institute, Detroit, MI USA
[4]Chemistry and Synthesis Center, National Heart, Lung, and Blood Institute, Rockville, MD USA
[5]Center for Cancer Research, National Cancer Institute, National Institutes of Health, Bethesda, MD USA
[6]XeUS Technologies LTD, Nicosia, Cyprus
[7]International Tomography Center, Novosibirsk, Russia
[8]Novosibirsk State University, Novosibirsk, Russia
[9]Boreskov Institute of Catalysis SB RAS, Novosibirsk, Russia
[10]Department of Chemistry and Biochemistry, Southern Illinois University, Carbondale, IL USA
[11]Materials Technology Center, Southern Illinois University, Carbondale, IL USA
[12]Russian Academy of Sciences, Moscow, Russia

Parahydrogen Induced Polarization (PHIP) is a simple and fast hyperpolarization approach, which holds the key to revolutionizing clinical production of HP contrast agents. Parahydrogen (p-H$_2$) is employed as a source of polarization by both hydrogenative PHIP and its non-hydrogenative variant (SABRE) allowing hyperpolarization of a wide range of biologically relevant compounds. In those cases, p-H$_2$-derived polarization is often transferred to other spin-1/2 nuclei including ^{13}C, ^{15}N, ^{1}H, ^{31}P, ^{19}F, and others reaching nuclear spin polarization (*P*) of >50% in some cases. Therefore, we report on robust and inexpensive design of liquid N$_2$-based p-H$_2$ generator (o-p catalyst-filled copper tubing spiral, Fig. 1a) for operation at up to 35 atm (1). The produced exiting p-H$_2$ gas is quantified by 'real-time' NMR spectroscopy using bench-top 1.4 T NMR spectrometer. The design reproducibility has been evaluated with N=3 devices. Moreover, we investigated ortho-para catalyst activation using exposure to high temperature to achieve production rate of 1,000 sccm with ~48% p-H$_2$ fraction (Fig. 1b, 1). We anticipate the reported design can be employed for p-H$_2$ production at higher flow rates of up to 4,000 sccm (2). The utility of the reported device was further evaluated for SABRE-SHEATH hyperpolarization of concentrated sodium [1-^{13}C]pyruvate, a metabolic contrast agent under investigation in numerous clinical trials. The study yielded ^{13}C signal enhancement of over 14,000-fold (Fig. 1c) at clinical relevant magnetic field of 1 T corresponding to approximately 1.2% ^{13}C polarization – if near 100% parahydrogen would have been employed, the reported value would be tripled to ^{13}C polarization of 3.5% (1).

REFERENCES: 1) Chapman et al. *Anal. Chem.* **2021** (accepted). **2**) Nantogma et al. *Anal. Chem.* **2021**, 10.1021/acs.analchem.0c05129.
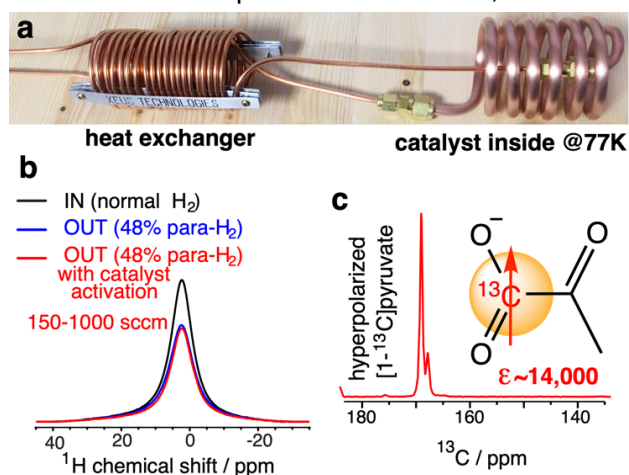
Figure 1. a) Annotated photo of p-H$_2$ generator for operation in liquid N$_2$ bath (77 K); b) Parahydrogen quantification using 1.4 T bench-top NMR spectrometer using 8 atm gas samples: 1024 scans, SW=5 kHz, t$_{acq}$=52 ms, ~102 s experimental time; c) NMR spectrum of SABRE-SHEATH hyperpolarized sodium [1-^{13}C]pyruvate yielding ^{13}C signal enhancement >14,000-fold at 1 T corresponding to approximately 1.2% ^{13}C polarization.

Pilot Quality Assurance Study of Batch-Mode Clinical-Scale Automated Generation-3 Xenon-129 Hyperpolarizer

Md Raduanul H. Chowdhury,[1] Jonathan R. Birchall,[1] Peter Nikolaou,[2] Michael J. Barlow,[3] Anton Shcherbakov,[4,5] Boyd M. Goodson,[6] Eduard Y. Chekmenev[1,7]

[1]Department of Chemistry, Ibio, Karmanos Cancer Institute, Wayne State University, Detroit, MI 48202, USA
[2]XeUS Technologies LTD, Nicosia, Cyprus
[3]Sir Peter Mansfield Imaging Centre, University of Nottingham, Nottingham, NG7 2RD, United Kingdom
[4]Smart-A, Perm, Perm Region, 614000, Russia, **[5]**Custom Medical Systems (CMS) LTD, Nicosia, Cyprus
[6]Department of Chemistry and Biochemistry, Southern Illinois University, Carbondale, Illinois 62901, USA
[7]Russian Academy of Sciences, Moscow, 119991, Russia

Dynamic detection of lung functionality is challenging using conventional pulmonary MRI largely because of low proton density in the lung. Using hyperpolarized (HP) ^{129}Xe as a contrast agent in MRI for the detection of lung's ventilation, diffusion and gas exchange process can mitigate the challenges of lung's dynamic detection. The major complications associated with the use of HP Xe gas is the cost and complexity associated with the polarization process. NMR hyperpolarization increases the differences between two nuclear spin state far beyond thermal equilibrium level, and this is done by the process called Spin-Exchange Optical Pumping (SEOP). We use a clinical-scale batch-mode generation-3 polarizer device to perform the SEOP process to generate high degree of polarization with fast build-up rates, Figure 1a-c. As a part of our Quality Assurance (QA) study we performed several sweeping experiments of key operational parameters which will establish a robust operational range e.g., sweeping resonance frequency, electromagnet current, and RF pulse duration, temperature, and others. The consistency and reproducibility of the production of HP Xe gas using the device is one of its key features, as in this QA study it took ~700 SEOP cell refill for a significant drop in polarization. We observed no substantial deterioration of SEOP cell performance even with ~600 gas mixture refills of the SEOP cell (in first fill %P_{max} = 52.4±1.7%, T_b = 18.9±2.1 mins and after 600 refills %P_{max} = 40.5±1.3%, T_b = 18.7±1.9 mins), Figure 1d. Moreover, the quantitative trends of the SEOP cell's T_1 values ingrained the observations. This high level of polarization with fast buildup-rates accompanied with high degree of consistency will pave the way for the future in vivo imaging studies and further will make it feasible for clinical use.

References: Birchall, J. R.; Nikolaou, P.; Coffey, A. M.; Kidd, B. E.; Irwin, R. K.; Murphy, M.; Molway, M.; Bales, L. B.; Goodson, B. M.; Barlow, M. J.; Chekmenev, E. Y., Batch-Mode Clinical-Scale Optical Hyperpolarization of Xenon-129 Using an Aluminum Jacket with Rapid Temperature Ramping. *Anal. Chem.* **2020,** *92* (6), 4309-4316.
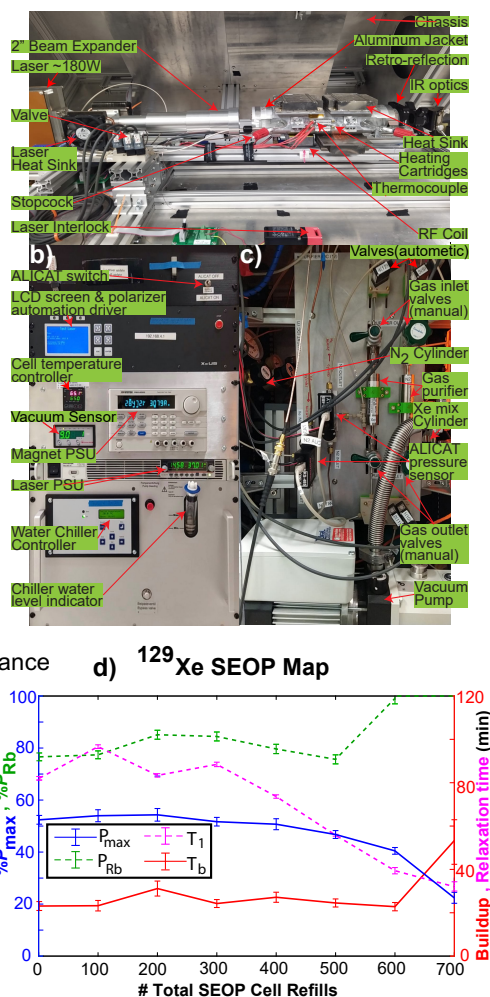
Figure 1. a) Annotated photo of open upper chassis of GEN-3 hyperpolarizer; b) Hyperpolarizer front panel; c) Internal hyperpolarizer gas-handling manifold; d) QA study data of ^{129}Xe polarization (%P_{max}), Rb polarization (P_{Rb}), buildup time-constant (T_b) and relaxation time (T_1) as a function of the SEOP cell refill cycle count at 75 °C.

Next-Generation Equipment for Parahydrogen-Based Hyperpolarization Experiments

Shiraz Nantogma,[a] Baptiste Joalland,[a] Ken Wilkens[b] and Eduard Y. Chekmenev[a,c]

[a] Department of Chemistry, Integrative Biosciences (Ibio), Wayne State University, Detroit, MI, 48202, USA
[b] Vanderbilt University Institute of Imaging Science (VUIIS), Nashville, TN 37232, USA
[c] Russian Academy of Sciences, Leninskiy Prospekt 14, Moscow, 119991, Russia

Parahydrogen-based polarization (PHIP) methods enable enhancement of NMR signals by several orders of magnitude and have significant translational potential for next-generation MRI contrast agents. The effectiveness of PHIP experiments depends on the level of parahydrogen enrichment and the manipulation of reaction conditions such as temperature, magnetic field, sample shuttling and sample detection times. We present an integrated PHIP polarizer for utility in a wide variety of parahydrogen-based hyperpolarization experiments in microtesla magnetic fields. The device features automated degaussing, regulated parahydrogen flow and pressure control, non-magnetic variable temperature module and many others. We report on the recent advancement in automated equipment for parahydrogen enrichment to >98.5% at a production rate of 4 standard liters per minute. This is made possible by the use of 3/16 in. outside diameter copper spiral tubing filled with ~20g iron-oxide catalyst. Contact time of parahydrogen with the catalyst under cryogenic temperature is optimized and well regulated by the use of a pulsed injection system to yield production rate of 4 standard liters per minute.
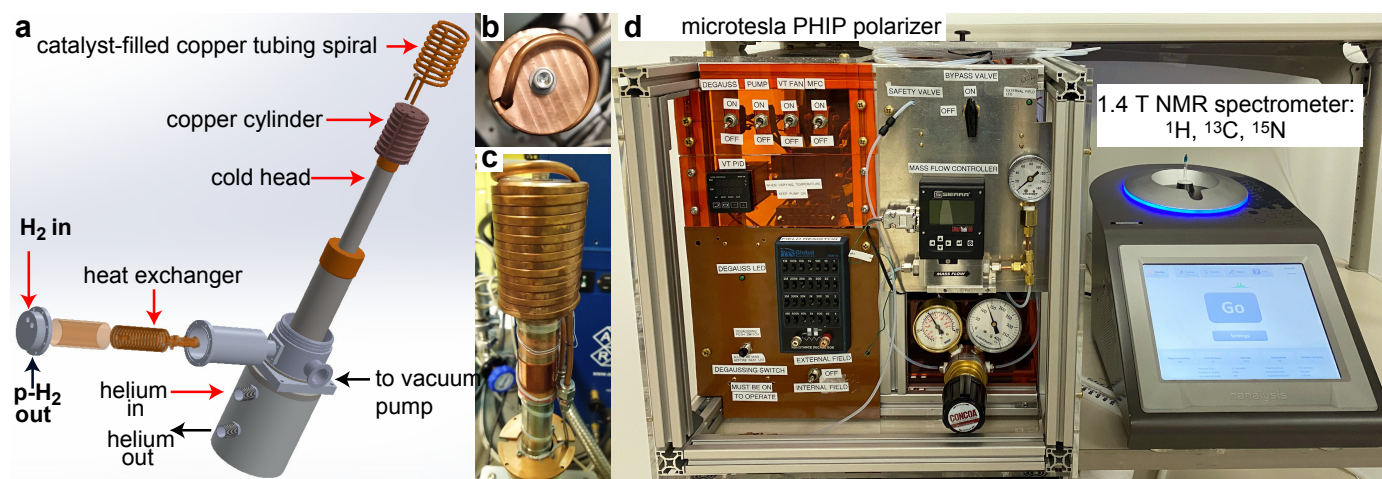
Figure 1. a) Annotated 3D rendering of cold head assembly of parahydrogen cold head; b) Top view of catalyst filled spiral with the top winding running along the length of copper core; c) Side view of catalyst filled spiral sitting on the cold head. The tubing employed in the heat exchanger is made of stainless steel; d) Integrated microtesla PHIP polarizer (mark 2.2) and a benchtop 1.4 T ^{1}H/^{13}C/^{15}N NMR spectrometer on a portable laboratory bench for PHIP experimentations.

REFERENCES: **(1)** Nantogma, S.; Joalland, B.; Wilkens, K.; Chekmenev, E. Y., Clinical-Scale Production of Nearly Pure (>98.5%) Parahydrogen and Quantification by Benchtop NMR Spectroscopy. *Anal. Chem.* **2021,** *93* (7), 3594–3601.
(2) Joalland, B.; Nantogma, S.; Chowdhury, M. R. H.; Nikolaou, P.; Chekmenev, E. Y., Magnetic Shielding of Parahydrogen Hyperpolarization Experiments for the Masses. *Magn. Reson. Chem.* **2021**, doi: 10.1002/mrc.5167.